

ADVERTIMENT. La consulta d'aquesta tesi queda condicionada a l'acceptació de les següents condicions d'ús: La difusió d'aquesta tesi per mitjà del servei TDX (www.tesisenxarxa.net) ha estat autoritzada pels titulars dels drets de propietat intel·lectual únicament per a usos privats emmarcats en activitats d'investigació i docència. No s'autoritza la seva reproducció amb finalitats de lucre ni la seva difusió i posada a disposició des d'un lloc aliè al servei TDX. No s'autoritza la presentació del seu contingut en una finestra o marc aliè a TDX (framing). Aquesta reserva de drets afecta tant al resum de presentació de la tesi com als seus continguts. En la utilització o cita de parts de la tesi és obligat indicar el nom de la persona autora.

ADVERTENCIA. La consulta de esta tesis queda condicionada a la aceptación de las siguientes condiciones de uso: La difusión de esta tesis por medio del servicio TDR (www.tesisenred.net) ha sido autorizada por los titulares de los derechos de propiedad intelectual únicamente para usos privados enmarcados en actividades de investigación y docencia. No se autoriza su reproducción con finalidades de lucro ni su difusión y puesta a disposición desde un sitio ajeno al servicio TDR. No se autoriza la presentación de su contenido en una ventana o marco ajeno a TDR (framing). Esta reserva de derechos afecta tanto al resumen de presentación de la tesis como a sus contenidos. En la utilización o cita de partes de la tesis es obligado indicar el nombre de la persona autora.

WARNING. On having consulted this thesis you're accepting the following use conditions: Spreading this thesis by the TDX (www.tesisenxarxa.net) service has been authorized by the titular of the intellectual property rights only for private uses placed in investigation and teaching activities. Reproduction with lucrative aims is not authorized neither its spreading and availability from a site foreign to the TDX service. Introducing its content in a window or frame foreign to the TDX service is not authorized (framing). This rights affect to the presentation summary of the thesis as well as to its contents. In the using or citation of parts of the thesis it's obliged to indicate the name of the author



UNIVERSITAT POLITÈCNICA DE CATALUNYA
BARCELONATECH

Departament de Teoria del Senyal
i Comunicacions



CONTRIBUTIONS TO GNSS-R EARTH REMOTE SENSING FROM NANO-SATELLITES

Ph.D. Thesis Dissertation by

Hugo Carreno-Luengo

Department of Signal Theory and Communications, Universitat Politècnica de
Catalunya – BarcelonaTech and Institute for Space Studies of Catalonia

Submitted to the Universitat Politècnica de Catalunya (UPC)
in partial fulfillment on the requirements for the degree of

Barcelona, November 2015

Advisor

Prof. Adriano José Camps Carmona



Acta de calificación de tesis doctoral

Curso académico:

Nombre y apellidos

Programa de doctorado

Unidad estructural responsable del programa

Resolución del Tribunal

Reunido el Tribunal designado a tal efecto, el doctorando / la doctoranda expone el tema de la su tesis doctoral titulada _____.

Acabada la lectura y después de dar respuesta a las cuestiones formuladas por los miembros titulares del tribunal, éste otorga la calificación:

☐ NO APTO ☐ APROBADO ☐ NOTABLE ☐ SOBRESALIENTE

(Nombre, apellidos y firma)		(Nombre, apellidos y firma)	
Presidente/a		Secretario/a	
(Nombre, apellidos y firma)	(Nombre, apellidos y firma)	(Nombre, apellidos y firma)	
Vocal	Vocal	Vocal	

_____, _____ de _____ de _____

El resultado del escrutinio de los votos emitidos por los miembros titulares del tribunal, efectuado por la Escuela de Doctorado, a instancia de la Comisión de Doctorado de la UPC, otorga la MENCIÓN CUM LAUDE:

☐ SÍ ☐ NO

(Nombre, apellidos y firma)		(Nombre, apellidos y firma)	
Presidente de la Comisión Permanente de la Escuela de Doctorado		Secretario de la Comisión Permanente de la Escuela de Doctorado	

Barcelona a _____ de _____ de _____

Acknowledgements

I would like to thank the Institute of Space Studies of Catalonia (IEEC) for my Ph.D. fellowship.

I would like to specially thank my Ph.D. Thesis advisor, Prof. Adriano Camps (UPC), for his guidance, dedication, advices and funding during these years.

I would like to thank Dr. Cinzia Zuffada (NASA-JPL), Dr. Manuel Martín-Neira (ESA-ESTEC) and Dr. Chris Ruf (University of Michigan) for their participation in the external review. Their comments, observations and suggestions have been included in this Ph.D. Thesis Dissertation.

I would like to thank the REXUS/BEXUS team for their collaboration, help and advice during the two stratospheric balloon campaigns. Special thanks to Dr. Natacha Callens (ESA) and Mr. Alexander Kinnaird (SSC) for their help during the flight campaign, and to Mr. Sylvain Vey (ESA) for his advice during the thermal analysis.

I would like to thank all the people of the Department of Signal Theory and Communications (TSC) for their support during these years, and for the collaboration during the project to several students (P. Vila, J.F. Munoz, A. Amèzaga, R. Olivé, D. Vidal, A. Cortiella, A. Bolet, J. Jané, J. Querol, G. Forte, and R. Díez) and to Dr. Xavi Bosch-Lluís, Dr. Hyuk Park, and Dr. Fran Fabra for their comments. I would like to thank Mrs. Pons and Khoe from the administration of the Department of TSC for their work and their contribution to the project specially during the BEXUS 17 campaign. Also special thanks to S. Cornara (Deimos Space), M. Hagenfeldt (Deimos Space), P. Palomo (Deimos Space), N. Catarino (Deimos Engenharia), and J. Carola (Deimos Engenharia) for the collaboration in the development of the ³Cat-2 space mission. Also special thanks to A. Rius (IEEC/ICE/CSIC) and E. Cardellach (IEEC/ICE-CSIC) to allow me the use of the data sets of both Baltic Sea air-borne experiments.

This project has received funding from the European Union's Seventh Framework Programme for research, technological development and demonstration under grant agreement "European GNSS-R Environmental Monitoring" no FP7-607126-E-GEM (Online Available: <http://www.e-gem.eu>), by the project "Aplicaciones avanzadas en radio ocultaciones y dispersometría utilizando señales GNSS y otras señales de oportunidad" of the Spanish Ministerio de Ciencia e Innovación (MICINN), grant no

AYA2011-29183-C02-01, by the ICREA Academia Awards 2009 and 2015, by the IEEC, and by the Helmholtz-Centre Potsdam - GFZ German Research Centre for Geosciences.

...and justice for all

Preface

The use of radio-navigation signals to perform Earth Remote Sensing is nowadays a matter of analysis by the Global Navigation Satellite Systems Reflectometry (GNSS-R) community. The access to space-borne data sets will benefit the evaluation of the performance of this passive approach for Earth Observation. On the other side, nano-satellites offer the possibility to change the paradigm of traditional space-borne missions in a much more cost-effective manner.

This Ph.D Thesis arises in this framework with the objective to study the feasibility to derive scientifically valuable geophysical parameters using GNSS-R data collected from a nano-satellite. The core of this Dissertation is: a) to find “the” solution to the problem imposed by time, budget, scientific requirements and the “unknown unknowns” of pioneer nano-sat technology; and b) to develop the satellite with a GNSS-R payload, to get it launched into space, and download reflectometry data. The author (HCL) has been the Principal Investigator (PI) of the BEXUS 17 and 19, and has coordinated a group of more than 10 undergraduate students who have been involved in hardware activities and subsystems tasks of both the payload and the platform.

Contents

Acknowledgements	v
Preface	ix
Contents	xi
List of Figures	xvii
List of Tables	xxix
List of Acronyms	xxxiii
PART I: INTRODUCTION	1
1. MOTIVATION	3
1.1 Justification of the work	4
1.2 Ph. D. Thesis structure	5
2. STATE OF THE ART	7
2. State of the art and historical overview	8
2.1 Radar interferometry from a single satellite	10
2.1.1 SWOT mission	10
2.1.2 CryoSat mission	13
2.2 Bistatic radar within a constellation of cooperative radar altimeters	15
2.3 Bistatic radar using GNSS reflected signals	15
3. FUNDAMENTALS ASPECTS OF GLOBAL NAVIGATION SATELLITE SYSTEMS REFLECTOMETRY	19
3.1 Introduction	20
3.2 Multi-constellation signals of opportunity	21
3.2.1 Global Positioning System (GPS)	21
3.2.2 Global Navigation Satellite System (GLONASS)	22
3.2.3 Galileo	23
3.3 GNSS signals structure	26
3.4 Multi-static scatterometry	29
PART II: THEORETICAL ELEMENTS	33
4. FUNDAMENTALS ASPECTS OF GNSS-R SCATTEROMETRY AND ALTIMETRY	35
4.1 GNSS-R over ocean	36
4.1.1 The ocean surface	36
4.1.2 The scattering of GNSS signals from the ocean surface	37

4.1.3 The main fundamental scientific observable: Delay Doppler Map (DDM).....	39
4.2 GNSS-R over boreal forests	41
4.2.1 Introduction to polarimetric scattering	41
4.2.2 The EMISVEG simulator	44
4.2.3 Simulations of the reflectivity over forests	49
4.2.4 Conclusions	55
PART III: EXPERIMENTAL VALIDATION OF THE ³CAT-2 PAYLOAD	57
5. THE RECONSTRUCTED GNSS-R TECHNIQUE: rGNSS-R	59
5.1 Introduction	60
5.2 The PYCARO instrument.....	62
5.3 Field experiments description: Cerdanilla's reservoir and Mediterranean Sea	66
5.4 Altimetric precision	70
5.5 Accuracy dependence on the elevation angle.....	75
5.6 Conclusions	76
6. EMPIRICAL SCATTEROMETRY STUDY IN THE CIEM WAVE CHANNEL	79
6.1 Introduction	80
6.2 Experiment description.....	82
6.2.1 Experimental set-up.....	82
6.2.2 Scenario and ground truth data.....	85
6.3 Experimental results: methodology and discussion	88
6.3.1 Number of specular points inside the scattering area	88
6.3.2 Water surface height measurements	93
6.3.3 Analysis of the coherent and incoherent components after retracking....	97
6.3.4 Evaluation of the effective small scale surface roughness	102
6.4 Final discussions.....	105
6.5 Conclusions	105
7. ESA AIRBORNE FLIGHTS OVER THE BALTIC SEA	107
7.1 Introduction	108
7.2 Altimetric performance	109
7.2.1 Conventional GNSS-R or complex cross-correlation technique using the clean code replica approach	109

7.2.2 Altimetric tracking point	111
7.2.3 Expected achievable height precision	113
7.3. Experiment description.....	115
7.3.1 Experimental set-up.....	115
7.3.2 Altimetric scenario	117
7.4 Results	118
7.4.1 Reliability of the theoretical model for height precision estimation	119
7.4.2 Height precision analysis.....	120
7.4.2.1 Achieved height precision	120
7.4.2.2 Comparative analysis with other airborne experiments	125
7.4.3. Dependence of the accuracy with the elevation angle.....	126
7.4.4. Relative mean dynamic topography	127
7.4.5 Sea slope measurement.....	129
7.5 Summary and conclusions	130
8. ESA BEXUS 17: CROSS-POLAR L1 C/A GPS SIGNALS	133
8.1 Introduction	134
8.2 Experimental set-up.....	135
8.3 First experimental evaluation of the reflected signals over boreal forests	138
8.4 First analysis of the total scattered field	150
8.5 Summary and conclusions	156
9. ESA BEXUS 19: MULTI-CONSTELLATION, DUAL-BAND AND DUAL-POLARIZATION SIGNALS	157
9.1 Introduction	158
9.2 Experimental set-up.....	159
9.3 Theoretical framework	161
9.4 Experimental results	163
9.4.1 Analysis of the coherent-to-incoherent scattering ratio.....	163
9.4.2 Scattering properties over boreal forests	169
9.4.3 Reflectivity maps.....	172
9.5 Summary and conclusions	177
10. ESA BEXUS 19: FIRST GNSS-R MULTI-CONSTELLATION POLARIMETRIC MEASUREMENTS AT DUAL-BAND	179
10.1 Introduction	180
10.2 Polarimetric measurements over boreal forests and lakes.....	181

10.3 Final discussions.....	188
10.4 Conclusions	189
PART IV: TOWARDS A SPACE-BORNE MULTI-CONSTELLATION, DUAL-FREQUENCY AND DUAL-POLARIZATION GNSS-R MISSION	191
11. ³Cat-2; AN EXPERIMENTAL NANO-SATELLITE FOR GNSS-R EARTH OBSERVATION: MISSION CONCEPT AND ANALYSIS	193
11.1 Introduction	194
11.2 Mission objectives	197
11.3 Mission concept.....	198
11.3.1 Orbit selection	198
11.3.2 Platform selection.....	198
11.3.3 Payload	201
11.3.4 In-orbit operations	206
11.4 Platform subsystems.....	208
11.4.1 Mechanical structure	208
11.4.2 Telemetry, tracking and command.....	210
11.4.3 Attitude determination and control system.....	212
11.4.4 Command and data handling system.....	214
11.4.5 Electrical power system.....	215
11.5 Mission analysis	217
11.5.1 Orbit evolution analysis.....	217
11.5.2 Mission budgets.....	221
11.6 Discussions and conclusions	229
12. CONCLUSIONS AND FUTURE RESEARCH LINES	231
12.1 Summary and conclusions.....	232
12.2 Future research lines.....	238
12.3 List of Publications.....	239
12.4 Participation in relevant projects	241
APPENDIX A: BEXUS EXPERIMENT SET-UP.....	243
A.1 Experiment description.....	244
A.1.1 Experiment set-up.....	244
A.2 Experiment interfaces	245
A.2.1 Mechanical.....	245

A.2.2 Electrical	249
A.2.3 Radio frequencies	249
A.2.4 Thermal.....	249
A.3 Main experiment components	250
A.4 Mechanical design	253
A.5 Electronics design.....	254
A.5.1 Electrical power system.....	254
A.5.2 Grounding strategy	255
A.6 Thermal design	256
A.7 Power system design	258
A.8 Software design	259
A.8.1 Command and data handling system	259
A.8.2 Ground station	264
A.9 Attitude determination system.....	265
A.10 Testing plan	266
A.11 Launch campaign preparation	269
APPENDIX B: ³Cat-2 REQUIREMENTS AND CONSTRAINTS	273
APPENDIX C: ³Cat-2 REQUIREMENTS TRACEABILITY MATRIX	289
APPENDIX D: ³Cat-2 RISK REGISTER.....	295
Bibliography.....	301

List of Figures

Figure 2.1. Artist's view of TOPEX/Poseidon [4].....	9
Figure 2.2. Artist's view of SWOT [1]	10
Figure 2.3. Spatial and temporal resolution inter-comparison between conventional nadir-looking radar altimeters and SWOT [1]	11
Figure 2.4. Artist's view of SWOT performance [1].....	12
Figure 2.5. Artist's view of CryoSat [10]	14
Figure 2.6. Accomodation and deployment of the PARIS antenna [3]	16
Figure 2.7. Proposed back-to-back double phased array antenna of PARIS-IoD [3]	17
Figure 3.1. Sketch of the GNSS-R approach. A receiver above the Earth's surface collects the direct and the Earth-reflected signals coming from areas around the specular points, the glistening zones.....	20
Figure 3.2. Graphical description of the GNSS signal spectra	25
Figure 3.3. The PAssive Reflectometry and Interferometry System (PARIS) concept [2].....	29
Figure 3.4. Number of specular reflection points over the geoid as a function of their latitude for a) GPS, b) GLONASS and c) Galileo (5 satellites). Parameters: Full elevation range $[0^\circ, 90^\circ]$, all satellites in view, temporal sampling 100 s.....	30
Figure 3.5. Iso-delay and iso-Doppler lines in a bistatic configuration [2]	31
Figure 4.1. (a) Scattering over the ground surface, (b) direct scattering over the canopy, (c) multiple scattering involving both the soil and the canopy, and (d) multiple scattering involving both the soil and the trunks.	47
Figure 4.2. (a) Simulated scattering area for an elevation angle of $\theta_e = 72^\circ$, (b) simulated scattering area for an elevation angle of $\theta_e = 54^\circ$, (c) simulated scattering area for an elevation angle of $\theta_e = 35^\circ$, (d) simulated 3-D geometry of a single tree over a tilted soil surface	50
Figure 4.3. Simulated reflectivity for a biomass density of 725 tress/ha over leaves: (a) Rayleigh approximation ideal needle, (b) Rayleigh approximation needle, (c) Generalized Rayleigh Gans approximation needle; and leaves-soil interactions: (d) Rayleigh approximation ideal needle-Choudhury, (e) Rayleigh approximation needle-Choudhury, and (f) Generalized Rayleigh Gans approximation needle-Choudhury	53

Figure 4.4. Cross- and co-polar reflectivity simulations over forests: (a,b,c) direct scattering (canopy, soil) and (d,e,f) multiple scattering (canopy-soil interactions), for a biomass density of (a,d) 725 trees/ha, (b,e) 150 trees/ha, and (c,f) 72 trees/ha	54
Figure 4.5. Increment of (a) cross- and (b) co-polar reflectivity over forests from a biomass density of 72 trees/ha to 725 trees/ha.....	55
Figure 5.1. (a) View of the PYCARO instrument connected to a laptop. (b) View of the two Antcom [®] omnidirectional antennas attached to a 3 m boom used to collect both, the direct and the Earth-reflected GPS signals	60
Figure 5.2. Aerostatic balloon where the experiment took place. Arrow indicates position of the 2 m mast.....	62
Figure 5.3. Skyvan Short SC-7 during the preparatory activities. PYCARO was tested for first time over rough sea surface conditions.....	62
Figure 5.4. Block diagram of the PYCARO instrument. The correlation approach used in the down-looking channel by PYCARO providing P code processing of the encrypted GPS signals without knowledge of the encrypted code, in addition to the C/A code cGNSS-R is sketched. Both the up-looking and the down-looking channels use a similar correlation approach	63
Figure 5.5. (a) View of the surface water at the Cernadilla water reservoir during the first experiment. (b) View of the Pont del Petroli pier. The experimental set-up during the second field experiment was placed at the edge of the pier	64
Figure 5.6. (a) . View of the Laboratori d'Enginyeria Marítima facility at the Pont del Petroli. (b) View of the monostatic K-band (26 GHz) radar altimeter VEGAPULS 62 [76] used during the Mediterranean Sea experiment	65
Figure 5.7. Arrangement of the instrumental set-up during the Pont del Petroli pier experiment.....	65
Figure 5.8. Sample sea wave`s profile as a function of the GPS time provided by the monostatic K-band (26 GHz) radar VEGAPULS 92 and PYCARO employing both the C/A-L1 and P(Y)-L2 signals. Satellite`s elevation angle $\theta_e = 70^\circ$	66
Figure 5.9. (a) Correlation between the temporal series (~ 9 s) of the measured SSH using the monostatic radar and the PYCARO instrument (C/A GPS code)	68
Figure 5.9. (b) Correlation between the temporal series (~ 9 s) of the measured SSH using the monostatic radar and the PYCARO instrument (P(Y) GPS code)	68
Figure 5.10. (a) Sample Sea Surface Height (SSH) fluctuations as measured by the monostatic K-band radar during the experiment over the Mediterranean Sea	69

Figure 5.10. (b) Phase evolution of the tracked GPS signals after scattering on the Mediterranean Sea during the experiment at the Pont del Petroli pier	69
Figure 5.11. C/A and P(Y) derived height precision as a function of the incoherent averaging in case of smooth surface at mid-low satellite's elevation angles (θ_e from 50° to 55°), and a mean platform's height over the surface $h = 65$ m.....	71
Figure 5.12. C/A and P(Y) derived height precision as a function of the incoherent averaging in case of rough surface at mid-low satellite's elevation angles (θ_e from 35° to 42°), and a mean platform's height over the surface $h = 4.76$ m.....	71
Figure 5.13. Improvement factor of P(Y) altimetry as compared to C/A altimetry in a smooth surface scenario at mid-low satellite's elevation angles (θ_e from 50° to 55°), and a mean platform's height over the surface $h = 65$ m	72
Figure 5.14. Improvement factor of P(Y) altimetry as compared to C/A altimetry in a rough surface scenario at mid-low satellite's elevation angles (θ_e from 35° to 42°), and a mean platform's height over the surface $h = 4.76$ m	72
Figure 5.15. Comparison of the ratio of the reflected and the direct-SNR for the C/A and the P(Y) GPS codes in case of rough surface at high and mid-low satellite's elevation angles and a mean platform's height over the surface $h = 4.76$ m.....	73
Figure 5.16. C/A and P(Y) derived height precision as a function of incoherent averaging in case of rough surface at high satellite's elevation angles (θ_e from 70° to 75°), and a mean platform's height over ther surface $h = 4.76$ m.....	74
Figure 5.17. Improvement factor of P(Y) altimetry as compare with C/A altimetry in a rough surface scenario at high satellite's elevation angle (θ_e from 70° to 75°), and a mean platform's height over the surface $h = 4.76$ m	74
Figure 6.1. View of the CIEM wave channel at the Laboratori d'Enginyeria Marítima (Universitat Politècnica de Catalunya). Wave channel dimensions are: width = 3 m, length = 100 m, and depth = 5 m	81
Figure 6.2. CESSNA EC-KOQ at the Aeroclub Barcelona-Sabadell.....	82
Figure 6.3. Sea Surface Height (SSH) as measured by PYCARO and Jason-2. These results correspond to an aircraft experiment performed over the Mediterranean Sea on September 2012	82
Figure 6.4. View of the experiment set-up: SMU 200 A vector signal generator, PYCARO instrument, and the two 15 dB gain antenna arrays.....	83
Figure 6.5. View of the HR Wallingford Wave Probe Monitor used as a reference system during the experiment (encircled on the left hand side)	84

Figure 6.6. (a) Correlation celerity vs. wave height for a SWH = 36 cm. (b) Correlation celerity vs. wave height for a SWH = 64 cm. (c) Correlation period vs. wave height for a SWH = 36 cm. (d) Correlation period vs. wave height for a SWH = 64 cm. (f) Slopes distribution for a SWH = 36 cm. (c) Slopes distribution for a SWH = 64 cm.....	86
Figure 6.7. Clusters of specular points distributed over the water surface profile as computed using the temporal series of data provided from the HR Wallingford wave probe monitor for a SWH = 36 cm and $\theta_e = 45^\circ$	88
Figure 6.8. Specular points distributions computed using the temporal series of data provided from the HR Wallingford wave probe monitor for a: (a) SWH = 36 cm and $\theta_e = 45^\circ$, (b) SWH = 64 cm and $\theta_e = 45^\circ$, (c) SWH = 36 cm and $\theta_e = 86^\circ$, and (d) SWH = 64 cm and $\theta_e = 86^\circ$	90
Figure 6.9. Analysis of the electromagnetic interaction of the GPS signals and the scattering surface in a bistatic scenario. The phase (after retracking) distribution of the scattered field is time and space-located over the temporal evolution of the SSH as measured by the PYCARO reflectometer. This analysis has been performed with a SWH = 36 cm, and an elevation angle of $\theta_e = 86^\circ$	91
Figure 6.10. Normalized reflected signal power amplitude fluctuations due to the phase (after retracking) changes induced by the scattering surface. This analysis has been performed with a SWH = 36 cm, and an elevation angle of $\theta_e = 86^\circ$	91
Figure 6.11. Surface height distributions obtained using the HR Wallingford wave probe monitor for a: (a) SWH = 36 cm and (b) SWH = 64 cm. Corresponding wave surface spectra for a: (c) SWH = 36 cm and (d) SWH = 64 cm at the CIEM	93
Figure 6.12. For an elevation angle of (a,b) $\theta_e = 60^\circ$, (c,d) $\theta_e = 75^\circ$, (e,f) $\theta_e = 86^\circ$, sample waves profile as measured by PYCARO using the C/A code and by the water level sensor for a (a,c,e) SWH = 36 cm and for (d,e,f) SWH = 64 cm.....	94
Figure 6.13. 6.13. For an elevation an elevation angle of (a,b) $\theta_e = 60^\circ$, (c,d) $\theta_e = 75^\circ$, (e,f) $\theta_e = 86^\circ$, water surface spectra as measured by PYCARO using the C/A code for (a,c,e) SWH = 36 cm, and (b,d,f) for SWH = 64 cm.....	96
Figure 6.14. 6.14. At an elevation angle of (a,b) $\theta_e = 60^\circ$, (c,d) $\theta_e = 75^\circ$, and (e,f) $\theta_e = 86^\circ$, (a,c,e) histogram of the phase and (d,e,f) amplitude of the signals after retracking for a SWH = 36 cm.....	98
Figure 6.15. Scattered field complex plane representation for a SWH = 36 cm at an elevation angle of (a) $\theta_e = 60^\circ$, (b) 75° , and (c) 86°	99

Figure 6.16. SNR of the reflected signal for three different surface states and for an elevation angle in the range from $\theta_e = 45^\circ$ to $\theta_e = 86^\circ$. Figure obtained using a best-fit approximation of the experimental data over elevation ranges at $\theta_e = 45^\circ$, $\theta_e = 60^\circ$, $\theta_e = 75^\circ$, and $\theta_e = 86^\circ$	101
Figure 6.17. Theoretical log-logistic PDF approximation to the small scale surface roughness distributions for an elevation angle of (a,b) $\theta_e = 45^\circ$, (c,d) $\theta_e = 60^\circ$, (e,f) $\theta_e = 75^\circ$, (g,h) $\theta_e = 86^\circ$; for (a,c,e,g) SWH = 36 cm and (b,d,f,h) for SWH = 64 cm,. Note: The distributions of the small scale surface roughness have been derived using the standard deviation of the signal before retracking	104
Figure 7.1. Skyvan Short SC-7 (Laboratory of Space Technology) at the Helsinki airport	115
Figure 7.2. (a) Trajectory of the Skyvan during the first experiment. (b) First flight instrumentation scheme. Note: PS 1, 2 are the power splitters 1 and 2, Topcon is a GPS receiver, and Eth is an Ethernet connection [108].....	116
Figure 7.3. (a) Trajectory of the Skyvan during the second experiment. (b) Second flight instrumentation scheme. Note: PS are the power splitters, Topcon and Trimble are GPS receivers, and Eth is an Ethernet connection [108]	116
Figure 7.4. Sample direct and reflected integrated waveforms during the first flight [$T_c = 1$ ms and $N_{inc} = 1,000$]	117
Figure 7.5. (a) Reflected waveform values at the point of maximum derivative. (b) Elevation angle of the satellite PRN12 as function of the GPS time. (c) Reflected waveform derivative values at the point of maximum derivative. (d) Validation of the theoretical precision expectation with real data from the second airborne experiment. Note: from GPS Time from ~ 5.35 h to ~ 6.35 h the elevation angles are larger than 75°	119
Figure 7.6. (a) Height precision: $h = 500$ m, θ_e from 73° to 76° , GPS Time from 16.4 h to 16.6 h, $v_{aircraft} = 302$ km/h. (b) Allan's standard deviation: $h = 500$ m, θ_e from 73° to 76° , GPS Time from 16.4 h to 16.6 h, $v_{aircraft} = 302$ km/h. (c) Height precision: $h = 150$ m, θ_e from 62° to 66° , GPS Time from 17.5 h to 17.7 h, $v_{aircraft} = 205$ km/h. (d) Allan's standard deviation: $h = 150$ m, θ_e from 62° to 66° , GPS Time from 17.5 h to 17.7 h, $v_{aircraft} = 205$ km/h. (e) Height precision: $h = 3,000$ m, θ_e from 66° to 85° , GPS Time from 5.4 h to 6.6 h, $v_{aircraft} = 237$ km/h. (f) Allan's standard deviation: $h = 3,000$ m, θ_e from 66° to 85° , GPS Time from 5.4 h to 6.6 h, $v_{aircraft} = 237$ km/h. (g) Height precision: $h = 3,000$ m, θ_e from 70° to 77° , GPS Time from 5.6 h to 6.2 h,	

$v_{\text{aircraft}} = 237 \text{ km/h}$. (h) Allan's standard deviation: $h = 3,000 \text{ m}$, θ_e from 70° to 77° , GPS Time from 5.6 h to 6.2 h, $v_{\text{aircraft}} = 237 \text{ km/h}$ 122

Figure 7.7. Accuracy analysis considerations with elevation angle and flight height parameters. The mean elevation angle of each GPS satellite is: $\theta_{e,\text{mean}} = 73^\circ$ (yellow), $\theta_{e,\text{mean}} = 46^\circ$ (red), $\theta_{e,\text{mean}} = 24^\circ$ (blue), $\theta_{e,\text{mean}} = 21^\circ$ (green). Note: Dispersion in measurements at the flight range from 150 m to 200 m, at 350 m, and at 500 m, is due to changes in the elevation angle of the GPS satellites during the experiment, since the evolution of the constellation's geometry with time.....126

Figure 7.8. (a) Sea surface topography provided by Jason-2 at the specular point for PRN 25. (b) Sea surface topography provided by GOLD-RTR at the specular point for PRN 25: $h = 500 \text{ m}$ height, θ_e from 73° to 76° , GPS Time from 16.4 h to 16.6 h, $v_{\text{aircraft}} = 302 \text{ km/h}$. (c) Sea surface topography provided by Jason-2 at the specular point for PRN 12. (d) Sea surface topography provided by GOLD-RTR at the specular point for PRN 12: $h = 3,000 \text{ m}$, θ_e from 80° to 84° , GPS Time from 5.5 h to 5.7 h, $v_{\text{aircraft}} = 237 \text{ km/h}$. (e) Difference between sea surface topography measured by Jason-2 and GOLD-RTR at the specular point for PRN 25: $h = 500 \text{ m}$ height, θ_e from 73° to 76° , GPS Time from 16.4 h to 16.6 h, $v_{\text{aircraft}} = 302 \text{ km/h}$. (f) Difference between sea surface topography measured by Jason-2 and GOLD-RTR at the specular point for PRN 12: $h = 3,000 \text{ m}$, θ_e from 80° to 84° , GPS Time from 5.5 h to 5.7 h, $v_{\text{aircraft}} = 237 \text{ km/h}$ 128

Figure 7.9. Analysis of the capability of the proposed technique to detect geoid undulation changes: $h = 3,000 \text{ m}$, θ_e from 82° to 84° , GPS Time from 5.6 h to 5.8 h, $v_{\text{aircraft}} = 237 \text{ km/h}$129

Figure 8.1. (a) BEXUS stratospheric balloon during take-off at Esrange Space Center. (b) Typical BEXUS configuration: $12,000 \text{ m}^3$ balloon, valve, cutter, parachute, Esrange Balloon Service System (EBASS), flight train, Argos GPS and Air Traffic Control (ATC) Transponder (AGT), strobe light, radar reflector, and gondola. Total length of the system is up to 75 m [130].....136

Figure 8.2. Flight height during the experiment as a function of the GPS Time (10 10 2013)137

Figure 8.3. The track of the BEXUS 17 during the experiment. The trajectory was a single track from the Esrange Space Center (latitude $67^\circ 53' \text{N}$, longitude $21^\circ 04' \text{E}$) to Juujarvi (latitude $66^\circ 24' \text{N}$, longitude $27^\circ 18' \text{E}$).....137

Figure 8.4. (a) Nadir-looking antenna inside the thermally insulating radome. (b) Image of the thermally insulating radome at the bottom of the gondola	138
Figure 8.5. Evolution of the coherent reflectivity over the different scattering contributing media of the forest (soil, canopy, canopy-soil, and soil-trunk) as a function of the elevation angle at a flight height of $h \sim 27,000$ m	143
Figure 8.6. (a) Ground truth plots in Krycklan (green) and Remningstorp (blue). (b) Krycklan site for airborne lidar height vs. airborne lidar-derived biomass [135] ...	144
Figure 8.7. Global map of forest height produced from NASA's ICESAT/GLAS, MODIS, and TRMM sensors [136]	144
Figure 8.8. (a) Scattering over the ground surface, (b) direct scattering over the canopy, (c) multiple scattering involving both the soil and the canopy, and (d) multiple scattering involving both the soil and the trunks	145
Figure 8.9. Total scattered field (over boreal forests) amplitude distribution histogram at a flight height of $h \sim 27,000$ m and for an elevation angle in the range $\theta_e = [35^\circ, 72^\circ]$. There are four main peaks (larger number of samples at these four identified amplitude levels): $\sim 50, \sim 190, \sim 420, \sim 520$ (A.U.).....	147
Figure 8.10. Iso-Range (green-lines) and Iso-Doppler (blue-lines) lines for different flight conditions: a) $h = 1,000$ m and $\theta_e = 45^\circ$, b) $h = 1,000$ m and $\theta_e = 75^\circ$, c) $h = 10,000$ m and $\theta_e = 45^\circ$, d) $h = 10,000$ m and $\theta_e = 75^\circ$, e) $h = 27,000$ m and $\theta_e = 45^\circ$, f) $h = 27,000$ m and $\theta_e = 75^\circ$	149
Figure 8.11. Reflected power evolution as a function of the flight height and the scattering media. This figure was derived using the highest peak of the WFs and it shows that the total reflected power is dominat by the coherent component since the evolution is roughly constant as a function of the flight height. Note that the variation of the elevation angle was low since the corresponding satellite was in the region around its maximum elevation angle. This situation is different to that in Fig. 8.9. In there, the variation of the elevation angle is high so that there are large variation of the reflected power.....	150
Figure 8.12. (a) Scattered field complex plane representation for a flight height $h = [0, 5,000]$ m, and an elevation angle in the range $\theta_e = [24^\circ, 35^\circ]$. (b) Scattered field complex plane representation for a flight height $h = [20,000, 25,000]$ m, and an elevation angle in the range $\theta_e = [21^\circ, 30^\circ]$. (c) Scattered field complex plane representation for a flight height $h \sim 27,000$ m, and an elevation angle in the range $\theta_e = [30^\circ, 43^\circ]$. (d) Scattered field complex plane representation for a flight height	

$h = [0, 5,000]$ m, and an elevation angle in the range $\theta_e = [66^\circ, 68^\circ]$. (e) Scattered field complex plane representation for a flight height $h = [20,000, 25,000]$ m, and an elevation angle in the range $\theta_e = [65^\circ, 71^\circ]$. (f) Scattered field complex plane representation for a flight height $h \sim 27,000$ m, and an elevation angle in the range $\theta_e = [57^\circ, 68^\circ]$	152
Figure 8.13. (a) Evolution of the ratio of the coherent to incoherent scattering as a function of the flight height and for an elevation angle in the range $\theta_e = [60^\circ, 70^\circ]$. (b) Evolution of the weight of the coherent to incoherent scattering as a function of the flight height and for an elevation angle in the range $\theta_e = [25^\circ, 45^\circ]$	154
Figure 8.14. (a) Carrier phase standard deviation distribution for a flight height of $h \sim 27,000$ m and an elevation angle $\theta_e = [58^\circ, 70^\circ]$. (b) Carrier phase standard deviation distribution for a flight height of $h \sim 27,000$ m and an elevation angle $\theta_e = [30^\circ, 40^\circ]$	155
Figure 9.1. BEXUS 19 stratospheric balloon during take-off at Esrange Space Center. Typical BEXUS configuration: 12,000 m ³ balloon, valve, cutter, parachute, Esrange Balloon Service System (EBASS), flight train, Argos GPS and Air Traffic Control (ATC) transponder (AGT), strobe light, radar reflector, and gondola. Total length of the system is up to 75 m [130]. Photo Credits: SNSB-K. Dannenberg	160
Figure 9.2. Up-looking patch antenna and down-looking antenna array inside the thermally insulating radomes on-board the BEXUS 19 gondola.....	161
Figure 9.3. Scattered complex field (peak of the complex waveform, T_c from Table 9.2, no incoherent averaging) for an elevation angle of $\theta_e = [45^\circ, 70^\circ]$ and a flight height $h \sim 27,000$ m. GPS L1 C/A (a) boreal forests and (b) lakes, GPS L2 C (c) boreal forests and (d) lakes	165
Figure 9.3. Scattered complex field (peak of the complex waveform, T_c from Table 9.2, no incoherent averaging) for an elevation angle of $\theta_e = [45^\circ, 70^\circ]$ and a flight height $h \sim 27,000$ m. GLONASS L2 C/A (e) boreal forests and (f) lakes, and Galileo E1 BC (g) boreal forests and (h) lakes.....	166
Figure 9.4. Height fluctuations of the scatterers and post coherent-correlation SNR over boreal forests for an elevation angle $\theta_e = [45^\circ, 70^\circ]$ and a flight height $h \sim 27,000$ m. GPS L1 C/A boreal forests (a,b), GPS L2 C boreal forests (c,d), GLONASS L2 C/A boreal forests (e,f), and Galileo E1 BC boreal forests (g,h)....	170

Figure 9.5. Along-track reflected phase oscillations and spectrograms for (a) and (c): GLONASS L2 CA (boreal forests), and for (b) and (d) GPS L2 C (lakes areas), respectively	172
Figure 9.6. Cross-polar reflectivity maps (LHCP-reflected) geolocated over the nominal specular points over boreals forests and lakes for GPS signals: (a) L1 C/A, (b) L2 C, (c) L1 P(Y), and (d) L2 P(Y)	175
Figure 9.7. Cross-polar reflectivity maps (LHCP-reflected) geolocated over the nominal specular points over boreals forests and lakes for GLONASS signals: (a) L1 C/A, (b) L2 C/A, (c) L2 P; and (d) Galileo E1 BC signals	176
Figure 10.1. Measured polarimetric ratios for a flight height of 27,000 m and an elevation angle $\theta_e = 70^\circ$ for (a) GPS L1 C/A, (b) GPS L2 C, (c) GPS L1 P(Y), and (d) GPS L2 P(Y)	185
Figure 10.2. Measured polarimetric ratios for a flight height of 27,000 m and an elevation angle $\theta_e = 70^\circ$ for (a) GLONASS L1 C/A, (b) GLONASS L2 C/A, (c) GLONASS L2 P; and for an elevation angle $\theta_e = 60^\circ$ for (d) Galileo E1 BC	186
Figure 11.1. Artist view of the 1U, 2U, and 6U CubeSat configurations considered during the ³ Cat-2 mission feasibility study: 1U (a), 2U, (b, c, d, e), 6U (f)	199
Figure 11.2. (a) Image of the ³ Cat-2 Engineering Model (EM) with the payload inside the 3 mm thickness Al anodised box (in black). (b) Image of the ³ Cat-2 Engineering Model (EM) with the payload inside the 3 mm thickness Al anodised box (in black)	201
Figure 11.3. (a) Image of the ³ Cat-2 EM: Payload OBC, magnetorquers, battery pack, UHF/VHF transceiver, 1U stack for switching matrix, 3 mm thickness payload Al box (3U stacks), aperture for star tracker, and UHF/VHF antennas deployment mechanisms. (b) Image of the ³ Cat-2 EM with the nadir-looking antenna array integrated at the top of the structure	202
Figure 11.4. Antenna array radiation patterns and gain values for both frequencies (L1, and L2) and for both polarizations (LHCP and RHCP)	204
Figure 11.5. Sketch of the main modules of the ³ COPS orchestrator. It identifies the internal modules (Payload Management Module (PMM), Automatic Module (AM) and Log Module (LOG)) and the internal/external interfaces. The orange arrows represent the connections with the payload subsystems, related with hardware interfaces. The grey arrows are related with the internal software interfaces. Image credits Deimos Engenharia	205

Figure 11.6. Satellite state diagram. The satellites operational modes are: Start-Up (SU), Sun-Safe (SS), Nominal and Survival. [O.6] The exits of the Nominal mode shall be: a) Exit to SS mode upon SS mode triggers (autonomously), b) exit to SS mode through Ground Station (GS) telecommands, c) exit to Survival mode upon SS mode triggers (autonomously), d) exit to Survival mode through GS telecommands. [O.12] The triggers of the SS mode shall be: a) EPS fault: Battery voltage < 90%, b) ADCS fault: Any failure that endangers power so that battery voltage < 90%, c) CDHS fault. [O.13] The SS mode exist shall be only possible by GS telecommands to: a) Nominal mode, b) Survival mode, c) SU mode. [O.17] The triggers of the Survival mode shall be: a) EPS critical fault: Battery voltage < 80%, b) ADCS critical fault: any failure that endangers power so that battery voltage < 80%, c) CDHS critical fault. [O.18] The Survival mode exist shall only possible to Sun Safe mode by GS telecommands. [O.57] The exits of the SU mode shall be: a) exit to Nominal mode upon SU mode triggers (autonomously), b) exit to Nominal mode through GS telecommands, c) exit to SS mode upon Start-up mode triggers (autonomously), d) exit to SS mode through GS telecommands, e) exit to Survival mode upon SU mode triggers (autonomously), f) exit to Survival mode through GS telecommands	206
Figure 11.7. Antenna radiation pattern of the two pairs (UHF-uplink, VHF-downlink) of orthogonal monopoles. Image credits ISIS Space	209
Figure 11.8. Configuration of the VHF (Ant S1 A1 and Ant S1 A2) and UHF (Ant S2 A1 and AntS2 A2) monopoles in the CubeSat. Image credits ISIS Space.....	210
Figure 11.9. Orbit evolution analysis as a function of the ballistic coefficient and the lifetime: Variation of the orbit mean altitude for a) $H_{ref} = 510$ km, and b) $H_{ref} = 613$ km. Mean LTAN variations for c) $H_{ref} = 510$ km, and d) $H_{ref} = 613$ km. Image credits Deimos Space	218
Figure 11.10. Maximum across-track angle required for global coverage from 6 to 10 days of revisit time as a function of the reference orbit altitude. Image credits Deimos Space	219
Figure 11.11. End-Of-Life (EOL) orbit mean altitude decay for a) $H_{ref} = 613$ km, and $A_{eff} = 0.022 \text{ m}^2$, b) $H_{ref} = 510$ km and $A_{eff} = 0.022 \text{ m}^2$, c) $H_{ref} = 613$ km, and $A_{eff} = 0.077 \text{ m}^2$, and d) $H_{ref} = 510$ km and $A_{eff} = 0.077 \text{ m}^2$. Image credits Deimos Space	220
Figure 11.12. Satellite temperature evolution as a function of the time	228
Figure A.1. TORMES 2.0 placement in the M-Egon gondola.	244

Figure A.2. TORMES 2.0 down-looking radome attached to the M-Egon gondola.	245
Figure A.3. TORMES 2.0 up and limb-looking radomes attached to the M-Egon gondola.	246
Figure A.4. Internal interface of the experiment with the gondola.	247
Figure A.5. Interface of the radome-1 with the gondola.	248
Figure A.6. Grounding sketch.	255
Figure A.7. View of the results of the achieved temperatures in the down-looking antenna in a steady situation. They have been provided by a finite analysis simulation using the package software ESATAN	256
Figure A.8. Sketch of the power strategy for “on ground” and “flight” configuration. During “on ground” activities the two battery inputs are substituted by external power	258
Figure A.9. Boot sequence process	260
Figure A.10. Telecommand management process	261
Figure A.11. Housekeeping management process	263
Figure A.12. Ground Station (GS) process	264
Figure A.13. Attitude Determination System (ADS) flow diagram	265
Figure A.14. Flow of the testing campaign for the complete experiment set-up.	266
Figure A.15. Flow of the testing campaign for the payload.	267
Figure A.16. Flow of the testing campaign for the platform.	267
Figure B.1. Body reference frame.	281

List of Tables

Table 3.1. Parameters of the GNSS signals: GPS L1 C/A, GPS L2 P(Y), GPS L2 C, Galileo E1 BC, GLONASS C/A L1 and L2, and GLONASS L2 P. (NA: Not Available).....	24
Table 6.1. Height of the antenna over the surface, sizes of the footprint, the first Fresnel zone and the scattering cells, and cutoff wavenumbers as a function of the elevation angle. The antenna footprint is obtained as the intersection at different angles (elevation angles) of a plane (water surface mean) with the antenna radiation pattern. The scattering cell is obtained as the area on the water surface that allows to scatter forward the GPS signals through the receiver antenna taking into account the slopes of the waves and the surface roughness.....	87
Table 6.2. Statistical analysis of the phase (after retracking) distribution of the scattered GPS signals over the CIEM wave channel at different elevation angles: $\theta_e = 60^\circ, 75^\circ$, and 86°	95
Table 6.3. Statistical analysis of the amplitude (after retracking) distribution of the scattered GPS signals over the CIEM wave channel at different elevation angles: $\theta_e = 60^\circ, 75^\circ$, and 86°	95
Table 6.4. Statistical analysis of the complex field distribution of the scattered GPS signals after retracking, over the CIEM wave channel at different elevation angles: $\theta_e = 60^\circ, 75^\circ$, and 86°	100
Table 6.5. Theoretical and experimental small scale roughness values, and correction term for SWH = 36 cm, and 64 cm for $\theta_e = 45^\circ, 60^\circ, 75^\circ$, and 86°	103
Table 7.1. Altimetric precision: $h = 500$ m, θ_e from 73° to 76° , GPS Time from 16.4 h to 16.6 h, $v_{\text{aircraft}} = 302$ km/h (values corresponding to Fig. 7.6a).....	123
Table 7.2. Altimetric precision: $h = 150$ m, θ_e from 62° to 66° , GPS Time from 17.5 h to 17.7 h, $v_{\text{aircraft}} = 205$ km/h (values corresponding to Fig. 7.6c).....	123
Table 7.3. Altimetric precision: $h = 3,000$ m, θ_e from 66° to 85° , GPS Time from 5.4 h to 6.6 h, $v_{\text{aircraft}} = 237$ km/h (values corresponding to Fig. 7.6e).....	124
Table 7.4. Altimetric precision: $h = 3,000$ m, θ_e from 70° to 77° , GPS Time from 5.6 h to 6.2 h, $v_{\text{aircraft}} = 237$ km/h (values corresponding to Fig. 7.6g)	124
Table 7.5. Jason-2 temporal and spatial data window during both experiments	127

Table 8.1. Amount of coherent scattering and incoherent scattering, asymmetry factor and residual phase std. deviation over soil, canopy, canopy-soil, and soil-trunk as a function of the flight height and the elevation angle	153
Table 9.1. Amount of coherent and incoherent scattering, reflected phase oscillations std. deviation over boreal forests and lakes as a function of the elevation angle for: GPS, GLONASS and Galileo signals at a flight height of $h \sim 27,000$ m.....	167
Table 9.2. Optimum delay and phase locked loop parameters used during the float phase of the experiment for GPS [146], GLONASS [147, 148] and Galileo signals [149].....	168
Table 9.3. Semi-major axis of the first chip iso-delay ellipse, semi-major axis of the first Fresnel zone at different elevation angles ($\theta_e = 45^\circ$ and $\theta_e = 70^\circ$) for GPS, GLONASS and Galileo signals	173
Table 10.1. Mean polarimetric ratio over forests and lakes for GPS (L1 C/A, L2 C, L1 P(Y) and L2 P(Y)), GLONASS (L1 C/A, L2 C/A and L2 P) and Galileo (E1 BC) signals during the float phase of BEXUS 19 flight.....	184
Table 10.2. Signal-to-Noise Ratio at RHCP y LHCP of the direct GPS (L1 C/A, L2 C, L1 P(Y) and L2 P(Y)), GLONASS (L1 C/A, L2 C/A and L2 P) and Galileo (E1 BC) signals at as function of the elevation angle during the float phase of BEXUS 19 flight.....	184
Table 10.3. Summary of the key observation and simulation results	190
Table 11.1. Overview of the most relevant subsystems for TechDemoSat-1, CyGNSS and PARIS-IoD.....	196
Table 11.2. Key mission requirements.....	199
Table 11.3. Different satellite configurations considered during the feasibility study	200
Table 11.4. Technical specifications of the mechanical structure.....	209
Table 11.5. Technical specifications of the S-band transmitter	211
Table 11.6. Technical specifications of the UHF/VHF transceiver	211
Table 11.7. Technical specifications of the UHF/VHF antennas.....	211
Table 11.8. Technical specifications of the magnetorquers	214
Table 11.9. Technical specifications of the platform OBC.....	215
Table 11.10. Technical specifications of the EPS.....	216
Table 11.11. Technical specifications of the additional battery pack	216
Table 11.12. Technical specifications of the solar panels.....	216

Table 11.13. Mass budget	222
Table 11.14. Power budget without ground station access	223
Table 11.15. Power budget with 1 ground station access	223
Table 11.16. Link budget: down-link telemetry.....	225
Table 11.17. Link budget: down-link scientific data	226
Table 11.18. Link budget: up-link telecommands.....	227
Table 11.19. Data budget of the ³ Cat-2 (ADCS error free).....	228
Table A.1. Technical specifications of the experiment components.....	250
Table A.2. Technical specifications of the experiment components.....	251
Table A.3. Mass budget.....	251
Table A.4. Experiment summary. Note: The values of the Center Of Gravity (COG) of the different components are referred to a dextro-rotarory Cartesian reference system with origin in the geometric centre of the M-Egon gondola and the x axis orthogonal to one lateral of the gondola	252
Table A.5. External elements and racks attachment summary	253
Table A.6. Energy budget	259
Table A.7. Preparations and test activities at Esrange Space Center	269
Table A.8. Timeline for countdown and flight.....	271
Table B.1. Acceleration characteristics	286
Table B.3. Sine vibration test characteristics	286
Table B.4. Random vibration test characteristics.....	287
Table B.5. Shock vibration test characteristics	287
Table C.1. Requirements Traceability Matrix (RTM)	290
Table D.1. ³ Cat-2 Risk Register	296

List of Acronyms

ACF	Auto-Correlation Function
ADCS	Attitude Determination and Control System
ADS	Attitude Determination System
AGC	Automatic Gain Control
AGT	Argos GPS and ATC Transponder
AM	Automatic Module
AMR	Advanced Microwave Radiometer
ATC	Air Traffic Control
BEXUS	Balloon EXperiments for University Students
BOC	Binary Offset Carrier
BPKS	Binary Phase Shift Keying
CDHS	Command and Data Handling System
CDMA	Code Division Multiple Access
cGNSS-R	Conventional Global Navigation Satellite Systems Reflectometry
CIEM	Canal d'Investigació i Experimentació Marítima
CNES	Centre National d'Études Spatiales
COG	Center Of Gravity
³COPS	³ Cat-2 Orchestration Payload System
CoSMOS	Campaign for validating the Operation of SMOS
COTS	Commercial Off The Shelf
CRB	Cramer-Rao Bound
CyGNSS	Cyclone Global Navigation Satellite System
DDM	Delay Doppler Map
DLL	Delay Locked Loop
DLR	German Aerospace Center
DORIS	Doppler Orbit and Radio Positioning Integration by Satellite
DSSS	Direct Sequence Spread Spectrum

EBASS	Esrange Balloon Service System
ECF	Earth Centered Fixed
ECI	Earth Centered Intertial
eLISA	Evolved Laser Interferometer Space Antenna
EM	Engineering Model
EMC	Electromagnetic Compatibility
EKF	Extended Kalman Filter
EPS	Electrical Power System
ERS	European Remote Sensing satellite
ESA	European Space Agency
FDMA	Frequency Division Multiple Access
FM	Flight Model
FOV	Field Of View
GEO	Geosynchronous Equatorial Orbit
GEROS-ISS	GNSS rEfectometry, Radio Occultation and Scatterometry on-board International Space Station
GIOVE	Galileo In-Orbit Validation Element
GLONASS	GLObal NAVigation Satellite System
GNSS	Global Navigation Satellite System
GNSS-R	Global Navigation Satellite Systems Reflectometry
GNU	GNU's Not Unix
GOLD-RTR	GPS Open-Loop Differential Real-Time Receiver
GPIU	General Purpuse Input/Output
GPS	Global Positioning System
GRG	Generalized Rayleigh-Gans
GS	Ground Station
GSO	GeoSynchronous Orbit
GUI	Graphical User Interface
ICD	Interface Control Document

ICE	Institut de Ciències de l’Espai
IEEC	Institute Space Studies Catalonia
iGNSS-R	Interferometric Global Navigation Satellite Systems Reflectometry
IGSO	Inclined GeoSynchronous Orbit
IOV	In Orbit Validation
IPT	Interference Pattern Technique
IRNSS	Indian Regional Navigation Satellite System
ISL	Inter-Satellite Link
KA	Kirchhoff Aproximation
KAGO	Kirchhoff Aproximation Geometrics Optics
LEO	Low Earth Orbit
LHCP	Left Hand Circular Polarization
LNA	Low Noise Amplifier
LQR	Linear Quadratic Regulator
LRA	Laser Retro-reflector Array
LRF	Launcher Reference Frame
LTAN	Local Time of Ascending Node
LV	Launch Vehicle
MCS	Multilevel Coded Spreading
MEO	Medium Earth Orbit
MFSK	Multiple Frequency Shift Keying
MLE	Maximum Likelihood Estimates
MPPT	Maximum Power Point Tracking
NA	Not Available
NASA	National Aeronautics and Space Administration
OBC	On Board Computer
ODTS	Orbit Determination and Time Synchronization
OS	Operative System

PARIS IoD	PAssive Reflectometry and Interferometry System In-Orbit-Demonstrator
PDF	Probability Density Function
PHM	Passive Hydrogen Maser
PLL	Phase Locked Loop
PMM	Payload Management Module
P-POD	Poly-Picosatellite Orbital Deployer
PRN	Pseudo-Random Noise
PVT	Position Velocity Time
PYCARO	P(Y) and C/A ReflectOmeter
RAAN	Right Ascension of the Ascending Node
RAFS	Rubidium Atomic Frequency Standard
RBF	Remove Before Flight
REXUS	Rocket EXperiments for University Students
RF	Radio Frequency
rGNSS-R	Reconstructed-code Global Navigation Satellite Systems Reflectometry
RH	Relative Humidity
RHCP	Right Hand Circular Polarization
RMDT	Relative Mean Dynamic Topography
RMS	Root Mean Square
RTM	Requirements Traceability Matrix
RTOS	Real Time Operating System
SAR	Synthetic Aperture Radar
SD	Secure Digital
SDR	Software Defined Radio
SGP4	Simplified General Perturbation 4
SIRAL	SAR/Interferometric Radar ALtimeter
SIS	Signal-In-Space

SLA	Sea Level Anomaly
SMOS	Soil Moisture and Ocean Salinity satellite
SNR	Signal-to-Noise Ratio
SS	Sun Safe
SSA	Small Slope Approximation
SSH	Sea Surface Height
SSO	Sun-Synchronous Orbit
SU	Start Up
SV	Space Vehicle
SWH	Significant Wave Height
SWOT	Surface Water Ocean Topography satellite
TCS	Thermal Control Subsystem
TLE	Two Line Elements
TORMES	TOpography from Reflectometric Measurements: an Experiment from the Stratosphere
TSM	Two-Scale composite Model
TTC	Telemetry Tracking and Command
UDP	User Datagram Protocol
UPC	Universitat Politècnica de Catalunya
UK	United Kingdom
UK DMC	United Kingdom Disaster Monitoring Constellation
WAF	Woodward Ambiguity Function
WF	Waveform
WGS	World Geodetic System

PART I:

INTRODUCTION

1

1. MOTIVATION

1.1 Justification of the work

Oceans distribute heat, salt, carbon, nutrients, and other chemicals around the world. The ocean circulation is therefore a key factor to understand the climate as well as the ocean's role in the uptake of carbon, the distribution of biomass, and other societal issues related to the oceans [1]. Direct measurement of ocean's currents velocity is difficult due to the turbulent regime of the flow. However, the instantaneous velocity at every point of the ocean does not provide useful information for the study of ocean circulation at scales larger than 10 km. Instead, a spatially and temporally averaged velocity field is required. This smoothed flow has a special property so-called geostrophic balance: force from the surface's slope matches the Coriolis force on currents. This surface pressure field can be computed from the elevation relative to the geoid, the ocean's geopotential surface. The sea surface elevation relative to the geoid is called the ocean's surface topography, which provides a very effective approach to compute the large-scale, low-frequency surface current velocity of the ocean. This geostrophic component of the ocean circulation varies vertically in relation to the density distribution in the ocean. Therefore ocean surface topography is an important dynamic boundary condition to determine the three-dimensional structure of the ocean circulation.

Global Navigation Satellite Systems Reflectometry (GNSS-R) techniques can improve the spatial and temporal resolutions of altimetric products, since the multi-static configuration allows to perform measurements over many points along directions away from nadir. The performance of GNSS-R techniques for ocean altimetry [2, 3] relies on the evaluation of the feasibility to measure the Sea Surface Height (SSH), and its changes with enough precision and accuracy. However, the ultimate accuracy and precision of conventional¹ and “interferometric”² GNSS-R techniques for mesoscale ocean altimetry are still a matter of study in the scientific community.

¹ Cross-correlation of the reflected signal with a locally-generated replica of the transmitted signal.

² Cross-correlation of the direct and the reflected signals.

1.2 Ph. D. Thesis structure

This Ph. D. Thesis Dissertation arises in this framework with the main purpose to contribute to analyze the feasibility of the GNSS-R techniques. The fundamental objective of this work and the kick-off of this Ph.D. Thesis was the design and development of a nano-satellite (including the platform and the payload) for GNSS-R Earth Remote Sensing. The list of refereed publications on which this candidate is principal author is included in Section. 12.3. Two main research lines have been carried out in parallel towards the design and the validation of the payload and the space-borne platform. This Dissertation is structured in four parts:

- **Part I:** Introduction, motivation and state-of-the-art.
- **Part II:** Theoretical elements of GNSS-R including theoretical simulations.
- **Part III:** Experimental validation of the mission payload over ocean and boreal forests.
- **Part IV:** Towards a space-borne multi-constellation, dual-frequency, and dual-polarization GNSS-R mission.

The validation of the payload is described through 6 different Chapters (5-10). Each chapter corresponds to a different step in the verification of the scientific mission requirements, from the Earth's surface-level to a 27,000 m stratospheric balloon flight:

- **Surface level:** Mediterranean Sea and CIEM wave channel at UPC premises.
- **Air-borne:** Two ESA-sponsored air-borne flights over the Baltic Sea performed during the PARIS IoD feasibility study.
- **Stratosphere:** Two ESA-sponsored stratospheric balloon flights over boreal forests North of Sweden in the frame of the REXUS/BEXUS project. The experimental evidence during the first flight (October 2013) showing that the peak of the power waveform had a multi-modal behaviour, indicating that different scattering mechanisms may be taking place, triggered the simulation study performed in Section 4.2.3. A second flight (October 2014) was performed using a new version of the GNSS-R reflectometer (including multi-constellation, dual-polarization and dual-frequency capabilities) because of

the failure in the E-Link of the organizers. This flight confirmed and expanded previous results.

The scientific/technological development achieved during these campaigns have been very useful to the design of the payload, to the optimization of the payload parameters for different Earth surface targets, as well as for the relevance of the scientific results themselves. The platform is finally described in Chapter 11. There, the mission concept of operations, and the instrumentation are carefully described.

2

2. STATE OF THE ART

2. State of the art and historical overview

Ocean's surface topography is only a minor difference from the geoid, which has a range of about 200 m relative to the reference ellipsoid. Therefore, the first order SSH essentially represents the geoid. Along-track nadir altimetry observations have been essential to improve the understanding of the small-scale features of the marine geoid, and of the ocean's bathymetry. However, mesoscale ocean altimetry remains a challenge in satellite Remote Sensing. It is of great interest for oceanographers trying to validate their models of ocean circulation with real data. The measurement of the shape of sea surface has thus very important applications to oceanography, geodesy and geodynamics.

Since the very first space-borne altimeters on-board Skylab, GEOS-3 and SeaSat back in the 1970's, little has changed in the way of performing ocean altimetry from space, i.e., by using a nadir looking radar.

TOPEX/Poseidon (NASA/CNES) was launched into orbit in 1992 [4]. It determined globally and with high accuracy the seasonal cycle and other temporal variabilities of the ocean for the first time. Jason-1 (NASA/CNES 2001) continues the task of providing the important oceanographic data time-series [5] originated by TOPEX/Poseidon (Fig. 2.1), carrying updated versions of the same instruments. As other earlier missions, Jason-2/OSTM (NASA/CNES/NOAA/EUMETSAT 2008) is extending the climate data record [6] by providing a long-term survey of Earth's oceans, tracking ocean circulation patterns, and measuring sea-surface heights and the rate of sea-level rise. These are key factors in understanding climate change. Each spacecraft carries 5 similar or identical instruments. In particular, Jason-2/OSTM payload is composed of: the Poseidon-3 dual-frequency altimeter; the Advanced Microwave Radiometer (AMR) to measure the "wet delay" due to atmospheric water vapor; and three positioning systems: the Doppler Orbit and Radio Positioning Integration by Satellite (DORIS) Doppler orbitography beacon, a Laser Retro-reflector Array (LRA), and a Global Positioning System (GPS) receiver.

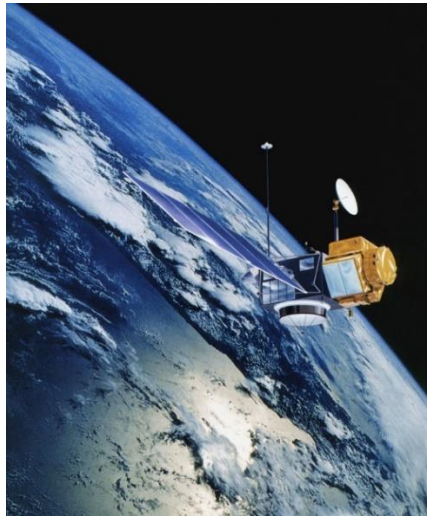


Fig. 2.1. Artist's view of TOPEX/Poseidon [4].

ESA's European Remote Sensing satellites (ERS), ERS-1 and -2 [7] were launched in 1991, and 1995 respectively. Their payloads included a synthetic aperture imaging radar, a radar altimeter, and specific instruments to measure ocean surface temperature and wind fields. ERS-2 added an additional sensor for atmospheric ozone monitoring. The two satellites acquired a combined data set extending over two decades. Envisat [8] was ESA's successor to ERS. Envisat was launched in 2002, being the largest civilian Earth Observation mission ever. It carried 10 instruments on-board, and its weight was around eight tons. More advanced imaging radar, radar altimeter and temperature-measuring radiometer instruments extended ERS data sets. This is supplemented by new instruments including a medium-resolution spectrometer sensitive to both land features and ocean colour. Envisat also carried two atmospheric sensors to monitor trace gases. Note that on 08 04 2012 Envisat finished its operational life in orbit.

Constellations of a few of such nadir-looking altimeters are being exploited to increase the spatial and the temporal sampling of the ocean. Even, there have been proposals to use many radar altimeters on large constellations of commercial communications satellites, such on-board the satellites of the next generation of Iridium's space segment.



Fig. 2.2. Artist's view of SWOT [1].

In parallel several new concepts have been proposed to improve the resolution of the altimetric data sets. The main concepts are described in the following.

2.1 Radar interferometry from a single satellite

2.1.1 SWOT mission

In October 2007, the SWOT (Surface Water Ocean Topography) Science Working Group was formed under the auspices of NASA and CNES with participants of oceanography and land surface hydrology from the international community [1]. Five years after this meeting, NASA announced that SWOT (Fig. 2.2) will be launched in 2019. The goal of this Earth Observation mission is to develop a new measurement technique using radar interferometry to obtain wide-swath measurements of surface elevation at high resolution over both ocean and land. Since 1993 the measurement of the ocean surface topography by satellite radar altimeters has made fundamental advances in our understanding of the large-scale ocean circulation, and its role on climate change.

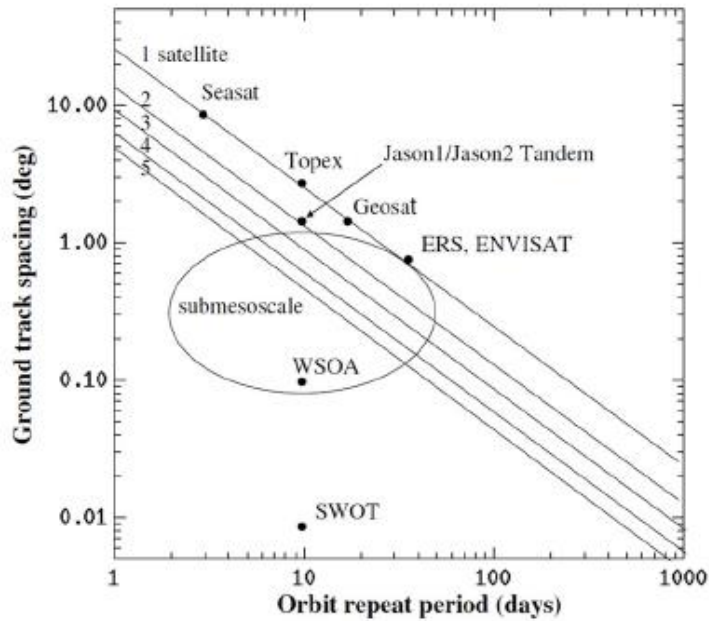


Fig. 2.3. Spatial and temporal resolution inter-comparison between conventional nadir-looking radar altimeters and SWOT [1].

However, as in the atmosphere, ocean circulation is dominated by turbulent eddies. The most energetic ocean eddies have scales around 100 km which is about 10 times less than the scale of atmospheric storms. Even with combined data from multiple altimeters, the ocean eddy field cannot be well sampled by existing altimetry missions. Figure 2.3 shows the characteristics of spatial and temporal sampling by multiple conventional nadir-looking altimeters in comparison to the one that would be gathered by SWOT, as proposed.

Based on the observations from the TOPEX/Poseidon-Jason-1 tandem mission, which provided only suboptimal sampling of the eddy fields, it has been reported [9] that the eddy kinetic energy dominates the total kinetic energy of ocean circulation. Ocean model simulations have suggested that only by including realistic eddies in the model the simulated ocean heat transport can approximate observations. Observations that fully resolve ocean eddies are required to improve the ocean circulation. Conventional altimeters use pulse-limited ranging technique to measure the range of the instrument above the surface.

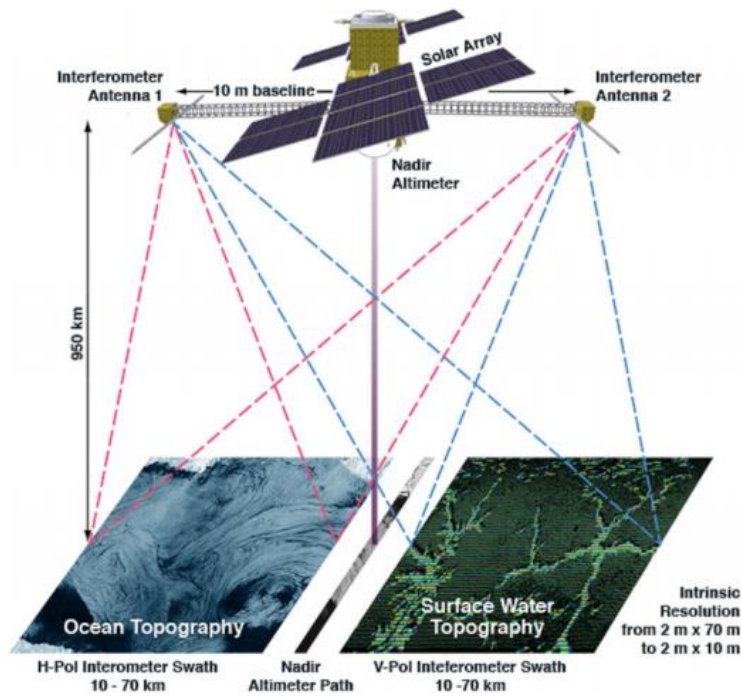


Fig. 2.4. Artist's view of SWOT performance [1].

The finite footprint of the radar is determined by the width of the radar's pulse and the altitude of the spacecraft. The footprint diameter of TOPEX/Poseidon varies from 2 km over calm seas to 10 km over rough seas of 10 m Significant Wave Height (SWH). The radar requires precise nadir pointing to obtain the range measurement between the radar and its nadir on the surface. The major limitations of the technique include errors in radar waveform analysis, and land contamination near the coast line and islands. These limitations can be overcome by radar interferometry techniques.

Nadir-looking conventional altimeters are designed to track the leading edge of the radar return signals coming from the nadir. Radar interferometry determines the location of the target by measuring the relative delay (or phase shift) between the signals from two antennas that are separated by a baseline distance (Fig. 2.4). Using geometric relationships, the location of the range measurements in the plane of the observation can be determined. The measurement triangle is made up of the baseline B , and the range from the two antennas to the surface's target, r_1 and r_2 . The baseline

is known by construction, and the knowledge of the spacecraft attitude. The range r_1 is determined by the system timing measurements. The range difference between r_1 and r_2 is determined by measuring the relative phase delay shift ϕ between the two signals. The phase shift ϕ is related to the range difference Δr , by equation $\phi = 2\pi\Delta r / \lambda$, where λ is the radar electromagnetic wavelength. The additional information required to determine the measurement location, the incidence angle θ_i , can be obtained from the range difference by means of the relationship $\phi = 2\pi B \sin \theta_i / \lambda$. Given these measurements, the surface height h above a reference plane can be obtained using the equation $h = H - r_1 \cos \theta_i$, where H is the height of the platform above the reference.

If both antennas are Synthetic Aperture Radars (SAR), the interferometric system is then able to provide two swaths of SSH measurements in parallel to the flight direction. The spatial resolution of the measurement is dependent on the bandwidth (the range resolution in the cross-track direction) and the antenna size (the azimuth resolution in the along-track direction). A major difference between conventional altimetry and interferometry is that the interferometric measurement of the range relies on the complex phase information, which is available for each imaged pixel in the scene. In contrast, the altimeter measurement relies on the power and the specific shape of the leading edge of the return waveform, which is only available at nadir. Thus, the interferometric measurement of the range is intrinsically more accurate than the altimeter measurement, and available for all imaged points in the scene. Furthermore, the pixel size, on the order of tens of meters, is much smaller than the pulse-limited footprint of the conventional altimeter, and thus much less prone to land (or ice) contamination.

2.1.2 CryoSat mission

CryoSat is an ESA mission to monitor variations in the extent and thickness of polar ice. The information provided on the behavior of coastal glaciers is key to improve the predictions of future sea-level rise. The CryoSat-1 spacecraft was lost during the launch failure in 2005, and CryoSat-2 (Fig. 2.5) was launched in 2010. Its primary objective is to quantify the Arctic sea ice thinning due to global warming.



Fig. 2.5. Artist's view of CryoSat [10].

Additional scientific objectives include the analysis of the extent to which the Antarctic and Greenland ice sheets are contributing to global sea level rise. CryoSat-2's primary payload is the SAR/Interferometric Radar Altimeter (SIRAL), which has extended capabilities to meet the requirements to measure the ice-sheet elevation and sea-ice freeboard. CryoSat-2 also carries three star trackers to measure the orientation of the baseline. In addition, the DORIS radio-receiver and a small LRA ensures that CryoSat-2's position can be accurately tracked. Unlike conventional radar altimeters, the CryoSat-2 altimeter sends a burst of pulses with an interval 10 times smaller. The returning echoes are correlated, and by treating the whole burst at once, the data processor separates the echo into cross-track strips by exploiting the slight frequency shifts (caused by the Doppler effect) in the forward- and aft-looking parts of the beam.

2.2 Bistatic radar within a constellation of cooperative radar altimeters

The study of a satellite constellation of pulse-limited radar altimeters for ocean, land and ice observations was recommended at the Consultative Meeting on Imaging Altimeter Requirements and Techniques held in 1990 at the Mullard Space Science Laboratory, University College, London UK, and sponsored by ESA [11]. Based on this recommendation, ESA conducted a study of a constellation of pulse-limited nadir-looking radar altimeters. The conclusion of this study was that a constellation of eight satellites was needed to achieve a goal sampling requirement for mesoscale ocean observations with a seven-day revisit time, and a 50 km spatial resolution [12]. However the difficulty to implement such a constellation due to the required number of satellites made it unattractive and other possibility was sought. In particular an internal ESA-study identified a constellation of bistatic satellite altimeters synchronized (in space and in time) through GNSS signals as a potential way to obtain the spatial and temporal coverage for ocean applications. The payload of the three satellites of the proposed constellation would consist of ku/S-band bistatic altimeter plus a GNSS receiver.

2.3 Bistatic radar using GNSS reflected signals

The Global Navigation Satellite Systems (GNSS), were first conceived and implemented for navigation purposes, but they have also been used for Earth observation. Scientific applications of the GNSS signals include measuring seismic tectonic motions, Earth orientation, and polar motion, gravimetry, neutral atmospheric temperature and water vapor profiling, and ionospheric electron density profiling [13]. All of these applications have been well proven and provide new ways to enhance our knowledge about the Earth and its environment. More recent and less developed applications explore the possibility to use the GNSS signals scattered off the ocean and sensed by an air-borne or space-borne receiver in a bistatic radar geometry, as a means of performing altimetry and scatterometry. When considering a constellation of multiple GNSS transmitters and one such receiver, a multi-static system is obtained, capable of intercepting scattered signals from several areas of the Earth's

surface simultaneously. As in traditional altimetry, the bistatic GNSS reflected signals can be analyzed to derive three important descriptors of the ocean surface: the bistatic path delay from the ocean height, the ocean's surface wind, and the ocean Significant Wave Height (SWH).

At present two main different GNSS-R techniques have been studied. The so-called conventional GNSS-R (cGNSS-R) technique consists of performing the cross-correlation of the reflected signal with a locally-generated clean replica of the transmitted signal. Another approach is the so-called interferometric GNSS-R (iGNSS-R) technique, which is based on the direct cross-correlation of the direct and the reflected signals. This second approach allows to use the full bandwidth of the signals, at the expense of noisier waveforms, which can only be (partially) overcome by using large steerable antennas with a high directivity (Figs. 2.6 and 2.7). Both GNSS-R techniques can improve the spatial and temporal resolutions of altimetric products, since the multi-static configuration allows to perform measurements over many points along directions away from nadir. However, at present, the ultimate accuracy and precision of conventional and interferometric GNSS-R techniques for mesoscale ocean altimetry are still a matter of debate in the scientific community.

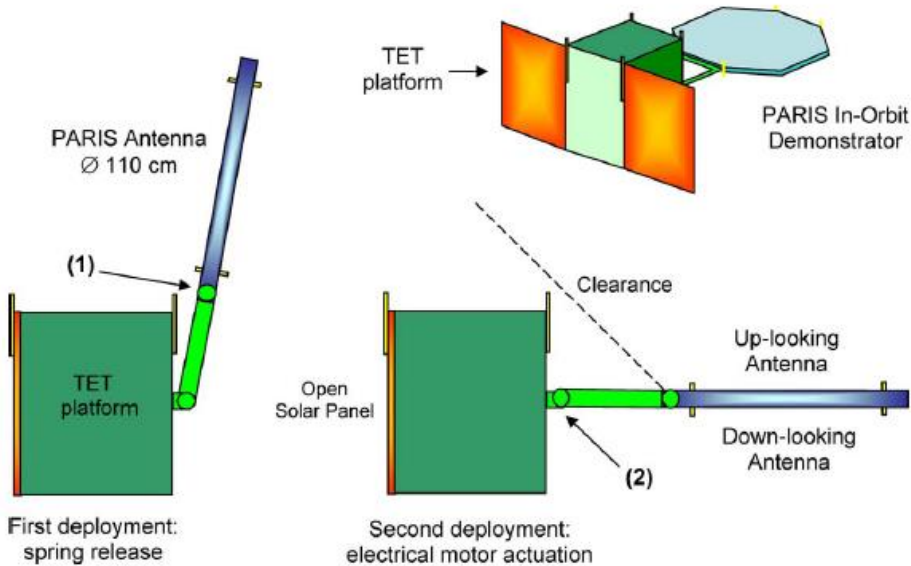


Fig. 2.6. Accommodation and deployment of the PARIS-IoD antenna [3].

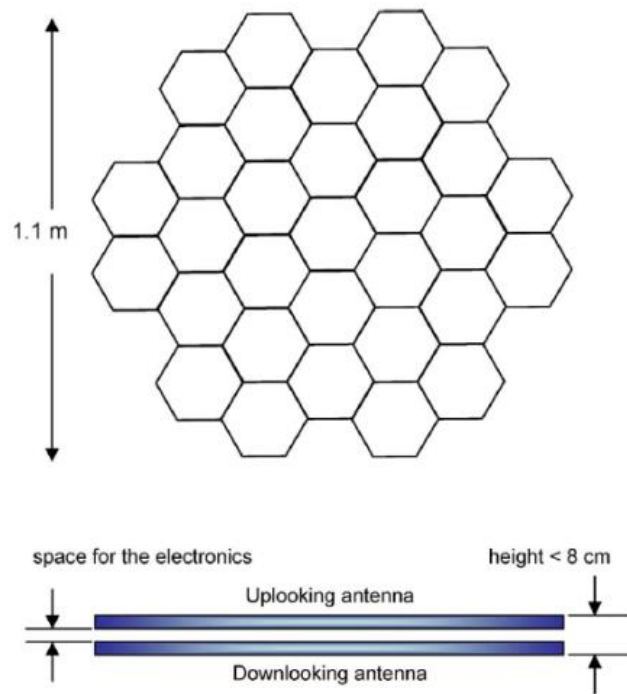


Fig. 2.7. Proposed back-to-back double phased array antenna of PARIS-IoD [3].

3

3. FUNDAMENTALS ASPECTS OF GLOBAL NAVIGATION SATELLITE SYSTEMS REFLECTOMETRY

3.1 Introduction

The concept of GNSS-based altimetry (Fig. 3.1) was first proposed by Martín-Neira in 1993 [2]. In 1994, the evidence that GPS navigation signals could be collected after scattering on the sea surface from air-borne altitudes was reported [14]. Since then, several additional theoretical work modeling the expected signal waveform and accuracy have appeared (e.g [15-17]). Experimental campaigns to characterize GPS altimetry from a fixed location over a lake [18], from an aerostatic balloon over a lake [19], and from an airborne platform [20-24], have been conducted. The first GPS reflections from space were detected from the analysis of the data collected during Space-borne Imaging Radar-C (SIR-C) mission on board the Space Shuttle [25]. On 27 September 2003 the Surrey Satellite Technology Ltd. GPS reflectometry instrument onboard United Kingdom Disaster Monitoring Constellation (UK-DMC-1) was launched. It was the first space-borne instrument dedicated to the reception of Earth-reflected GPS signals. It received only L1 frequency, and hence, ionospheric errors could not be corrected. Moreover, the antenna gain was too low (< 12 dB) to provide sufficient Signal-to-Noise Ratio (SNR), a necessary condition to obtain the required precision. Despite this, it was a proof of concept of an operational GNSS-R system.

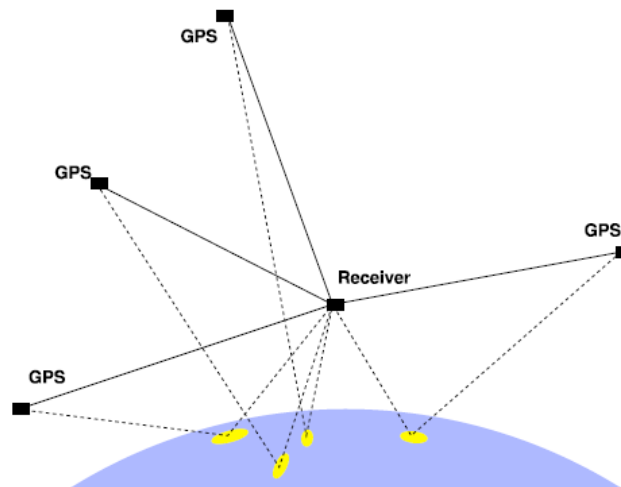


Fig. 3.1. Sketch of the GNSS-R approach. A receiver above the Earth's surface collects the direct and the Earth-reflected signals coming from areas around the specular points, the glistening zones. Image Credits IEEC/ICE - E. Cardellach.

3.2 Multi-constellation signals of opportunity

In a near future, four GNSS constellations will cover the Earth with navigation signals: GPS (24 Medium Earth Orbit (MEO) operational satellites), GLONASS (24 MEO operational satellites), Galileo (27 MEO operational satellites) and COMPASS (3 Inclined GeoSynchronous Orbit (IGSO), 27 MEO and 5 Geosynchronous Equatorial Orbit (GEO) operational satellites). Additionally, three regional constellations will increase the number of available signals for Remote Sensing purposes: QZSS (3 GeoSynchronous Orbit (GSO) operational satellites), IRNSS (3 GEO and 4 GSO operational satellites), and BEIDOU (5 GEO operational satellites). The main parameters of GPS, GLONASS and Galileo signals used in this Ph. D. Dissertation are summarized in Table 3.1 and Fig. 3.2.

3.2.1 Global Positioning System (GPS)

The GPS is a robust operational constellation consisting on 31 operational Space Vehicles (SV) (although the baseline constellation consists on 24 SVs plus three operational spares) distributed over six orbital planes, separated by 60° Right Ascension of the Ascending Node (RAAN), with an orbital inclination of 55° , and with an orbital radius of about 26,600 km. Each satellite orbits the Earth twice each sidereal day, and the same ground track is repeated once a day. Therefore, the same constellation geometry can be observed every SI (International System of Units) day with about 4 minutes of bias. At the time of writing this Ph.D. Thesis the constellation is composed of the following satellites: 3 GPS IIA (L1 C/A, L1 P(Y), L2 P(Y)), 12 GPS IIR (L1 C/A, L1 P(Y), L2 P(Y)), GPS IIR-M (L1 C/A, L1 P(Y), L2 P(Y), L2C, L1M, L2M), and 9 GPS IIF (L1 C/A, L1 P(Y), L2 P(Y), L2C, L1M, L2M, L5). The latest launch was on March 25th 2015 and 3 GPS IIFs were deployed. In a near future the first GPS III will be launched providing up to four civil signals (L1 C/A, L1C, L2C, L5), and will use three improved Rubidium atomic clocks. The GPS ground-segment is composed by a primary master control station at Schriever Air Force Base (Colorado, USA), and ten dedicated ground antennas and monitor stations.

3.2.2 Global Navigation Satellite System (GLONASS)

The GLObal'naya NAvigatsionnaya Sputnikovaya Sistema or GLObal NAvigation Satellite System (GLONASS) was created by the Soviet Union and it became fully operational in 1995. Later, the constellation was reduced reaching a minimum of eight operational satellites in 2002. However, from 2010 it is again fully operational and in June 18th 2015 the constellation was composed of a total of 28 SVs (24 SVs operational, 2 SVs under check by the satellite prime contractor and 2 SVs in flight test phase). GLONASS rotates on three orbital planes (64.8° of inclination) separated by an angle of 120°, 8 satellites for each plane that are equally spaced from an angle of 45° in argument of latitude, and with an orbital radius of about 25,511 km. New SVs (GLONASS-K2) will improve GLONASS-M accuracy improvement and broaden application domain. In particular it is expected to achieve the following technical advantages: Longer guaranteed lifetime, modernization of SVs support systems, improvement of on-board synchronizer stability, advanced technologies for monitoring and control, orbit and clock data provision, additional payload and new signals (L1OF, L2OF, L1SF, L2SF, L1OC, L1SC, L2OC, L2SC, L3OC). GLONASS-K2 first launch is planned in 2018 and the key features are: a) SVs will allow accommodation of all on-board specialized equipment without any restrictions, b) on-board subsystems will provide operational conditions for the specialized instruments without any constraints for power consumption and thermal control, c) the maximum pointing error will be better than 0.25°, d) intersatellite link continuous operation during one cycle (reception-transmission) without restrictions, and e) possibility to accommodate additional payload to perform development test in space environment and to achieve flight qualification. The GLONASS ground control segment include: a) deployment of measuring station network in the Russia and Antarctica, b) deployment of uplink station network in Russia, c) deployment of global measuring station outside Russia, d) further use of crosslink functions for ephemerides and clock data provision, and e) creation of high-stable time scale based on distributed frequency standards synchronized versus the state frequency standard.

3.2.3 Galileo

In March 2002, the European Union and ESA agreed to develop the Galileo positioning system, which is expected to be fully functional by 2020. At the time of writing this Ph.D. Thesis, Galileo is under development, and it is expected to be compatible with the modernized GPS system. Receivers will be able to combine the signals from both Galileo and GPS satellites to increase accuracy significantly. Compared to the US's GPS and the Russian GLONASS, Galileo is designed specifically for civilian and commercial purposes. Two Galileo system test bed SVs Galileo In-Orbit Validation Element (GIOVE) A and B dedicated to take the first step of the in-orbit validation phase towards full deployment of Galileo were launched respectively in 2005 and 2008 and retired in 2012. Three In-Orbit Validation (IOV) SVs were launched from 2011 to 2012 being fully operational in 2015. Additionally, by November 2015 there are six more SVs (1 IOV and 5 Full Operational Capability (FOC) SVs) in commissioning phase. During 2016, 17 FOC SVs will be launched. The full constellation will consist of 30 SVs distributed over three orbital planes (56° inclination) with an orbital radius of approximately 26,600 km and with an orbital period of 14 h. Future technology advances will include: a) to improve robustness, quicker recovering from failures and to have a system that allows the Orbit Determination and Time Synchronization (ODTS) to provide long-term ephemerides (improvements of Passive Hydrogen Maser PHM, mini PHM, robust Rubidium Atomic Frequency Standard RAFS and cesium clocks or on-board ensemble combining and implementing eventually more clocks than in present (2015)), b) increasing SV capability while maintaining as a minimum the same launch cost efficiency (to confirm by test the capability of state-of-the-art electric propulsion subsystems), and c) enabling either communication and/or ranging capabilities (in-plane and inter-plane Inter-Satellite Links ISL, ODTS exploiting ISL ranging, communication capabilities used for navigation message dissemination and for improving system robustness). The activities related with the ODTS improvement are: a) several faster navigation message, b) improvement of the orbit modelling, c) advanced navigation message provision by using Signal-In-Space (SIS) spare bits/words (AltBOC, CBOC), d) enhancing fault detection mechanisms, e) adaptive

clock fitting, and f) enabling inter-satellite ranging ODTs for enhances accuracy and robustness if ISL is selected.

Table 3.1. Parameters of the GNSS signals: GPS L1 C/A, GPS L2 P(Y), GPS L2 C, Galileo E1 BC, GLONASS C/A L1 and L2, and GLONASS L2 P. (NA: Not Available)

GNSS system	GPS	GPS	GPS	GPS	Galileo	GLONASS	GLONASS	GLONASS
Code name	C/A	P(Y)	CM	CL	E1 OS	C/A	C/A	P
Center frequency (MHz)	1575.42	1227.6	1227.6	1227.6	1575.42	(1598.0625-1605.375) ± 0.511	(1242.93-1248.625) ± 0.511	(1242.93-1248.625) ± 0.511
Frequency band	L1	L2	L2	L2	E1	L1	L2	L2
Access technique	CDMA	CDMA	CDMA	CDMA	CDMA	FDMA	FDMA	FDMA
Modulation	BPSK (1)	BPSK (10)	BPSK (1) results of multiplexing two streams of 511.5 kHz		CBOC (6,1,1/11)	BPSK (0.511)	BPSK (0.511)	BPSK (0.511)
Sub-carrier frequency (MHz)	NA	NA	NA	NA	1.023 and 6.138 (Two sub-carriers)	NA	NA	NA
Chipping rate (MHz)	1.023	10.23	0.5115	0.5115	1.023	0.511	0.511	0.511
Signal component	Data	Data	Data	Pilot	Data	Pilot	Data	Data
Primary PRN code length	1023	6.19 x 10 ¹²	10230	767250	4092	511	511	NA
Code Family	Gold codes	Combination and short cycling of M sequences	M-sequence from a maximal polynomial of degree 27		Random Codes	M-sequences	M-sequences	NA
Secondary PRN code length	NA	NA	NA	NA	NA	25	NA	NA
Data rate	50 bps	50 bps	IIF 50 bps; IIR-M also 25 bps		250 bps	NA	50 bps	50 bps
Minimum received power (dBW)	-158.5	II/IIA/IIR -164.5 IIR-M -161.4 IIF -160.0	II/IIA/IIR -164.5 IIR-M -161.5 IIF -161.5	-157	-157	-161	-167	NA

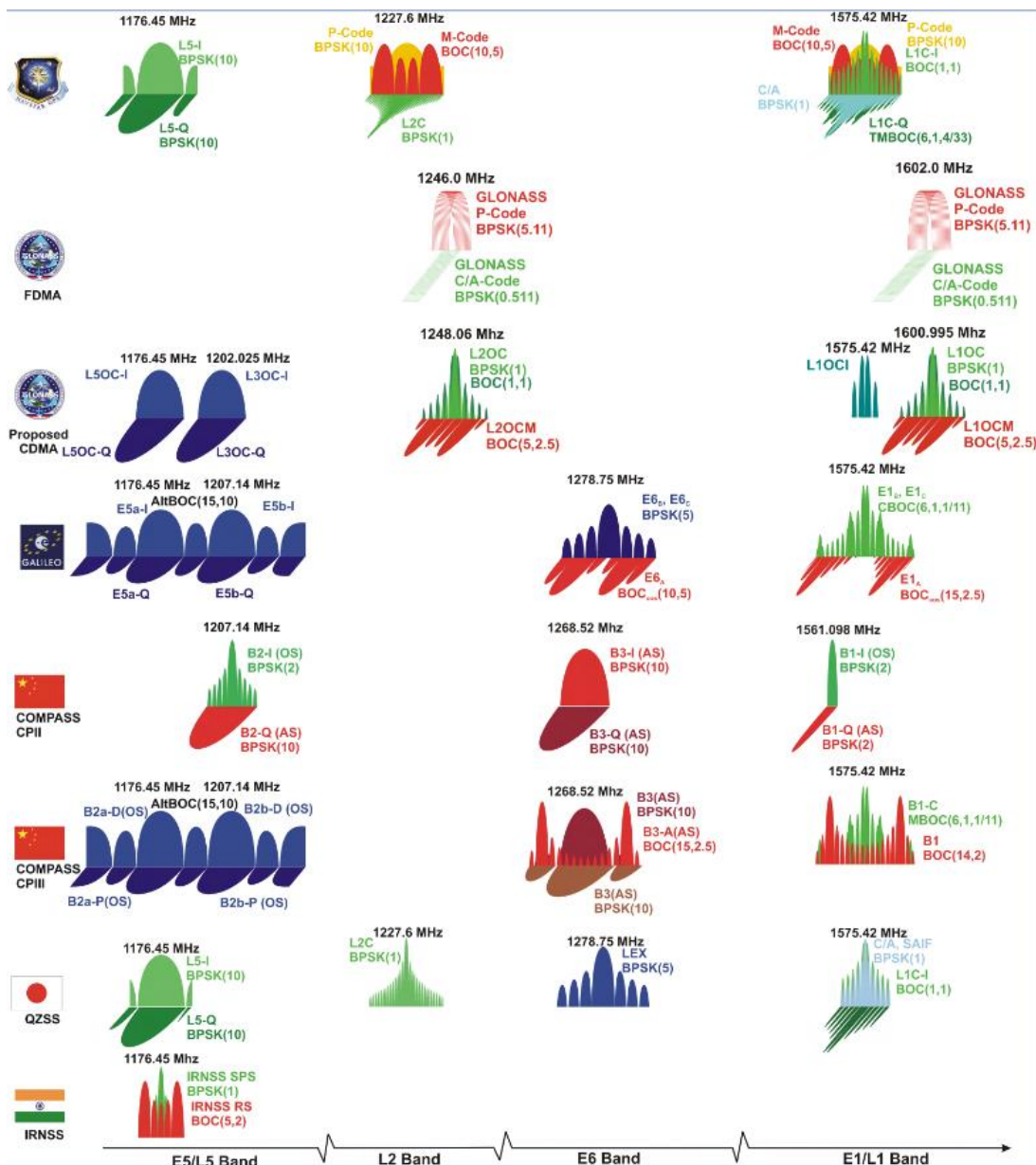


Fig. 3.2. Graphical description of the GNSS signal spectra. Image Credits Navipedia.

3.3 GNSS signals structure

GPS, Galileo and modern GLONASS signals use Direct Sequence Spread Spectrum (DSSS) to achieve Code Division Multiple Access (CDMA) with multiple Pseudo-Random Noise (PRN) codes (earlier GLONASS used DSSS with a single PRN code in conjunction with Frequency Division Multiple Access FDMA technique). DSSS is a particular case of Spread Spectrum (SS) technique. A DSSS signal can be represented as [26]:

$$s(t) = \sum_{q=-\infty}^{+\infty} c_q(t) p(t - q \frac{T_{\text{chip}}}{N}), \quad (3.1)$$

where c_q are the PRN code symbols, $p(t)$ is the chip waveform, t is the time, T_{chip} is the chip period, and N is the number of equal length divisions of one chip period. The performance of the DSSS navigation signals is mainly determined by the Auto-Correlation function (ACF) and the power spectral density. Under the hypothesis that the mean is constant and the correlation function does only depend on the time difference between t_1 and t_2 , that is, $\forall v \in \mathbb{R}$:

$$E\{s(t)\} = E\{s(t+v)\}, \quad (3.2)$$

$$E\{s(t_1)s^*(t_2)\} = \text{ACF}_s(t_1, t_2) = \text{ACF}_s(t_1+v, t_2+v) = \text{ACF}_s(t_1-t_2, 0), \quad (3.3)$$

the auto-correlation function can be defined as:

$$\begin{aligned} \text{ACF}_s(v) &= E\{s(t)s^*(t-v)\} = \\ &= \sum_q \sum_n E\{c_q c_n^*\} E\{p(t-qT_{\text{chip}}-\gamma)p^*(t-nT_{\text{chip}}-\gamma-v)\} = \\ &= \sum_m \sum_q E\{c_q c_{q-m}^*\} \frac{1}{T_c} \int_0^{T_c} p(t-qT_{\text{chip}}-\gamma)p^*(t-v-qT_{\text{chip}}+mT_{\text{chip}}-\gamma)dt \Big|_{m=q-n} = \\ &= \sum_m \sum_q \text{ACF}_c(m) \frac{1}{T_c} \int_0^{T_c} p(t-qT_{\text{chip}})p^*(t-v-qT_{\text{chip}}+mT_{\text{chip}})dt \Big|_{m=q-n}, \end{aligned} \quad (3.4)$$

where γ is an initial random shift in the signal that remains constant over time. A simplification of this equation is:

$$\text{ACF}_s(v) = \frac{1}{T_{\text{chip}}} \sum_m \text{ACF}_c(m) \text{ACF}_p(v - mT_{\text{chip}}). \quad (3.5)$$

The power spectral density is derived as the Fourier Transform (FT) of the autocorrelation of $s(t)$:

$$\begin{aligned} G_s(f) &= \text{FT}[\text{ACF}_s(t)] = \text{FT}\left[\frac{1}{T_{\text{chip}}} \sum_m \text{ACF}_c(m) \text{ACF}_p(v - mT_{\text{chip}})\right] = \\ &= \frac{1}{T_{\text{chip}}} \sum_m \text{ACF}_c(m) |P(f)|^2 e^{-j2\pi f m T_{\text{chip}}}, \end{aligned} \quad (3.6)$$

where $P(f)$ is the Fourier Transform of the chip waveform $p(t)$, and f is the frequency. The cross-correlation can be approximated as:

$$E\{c_q c_n^*\} \approx \delta_{qn}, \quad (3.7)$$

where δ is the Dirac's delta, and the power spectrum density simplifies to:

$$G_s(f) = \frac{|P(f)|^2}{T_{\text{chip}}} = f_{\text{chip}} |P(f)|^2, \quad (3.8)$$

where f_{chip} is the chip rate; because the PRN are random, non-periodic, identically distributed, equiprobable, and independent.

Multilevel Coded Spreading (MCS) Symbols are a generalization of Binary Phase Shift Keying (BPSK), and Binary Offset Carrier (BOC) modulations. Each spreading symbol is divided into a number of equal-length segments, each one is assigned to a deterministic value. The power spectral density of a MCS is:

$$S_{\text{MCS}}(j\omega) = \sum_{q=1}^n \int_{\frac{(q-1)T_{\text{chip}}}{n}}^{\frac{qT_{\text{chip}}}{n}} s_q e^{-j\omega t} dt = \frac{2}{\omega} \sin\left(\frac{\omega T_{\text{chip}}}{2n}\right) e^{\frac{j\omega T_{\text{chip}}}{2n}} \sum_{q=1}^n s_q e^{-\frac{jq\omega T_{\text{chip}}}{n}}, \quad (3.9)$$

where n is the number of symbols in one chip. The expression in the frequency domain is:

$$S_{\text{MCS}}(f) = e^{-\frac{j\pi f}{nf_{\text{chip}}}} \frac{\sin\left(\frac{\pi f}{nf_{\text{chip}}}\right)}{\pi f} \sum_{q=1}^n s_q e^{-j2\pi f q / nf_{\text{chip}}}. \quad (3.10)$$

The power spectral density is derived as:

$$G_{\text{MCS}([\bar{s}],f_{\text{chip}})}(f) = G_{\text{MCS}([\bar{s}],f_{\text{chip}})} = f_{\text{chip}} \frac{\sin^2\left(\frac{\pi f}{nf_{\text{chip}}}\right)}{(\pi f)^2} \left| \sum_{q=1}^n s_q e^{-\frac{2\pi f q}{nf_{\text{chip}}}} \right|^2. \quad (3.11)$$

Under the hypothesis that the sequence is composed of real coefficients $s_q = s_q^*$, it is derived that [26]:

$$\begin{aligned} \left| \sum_{q=1}^n s_q e^{-\frac{j2q\pi f}{nf_{\text{chip}}}} \right|^2 &= \left(\sum_{q=1}^n s_q e^{-\frac{j2q\pi f}{nf_{\text{chip}}}} \right) \left(\sum_{q=1}^n s_q e^{-\frac{j2q\pi f}{nf_{\text{chip}}}} \right)^* = \\ &= \left(\sum_{q=1}^n s_q e^{-\frac{j2q\pi f}{nf_{\text{chip}}}} \right) \left(\sum_{q=1}^n s_q^* e^{-\frac{j2q\pi f}{nf_{\text{chip}}}} \right) = \\ &= 2 \sum_{d=1}^n \sum_{q'=1}^n s_d s_{q'} \cos[(q'-d) \frac{\omega T_{\text{chip}}}{n}] - \sum_{d=1}^n s_d^2. \end{aligned} \quad (3.12)$$

Finally, the general expression for the power spectral density is:

$$G_{\text{MCS}([s],f_c)}(f) = f_{\text{chip}} \frac{\sin^2\left(\frac{\pi f}{nf_{\text{chip}}}\right)}{(\pi f)^2} \left\{ 2 \sum_{d=1}^n \sum_{q'=1}^n s_d s_{q'} \cos[(q'-d) \frac{\omega T_{\text{chip}}}{n}] - \sum_{d=1}^n s_d^2 \right\}. \quad (3.13)$$

3.4 Multi-static scatterometry

Dr. Manuel Martín-Neira stated in 1993 [2]: “As was recognised during the Consultative Meeting on Imaging Altimeter Requirements and Techniques held in June 1990 at Mullard Space Science Laboratory (UK), the ability to carry out high-precision ocean altimetry over a swath with high spatial resolution would revolutionise many fields of earth science: Some form of multi-beam altimetry would offer the possibility of achieving satisfactory sampling of the ocean mesoscale flows, and would, in addition, improve the ability to study other spatially and temporally variable oceanographic phenomena such as wave and wind fields, and ocean sea-ice interactions. The PARIS concept is directly towards such a multi-beam altimetry objective”.

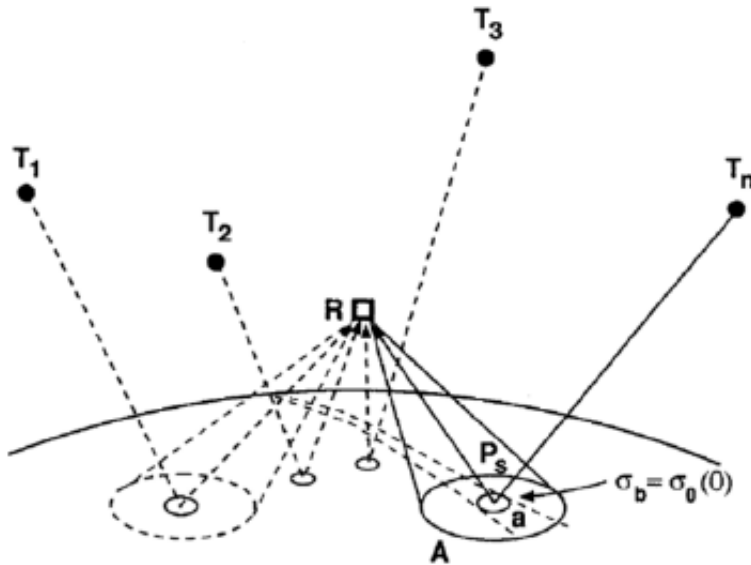


Fig. 3.3. The PASSIVE Reflectometry and Interferometry System (PARIS) concept [2].

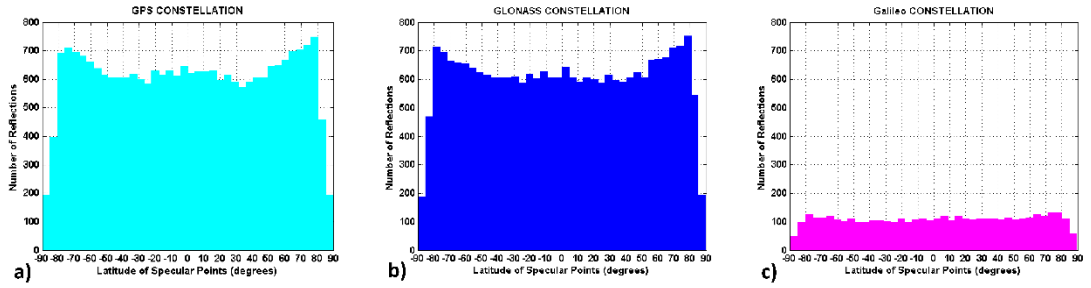


Fig. 3.4. Number of specular reflection points over the ellipsoid as a function of their latitude for a) GPS, b) GLONASS and c) Galileo (5 satellites). Parameters: Full elevation range $[0^\circ, 90^\circ]$, all satellites in view, temporal sampling 100 s.

Figure 3.3 represents the PASSive Reflectometry and Interferometry System (PARIS) concept: a receiver with an up-looking and a down-looking antenna to collect simultaneously the direct and the Earth-reflected signals respectively. PARIS was originally proposed as an interferometric system (iGNSS-R), that is, the direct and the reflected signals are cross-correlated to each other to obtain the data. The direct cross-correlation of the direct and the reflected signals allows to use the full power spectral density. Therefore, the composite autocorrelation function is much narrower than the corresponding only to the C/A code, so that the leading edge of the waveform is steeper. On the other side, the SNR in the interferometric approach is lower because the presence of thermal noise in both inputs of the cross-correlation. Additionally, the spatial resolution of GNSS-R is determined by the Woodward Ambiguity Function (WAF), being smaller in the case of iGNSS-R as compared with cGNSS-R. Therefore, in the former case the reflected signal power is lower. As a main conclusion, the iGNSS-R provides better altimetric performance as a factor ~ 3 depending of the SNR. A different GNSS-R correlation approach is prososed in this Ph.D. Dissertation, the so-called reconstructed GNSS-R or rGNSS-R. This technique is further described in Chapter 5.

The GNSS-R concept can be understood as a multi-static radar because of the simultaneously existence of multiple signals of opportunity, being the scattered signal received from an area around the nominal specular point (the so-called “glistering

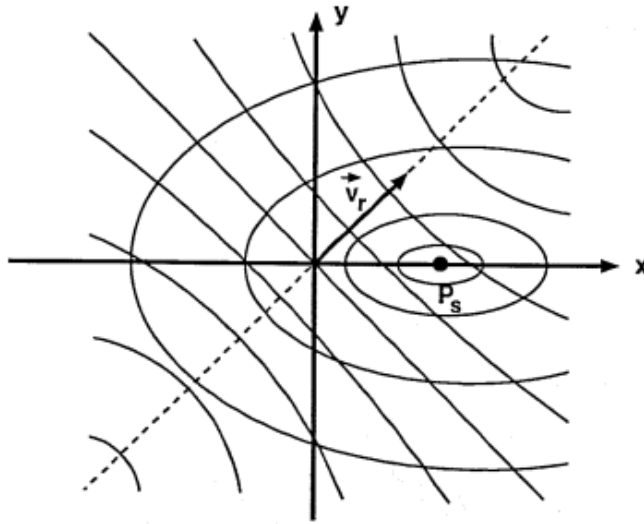


Fig. 3.5. Iso-delay and iso-Doppler lines in a bistatic configuration [2].

zone”) because of the low power of these radio-navigation signals. On the other side, due to the low power consumption of this passive and relatively economic approach, a constellation of small satellites could be use to increase the temporal resolution of a single satellite. This Ph.D. Thesis further investigates the use of GNSS-R from the ³Cat-2 nano-satellite. The obtained results could benefit future operational constellations of small satellites.

As a consequence of the amount of simultaneous signals of opportunity, the spatial coverage obtained by the nadir-looking antenna is characterized by an irregular grid with several gaps. The ³Cat-2 mission will use GPS, GLONASS, Galileo and COMPASS signals. The spatio-temporal sampling is evaluated on-board to perform the scheduling of the GNSS-R activities autonomously as a function of the elevation angle and the number of satellites in view. The Simplified General Perturbation 4 (SGP4) orbit propagator is used to propagate the orbit parameters of the GNSS satellites (transmitters) and the ³Cat-2 (receiver) using properly Two Line Elements (TLEs). The position of the specular points³ over the ellipsoid is then calculated. The distribution of the specular reflection points as a function of their latitude is shown in Figs. 3.4a,b,c respectively for GPS, GLONASS and Galileo. The scenario

³ The Earth Surface is considered totally smooth in the computation of the specular points.

corresponds to the nominal orbit of the ³Cat-2 during 1 day and with a temporal sampling in the along-track direction of 100 s. All the operational satellites of each GNSS constellation are used in the simulation and the full-range of elevation angles is used. There are ~ [600, 700] specular points for GPS and GLONASS, being ~ 100 for Galileo (5 satellites) up to 80° latitude.

Finally, the scattering geometry is defined by the iso-delay and iso-Doppler lines in a bistatic configuration (Fig. 3.5). The iso-delay lines can be approximated by ellipses (intersection of equal-delay ellipsoid formed by the navigation signals and the Earth's surface) around the nominal specular point (P_s) while the iso-Doppler lines determined by the Sinc-function can be approximated as:

$$f_D = f_c \pm \frac{1}{2T_c} = \frac{1}{\lambda} [\bar{v}_t \bar{m} - \bar{v}_r \bar{n}], \quad (3.14)$$

where f_D is the Doppler shift, f_c is the center frequency, λ is the electromagnetic wavelength, T_c is the coherent integration time, \bar{v}_r is the receiver velocity, \bar{v}_t is the transmitter velocity, \bar{m} and \bar{n} are the unit vectors of the incident and the scattered waves respectively.

PART II:

THEORETICAL ELEMENTS

4

4. FUNDAMENTALS ASPECTS OF GNSS-R SCATTEROMETRY AND ALTIMETRY

4.1 GNSS-R over ocean

This Section describes the ocean surface and presents a GNSS-R scattering model.

4.1.1 The ocean surface

The ocean surface is a random rough surface. The standard deviation of the surface height variation σ and the surface correlation length L describe the statistical variation of the random component of surface height relative to a reference surface. This reference surface for the ocean case is the surface mean, since there are only random variations. The standard deviation of the surface height is modelled as [27, pp. 423]:

$$\sigma = (\overline{z^2} - \bar{z}^2)^{1/2}, \quad (4.1)$$

where \bar{z} is mean height of an area (L_x, L_y) of the surface statistically representative. It is defined as [27, pp. 423]:

$$\bar{z} = \frac{1}{L_x L_y} \int_{-L_x/2}^{L_x/2} \int_{-L_y/2}^{L_y/2} z(x, y) dx dy, \quad (4.2)$$

and the second moment is defined as [27, pp. 423]:

$$\overline{z^2} = \frac{1}{L_x L_y} \int_{-L_x/2}^{L_x/2} \int_{-L_y/2}^{L_y/2} z^2(x, y) dx dy. \quad (4.3)$$

Equation 4.1 can be reduced to a one dimensional formulation in the case of a surface that can be assumed to be statistically independent of the azimuthal dimension. In this situation, the standard deviation is given by [27, pp. 423]:

$$\sigma = \left[\frac{1}{N-1} \left(\sum_{i=1}^N (z_i)^2 - N(\bar{z})^2 \right) \right]^{1/2}, \quad (4.4)$$

where:

$$\bar{z} = \frac{1}{N} \sum_{i=1}^N z_i, \quad (4.5)$$

and N is the number of samples. In the one dimensional case, the normalized autocorrelation function for the surface profile is obtained as [27, pp. 423]:

$$\rho(x') = \frac{\int_{-L_x/2}^{L_x/2} z(x)z(x+x') dx}{\int_{-L_x/2}^{L_x/2} z^2(x) dx}. \quad (4.6)$$

This observable provides information about the degree of similarity between the height z at a point x , and at a point x' . The surface correlation length L is defined as the displacement x' for which $\rho(x')$ equals $1/e$.

The degree of roughness of a surface can be defined as a function of the standard deviation of the surface height variation and the surface correlation length. A simpler definition of smooth-surface is provided by the Rayleigh criteria. It states that the surface can be considered smooth if the phase difference between two reflected waves is lower than $\pi/2$ rad [27, pp. 427]:

$$SWH < \frac{\lambda}{8 \sin \theta_e}, \quad (4.7)$$

where SWH is the Significant Wave Height, and θ_e is the elevation angle.

4.1.2 The scattering of GNSS signals from the ocean surface

There are different approaches to model surface scattering, including “point scatterers” and “facets”. The former one assumes that the surface scattering is created by many point scatterers. However the most common approach is the use of facets models. The rough surface is approximated by a series of small planar facets, each one tangential to the surface. The incident signal wavelength is used to define the facets sizes. In the case of facets with finite size of both the slope distribution and the PDF for facet size must be used. On the other size, when the facet size is infinite (relative to the signal wavelength) only the slope distribution is required to be estimated. This is the so-called “geometric-optics” scattering model.

In the Kirchhoff Approximation (KA) the scattered field $u(t)$ is obtained as [16]:

$$u(t) = -\frac{\sqrt{P_t} e^{jk(R_t+R_r)}}{4\pi j} \int \Re \frac{\sqrt{G_t G_r \lambda^2}}{R_r R_t \sqrt{4\pi}} a\left(t - \frac{R_r + R_t}{c}\right) \frac{q^2}{q_z} e^{-2\pi j(f_c + f_D)t} e^{-j\bar{q}\bar{r}} d\bar{\rho}, \quad (4.8)$$

where t is the time, $k = 2\pi/\lambda$ is the wavenumber, λ is the electromagnetic wavelength, $j = \sqrt{-1}$, R_t is the distance from the nominal specular point to the transmitter, R_r is the distance from the nominal specular point to the receiver, G_r and G_t are the gain of the receiver and the transmitter antennas respectively, P_t is the transmitter power, \Re is the reflection coefficient, a is the modulating PRN code, c is the speed of light, \bar{q} is the scattering vector, \bar{r} is the vector from the nominal specular point to the scattering point, and $\bar{\rho}$ is the projection of \bar{r} on the horizontal plane.

Under the Stationary-Phase approximation, the scattered field $u(t)$ in a region around a single specular point on the ocean surface $\bar{\rho} = \bar{\rho}_s$, can be approximated as [28]:

$$u(t) \approx -\frac{\sqrt{P_t G_t} e^{jk(R_t+R_r)}}{4\pi j} \left[\Re \frac{\sqrt{G_r \lambda^2}}{R_r R_t \sqrt{4\pi}} a\left(t - \frac{R_r + R_t}{c}\right) \frac{q^2}{q_z} e^{-2\pi j(f_c + f_D)t} e^{-j\bar{q}\bar{r}} \frac{-j2\pi\delta}{q_z |\zeta_{xx}\zeta_{yy} - \zeta_{xy}^2|^{1/2}} \right]_{\bar{\rho}=\bar{\rho}_s}, \quad (4.9)$$

where: $\delta = -1$ for a relative maximum, $\delta = 1$ for a relative minimum, and $\delta = j$ for a saddle point. The factor $\zeta_{xx}\zeta_{yy} - \zeta_{xy}^2$ is linked with to local principal radii of curvature at any point as [28]:

$$|r_x r_y| = \frac{(1 + \zeta_x^2 + \zeta_y^2)^2}{|\zeta_{xx}\zeta_{yy} - \zeta_{xy}^2|}. \quad (4.10)$$

In particular, at a single specular point on the ocean surface $\bar{\rho} = \bar{\rho}_s$ [28]:

$$|\zeta_{xx}\zeta_{yy} - \zeta_{xy}^2|_{\bar{\rho}=\bar{\rho}_s}^{1/2} = \frac{q^2}{q_z^2} \frac{1}{|r_x r_y|^{1/2}} \Big|_{\bar{\rho}=\bar{\rho}_s}. \quad (4.11)$$

Then, the scattered field by the i^{th} specular point is obtained after proper substitution this factor into Eqn. 4.9 [28]:

$$u(t) \approx e^{jk(R_t+R_r)} \Re \frac{\sqrt{P_t G_t G_r \lambda^2}}{\sqrt{4\pi R_r R_t}} a(t - \frac{R_r + R_t}{c}) e^{-2\pi j(f_c + f_D)t} e^{-j\bar{q}\bar{r}} \frac{\delta q_z |r_x r_y|^{1/2}}{2} \bigg|_{\bar{\rho}=\bar{\rho}}. \quad (4.12)$$

Finally, the total scattered field by a delay-Doppler cell will consists on the sum of a random number $N_m(t)$ of contributions from the specular points inside the cell as [28]:

$$U_m(t) = \sum_{i=1}^{N_m(t)} e^{jk(R_t+R_r)} \Re \frac{\sqrt{P_t G_t G_r \lambda^2}}{\sqrt{4\pi R_r R_t}} a(t - \frac{R_r + R_t}{c}) e^{-2\pi j(f_c + f_D)t} e^{-j\bar{q}\bar{r}} \frac{\delta q_z |r_x r_y|^{1/2}}{2} \bigg|_{\bar{\rho}=\bar{\rho}}. \quad (4.13)$$

The factors that are slowly varying on the positioning vector $\bar{\rho}$ can be approximated at the cell center. Therefore the total scattered field by a cell is modeled as [28]:

$$U_m(t) = \Re_m \frac{\sqrt{P_{tm} G_{tm} G_{rm} \lambda^2}}{\sqrt{4\pi R_{rm} R_{tm}}} \frac{e^{jk(R_{tm}+R_{rm})}}{2} a(t - \tau_m) e^{-2\pi j(f_{cm} + f_{Dm})t} \sum_{i=1}^{N_m(t)} A_i(t) e^{j\phi_i(t)}. \quad (4.14)$$

This model is valid for both coherent and incoherent scattering through the statistical characterization of the random sum.

4.1.3 The main fundamental scientific observable: Delay Doppler Map (DDM)

The scattering of GNSS signals is originated in an area around the nominal specular point. In general, the scattered field contains both a coherent and an incoherent component in different proportions. The coherent scattering area is limited to the first Fresnel zone. On the other side, the incoherent scattering which is also centered in the nominal specular direction, is limited by an area (glistening zone) much larger than the first Fresnel zone. GNSS-R bistatic incoherent scattering model is derived for a large Rayleigh parameter, following the geometric optics limit applied to the case of diffuse scattering regime.

There are several correlation techniques to detect the GNSS signals. The most common one is the conventional GNSS-R or cGNSS-R. The scattered electromagnetic field is cross-correlated with a replica of the known GNSS codes as [16]:

$$Y(t_0, \tau, f) = \int_0^{T_c} a(t_0 + t') u(t_0 + t' + \tau) e^{2\pi j(f_c + f)t'} dt', \quad (4.15)$$

where T_c is the coherent integration time, and f is the Doppler frequency compensation term. In a general scenario, T_c has to be set relatively small because the phase changes of individual specular reflection points introduces a random phase behavior which creates speckle. This source of multiplicative noise limits the coherent integration to a lower value than the signal coherence time. As a consequence, a long incoherent averaging has to be performed to reduce the effects of the speckle noise. Upon substitution of Eqn. 4.8 or Eqn. 4.14 in Eqn. 4.15, and assuming that the scene is time-invariant during the coherent integration time, it is respectively derived the so-called Delay Doppler Map (DDM) under the classical KA [16]:

$$Y(t_0, \tau, f) = -\frac{T_c \sqrt{P_t}}{4\pi j} \int \Re \frac{\sqrt{G_t G_r \lambda^2}}{R_r R_t \sqrt{4\pi}} \chi(\delta\tau, \delta f) e^{-2\pi j(f_D - f)} e^{jk(R_t + R_r)} \frac{q^2}{q_z} d^2 \bar{\rho}, \quad (4.16)$$

or under a stochastic model for instantaneous bistatic radar returns which models the scattering inside small enough delay-Doppler cells as the sum of a random number of contributions from inner specular points as [28]:

$$Y(t_0, \tau, f) = \sum_m T_c \Re_m \frac{\sqrt{P_{tm} G_{tm} G_{rm} \lambda^2}}{\sqrt{4\pi R_{rm} R_{tm}}} \frac{e^{jk(R_{tm} + R_{rm})}}{2} a(t - \tau_m) e^{-2\pi j(f_{Dm} + f_m)t} \sum_{i=1}^{N_m(t)} A_i(t) e^{j\phi_i(t)} \chi(\delta\tau_m, \delta f_m), \quad (4.17)$$

where $\chi(\delta\tau, \delta f)$ is the Woodward Ambiguity Function (WAF) which can be approximated by the product of two functions on $\delta\tau$ (delay difference) and δf (Doppler difference):

$$\chi(\delta\tau, \delta f) \approx \text{ACF}(\delta\tau) S(\delta f), \quad (4.18)$$

where $\text{ACF}(\delta\tau)$ is the auto-correlation function of the PRN codes and is the system impulse response in the frequency domain:

$$S(\delta f) = \frac{1}{T_c} \int_0^{T_c} e^{-2\pi j \delta f t'} dt' = \frac{\sin(\pi \delta f T_c)}{\pi \delta f T_c} e^{-\pi j \delta f T_c}. \quad (4.19)$$

However, since the scattered signal is of even weaker amplitude than the direct one and additionally it suffers from speckle noise, a large number of incoherent averages have to be done to improve the Signal-to-Noise Ratio (SNR):

$$\left\langle |Y(t_0, \tau, f)|^2 \right\rangle = \frac{1}{N_{\text{inc}}} \sum_{i=1}^{N_{\text{inc}}} |Y(t_{0,i}, \tau, f)|^2. \quad (4.20)$$

A useful representation of the average scattered power, the so-called Delay Doppler Map (DDM) can be obtained as:

$$\left\langle |Y(t_0, \tau, f)|^2 \right\rangle \approx \frac{P_t \lambda^2 T_c^2}{(4\pi)^3} \int \frac{G_t G_r}{R_r^2 R_t^2} \sigma_{pq}^0 \chi^2(\delta\tau, \delta f) d^2 \bar{\rho}, \quad (4.21)$$

where σ_{pq}^0 is the bistatic radar coefficient, that under the geometric optics limit, it can be expressed through the probability density function of the slopes $P(\bar{s})$ as:

$$\sigma_{pq}^0 = \frac{\pi |\mathfrak{R}|^2 q^4}{q_z^4} P\left(-\frac{\bar{q}_\perp}{q_z}\right), \quad (4.22)$$

where p and q are respectively the polarization of the incident and the scattered electromagnetic wave.

4.2 GNSS-R over boreal forests

This Section introduces the GNSS-R theoretical model over forests used to perform the simulation of the coherent reflectivity. The results are analyzed.

4.2.1 Introduction to polarimetric scattering

The incident energy flux Φ_i over an object is reflected Φ_r , absorbed Φ_a and transmitted Φ_t in different proportions. Once the energy equilibrium is reached the absorptivity is zero and the object starts to emit energy Φ_e . The relationships between the reflectivity Γ , the transmissivity T , the absorptivity a , and the emissivity e is:

$$\Gamma = \frac{\Phi_r}{\Phi_i}, \quad T = \frac{\Phi_t}{\Phi_i}, \quad a = \frac{\Phi_a}{\Phi_i}, \quad e = \frac{\Phi_e}{\Phi_i}. \quad (4.23)$$

Additionally, the energy conservation law establish that:

$$1 = \Gamma + T + a, \quad (4.24)$$

or

$$1 = \Gamma + T + e. \quad (4.25)$$

The reflectivity links the incident and the reflected energy over an object. The energy is generally scattered over several directions, however in case of specular reflection there is only one direction.

The power of the reflected radiation $P(\theta, \phi)$ is described by the radar equation as [27, pp. 170-171]:

$$P(\theta_{ei}, \phi_i) = \frac{\lambda^2}{(4\pi)^3} \int \frac{P_t(\theta_{ei}, \phi_i) G_t G_r}{R^4} \sigma_{pq}^0(\theta_{es}, \phi_s; \theta_{ei}, \phi_i) dA, \quad (4.26)$$

where P_t is the transmitted power, R is the distance between the transmitter and the object, G_t is the gain of the transmitter antenna, G_r is the gain of the receiver antenna, σ_{pq}^0 is the bistatic scattering coefficient, θ_{ei} and ϕ_i are the elevation and the azimuth angles of the incident wave, θ_{es} and ϕ_s are the elevation and the azimuth angles of the scattered wave, and A is the area of the object. Since σ_{pq}^0 depends on the characteristic of the object at a frequency and at a incident direction, it can be defined as [27, pp. 175]:

$$\sigma_{pq}^0(\theta_{es}, \phi_s; \theta_{ei}, \phi_i) = \frac{4\pi R^2 |\bar{E}_r^s|^2}{A |\bar{E}_t^i|^2}, \quad (4.27)$$

where \bar{E}_t^i and \bar{E}_r^s are respectively the incident and the scattered electromagnetic field. Another way to link the incident and the scattered fields is through the so-called scattering matrix $\bar{\bar{S}}$ [27, pp. 167]:

$$\begin{bmatrix} \bar{E}_v^s \\ \bar{E}_h^s \end{bmatrix} = \frac{e^{jkR}}{R} \begin{bmatrix} S_{vv} & S_{vh} \\ S_{hv} & S_{hh} \end{bmatrix} \begin{bmatrix} \bar{E}_v^i \\ \bar{E}_h^i \end{bmatrix}, \quad (4.28)$$

where subscripts v and h denote vertical and horizontal polarizations, respectively. The four scattering amplitudes characterize the scattering behaviour of the object for the four possible combinations of the v and h polarization orientations of the incident and scattered fields. Each may be a real or complex quantity and may be a function of not only the target shape, size, orientation, permittivity, and conductivity, but also of the illumination and scattering angles [27, pp. 167]. Finally, the reflectivity can be obtained as [27, pp. 252]:

$$\Gamma_p(\theta_{ei}, \phi) = \frac{1}{4\pi \sin \theta_{ei}} \iint_{2\pi} [\sigma_{pp}^0(\theta_{es}, \phi_s; \theta_{ei}, \phi) + \sigma_{pq}^0(\theta_{es}, \phi_s; \theta_{ei}, \phi)] \cos \theta_{es} d\theta_{es} d\phi_s, \quad (4.29)$$

where σ_{pp}^0 is the co-polar scattering coefficient, and σ_{pq}^0 is the cross-polar scattering coefficient.

The Stokes vector \bar{F} determines completely the polarization of an electromagnetic wave. However, in Radiometry it is common to use the modified Stokes vector \bar{F}_m (analogous to the emissivity Stokes vector) as [27, pp. 168]:

$$\bar{F}_m = \begin{bmatrix} I_h \\ I_v \\ U \\ V \end{bmatrix} = \begin{bmatrix} \langle \bar{E}_h \bar{E}_h^* \rangle \\ \langle \bar{E}_v \bar{E}_v^* \rangle \\ 2 \operatorname{Re} \langle \bar{E}_v \bar{E}_h^* \rangle \\ 2 \operatorname{Im} \langle \bar{E}_v \bar{E}_h^* \rangle \end{bmatrix}. \quad (4.30)$$

The transmissivity Stokes vector is defined as [27, pp. 257]:

$$\begin{bmatrix} T_h \\ T_v \\ T_U \\ T_V \end{bmatrix} = T_0 \begin{bmatrix} e_h \\ e_v \\ e_U \\ e_V \end{bmatrix} = C \begin{bmatrix} \langle \bar{E}_h \bar{E}_h^* \rangle \\ \langle \bar{E}_v \bar{E}_v^* \rangle \\ 2 \operatorname{Re} \langle \bar{E}_v \bar{E}_h^* \rangle \\ 2 \operatorname{Im} \langle \bar{E}_v \bar{E}_h^* \rangle \end{bmatrix}, \quad (4.31)$$

where T_0 and C are respectively the physical temperature and a constant. Assuming the transmissivity is equal to zero, it is possible to determine the emissivity as [27, pp. 252]:

$$e_p(\theta, \phi) = 1 - \frac{1}{4\pi \sin \theta} \iint_{2\pi} [\sigma_{pp}^0(\theta_s, \phi_s; \theta, \phi) + \sigma_{pq}^0(\theta_s, \phi_s; \theta, \phi)] \cos \theta_s d\theta_s d\phi_s, \quad (4.32)$$

Another important concept is the reciprocity theorem, which states that it is equivalent to consider the issue where a radar antenna emits a beam over an object which scatters the electromagnetic field, and then the scattered energy is collected by a receiver antenna, or the problem of Radiometry where the atmosphere radiates energy in all directions over an object, which once it is in thermal equilibrium it emits the energy so that it can be measured by a radiometer.

4.2.2 The EMISVEG simulator

The EMISVEG simulator was originally developed [29, 30] to compute the polarimetric Stokes emission vector (the horizontal T_h and vertical T_v brightness temperatures, and the third T_U , and fourth T_V Stokes parameters) of vegetation-covered soils at low microwave frequencies. A validation of the model with L-band (1,400-1,427 MHz) data from the SMOS REFLEX 2004 field experiment was performed [31]. In the frame of this work, it has been modified to evaluate the forward coherent reflectivity over boreal forests at L1 (1,575 MHz) at circular polarization following the Forward Scattering Alignment (FSA) convention.

The scattering model should satisfy the following premises to properly simulate the properties of GNSS Reflectometry: a) realistic 3-D spatial structure of a forest, in which every scatterer has its deterministic location, b) accurate generation of tree structures based on physical parameters, c) account for the coherent effects that may exist in different scatterers, d) account for the scattering contribution from the scatterers in the forest canopy, and also for the direct scattering of the rough ground surface, e) the scattered fields of adjacent trees in a forest stand are assumed to be uncorrelated, f) the effect of attenuation and phase change of the coherent wave propagating in the random media, and g) only the scattering in the forward direction has to be accounted for.

The total scattered field in circular polarization within the first Fresnel zone can be written as a function of the position of the nominal specular point \bar{p} as follows:

$$\begin{aligned} \bar{E}^s(\bar{\rho}(t)) = & \bar{E}_{\text{soil}}^s(\bar{\rho}(t)) + \bar{E}_{\text{forest}}^{\text{s,leaves}}(\bar{\rho}(t)) + \bar{E}_{\text{forest}}^{\text{s,leaves_soil}}(\bar{\rho}(t)) + \bar{E}_{\text{forest}}^{\text{s,soil_leaves}}(\bar{\rho}(t)) + \\ & \bar{E}_{\text{forest}}^{\text{s,branches}}(\bar{\rho}(t)) + \bar{E}_{\text{forest}}^{\text{s,branches_soil}}(\bar{\rho}(t)) + \bar{E}_{\text{forest}}^{\text{s,soil_branches}}(\bar{\rho}(t)), \end{aligned} \quad (4.33)$$

where \bar{E}_{soil}^s , $\bar{E}_{\text{forest}}^{\text{s,leaves}}$, $\bar{E}_{\text{forest}}^{\text{s,leaves_soil}}$, $\bar{E}_{\text{forest}}^{\text{s,soil_leaves}}$, $\bar{E}_{\text{forest}}^{\text{s,branches}}$, $\bar{E}_{\text{forest}}^{\text{s,branches_soil}}$, and $\bar{E}_{\text{forest}}^{\text{s,soil_branches}}$ are the total forward scattered fields by soil surface, leaves, multiple interactions involving both soil and leaves, branches (tree trunks are also included in the simulations), and multiple interactions involving branches and soil. Since the specular reflection point changes with time, the values of the electric fields in Eqn. 4.33 are also a function of time. The intrinsic nature of the model provides the capability to analyse the validity or not of the hypothesis based on the experimental results shown in Chapters 8-10. The Choudhury method [32] is used to simulate the direct scattering of the GPS signals \bar{E}_{soil}^s over the ground surface. To the first order of approximation, the scattering from every type of forest element is approximated by the superposition of the scattered field from each scatterer within the tree structure. Hence, neglecting the effect of multiple scattering among the scatterers, the scattered field from a single tree for every type of forest element can be evaluated by [33]:

$$\bar{E}_{\text{s,element}}^s = \frac{e^{jkr}}{r} \sum_{n=1}^N e^{j\phi_n} \bar{S}_n^{\text{interaction}} \bar{E}_0^{\text{i,element}}, \quad (4.34)$$

where $j = \sqrt{-1}$ is the imaginary unit, N is the total number of the scatterers within the tree structure, $\bar{S}_n^{\text{interaction}}$ is the scattering matrix in circular polarization of the n^{th} scatterer above the soil corresponding to a forest element, ϕ_n is a phase compensation term accounting for the shift of the phase reference from the local coordinate system of the n^{th} scatterer to the global coordinate phase reference, and $\bar{E}_0^{\text{i,element}}$ is the amplitude of the incident electromagnetic wave. Denoting the position of the n^{th} scatterer in the global coordinate system by \bar{r}_n , ϕ_n is given by [33]:

$$\phi_n = (\bar{k}_i - \bar{k}_s) \cdot \bar{r}_n, \quad (4.35)$$

where \bar{k}_i and \bar{k}_s are, respectively, the unit vectors representing the propagation direction of the incident and the scattered fields.

The forest element scattered field $\bar{E}_{\text{forest}}^{s,\text{element}}$ is modeled taking into account the effect of attenuation and phase change of the coherent wave $\bar{E}^{s,\text{element}}$ propagating in the random media (boreal forest). Based on Foldy's approximation [34], the variation of the mean field $\bar{E}_{\text{forest}}^{s,\text{element}}$ with respect to the distance s along the direction \bar{k} is generally governed by:

$$\frac{d\bar{E}_{\text{forest}}^{s,\text{element}}}{ds} = jK\bar{E}_{\text{forest}}^{s,\text{element}}, \quad (4.36)$$

where K is the effective propagation constant. Using eigen-analysis, the differential Eqn. 4.36 is solved and the solution is given by:

$$\bar{E}_{\text{forest}}^{s,\text{element}} = e^{jk_0s}\bar{T}(s, \bar{k})\bar{E}_{\text{forest}}^{s,\text{element},0}, \quad (4.37)$$

where \bar{T} is the transmissivity matrix accounting for the extinction due to scattering and absorption, and $\bar{E}_{\text{forest}}^{s,\text{element},0}$ is the forest scattered field at $s=0$.

To account for this last term and for the bistatic nature of the GNSS reflectometry, the expressions for the scattering matrix as proposed in [33] in the forward-scatter direction of each different forest element interactions $\bar{S}_n^{\text{interaction}}$ are modeled as follows:

$$\bar{S}_n^{\text{element}} = \bar{T}_n^i \bar{S}_n^0(\bar{k}_s, \bar{k}_i) \bar{T}_n^i, \quad (4.38)$$

$$\bar{S}_n^{\text{element,soil}} = e^{j\tau_n} \bar{T}^t \bar{R}(\bar{k}_s, \bar{k}_{gs}) \bar{T}_n^r \bar{S}_n^0(\bar{k}_{gs}, \bar{k}_i) \bar{T}_n^i, \quad (4.39)$$

$$\bar{S}_n^{\text{soil,element}} = e^{j\tau_n} \bar{T}_n^i \bar{S}_n^0(\bar{k}_s, \bar{k}_{gi}) \bar{T}_n^r \bar{R}(\bar{k}_{gi}, \bar{k}_i) \bar{T}^t, \quad (4.40)$$

where $\bar{S}_n^{\text{element}}$, $\bar{S}_n^{\text{element,soil}}$, and $\bar{S}_n^{\text{soil,element}}$ are the direct scattering, the element-soil scattering and the soil-element scattering, matrices respectively. \bar{T}_n^i , \bar{T}_n^r , and \bar{T}^t are the transmissivity matrices, respectively, for the direct, reflected, and total traveling

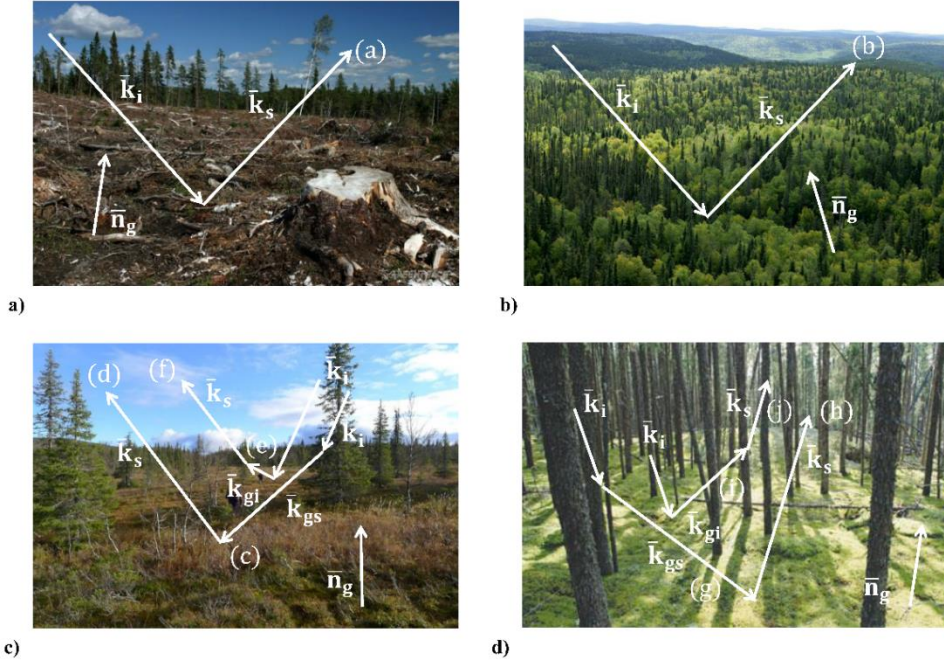


Fig. 4.1. (a) Scattering over the ground surface, (b) direct scattering over the canopy, (c) multiple scattering involving both the soil and the canopy, and (d) multiple scattering involving both the soil and the trunks.

path, $\bar{\bar{R}}$ is the reflection matrix of the rough tilted ground plane whose elements are derived as per Wang and Choudhury [35, pp. 1540-1541], and:

$$\bar{k}_{gi} = \bar{k}_i - 2\bar{n}_g(\bar{n}_g\bar{k}_i), \quad (4.41)$$

$$\bar{k}_{gs} = \bar{k}_s - 2\bar{n}_g(\bar{n}_g\bar{k}_s), \quad (4.42)$$

$$\tau_i = -2k_0(\bar{n}_g\bar{n}_g)(\bar{n}_g\bar{k}_i), \quad (4.43)$$

$$\tau_s = 2k_0(\bar{n}_g\bar{n}_g)(\bar{n}_g\bar{k}_s), \quad (4.44)$$

where the phase terms τ_i and τ_s account for the extra path lengths of the image excitation and the image scattered waves, respectively, and \bar{k}_i , \bar{k}_s , \bar{k}_{gi} , \bar{k}_{gs} and \bar{n}_g are defined in Fig. 4.1.

The electromagnetic models selected for the expression of the bistatic scattering matrices $\bar{\bar{S}}_n^0$ are the Semiexact Solution for the branches [36], and the Generalized Rayleigh-Gans Approximation for a needle in the case of leaves [37].

The incident L1 GPS signals after the scattering over the ground surface ((a) in white in Fig. 4.1a) are collected by the receiver (P(Y) and C/A ReflectOmeter). The direct scattering over the canopy attenuates and scatters forward the incident GPS signals without reaching the trunks. The incident GPS wavefront is first scattered by the canopy ((b) in white in Fig. 4.1b). There is a component in the specular direction, but also, a fraction of it penetrates the trunks, reaches the ground ((c) in white in Fig. 4.1c) and is reflected on the ground, and travels up through the upper layers to the receiver ((d) in white in Fig. 4.1c). As a complement of the latter contribution, ground reflection ((e) in white in Fig. 4.1c) followed by specular scattering over the canopy ((f) in white in Fig. 4.1c) is also considered. The incident wave propagates through the upper layers and is attenuated by them before it scatters over the ground. The upward reflected GPS signals penetrate the trunks and are scattered by the canopy. As the last contribution, specular scattering on the trunks ((g) in white in Fig. 4.1d) followed by ground reflection ((h) in white in Fig. 4.1d) is considered. This mechanism is similar to the canopy-soil one. However, the scattering process occurs in the trunks instead of the canopy, and the canopy acts as an attenuating medium. Ground reflection ((i) in white in Fig. 4.1d) followed by trunk specular scattering ((j) in white in Fig. 4.1d) complements the latter mechanism, being similar to the soil-canopy mechanism.

The statistics of the scattered field are approximated from a Monte-Carlo simulation in which a large number of tree structures are generated using stochastic L-systems [38] and then the scattering matrix of all generated trees are computed. The total forest element scattered field in circular polarization $\bar{E}_{\text{forest}}^{\text{s,element}}$ is obtained as the mean of 100 Monte-Carlo realizations to average the position of the scatterers. A large number of fractal-generated trees (725, 150 and 72 trees/ha) is considered during the Monte-Carlo simulations to characterize the statistics of the scattered signals. Finally, the reflectivity is defined as:

$$\Gamma = \frac{1}{4\pi \sin \theta_{ei}} \iint \sigma^0 d\Omega_s = \frac{1}{4\pi \sin \theta_{ei}} \iint \frac{|\bar{E}_s|^2 / A}{|\bar{E}_i|^2 / 4\pi R^2} \cos \theta_{es} d\phi_s d\theta_{es}, \quad (4.45)$$

where θ_{ei} is the elevation angle of the incident wave, θ_{es} and ϕ_s are the elevation and azimuth angles of the scattered wave, and σ^0 is the forward scattering coefficient, A is the illuminated area, and the integration is carried out over the upper half space. Since around the direction of specular reflection the coherent component is much larger than the incoherent one, the integrand in Eqn. 4.45 tends to a delta function. This allows reducing the integration limits around the specular direction. In our case, after inspection of the integrand, it was concluded that the contributions beyond a $4^\circ \times 4^\circ$ domain had a negligible contribution to the computed reflectivity value.

4.2.3 Simulations of the reflectivity over forests

Simulations of the reflectivity at L1-band over forests have been performed with a modified version of EMISVEG using signals at Right Hand Circular Polarization (RHCP) and Left Hand Circular Polarization (LHCP). In the considered scattering model, individual tree components located above a tilted dielectric rough plane are illuminated by the electromagnetic field and the scattered fields are computed, and then added coherently as in [33]. Branches and tree trunks are modeled by stratified dielectric cylinders, arranged following a fractal geometry described by Lindenmayer systems [39]. The leaves are modeled by dielectric needles, and are added to the tree model. This scattering model preserves the phase of scattering fields from scatterers (leaves, branches, and trunks) in the simulation of this coherent signature from the forest. The effect of attenuation and phase change of the coherent wave propagating in the forest media is also taken into account using the Foldy's approximation [34].

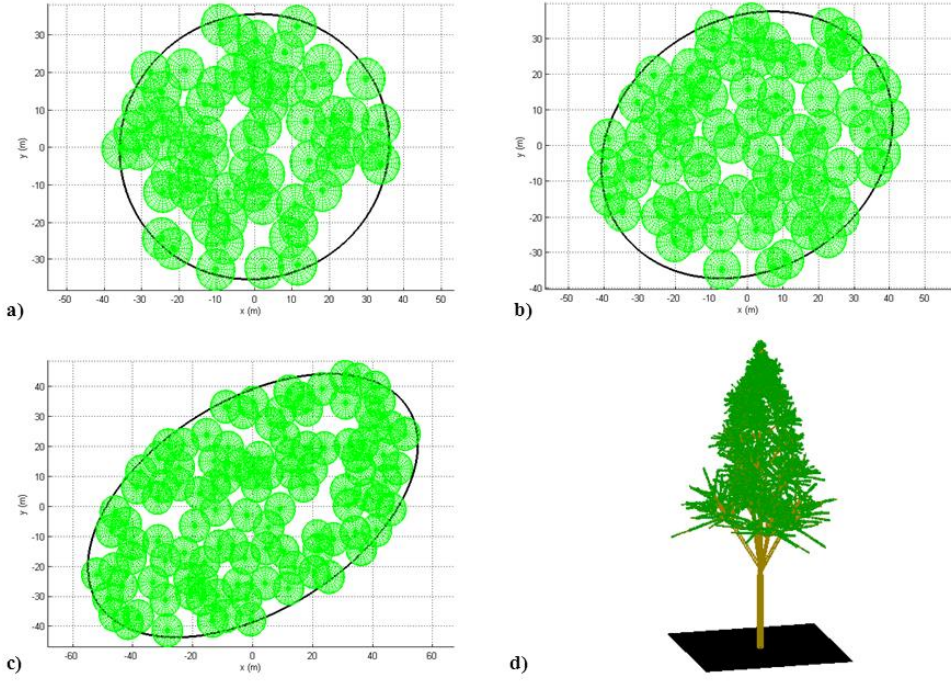


Fig. 4.2. (a) Simulated scattering area for an elevation angle of $\theta_e = 72^\circ$, (b) simulated scattering area for an elevation angle of $\theta_e = 54^\circ$, (c) simulated scattering area for an elevation angle of $\theta_e = 35^\circ$, (d) simulated 3-D geometry of a single tree over a tilted soil surface.

The scattering matrix $\bar{\bar{S}}$ was transformed from linear to circular polarization. This matrix relates the components of the scattered field \bar{E}^s and the incident field \bar{E}^i for all the polarimetric combinations:

$$\begin{bmatrix} \bar{E}_{RHCP}^s \\ \bar{E}_{LHCP}^s \end{bmatrix} = \frac{e^{jkR}}{R} \begin{bmatrix} S_{RHCP-RHCP} & S_{RHCP-LHCP} \\ S_{LHCP-RHCP} & S_{LHCP-LHCP} \end{bmatrix} \begin{bmatrix} \bar{E}_{RHCP}^i \\ \bar{E}_{LHCP}^i \end{bmatrix}, \quad (4.46)$$

where R is the distance from the specular point to the receiver. Subscripts **RHCP** and **LHCP** denote Right Hand Circular Polarization and Left Hand Circular Polarization, respectively.

These simulations provide reflectivity values for the soil, branches (tree trunks are also included into the simulations), leaves and multiple reflections involving leaves-soil and branches-soil interactions as in [40, 41].

The vegetation height was set to be ~ 20 m (Fig. 4.2) based on the available ground truth data⁴, and the scattering area was set to be equal to the first Fresnel zone A_{Fresnel} . A much lower tree density for a biomass density of 100 t/ha over North of Sweden (725 trees/ha instead $\sim 2,700$ trees/ha as in [42] for a tree height ~ 20 m) was required to make the simulations feasible; however results can be extrapolated the experimental work in the Chapters 8, 9, and 10. The electromagnetic models selected for the expression of the bistatic scattering matrices were the Semi-Exact solution for the branches $\bar{\bar{S}}_{\text{branches}}$ [36], the Generalized Rayleigh-Gans (GRG) approximation for a needle in the case of leaves $\bar{\bar{S}}_{\text{needle}}$ [37], and the Choudhury method for the soil $\bar{\bar{S}}_{\text{soil}}$ [32]. The Semi-Exact solution was selected because the radii of curvature of the branches of Northern Sweden forests is not an order of magnitude larger than the signals wavelength used in the simulations ($\lambda_{\text{LI}} = 19$ cm). The Physical Optics approximation for higher frequencies provides a fast algorithm when the radius of tree branches is large as compared to the wavelength [36]. The Generalized Rayleigh-Gans approximation for a needle was selected to evaluate the scattering on leaves because: a) needles are the best geometrical approximation for leaves in coniferous vegetation, and b) GRG is valid for a scatterer with at least one of its dimensions small as compared to the signals wavelength [37]. Nonetheless, several simulations were performed to evaluate the differences with other methods: Rayleigh approximation for an ideal needle (Fig. 4.3a), Rayleigh approximation for a needle (Fig. 4.3b), and the GRG approximation for a needle (Fig. 4.3c). Additionally, the leaves-soil scattering mechanism was evaluated using the same scattering methods for the leaves, and the Choudhury method [32] to account for the electromagnetic interaction with the soil (Figs. 4.3d,e,f). These simulations show that there are several differences: a) a larger dynamic range of the co-polar reflectivity over leaves using the GRG method (~ 30 dB) as compared to that obtained with the Rayleigh approximation for an ideal needle (~ 20 dB); and b) both the cross- and the co-polar reflectivities for leaves-soil interactions.

The cross-polar values are under-estimated as compared to the GRG-Choudhury method (from ~ 10 dB at low elevation angles $\theta_e \sim 10^\circ$ to ~ 20 dB for high elevation angles $\theta_e \sim 80^\circ$). On the other side, the co-polar reflectivity levels are under-

⁴ The simulations were done to help the interpretation of results in Chapters [8, 10]. The experiment performed North of Sweden is described there.

estimated ~ 20 dB using the Rayleigh approximation for an ideal needle for low elevation angles $\theta_e \sim 10^\circ$.

After these previous considerations, the cross- and co-polar reflectivity coefficients are analyzed as a function of the elevation angle in the range $\theta_e = [10^\circ, 80^\circ]$ for three different biomass densities 725 trees/ha (Figs. 4.4a-single reflections, d-multiple reflections), 150 trees/ha (Figs. 4.4b-single reflections, e-multiple reflections) and 72 trees/ha (Figs. 4.4c-single reflections, f-multiple reflections). The co-polar component over soil-surface is dominant for low elevation angles up to $\theta_e \sim 30^\circ$, while the cross-polar is the highest component for larger elevation angles. Actually, this corresponds to the Brewster angle, which is a property of the reflector type and indicates the change of polarity of the vertical component of incident electromagnetic field after being reflected [43]. A common characteristic to the full ranges of biomass densities and elevation angles under study is the order of reflectivity levels. First of all the soil surface, which is followed by reflectivity levels over branches and leaves.

The study of multiple reflections involving both leaves-soil and soil-leaves, and both branches-soil & soil-branches shows that the cross-polar component is the highest for low elevation angles up to $\theta_e \sim 30^\circ$, while the co-polar one is the highest component for higher elevation angles. This inversed-behaviour as compared to single reflections is due the double polarization changes induced by, first from RHCP to LHCP, and then from LHCP to RHCP.

The reflectivity difference between a biomass density of 725 trees/ha and 72 trees/ha is analyzed for elevation angles in the range $\theta_e = [10^\circ, 80^\circ]$ for the cross-polar (Fig. 4.5a), and the co-polar (Fig. 4.5b) scattered signals. The cross-polar increments for leaves and branches are $\sim [10, 20]$ dB for elevation angles in the range $\theta_e = [10^\circ, 80^\circ]$. An increment as a factor of 10 in the biomass density (from 72 trees/ha to 725 trees/ha) is translated into an increment of reflectivity over leaves and branches as high as 20 dB. On the other side, the elevation angle has a large impact on the soil and vegetation-soil scattering mechanisms. In particular, the cross-polar signal evolves from $[-30, -40]$ dB to $[-10, +10]$ dB when the elevation angle increases from 10° to 80° (Fig. 4.5a). The lower reflectivity levels for higher biomass densities at low elevation angles are due to the larger signal attenuation due to the larger geometric

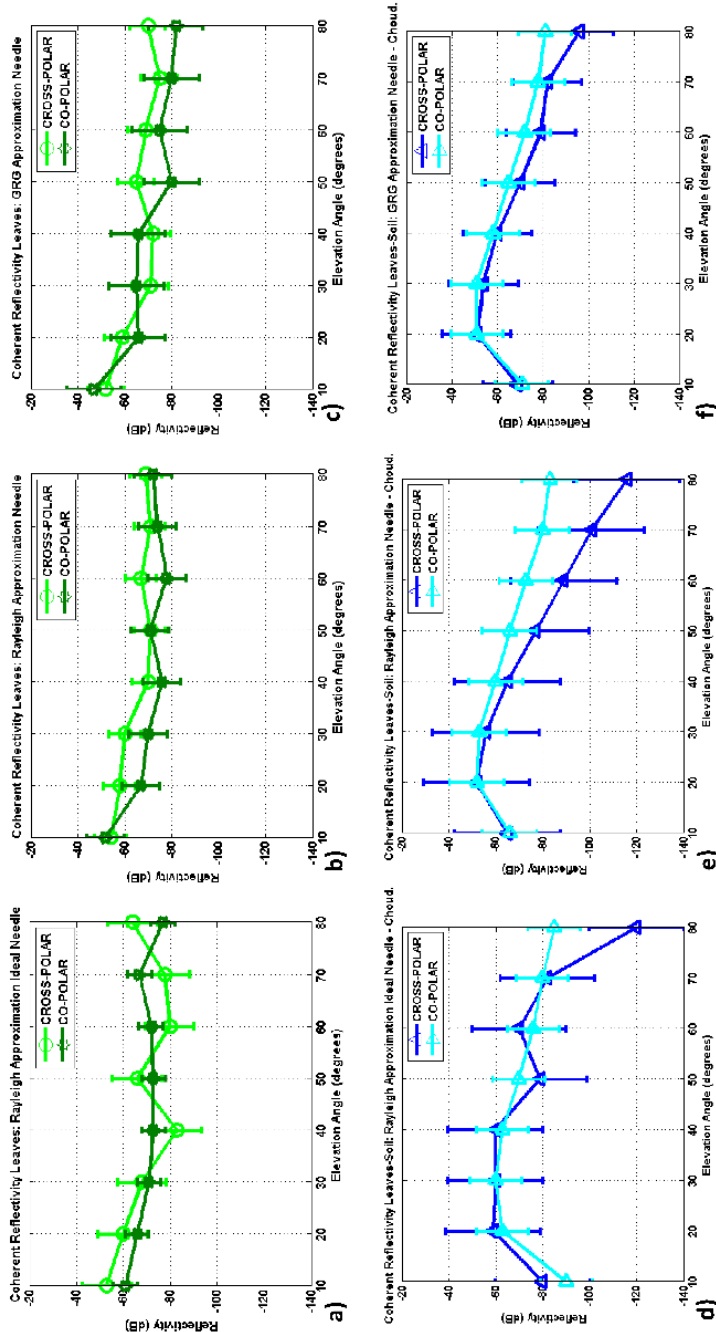


Fig. 4.3. Simulated reflectivity for a biomass density of 725 tress/ha over leaves: (a) Rayleigh approximation ideal needle, (b) Rayleigh approximation needle, (c) Generalized Rayleigh Gans approximation needle; and leaves-soil interactions: (d) Rayleigh approximation ideal needle-Choudhury, (e) Rayleigh approximation needle-Choudhury, and (f) Generalized Rayleigh Gans approximation needle-Choudhury.

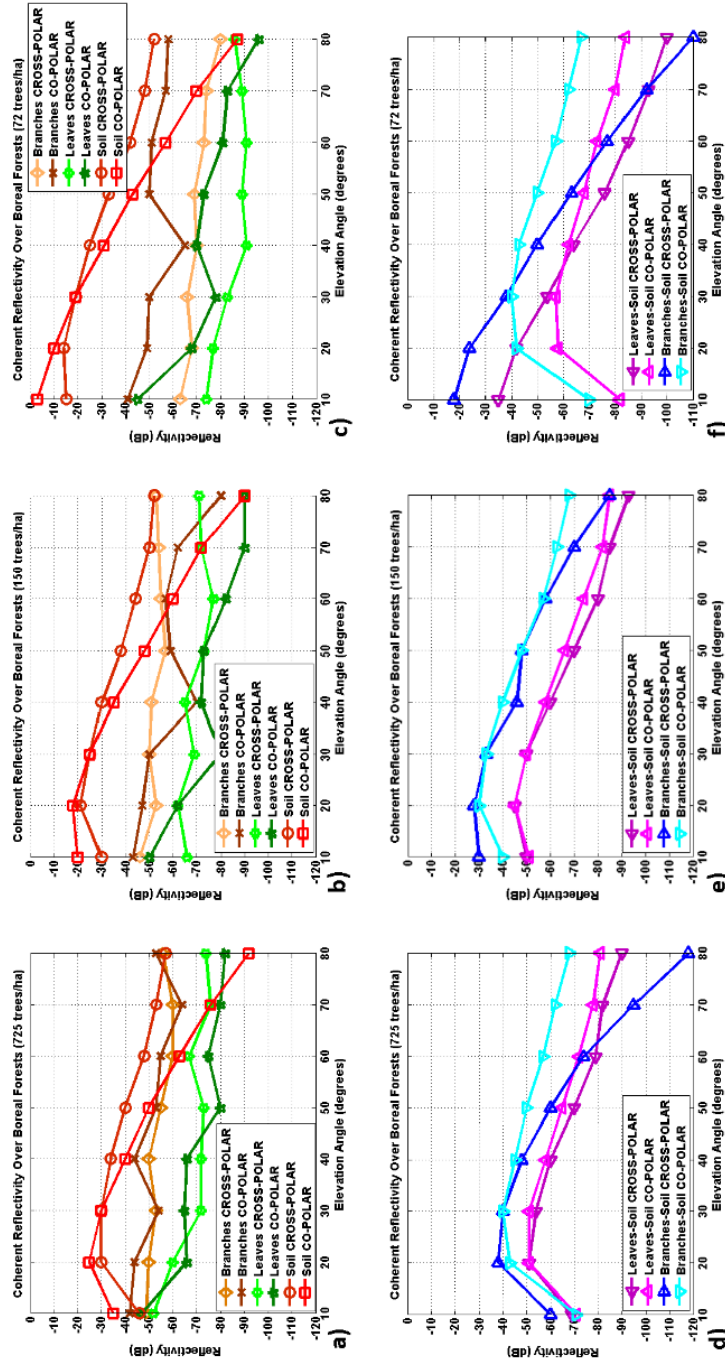


Fig. 4.4 Cross- and co-polar reflectivity simulations over forests: (a,b,c) direct scattering (canopy, soil) and (d,e,f) multiple scattering (canopy-soil interactions), for a biomass density of (a,d) 725 trees/ha, (b,e) 150 trees/ha, and (c,f) 72 trees/ha.

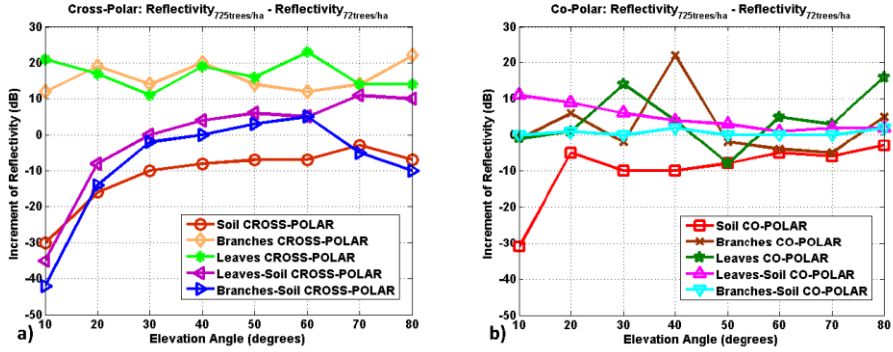


Fig. 4.5. Increment of (a) cross- and (b) co-polar reflectivity over forests from a biomass density of 72 trees/ha to 725 trees/ha.

path through the forests. The comparison with the evolution of the co-polar component (Fig. 4.5b) contains additional information. The soil reflectivity increments are similar to the cross-polar case. However, the co-polar reflectivity increments for branches-soil mechanism roughly fluctuates around 0 dB, while for the case of leaves-soil scattering the increment of reflectivity decreases from 10 dB to 0 dB.

4.2.4 Conclusions

This work has first presented the evolution of the reflectivity as a function of the elevation angle over boreal forests using simulations of the cross- (reflected LHCP) and co-polar (reflected RHCP) scattered fields over soil and canopy but also including canopy-soil interactions for three different levels of biomass density (725 trees/ha, 150 trees/ha and 72 trees/ha). The canopy (branches, leaves) reflectivity variations for larger density levels, are found to have a dependence with the elevation angle, the polarization of the reflected signal and the scatterer type. Cross-polar canopy reflectivity increments are $\sim [10, 20]$ dB for elevation angles in the range $\theta_e = [10^\circ, 80^\circ]$. On the other side, attenuation due to signal propagation through forests leads to lower reflectivity values over soil as lower is the elevation angle, independently of the

polarization. However, the polarization is found to be an important parameter that determines the reflectivity levels of canopy-soil interactions. Increments of canopy-soil cross-polar reflectivity values have a similar trend than those corresponding to soil scattering. Nonetheless, for elevation angles larger than $\sim 30^\circ$ the former scattering mechanism shows a higher increment of reflectivity as compared to scattering only over the soil. Additionally it is found that leaves-soil co-polar reflectivity levels reduces from 10 dB to 0 dB for elevation angles in the range $[10^\circ, 80^\circ]$, while for branches-soil interactions is roughly constant around zero.

PART III:
EXPERIMENTAL VALIDATION OF THE ³CAT-2
PAYLOAD

5

5. THE RECONSTRUCTED GNSS-R TECHNIQUE: rGNSS-R

5.1 Introduction

In 1988 the concept of multistatic scatterometry was first proposed by Hall and Cordey [44]. In 1993, the concept of GNSS-based multi-static altimetry was first proposed by Martín-Neira [2]. The first reflected GPS signals were accidentally collected by a French military aircraft testing a GPS receiver and reported in 1994 [14]. The ultimate achievable altimetric precision [2, 3] of future GNSS-R space missions is still under study [45-47]. The Phase-A studies of ESA's PAssive Reflectometry and Interferometry System In-Orbit Demonstrator mission (PARIS-IoD) [3] finished in December 2012 showing that the mission is feasible and would provide scientific products complementary to those derived using conventional nadir-looking altimeters. In June 2012, NASA approved the Cyclone Global Navigation Satellite System mission (CyGNSS) [48], consisting of 8 GPS-R receivers deployed on a constellation of micro-satellites. The technical approaches and applications of both missions are different. While the PARIS IoD main objective is mesoscale altimetry, that of CyGNSS is scatterometry to infer wind speed, and while PARIS IoD uses interferometric GNSS-R (cross-correlation of the direct and reflected signals), CyGNSS uses conventional GNSS-R (cross-correlation of the reflected signal with a locally-generated replica of the transmitted one).

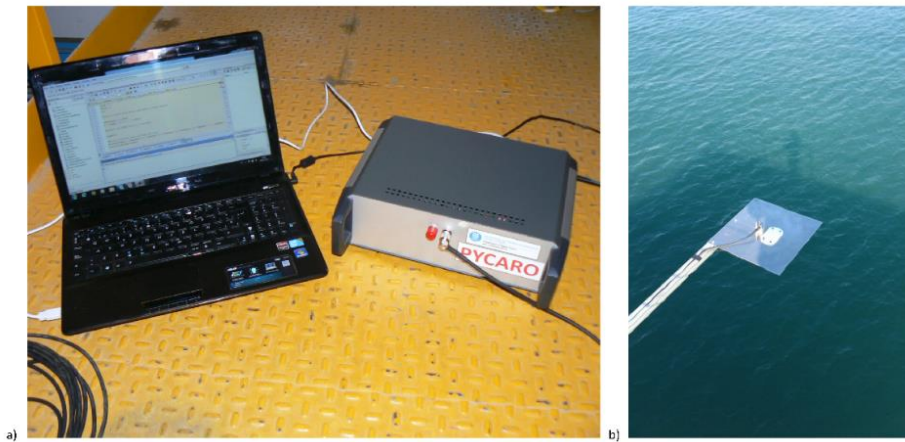


Fig. 5.1. (a) View of the PYCARO instrument connected to a laptop. (b) View of the two Antcom[®] omnidirectional antennas attached to a 3 m boom used to collect both, the direct and the Earth-reflected GPS signals.

For navigation purposes it is known (e.g. [49]) that the ten-fold faster chipping rate of the P(Y) GPS code, as compared to the C/A GPS code, leads to a sharper autocorrelation function (ACF), and a higher ranging precision. However, the P(Y)⁵ is not publicly available. To that end, the PAssive Reflectometry and Interferometry System (PARIS) concept [3] was conceived as an interferometric system (iGNSS-R) to allow the access to the full GNSS (GPS and Galileo) signal bandwidths, without having access to the encrypted P(Y) and M signals [50]. In iGNSS-R the cross-correlation of the direct and the reflected signals is performed, and therefore, high-gain and steerable antennas are required to partially compensate for the poorer Signal-to-Noise Ratio (SNR) of the direct signal as compared to the conventional GNSS-R (cGNSS-R). Several cGNSS-R instruments have been developed using either a software [51-54], or a hardware [55-63] approach. However during the last years hardware receivers have gained more popularity because of the advances in digital signal processing and because the signal processing can be performed in real time. More recently, in 2010 the iGNSS-R was experimentally tested for first time from a static point in the Zeeland Bridge [64], and later in 2011 from two aircraft flights [65, 66] over the Gulf of Finland showing a two-fold improvement factor as compared to cGNSS-R, in agreement with the theoretical analyses performed in [45, 46, 67, 68, 69], which include speckle noise and the correlation between consecutive waveforms as one of the main error sources of the height estimation.

In Section 5.2, a new GNSS-R instrument (PYCARO: P(Y) and C/A ReflectOmeter) designed for altimetric applications using synergetically concepts from cGNSS-R and iGNSS-R is described (Figs. 1a,b). Section 5.3 describes two field experiments performed to test this new technique in a real scenario and presents the analysis of the results. These results depend, among other factors, on the different sources of noise in the measurement of the altimetric observables. An analysis of the dependence of the accuracy of the altimetric measurements on the satellite's elevation angles is also presented and compared to the results of a monostatic K-band radar altimeter. Finally, Section 5.4 summarizes the main results of this study.

⁵ S. Lowe et al. performed a cGNSS-R experiment using the encrypted P(Y) GPS code, but not in real time [20], and B. Wilmhoff et al. employed the encrypted P(Y) code to perform a real time experiment over the sea [23].

5.2 The PYCARO instrument

Despite the previous evidence of phase-tracked Earth-reflected GPS signals [14] it is generally assumed [70] that sea forward-scattering at L band is dominated by the diffuse component of the signal (incoherent scattering). Recently, a balloon experiment was carried out over the Canyelles dam on February 3rd 2011 [71], showing that the scattered signal can be phase-tracked over smooth water (reservoir's surface) and even over the rough land's surface with rugged topography (Fig. 5.2). Then, the prototype of PYCARO was also tested over the Baltic Sea on June 21st 2011 (Fig. 5.3) for the development of the instrument.



Fig. 5.2. Aerostatic balloon where the experiment took place. Arrow indicates position of the 2 m mast.



Fig. 5.3. Skyvan Short SC-7 during the preparatory activities. PYCARO was tested for first time over rough sea surface conditions.

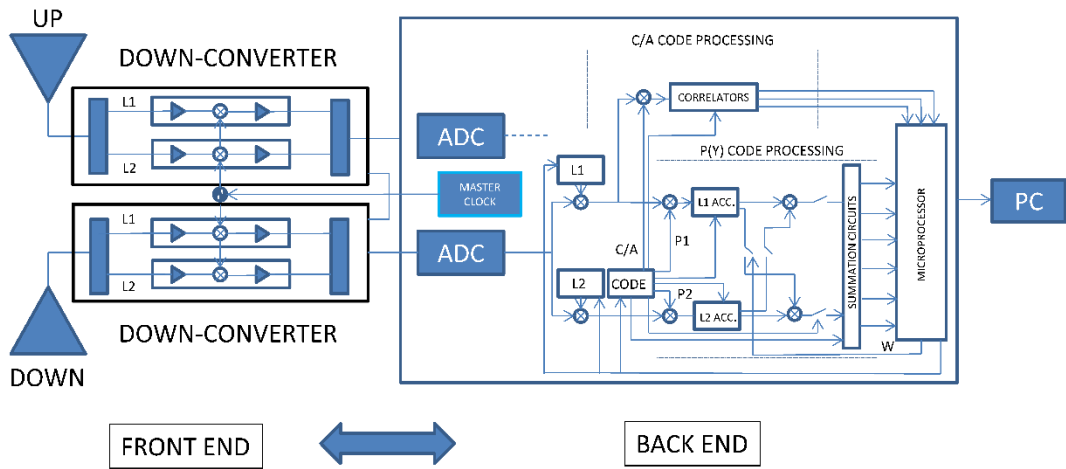


Fig. 5.4. Block diagram of the PYCARO instrument. The correlation approach used in the down-looking channel by PYCARO providing P code processing of the encrypted GPS signals without knowledge of the encrypted code, in addition to the C/A code cGNSS-R is sketched. Both the up- and the down-looking channels use a similar correlation approach.

For this Ph.D. Thesis a new instrument has been developed [72]. It is focused on altimetry applications, tracking the C/A & P(Y) GPS signals. As it will be shown the system allows a precise determination of the ocean topography with high spatial resolution. The PYCARO instrument (pat. pending; Figs. 5.1a and b) is a dual band (L1, L2) receiver with two synchronous RF inputs⁶ (Fig. 5.4). Altimetric observables are performed from the difference between measurements of the delays of the direct and the reflected signals.

As in a cGNSS-R the correlation with clean replicas of the C/A code are computed. Additionally, since the P-code⁷ is transmitted at L1 and L2, PYCARO separately correlates the L1 and the L2 signals of the same receiver with a model of the P-code and counter-rotates them with a model carrier using a P-code method for processing encrypted GPS signals without knowledge of the encrypted code [73]. The main lobe

⁶ The up-looking and the down-looking channels use the same correlation approach and there is no interaction between them. In the following the text refers to the latter channel.

⁷ The PYCARO instrument uses a model of the P-code. It does not possess the encrypted P(Y) signal, but takes advantage of it using a novel correlation technique first presented in [72].

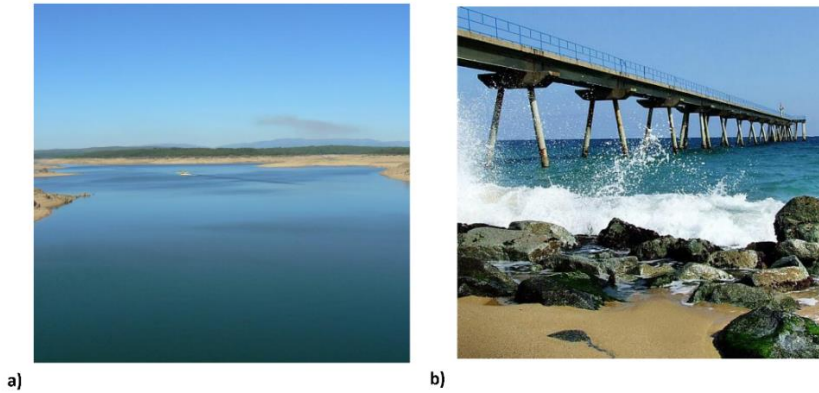


Fig. 5.5. (a) View of the surface water at the Cernadilla water reservoir during the first experiment. (b) View of the Pont del Petroli pier. The experimental set-up during the second field experiment was placed at the edge of the pier.

of the spectrum of the $P(Y)$ is 20.46 MHz wide from null-to-null. After removal of the P-code modulation, the W-code modulation spreads the energy over ± 500 kHz which translates into a reduced bandwidth of 1 MHz. The L1-Y and L2-Y signals, after P-code correlation, have on them only the W-bit modulation with a bandwidth⁸ of approximately 1 MHz [74]. The resulting correlation products are then summed and dumped over successive W chips to increase the Signal-to-Noise Ratio (SNR). For both the L1 and the L2 signals, the sign of the prompt in-phase sum is then extracted as an estimate of the W-code sign.

To reduce the effect of the W-code sign flips, the W-code sign from L1 is multiplied times all correlation products from L2, and the W-code sign from L2 is multiplied times all correlation products from L1. PYCARO's block diagram is shown in Fig. 5.4, where the RF front-end and the signal processor back-end are sketched. The front-end is composed of two I and Q down-conversion chains, one for each antenna input,

⁸ This 20-times narrower bandwidth, as compared to the direct cross-correlation with the Y code, reduces the noise energy.



Fig. 5.6. (a) . View of the Laboratori d'Enginyeria Marítima facility at the Pont del Petroli (Badalona, Spain). (b) View of the monostatic K-band (26 GHz) radar altimeter VEGAPULS 62 [76] used during the Mediterranean Sea experiment.

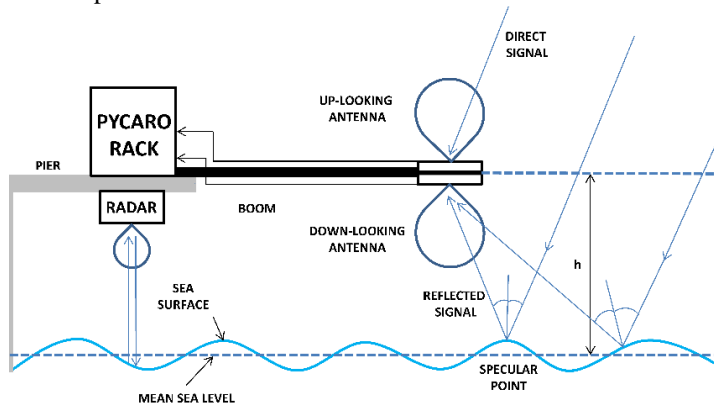


Fig. 5.7. Arrangement of the instrumental set-up during the Pont del Petroli pier experiment.

and a common system reference oscillator. The back-end is composed of two Analog-to-Digital Converters (ADC) that convert the two I and Q baseband signals into digital words, and a real-time signal processor that computes the waveforms for both, the C/A-L1 and the P(Y)-L1, L2 GPS codes. Since we are interested only in altimetric observations, only the lags in the leading edge and around the peak of the waveform need to be computed. Scatterometric measurements are also possible from the ratio of the peaks of both channels.

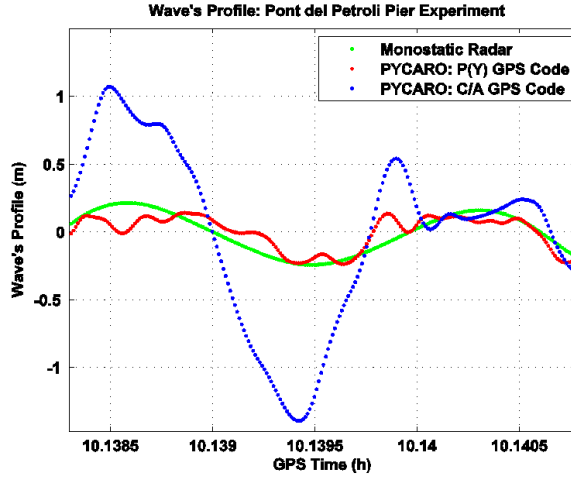


Fig. 5.8. Sample sea wave's profile as a function of the GPS time provided by the monostatic K-band (26 GHz) radar VEGAPULS 92 and PYCARO employing both the C/A-L1 and P(Y)-L2 signals. Satellite's elevation angle $\theta_e = 70^\circ$.

5.3 Field experiments description: Cerdanilla's reservoir and Mediterranean Sea

Two field experiments from two different static locations have been carried out using the PYCARO instrument. These experiments were conducted to analyze the impact of the water surface roughness on the achievable height precision provided by PYCARO using the C/A and the P(Y) GPS codes.

The first experiment took place at the Cernadilla water reservoir (Zamora, Spain) on August, 2012, and the second one was performed at the Pont del Petroli pier (Badalona, Spain) over the Mediterranean Sea on November 20th, 2012. The experimental set-up was composed by a rack containing the PYCARO instrument, a laptop, and two dual-band GPS Antcom[®] omnidirectional antennas [75, pp.118] for collecting the up and the down-looking signals, using right-hand and left-hand circular polarizations, respectively. The antennas were attached to a 3 meter mast parallel to the water surface during both field experiments (Figs. 5.5a,b). Furthermore, during the experiment over the Mediterranean Sea, in addition to the bistatic measurements provided by PYCARO, and the two omnidirectional antennas, a monostatic K-band (26 GHz) radar altimeter VEGAPULS 62 (Figs. 5.6a,b) was deployed as a reference

measurement system [76]. The radar was placed at the edge of the pier (Figs. 5.5b and 5.7) in a nadir-looking configuration for real-time monitoring of the Sea Surface Height (SSH).

In Cernadilla reservoir experiment the water surface was extremely calm (Fig. 5.5a), and therefore, the reflected signal consisted mostly of the coherent component, while in the Pont del Petroli pier experiment the water was relatively calm, with peak-to-peak waves of ~ 40 cm.

The incoherent processing of the scattered field imposes an averaging of the signals over the glistening zone that limits the achievable spatial resolution. This Section shows a sample of the temporal sea surface profile as measured by the PYCARO instrument using the P(Y) and the C/A GPS codes, which has been designed to track the phase of the GPS signals. The receiver was placed in a stationary position on the Pont del Petroli pier, at a low altitude over the sea surface ($h = 4.76$ m), being the radius of the first Fresnel zone 0.94 m and 1.06 m for the L1 and L2 signals respectively. The surface was relatively flat inside the Fresnel zone but just slowly moved up and down around ± 20 cm at a frequency of 0.14 Hz, a time scale much longer than the coherent integration time. Then, as a consequence, only one specular point is in view at each instant of time. This leads to a totally coherent signal collected in the antenna phase center during the coherent integration time. As a result, the sea waves profile can be derived using GPS reflected signals in a bistatic configuration. From the comparison between the temporal series of data provided by the monostatic K-band radar and the bistatically derived results, using PYCARO (Fig. 5.8), a Pearson linear correlation coefficient of 0.80 and 0.86 at L1 & L2 frequencies is obtained, respectively (Figs. 5.9a,b).

The Significant Wave Height (SWH) measured by the the monostatic radar was 36 cm (Fig. 5.10a), being the mean platform's height over the mean sea surface $h = 4.765 \pm 0.002$ m. Note that this SWH at L band (L1 frequency $f_{L1} = 1.575$ GHz, L2 frequency $f_{L2} = 1.227$ GHz), and for a satellite's elevation angle θ_e in the range

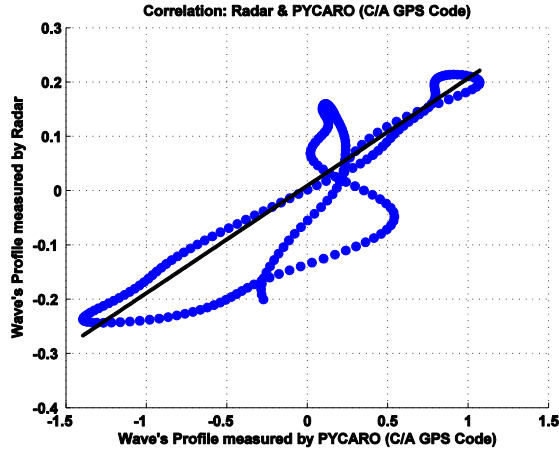


Fig. 5.9. (a) Correlation between the temporal series (~ 9 s) of the measured SSH using the monostatic radar, and the PYCARO instrument (C/A GPS code).

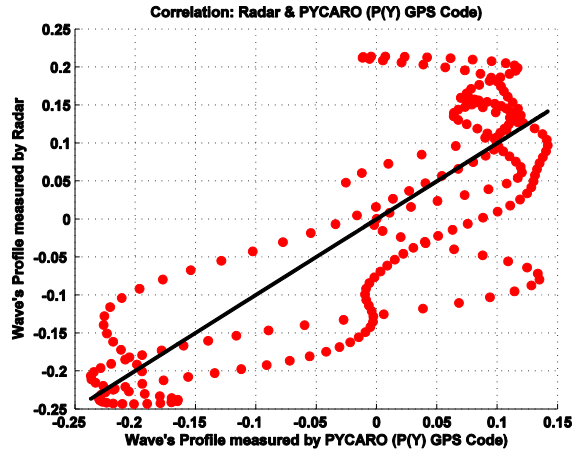


Fig. 5.9. (b) Correlation between the temporal series (~ 9 s) of the measured SSH using the monostatic radar, and the PYCARO instrument (P(Y) GPS code).

from $\sim 5^\circ$ to 90° does not satisfy the Rayleigh criterion for a surface's to be considered smooth:

$$SWH < \frac{\lambda}{8 \sin \theta_e}, \quad (5.1)$$

where λ is the signal electromagnetic wavelength.

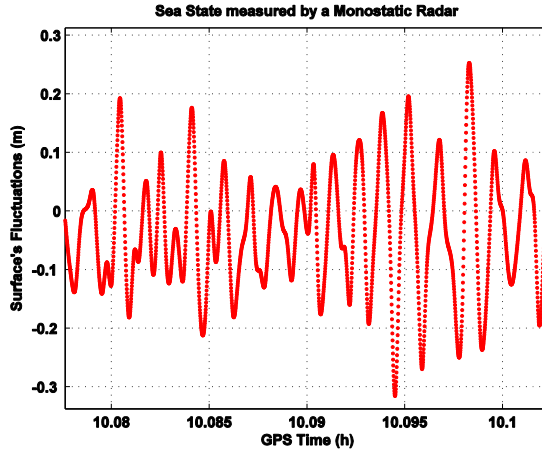


Fig. 5.10. (a) Sample Sea Surface Height (SSH) fluctuations as measured by the monostatic K-band radar during the experiment over the Mediterranean Sea.

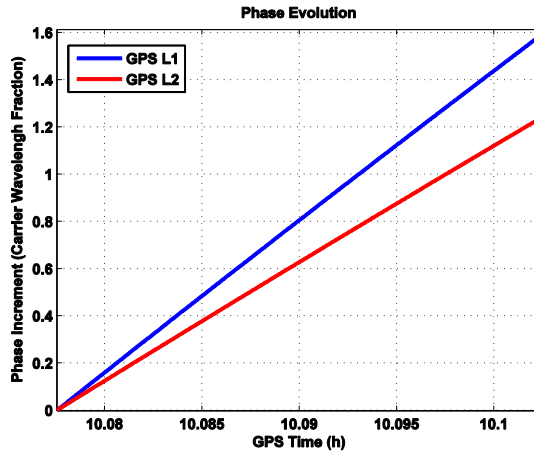


Fig. 5.10. (b) Phase evolution of the tracked GPS signals after scattering on the Mediterranean Sea during the experiment at the Pont del Petroli pier.

However, as it can be observed in Fig. 5.10b, PYCARO was able to track the phase of the scattered GPS signal during the experiment associated to the motion of the GPS satellite and (eventually) the receiver, the phase jumps of the Binary Phase Shift Keying (BPSK) modulation and even the changes in the SSH. This last phase term allows the dynamic compensation of the sea surface's motion. This is due to the fact that the surface was relatively flat, within the first Fresnel zone, and the Rayleigh criterion is satisfied. This leads to a coherence time of the signal long enough,

rendering it as a completely coherent during the coherent integration time. As a result, it is possible to measure the SSH with a precision and accuracy comparable to that of a GPS receiver, as it will be shown in the next section.

5.4 Altimetric precision

The results from the Cernadilla's Reservoir experiment are shown in Fig. 5.11. The height precisions with the C/A code ($\sigma_{C/A}$) and the P(Y) code ($\sigma_{P(Y)}$) are 8.4 cm and 4 cm respectively, for a coherent integration time of $T_c = 1$ ms, and an incoherent integration time $T_{inc} = 1$ s (Fig. 5.11). For integration times longer than ~ 60 s the achieved height precisions are $\sigma_{C/A} = 1.17$ cm and $\sigma_{P(Y)} = 0.50$ cm. Repeating these measurements at the Pont del Petroli, the achieved height precisions were $\sigma_{C/A} = 53.3$ cm and $\sigma_{P(Y)} = 42$ cm (Fig. 5.12), using a coherent integration time $T_c = 1$ ms, and an incoherent averaging time $T_{inc} = 1$ s. In this case, the achieved precisions at 60 s of averaging are $\sigma_{C/A} = 4$ cm and $\sigma_{P(Y)} = 2$ cm. It is observed, as expected, the larger the surface roughness, the larger the scatter of the altimetric observables, by a factor as large as 4 for both the C/A and the P(Y) codes considering 200 ms of averaging. However, the evolution of the achieved precision as a function of the averaging has a different behavior depending on the scenario and the GPS code. The larger surface roughness, the larger speckle noise (the phase changes of individual specular reflection points introduces a random phase behavior which creates speckle) so that it is required to increase the incoherent averaging to increase the achievable precision. This is the reason why $\sigma_{C/A}$ and $\sigma_{P(Y)}$ are lower in the Cernadilla's Reservoir experiment than over the results over the Mediterranean Sea. Note that the coherent integration time during the Pont del Petroli experiment was set to be relatively small $T_c = 1$ ms because potentially the coherence time could be low for a surface level platform in an un-controlled scenario over the ocean surface. Consequently, T_c was set to be 1 ms during the first experiment allowing the inter-comparison of both data sets.

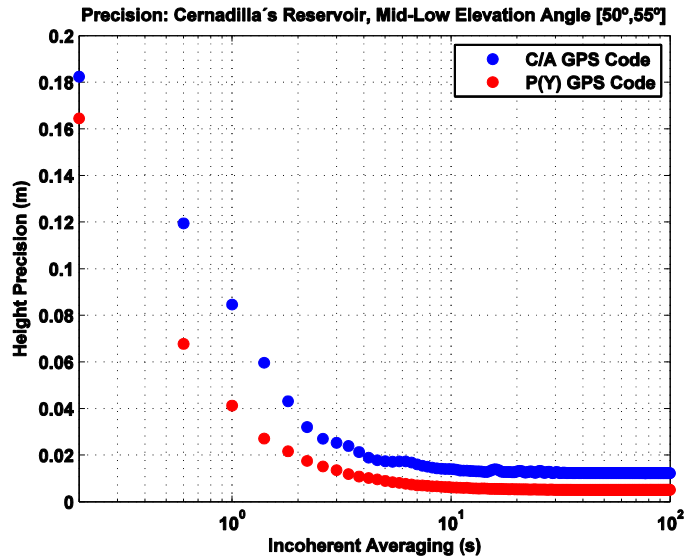


Fig. 5.11. C/A and P(Y) derived height precision as a function of the incoherent averaging in case of smooth surface at mid-low satellite's elevation angles (θ_e from 50° to 55°), and a mean platform's height over the surface $h = 65$ m.

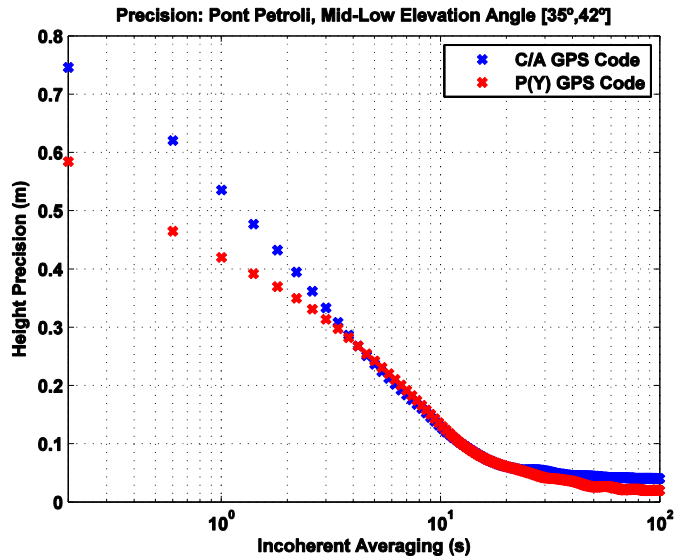


Fig. 5.12. C/A and P(Y) derived height precision as a function of the incoherent averaging in case of rough surface at mid-low satellite's elevation angles (θ_e from 35° to 42°), and a mean platform's height over the surface $h = 4.76$ m.

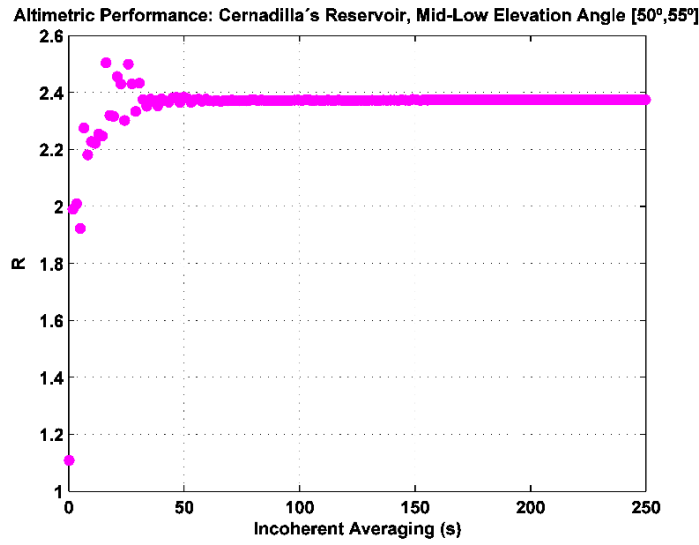


Fig. 5.13. Improvement factor of P(Y) altimetry as compared to C/A altimetry in a smooth surface scenario at mid-low satellite's elevation angles (θ_e from 50° to 55°) and a mean platform's height over the surface $h = 65$ m.

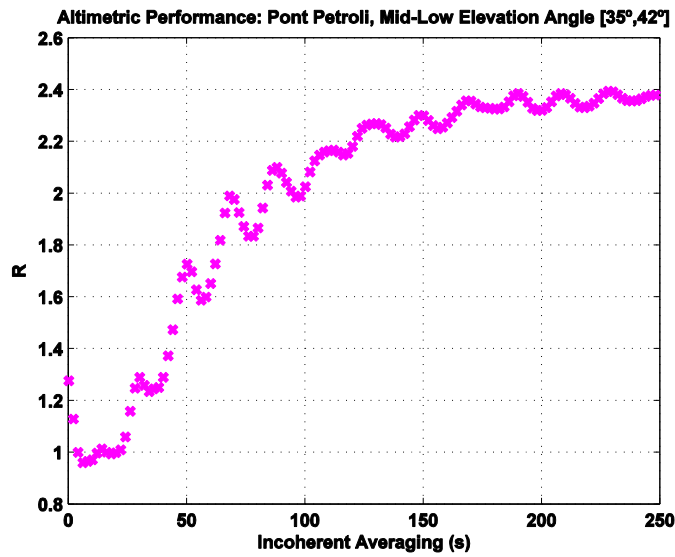


Fig. 5.14. Improvement factor of P(Y) altimetry as compared to C/A altimetry in a rough surface scenario at mid-low satellite's elevation angles (θ_e from 35° to 42°), and a mean platform's height over the surface $h = 4.76$ m.

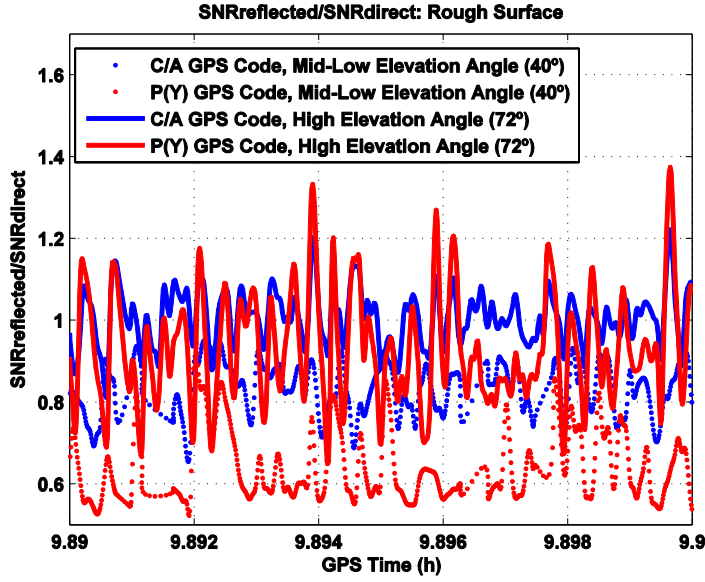


Fig. 5.15. Comparison of the ratio of the reflected and the direct-SNR for the C/A and the P(Y) GPS codes in case of rough surface at high and mid-low satellite's elevation angles and a mean platform's height over the surface $h = 4.76$ m.

The improvement factor $R = \sigma_{C/A} / \sigma_{P(Y)}$ of the P(Y) code altimetry as compared to the C/A code tends to 2.4 for both smooth and rough surface (Figs. 5.13 and 5.14) employing respectively an incoherent integration time of 30 s and 250 s. This means that, even for the quasi-specular surface of Cernadilla's Reservoir, the altimetric precision improvement is not reaching the ten-fold improvement as predicted by the steeper ACF of the P(Y) [77]. The achievable height precision, in addition to the surface roughness, depends on the SNR of the GPS signals which is a function, among other parameters, of the GPS satellites elevation angle as analyze in [3].

A GPS satellite with a high elevation angle θ_e from 70° to 75° is selected to analyze the influence of the SNR. The derived results are compared to the previous scenario (θ_e from 35° to 42°). The ratio of the reflected to the direct-SNR is computed as a function of the GPS time, which in case of high elevation angles, fluctuates around 1 for both, the C/A and P(Y) codes (Fig. 5.15). On the other hand, in case of low

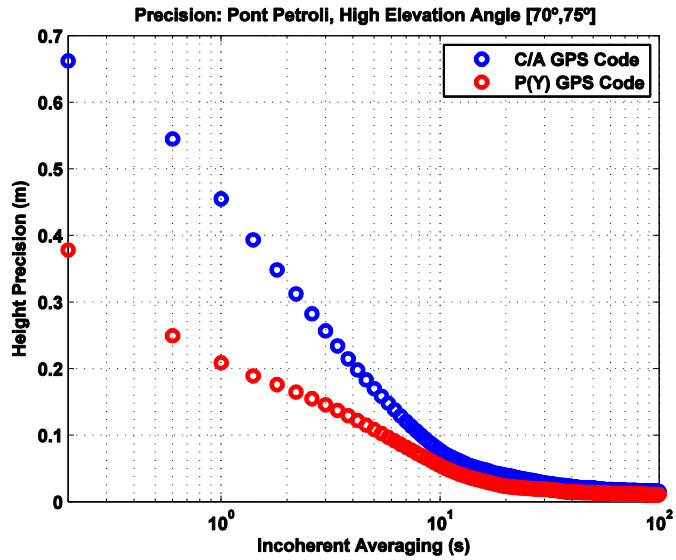


Fig. 5.16. C/A and P(Y) derived height precision as a function of incoherent averaging in case of rough surface at high satellite's elevation angles (θ_e from 70° to 75°), and a mean platform's height over the surface $h = 4.76$ m.

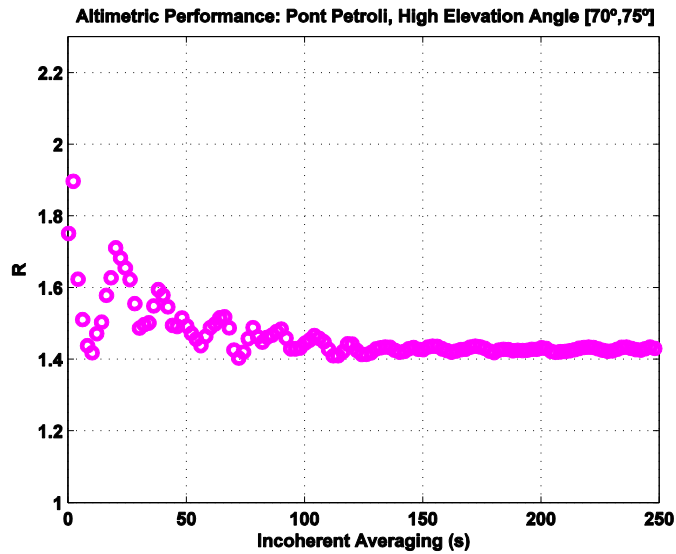


Fig. 5.17. Improvement factor of P(Y) altimetry as compare with C/A altimetry in a rough surface scenario at high satellite's elevation angle (θ_e from 70° to 75°), and a mean platform's height over the surface $h = 4.76$ m.

elevation angles, these ratios fluctuate around ~ 0.8 for the C/A code, and ~ 0.6 for the P(Y) code (Fig. 5.15).

The squaring losses of the P(Y) correlation technique implemented in PYCARO have a non-linear dependence with the SNR of the incoming signal [74]. The lower the SNR, the larger the squaring losses. As a consequence, the ratio of the SNR of the reflected P(Y) signal to the direct one decreases for lower elevation angles (Fig. 5.15). The lower the elevation angle, the larger the losses. Additionally, this ratio is lower as compared to that of the C/A signal for the same elevation angle, due to the squaring losses. This difference increases for lower elevation angles.

The higher the reflected-signal power in case of high elevation angle leads to a height precision of $\sigma_{C/A} = 7$ cm and $\sigma_{P(Y)} = 5$ cm for $T_c = 1$ ms, $T_{inc} = 10$ s, and under the same sea surface conditions that in the previous case (Fig. 5.16). On the other hand, despite the poorer SNR of the reflected P(Y) signals as compared to the C/A (Fig. 5.15), it is obtained an improvement factor of 2.4 (Fig. 5.14), being 1.4 (Fig. 5.17) when considering a more favorable scenario (higher signal power). From these results it can be concluded that, as compared to the C/A code, the P(Y)⁹ code achieves a better altimetric performance for low elevation angles, despite the lower SNR.

5.5 Accuracy dependence on the elevation angle

The measured mean platform's height h (distance from the sea surface to the common ground plane of the up, and down-looking antennas) provided by the differential measurement of the direct and the reflected ranges is compared against data provided by the monostatic radar. These bistatically derived values are, respectively, for high (θ_e from 70° to 75°) and mid- low (θ_e from 35° to 42°) satellite's elevation angles, 6.55 m and 6.44 m for C/A-L1 signal, and 6.32 m and 6.19 m for the P(Y)-L2 signals. Therefore, in addition to instrument calibration errors (not compensated for in this

⁹ The reflected waveform can be obtained as the convolution product of the power per unit delay and the Woodward Ambiguity Function. If the sea surface was a smooth surface, the shape of the reflected waveform is the same as the direct waveform. However, when the surface is not smooth the power spreads and the shape of the waveform becomes smoother. As a consequence the improvement factor is less than 10 [69, 77].

experiment), the electromagnetic bias, and the tracker bias affect the measurements¹⁰ [78, 79].

The tracker bias also depends on the GPS code chipping rate (P(Y) and C/A codes). The faster it is, the larger the slope of the waveforms is and, as a consequence, the lower the biases are [79]. As a consequence, the measured height values are apparently larger for the C/A-L1 signal than for the P(Y)-L2 signal, for both the high (6.55 m - 6.32 m = 23 cm bias) and the mid-low elevation angles (6.44 m - 6.19 m = 25 cm bias). Furthermore, it is observed a larger value of the mean platform's height over the mean sea surface, in case of high elevation angles, for both, the C/A-L1 (6.55 m - 6.44 m = 11 cm bias) and the P(Y)-L2 signals (6.32 m - 6.19 m = 14 cm bias). This is an experimental evidence¹¹ of the dependence of the electromagnetic bias [80] on the elevation angle, which agrees with previous results (Fig. 5.15): in case of high elevation angles the ratio of the reflected- to the direct-SNR fluctuates around 1, however for mid-low elevation angles, this value decreases depending on the frequency of the GPS signals. In case of the C/A-L1 this ratio fluctuates around 0.8, and around 0.6 when considering the P(Y)-L2 signal.

5.6 Conclusions

A new GNSS-R reflectometer architecture has been described, to the authors' knowledge, that allows to use the P(Y) code in real time. The results using the P(Y) code, from a static and low-altitude scenario over the Mediterranean Sea at high satellite's elevation angles, show 2 cm height precision for 20 s of incoherent averaging. In these conditions, the improvement factor as compared to the C/A code ($R = \sigma_{C/A} / \sigma_{P(Y)}$), stabilizes around 1.4 at 125 s of averaging. When analyzing this factor at mid-low elevation angles for both, smooth (Cernadilla's Reservoir) and rough (Mediterranean Sea) surfaces, it is inferred that the improvement factor

¹⁰ Both correlation channels (direct and reflected) have the same clock as time reference. Therefore, the clock-biases are compensated when computing the altimetric values from the difference between the measurements of the delays of the direct and the reflected signals.

¹¹ The larger the elevation angles are, the larger the contribution of the valleys to the scattered signal, increasing the signal power as a consequence. This effect is translated into a larger estimation of the platform's height over the mean sea surface as larger the satellite's elevation angles are.

stabilizes around $R = 2.4$ respectively at 35 s and 250 s of incoherent averaging. Then, the different biases have been analyzed as a function of the GPS codes (C/A and P(Y)) and the satellite's elevation angle. The measured bias induced by the sea state is larger for the C/A code as compared to the P(Y) code, for both high and mid-low elevation angles, due to the lower chipping rate. In addition, it has been observed that the estimated platform's height is larger at larger elevation angles, because of the larger contribution of the valleys to the reradiated signal. Furthermore the capability to measure the sea wave's profile has been demonstrated by comparing the data from a monostatic K-band radar and the PYCARO measurements employing the C/A-L1 and the P(Y)-L2 signals.

6

6. EMPIRICAL SCATTEROMETRY STUDY IN THE CIEM WAVE CHANNEL

6.1 Introduction

The first reported experimental evidence of GPS reflected signals dates back to 1994 [14], and it was stated that, since the Rayleigh criterion was not satisfied, the scattering was diffuse. In 1996, Garrison et al. [70] performed three different aircraft experiments over the ocean using a GPS receiver. Results showed that a specialized receiver must be developed to collect the Earth-reflected signals over a rough surface, because the scattering process distorts the signal, and the receiver lost tracking. In 2000, Zavorotny and Voronovich [16] developed a bistatic model of the ocean scattered GPS signals providing an analytical expression of the “waveforms” under the Kirchhoff approximation. Assuming that coherent scattering is negligible, the bistatic scattering coefficient was derived under the Geometric Optics limit, for a sea surface model with Gaussian distribution of the slopes, and a final expression of the “waveform” was derived. During the last decade, additional experimental [20, 24, 56, 66], and theoretical [45, 69, 81, 82] works have been performed to investigate the feasibility of this bistatic radar system to perform accurate ocean altimetry, usually with open-loop receivers, and using a model of the scattering geometry to center the delay and Doppler tracking windows.

In this experiment the P(Y) & C/A ReflectOmeter (PYCARO) is used. PYCARO is a closed-loop GNSS-R receiver with delay and Doppler tracking loops [72, 83] that uses conventional GNSS-R (cGNSS-R) for the open GPS codes (C/A) and reconstructed GNSS-R (rGNSS-R) for the encrypted ones. Due to limitations of the instrumentation, only synthetic GPS L1 C/A signals could be generated for this indoor experiment. Note that the GPS P(Y) code is encrypted and it is not publicly available. The coherent component of the scattered signals is studied experimentally in the Canal d'Investigació i Experimentació Marítima (CIEM) / UPC – BarcelonaTech wave channel [84] (Fig. 6.1). The results of this experiment are of interest in GNSS-R waves and coastal altimetry studies because of the low-altitude of the receiver over the surface and its static position¹². The monitoring of the local sea level has an increasing interest because it is an indicator of the global climate change [85]. In order to use space-borne

¹² Note that these results cannot be extrapolated to an air-borne or space-borne scenario.

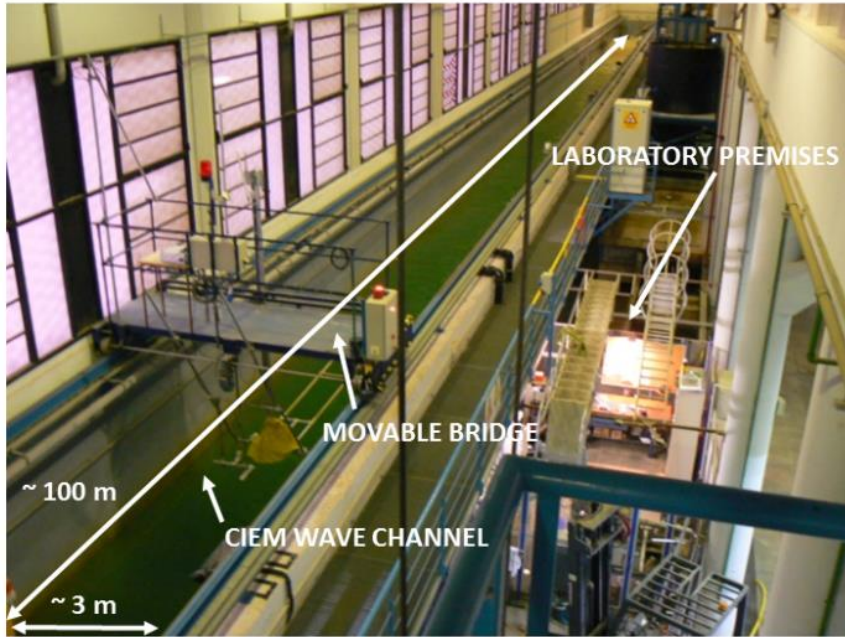


Fig. 6.1. View of the CIEM wave channel at the Laboratori d'Enginyeria Marítima (Universitat Politècnica de Catalunya). Wave channel dimensions are: width = 3 m, length = 100 m, and depth = 5 m.

altimeter data to compute the mean sea level variations over time, there is a need to account for biases and drifts in the instruments [86].

Section 6.2 describes the experimental set-up and the ground truth data generated during the experimental campaign. Section 6.3.1 studies the number of specular points inside the scattering area. Section 6.3.2 evaluates the performance for coastal applications. Section 6.3.3 analyzes the ratio of the coherent-to-incoherent components as observed by the PYCARO instrument. In Section 6.3.4, the GPS signals before retracking are used to infer the rms surface height of the small scale waves as observed by PYCARO. It is used to properly account for the coherent scattering over the small scale 1-D mechanically-driven waves. Finally, Section 6.4 summarizes the main results of this study.

6.2 Experiment description

This Section presents the experimental set-up and the ground truth data before the evaluation and the discussion of the results.

6.2.1 Experimental set-up

Coherent GNSS reflected signals have been tracked and reported in the past [87-90] for smooth water surface or grazing angle geometry, but never to high elevation angles over rough water. In 2012, the PYCARO GNSS-R instrument operated in close-loop mode flying along the Catalan coast (Fig. 6.2) was able to track the coherent reflected



Fig. 6.2. CESSNA EC-KOQ at the Aeroclub Barcelona-Sabadell.

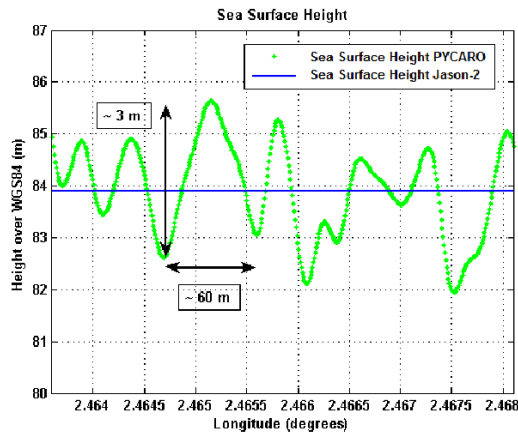


Fig. 6.3. Sea Surface Height (SSH) as measured by PYCARO and Jason-2. These results correspond to an aircraft experiment performed over the Mediterranean Sea on September 2012.

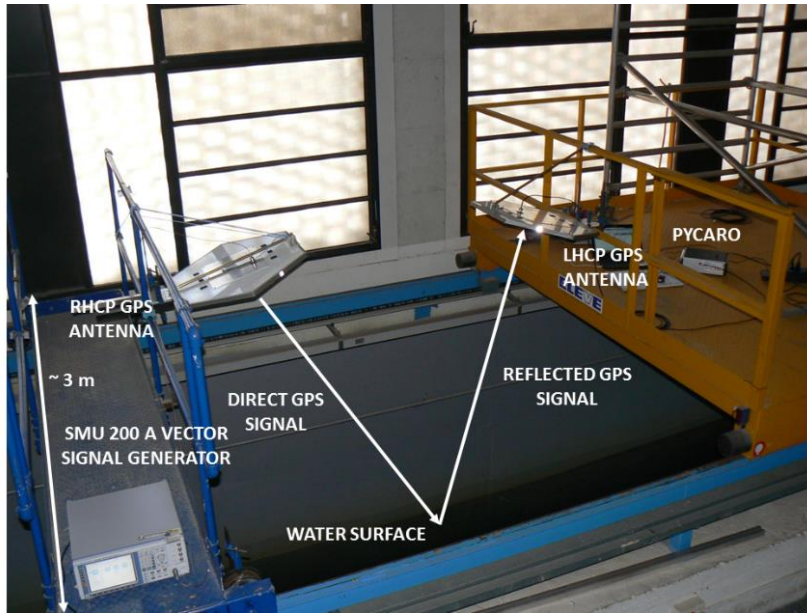


Fig. 6.4. View of the experiment set-up: SMU 200 A vector signal generator, PYCARO instrument, and the two 15 dB gain antenna arrays.

GPS signals (Fig. 6.3) under moderate-to-high wind conditions (> 11 m/s), and high elevation angles ($\theta_e > 30^\circ$) [72]. This result was quite surprising since it does not fit the present scattering models [16]. That evidence triggered the need to better understand the scattering mechanisms, and to that end, an experiment was performed during April 2013 in the CIEM water tank (Fig. 6.1), at the premises of the Civil Engineering School of the Universitat Politècnica de Catalunya–BarcelonaTech. Future work is required to further investigate this topic from an aircraft and to validate the result in Fig. 6.3.

Since this is an indoor facility, a Rohde & Schwarz SMU 200 A vector signal generator (Fig. 6.4 on the left) was used to synthesize controlled GPS L1 C/A signals [91]. One single PRN code was emitted at a time. Synthetic GPS signals were emitted using a 15 dB gain GPS Right-Hand Circular Polarized antenna (RHCP) array. The reflected signals were collected by a twin GPS antenna array with Left-Hand Circular Polarization (LHCP). The PYCARO GNSS-R instrument processed the data, and it was connected to a laptop for monitoring the instrument's parameters and log the data.

Both antennas were placed over the channel at static locations over two movable bridges¹³ (Fig. 6.4) at a height of ~ 3 m above the water (Table 6.1). The height of the antennas varied few centimeters because the inclination of their ground plane over the surface was adjusted as a function of the selected elevation angle. The separation of the bridges was adjustable so that the antenna footprints over the water surface overlapped for all elevation angles¹⁴ ($\theta_e = 45^\circ, 60^\circ, 75^\circ, 86^\circ¹⁵). The emitted GPS L1 C/A signal was calibrated to receive the same power level (direct signal) than in a real scenario ~ -130 dBm [92, pp. 75]. Two data sets of 30 min each were collected in the CIEM wave channel in which 1-D mechanically driven waves were created with a Significant Wave Height of 36 cm and 64 cm (Fig. 6.5).$



Fig. 6.5. View of the HR Wallingford Wave Probe Monitor used as a reference system during the experiment (encircled on the left hand side).

¹³ The antenna far field is at 1.6 m of the antenna and the distance of the antenna over the water surface is larger than 3 m.

¹⁴ GNSS satellites can be observed for much lower elevation angles. During this experiment only a limited number of days was available in the CIEM wave channel to perform the experiment. Authors decided to select elevation angles larger than 45° because it is the operational range of future missions.

¹⁵ The antennas could not be closer than the size of the ground planes, so that the maximum elevation angle was actually 86° , and not 90° .

6.2.2 Scenario and ground truth data

Ground truth data were recorded during the experiment. An HR Wallingford wave probe monitor located exactly in the center of the transmitter and receiver was used as a reference system to measure the time-evolution of the water level. The Pearson's linear correlation factors of the waves heights vs. the celerities and the periods are respectively 0.61 (Fig. 6.6a) and 0.53 (Fig. 6.6c) for a SWH = 36 cm, and 0.52 (Fig. 6.6b) and 0.42 (Fig. 6.6d) for a SWH = 64 cm. The wave's slopes distributions are reasonably well fitted by Rayleigh PDFs (Figs. 6.6e,f). The slopes were computed as the ratio of the height over the mechanical wavelength of individual water waves from the wave probe data. At a speed of the waves of 1.6 m/s (Figs. 6.6a,b) and with a period of the waves of 2.5 s (Figs. 6.6c,d), the wavelength is around 4 m. This means that during the coherent integration time $T_c = 20$ ms, the wave height difference inside the antenna footprint (Table 6.1) was as high as ~ 30 cm for a SWH = 64 cm (Fig. 6.6b). During the coherent integration time the roughness inside the first Fresnel zone [93] (Table 6.1) included waves heights as high as ~ 15 cm for celerities and waves periods lower than ~ 1.6 m/s and ~ 1.6 s, respectively (Figs. 6.6b,d). During this period of time the surface was practically frozen (the wave with phase velocity of 1.6 m/s will move horizontally by 3 cm), so that the signal was temporally coherent. As it will be shown later (Section 6.5), scattered waves collected by the receiver antenna get "reflected" in clustered regions, almost "facets" where a quasi-specular reflection takes place (Fig. 6.7). It could be stated that a "relaxed" specular reflection is taking place, with the scattering process taking place in many points around the nominal specular reflection point. A "relaxed" Rayleigh criterion is introduced to account for the small scale roughness of the surface with respect to the facet where the specular reflection is taking place. It is not satisfied during these periods which account for wavenumbers higher than the cutoff wavenumber (Table 6.1). During the experiment, PYCARO tracked the coherent component of the scattered field during large portions of the data set. In Section 6.3.3 the total scattered field is re-constructed to generate the scattered field by the complete footprint.

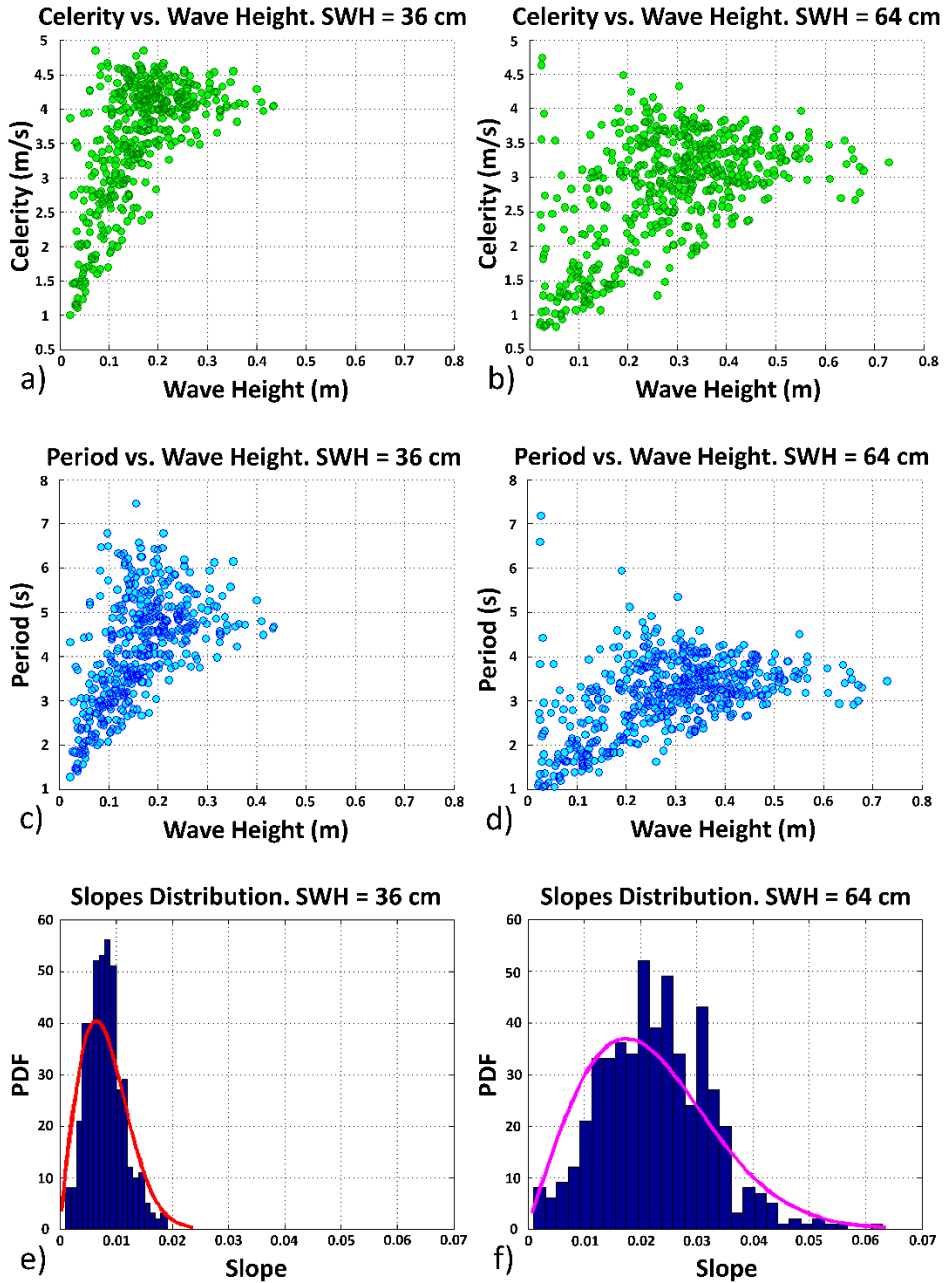


Fig. 6.6. (a) Correlation celerity vs. wave height for a SWH = 36 cm. (b) Correlation celerity vs. wave height for a SWH = 64 cm. (c) Correlation period vs. wave height for a SWH = 36 cm. (d) Correlation period vs. wave height for a SWH = 64 cm. (e) Slopes distribution for a SWH = 36 cm. (f) Slopes distribution for a SWH = 64 cm.

Table 6.1. Height of the antenna over the surface, sizes of the footprint, the first Fresnel zone and the scattering cells, and cutoff wavenumbers as a function of the elevation angle. The antenna footprint is obtained as the intersection at different angles (elevation angles) of a plane (water surface mean) with the antenna radiation pattern. The scattering cell is obtained as the area on the water surface that allows to scatter forward the GPS signals through the receiver antenna taking into account the slopes of the waves and the surface roughness.

θ_e (degrees)	45°	60°	75°	86°
Height (m), h	3.44	3.37	3.28	3.20
Main axis antenna footprint (m)	4.92	4	3.46	2.32
Major axis first Fresnel zone (m)				
$r_a = \sqrt{\lambda H / \sin\theta_e + \left(\lambda / 2\sin\theta_e\right)^2} / \sin\theta_e$	2.74	1.99	1.67	1.57
Minor axis first Fresnel zone (m)				
$r_b = r_a \sin\theta_e$	1.94	1.73	1.62	1.57
Main axis scattering cell (m)				
SWH = 36 cm, L_{scatt}	0.34	0.26	0.22	0.22
Main axis scattering cell (m)				
SWH = 64 cm, L_{scatt}	1.36	1.08	0.94	0.90
Cutoff wavenumber (rad/m)				
SWH = 36 cm, $N_{cutoff} = 2\pi / L_{scatt}$	18.48	24.16	28.56	28.56
Cutoff wavenumber (rad/m)				
SWH = 64 cm, $N_{cutoff} = 2\pi / L_{scatt}$	4.62	5.81	6.68	6.98

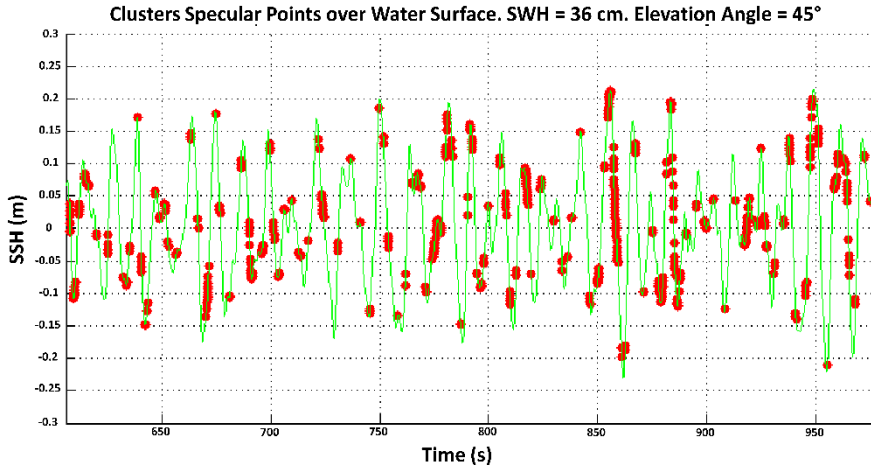


Fig. 6.7. Clusters of specular points distributed over the water surface profile as computed using the temporal series of data provided from the HR Wallingford wave probe monitor for a $SWH = 36$ cm & $\theta_e = 45^\circ$.

6.3 Experimental results: methodology and discussion

This Section describes the methodology of the experiment and contains the discussion of the results.

6.3.1 Number of specular points inside the scattering area

The forward-scattering mechanisms of the GPS signals over the sea surface is still a matter of investigation. Despite many models have been studied, including the Small Slope Approximation (SSA) model [94], and the Two-Scale Composite Model (TSM) [95], in the case of the GNSS-R the Geometrics Optics limit of the Kirchhoff Model (KAGO) is the one most widely used [16, 24, 25, 96] because of its simplicity, and its capability to reproduce the cross-polar experimental data in the forward direction. The scattering of electromagnetic waves from the sea is strongly affected by its roughness, being the total scattered field the combination of many electromagnetic waves coming from multiple individual scatterers on the surface. In this situation quasi-specular

reflections dominate since, according to the TSM this type of scattering is produced mostly by the large scale components of the surface.

This experiment focuses on the evaluation of the scattering due to the small scale¹⁶ of the water surface. To analyse the results obtained in this experiment, the shape of the water height is studied to assess the occurrence of specular points. The water surface is partitioned into 90,000 smaller surface patches equal to the number of coherent integration times ($T_c = 20$ ms) during each data set (the length of each data set is 30 min). The scattering field during each shot is given by [28]:

$$E_n(t) = W(\rho_n, t) \sum_{i=1}^{N_n(t)} A_{ni}(t) e^{j\phi_{hi}(t)}, \quad (6.1)$$

where t is the time, N_n is the number of specular points around the nominal one, A_{ni} is the amplitude (ruled by the local curvature of the water surface in the specular point [81]), $j = \sqrt{-1}$ is the imaginary unit, ϕ_{hi} is the phase defined as [28]:

$$\phi_{hi} = j(\varepsilon_i - 2\pi F_i t + kX_i), \quad (6.2)$$

where ε_i is the angular speed of the carrier, F_i is the Doppler shift of the i^{th} specular point, $k = 2\pi/\lambda$ is the carrier wavenumber, and X_i is the range between the i^{th} specular point and the scattering cell center. ϕ_{hi} is related to the ranges from the transmitter to the i^{th} specular point, and from it to the receiver through the variable X_i . Finally $W(\rho_n, t)$ is a deterministic, range-dependent term defined in [28] with ρ_n being the projection in the horizontal plane of the positioning vector of the scattering cell center.

For specular points inside a scattering cell, W can be assumed to be constant and equal to the corresponding value at the center of the scattering cell. The variations in the signals phase due to the variations in Doppler and position of the specular points around the nominal one can be modelled as an stochastic process [28].

The scattered field in the specular direction is composed of a coherent component, and a random Hoyt-distributed incoherent component [97, pp. 126]. The first one comes from the coherent combination of the scattering on the individual facets within

¹⁶ Roughness scales with associated wavenumbers higher than the cutoff wavenumber (Table 6.1).

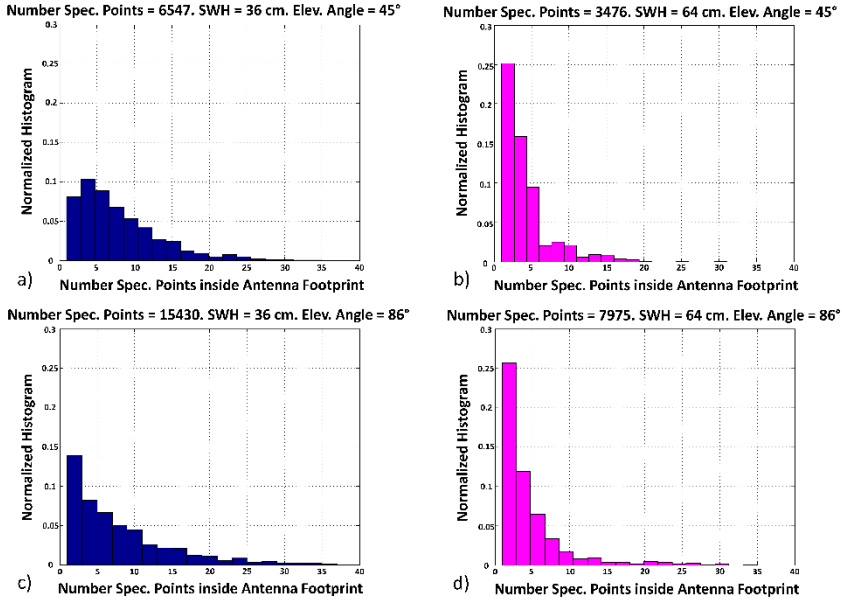


Fig. 6.8. Specular points distributions computed using the temporal series of data provided from the HR Wallingford wave probe monitor for a: (a) SWH = 36 cm and $\theta_e = 45^\circ$, (b) SWH = 64 cm and $\theta_e = 45^\circ$, (c) SWH = 36 cm and $\theta_e = 86^\circ$, and (d) SWH = 64 cm and $\theta_e = 86^\circ$.

the first Fresnel zone. The incoherent component is the result of the random combination of electromagnetic waves coming from other scatterers within the glistening zone that add together at the receiving antenna. It is also shown [97, pp. 150] that in directions different from the specular one, the scattering is always incoherent.

The specular points are identified continuously every 20 ms over the spatial¹⁷ surface profile when the local incident (θ_i) and the scattered (θ_s) angles are the same. The distribution of the specular points is not uniform, being characterized by different clusters (Fig. 6.7). This experimental result shows the micro-Doppler phenomenon [98] due to the small oscillations of the surface roughness. The normalized histograms

¹⁷ To transform the temporal domain into spatial surface profile a celerity value of 1.6 m/s was used, since this was the only data available from the wave probe.

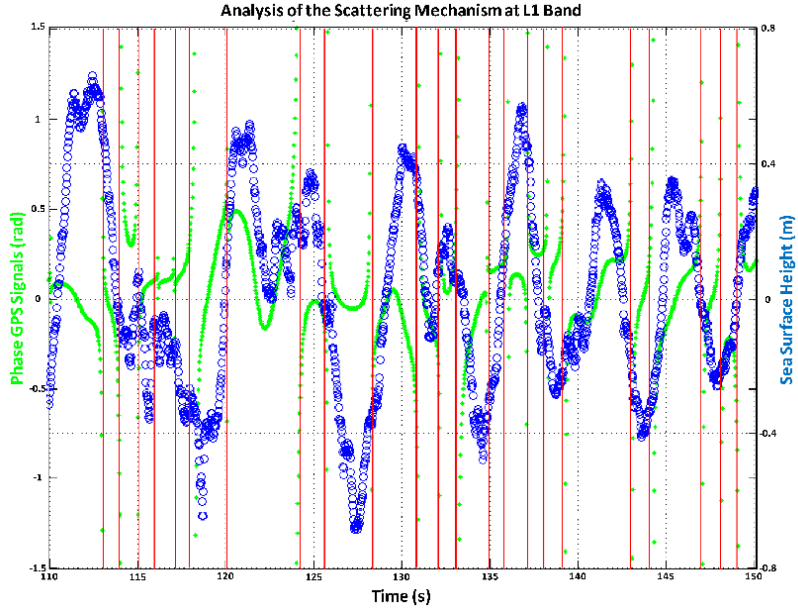


Fig. 6.9. Analysis of the electromagnetic interaction of the GPS signals and the scattering surface in a bistatic scenario. The phase (after retracking) distribution of the scattered field is time and space-located over the temporal evolution of the SSH as measured by the PYCARO reflectometer. This analysis has been performed with a $SWH = 36$ cm, and an elevation angle of $\theta_e = 86^\circ$.

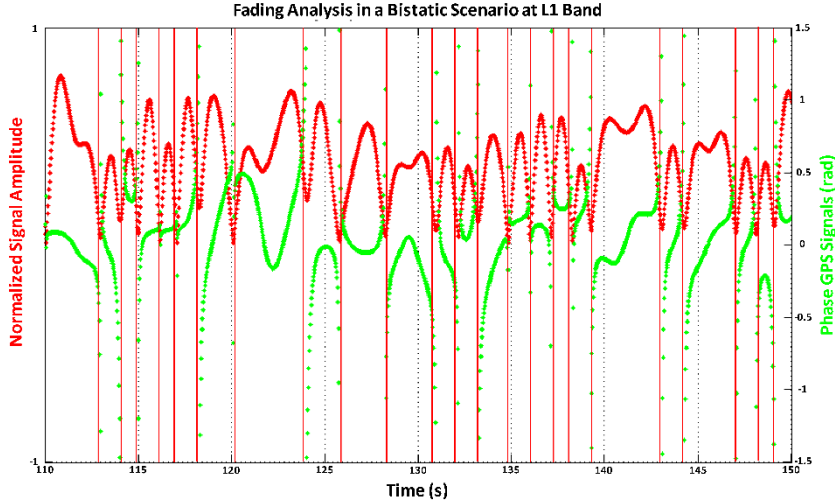


Fig. 6.10. Normalized reflected signal power amplitude fluctuations due to the phase (after retracking) changes induced by the scattering surface. This analysis has been performed with a $SWH = 36$ cm, and an elevation angle of $\theta_e = 86^\circ$.

of the number of specular points inside the antenna footprint every 20 ms are shown in Figs. 6.8a to d for $SWH = 36$ cm and $\theta_e = 45^\circ$, $SWH = 64$ cm and $\theta_e = 45^\circ$, $SWH = 36$ cm and $\theta_e = 86^\circ$, $SWH = 64$ cm and $\theta_e = 86^\circ$ respectively. The number of clusters with high number of specular points is larger for lower SWH . Additionally, it is derived that the total number of specular points is larger for lower SWH , and for larger elevation angles. Local diffraction effects [95] contribute to the time-continuous uninterrupted “Sea” Surface Height (SSH) measurements provided by the PYCARO reflectometer (Fig. 6.9).

Figure 6.9 shows the SSH as measured by PYCARO for a $SWH = 36$ cm, and $\theta_e = 86^\circ$. The total phase is important, but here surface deviations are inferred from phase changes only of the waveform peak. Any contribution (secondary specular points) away from the nominal one adds power at the trailing edge of the waveform although very close to the main peak due to the short differential delay. This process distorts the waveform and the peak becomes rounder. The $1\text{-}\sigma$ rms of the altimetric information is ~ 1 cm. Note that the sign of the phase of the received GPS signals (after retracking) changes at the wave valleys and crests, that is, when the surface starts “approaching” to the receiver or it starts “moving away” from it. These changes (see the vertical red lines in Fig. 6.9) in the phase of the signals after being retracked are related to the relative velocity of the target with respect to the receiver (induced Doppler frequency shift). Some of these changes are associated with the larger waves, but others with smaller waves that also produce changes in the relative velocity of the specular points with respect to PYCARO. Each specular point has a different relative phase, which contributes to the speckle noise, responsible for the power fluctuations in the reflected signals (see the vertical red lines in Fig. 6.10).

The number of scatterers N_n is related to the sea surface motion through the appearance and disappearance of specular points [99]. In the CIEM experiment this process was mostly due to the travel of the water waves. During a wave period, some specular points moved outside the antenna footprint and others moved inside from a neighboring footprint. The maximum measured value of the slopes was 0.02 and 0.06, for a $SWH = 36$ cm and for a $SWH = 64$ cm, respectively (Figs. 6.6e,f). The waves were identified using the so-called zero down-crossing method [100], which includes the celerities in the computation of the slopes (the horizontal scale threshold of the slopes’ PDF was ~ 1.7 m). The region on the surface that contributed in-phase

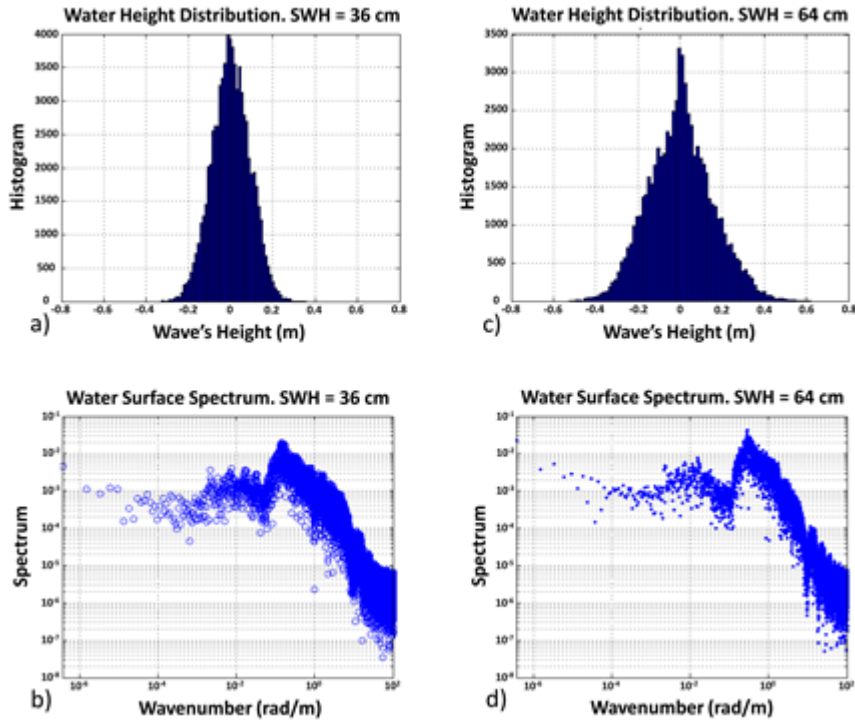


Fig. 6.11. Surface height distributions obtained using the HR Wallingford wave probe monitor for a: (a) SWH = 36 cm and (b) SWH = 64 cm. Corresponding wave surface spectra for a: (c) SWH = 36 cm, and (d) SWH = 64 cm at the CIEM.

to the reflected signal was actually a smaller region (scattering cell) than the first Fresnel zone, larger for higher values of SWH (Table 6.1). Larger SWH values led to larger scattering cell over the water surface.

6.3.2 Water surface height measurements

The performance of the PYCARO instrument has been evaluated for low altitude applications (e.g. coastal applications). The experiment and the data set generation were performed in a controlled manner. The height distributions of the two surface states obtained using the HR Wallingford wave probe are represented in Figs. 6.11a,b.

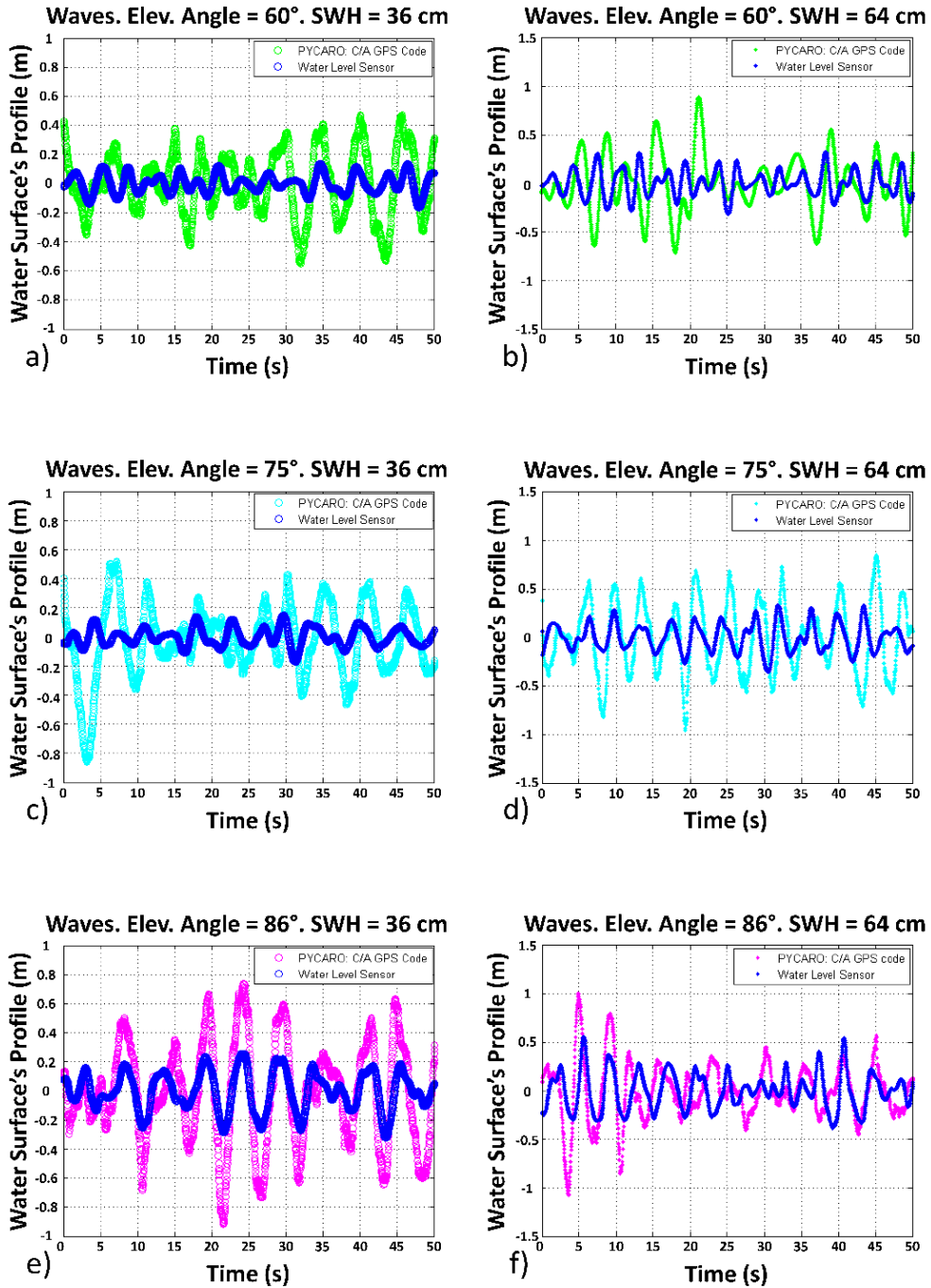


Fig. 6.12. For an elevation angle of (a,b) $\theta_e = 60^\circ$, (c,d) $\theta_e = 75^\circ$, (e,f) $\theta_e = 86^\circ$, sample waves profile as measured by PYCARO using the C/A code and by the water level sensor for a (a,c,e) SWH = 36 cm and for (d,e,f) SWH = 64 cm.

Table 6.2. Statistical analysis of the phase (after retracking) distribution of the scattered GPS signals over the CIEM wave channel at different elevation angles: $\theta_e = 60^\circ$, 75° , and 86° .

θ_e (degrees)	60°	75°	86°
Phase Std. Dev. (degrees)	13.4°	17.4°	19.1°
Phase Mean (degrees)	0.9°	-0.5°	1.2°
Phase Kurtosis	17.5	10.4	8.5
Phase Skewness	0.9	-0.06	-0.05

Table 6.3. Statistical analysis of the amplitude (after retracking) distribution of the scattered GPS signals over the CIEM wave channel at different elevation angles: $\theta_e = 60^\circ$, 75° , and 86° .

θ_e (degrees)	60°	75°	86°
Amplitude Std. Dev. (A.U.)	34	37	65
Amplitude Mean (A.U.)	152	195	209
Amplitude Kurtosis	3.91	3.44	2.74
Amplitude Skewness	-0.013	0.05	0.324

Their corresponding water surface spectra were derived from the times series provided by this sensor (Figs. 6.11c,d).

As a first step, the scattering in the time domain for different water surface states and transmitter elevation angles is analyzed. The instantaneous SSH relative to the mean water level in the channel as measured by the water level sensor and that derived using PYCARO (from the C/A code) are presented in Figs. 6.12a,c,e for a SWH = 36 cm, and in Figs. 6.12b,d,f for a SWH = 64 cm, respectively for different elevation angles: $\theta_e = 60^\circ$, 75° , and 86° .

The curve defined by the evolution in time of the geometric ranges (after scattering over the water surface) between the “GPS satellite” (transmitter) and the PYCARO instrument (receiver) was detrended to obtain the SSH. As it can be seen, the waves

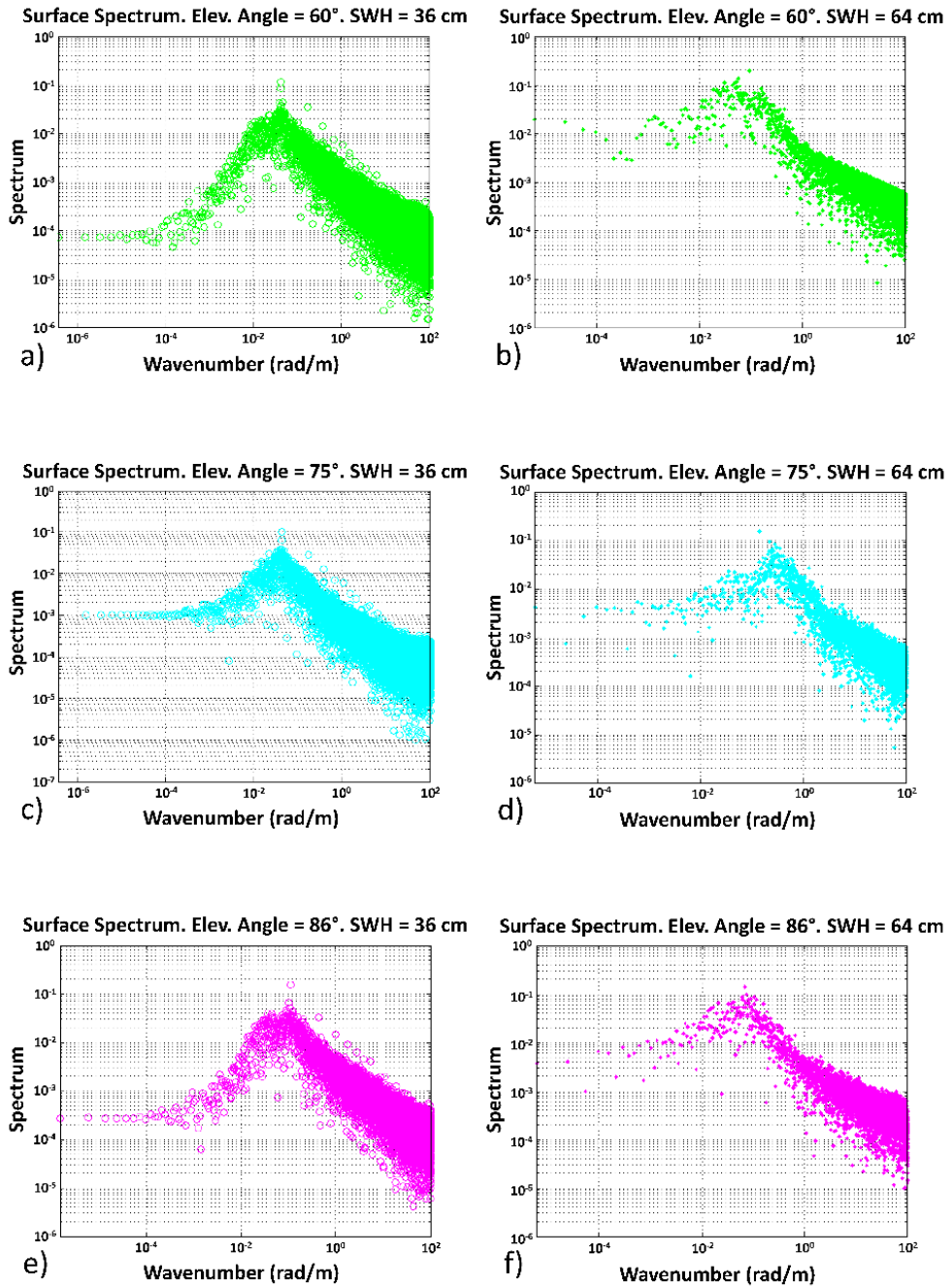


Fig. 6.13. For an elevation an elevation angle of (a,b) $\theta_e = 60^\circ$, (c,d) $\theta_e = 75^\circ$, (e,f) $\theta_e = 86^\circ$, water surface spectra as measured by PYCARO using the C/A code for (a,c,e) SWH = 36 cm, and (b,d,f) for SWH = 64 cm.

profile as measured by the level sensor (Fig. 6.12) is highly correlated with the one derived from PYCARO's observables obtained from the C/A code¹⁸.

Additionally, the water surface's spectra computed for the different surface states as measured by PYCARO for the different elevation angles ($\theta_e = 60^\circ, 75^\circ$, and 86°) are represented in Figs. 6.13a,c,e and Figs. 6.13b,d,f, respectively for a SWH = 36 cm and 64 cm. The Pearson's linear correlation coefficients of the level gauge sensor and the bistatically-derived results are 0.78, 0.85, and 0.81 for a SWH = 36 cm, and 0.34, 0.74, and 0.72 for a SWH = 64 cm, $\theta_e = 60^\circ, 75^\circ$, and 86° .

6.3.3 Analysis of the coherent and incoherent components after retracking

The phase of the signals after complex cross-correlation with the locally-generated C/A code, and after retracking (Figs. 6.14a,c,e) for different elevation angles ($\theta_e = 60^\circ, 75^\circ$, and 86°), and for a SWH = 36 cm is studied in this Section. The retracking algorithm implemented in the PYCARO reflectometer tends to align the sum of the I and Q components of the scattered field with the I axis, and switches 180° during each data bit reversal. The GPS satellites' motion (and eventually the receiver's motion as well) induces a change in the delay and the phase difference of the waveforms that needs to be compensated for the coherent and incoherent averaging.

The length of the data set is 30 min, sampled at 10 Hz showing that the random complex vectors add up together privileging a certain direction in the complex plane (Table 6.2 and Figs. 6.14a,c,e). As it can be appreciated, the phase's standard deviation of the retracked signals is actually quite small, which shows a strong coherent component being tracked. As the elevation angle increases from $\theta_e = 60^\circ$ to 86° , the phase standard deviation increases also from 13.4° to 19.1° (Table 6.2 and Figs. 6.14a,c,e), and the kurtosis decreases from 17.5 to 8.5 (Table 6.2). This is a clear indication that the amount of incoherent scattering increases (the PDF becomes

¹⁸ However, the amplitude estimated from PYCARO [83] is larger than that from the gauges. A similar behaviour was observed in a field experiment over the Mediterranean Sea (Fig. 5.8) using the GPS C/A code, but not with the GPS P(Y) code [83].

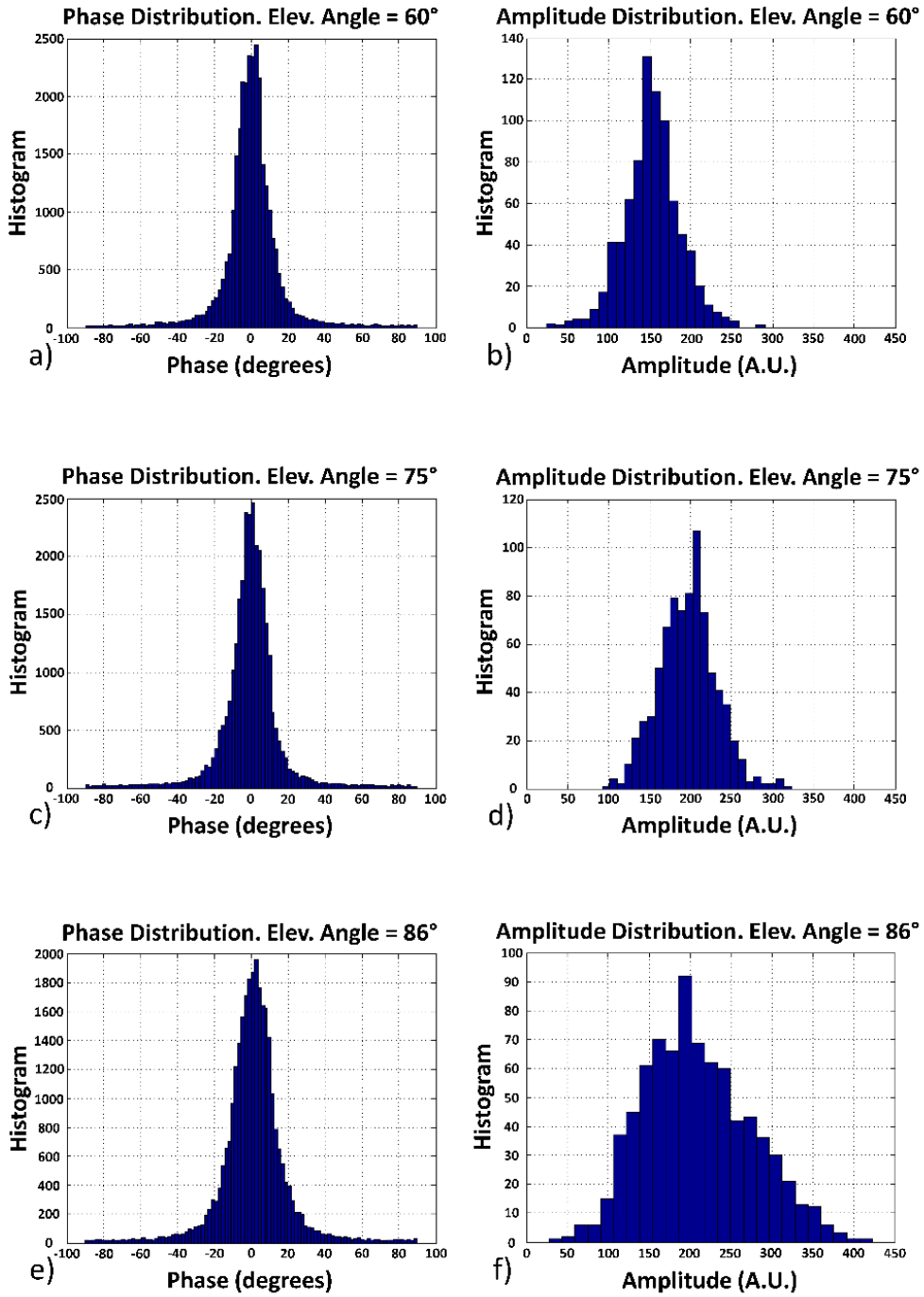


Fig. 6.14. At an elevation angle of (a,b) $\theta_e = 60^\circ$, (c,d) $\theta_e = 75^\circ$, and (e,f) $\theta_e = 86^\circ$, (a,c,e) histogram of the phase and (d,e,f) amplitude of the signals after retracking for a SWH = 36 cm.

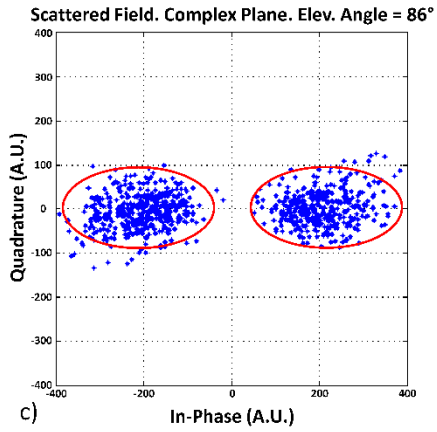
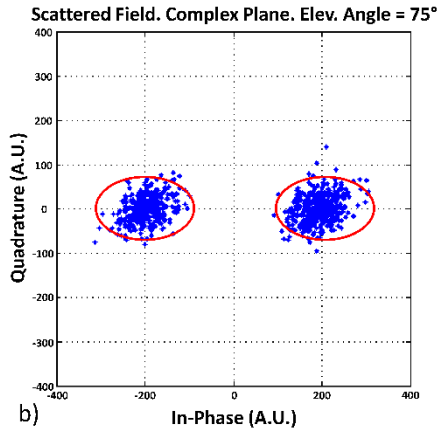
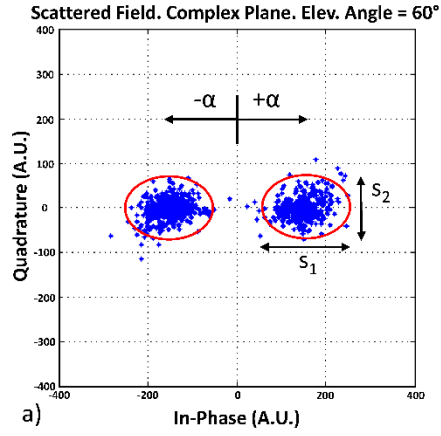


Fig. 6.15. Scattered field complex plane representation for a $SWH = 36$ cm at an elevation angle of (a) $\theta_e = 60^\circ$, (b) 75° , and (c) 86° .

Table 6.4. Statistical analysis of the complex field distribution of the scattered GPS signals after retracking, over the CIEM wave channel at different elevation angles: $\theta_e = 60^\circ, 75^\circ$, and 86° .

θ_e (degrees)	60°	75°	86°
Coherent Scattering: α^2 (A.U.)	22,939	37,725	43,992
Incoherent Scattering: $s_1 + s_2$ (A.U.)	23,648	38,392	46,307
Ratio Coherent to Incoherent			
Scattering: $B^2 = \alpha^2 / (s_1 + s_2)$ (A.U.)	0.97	0.97	0.95
Assymetry Factor: $K = s_1 / s_2$	39	39	30

more like a Gaussian one), due to the larger contribution of the wave crests and valleys at larger elevation angles. This is also in agreement with the evolution of the amplitude distribution, which tends to a Rayleigh distribution, as the elevation angle increases (Figs. 6.14b,d,f, and Table 6.3).

The ratio of the coherent-to-incoherent components as seen by the PYCARO instrument is derived using the total scattered field complex plane representation (Fig. 6.15). Each single measurement of the scattered complex field during the 30 min is represented. For a completely incoherent scattering, the distribution in the complex plane of the scattered field should theoretically follow a zero-mean 2-Dimensional Gaussian distribution with variances s_1 and s_2 [97, pp. 125]. However, experimental results (Figs. 6.15a to c) show that after retracking the total scattered field is displaced from the center by a certain value $\pm\alpha$ in the real axis (equal to the mean of the amplitude distribution) into two regions with an ellipsoidal shape, which proves the presence of a non-negligible coherent component in the specular direction. As explained before, the phase changes (Figs. 6.15a to c) are due to changes of the navigation bit sign, and the effect of the speckle noise. Thus, there are two regions displaced $\pm\alpha$ from the center. The relative weight of the coherent-to-incoherent components is quantified by the B parameter [97, pp. 126]:

$$B^2 = \frac{\alpha^2}{s_1 + s_2}. \quad (6.3)$$

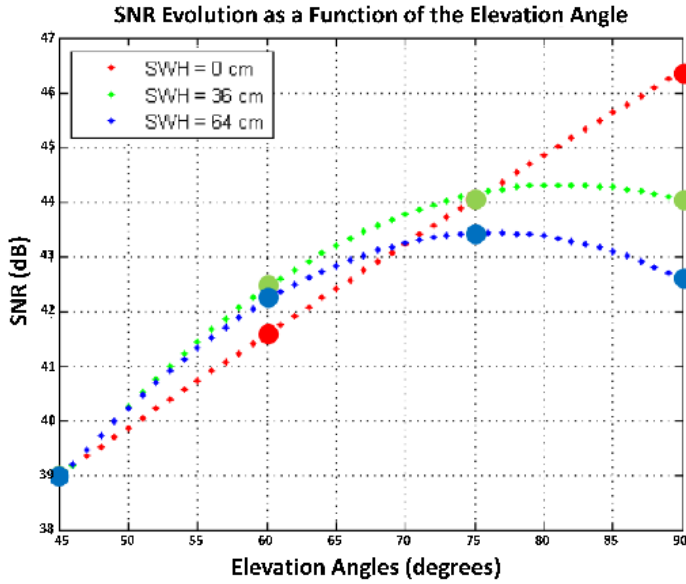


Figure 6.16. SNR of the reflected signal for three different surface states and for an elevation angle in the range from $\theta_e = 45^\circ$ to $\theta_e = 86^\circ$. Figure obtained using a best-fit approximation of the experimental data over elevation ranges at $\theta_e = 45^\circ$, $\theta_e = 60^\circ$, $\theta_e = 75^\circ$, and $\theta_e = 86^\circ$.

Note that B tends to ∞ for a totally coherent field ($s_1 = s_2 = 0$), and it is equal to 0 for a totally incoherent field ($\alpha = 0$). The results from this experiment show that the weight of the coherent component (B) reduces by $\sim 6\%$ (from 0.97 to 0.95) when the elevation angle increases from $\theta_e = 60^\circ$ to 86° (Table 6.4), while the incoherent scattering increases as the surface roughness increases, in agreement with the reduction of the asymmetry factor $K \cong s_1 / s_2$ (Table 6.4). At the same time, the larger the elevation angle, the larger the phase noise because of a larger “apparent” water surface roughness, but still much lower than the amplitude standard deviation.

The Signal to Noise Ratio (SNR) of the scattered field increases with increasing elevation angles (Fig. 6.16). The SNR evolution as a function of the elevation angle is derived using a best-fit approximation of the experimental data at $\theta_e = 45^\circ$, 60° , 75° , and 86° . For elevation angles θ_e larger than 60° the value of the SNR decreases with increasing values of the SWH (Fig. 6.16), because of the larger phase standard deviation (Figs. 6.15a to c). However, for lower elevation angles, the SNR tends to the same value in both cases: rough and flat surfaces.

6.3.4 Evaluation of the effective small scale surface roughness

In order to compare the GPS scattering data with a simple theoretical model, effective sea surface parameters are introduced [101]. However these parameters cannot be applied away from the specular direction because they depend on the geometry [17]. The reflectivity of the coherent scattering component can be derived as [35, pp. 1008]:

$$\Gamma_{\text{RHCP-LHCP}}^{\text{coh}} = |\Re_{\text{RHCP-LHCP}}(\theta_e)|^2 e^{-(2\sigma k \sin\theta_e)^2}, \quad (6.4)$$

where subscripts **RHCP** and **LHCP** denote the incident polarization (Right Hand Circular Polarization), and the scattered polarization (Left Hand Circular Polarization) respectively, $\Re_{\text{RHCP-LHCP}}$ is the Fresnel reflection coefficient, σ is the surface height standard deviation and k is the wavenumber. Note that for a flat surface, the surface height standard deviation (surface roughness) σ is zero, and the reflectivity reduces to the square of the amplitude of the Fresnel reflection coefficient. The phase standard deviation of the peak of the complex cross-correlation with the locally-generated C/A code before it is aligned (obviously with some residual noise) to the I axis was computed during the experiment¹⁹, in addition to the measurements of the phase after retracking. The experimental distributions of the before-retracking phase standard deviation σ_ϕ are linked to the rms surface height²⁰ (dispersion of the height's distribution of the small scale waves) as [97, pp. 246]:

$$\sigma = \frac{\sigma_\phi}{2k \sin\theta_e}. \quad (6.5)$$

The small scale surface roughness distributions (Eqn. 6.5) are represented in Fig. 6.17 for different elevation angles of $\theta_e = 45^\circ, 60^\circ, 75^\circ$, and 86° , for a SWH = 36 cm and 64 cm. These distributions are theoretically fitted by log-logistic PDFs (Fig. 6.17) [104]. The small scale surface roughness (rms surface height) values corresponding to the peak of the distributions are ~ 7.2 cm, ~ 4.4 cm, ~ 3.1 cm, and ~ 3.1 cm for a

¹⁹ Figure 4.14 in Valencia's Ph. D. Thesis [102] or Fig. 3a in [103] illustrates this point. In there, due to the movement of the transmitter, the phase also varied with time.

²⁰ The low elevation of the antenna acts as a high-pass filter. SWH is mainly determined by the large scale waves; waves with larger periods, larger heights and also with higher celerities (Fig. 6.6). The small scale rms surface heights values corresponding to the peak of the distributions (~ 3.1 cm, ~ 3.1 cm, ~ 4.4 cm, and ~ 7.2 cm) are the same for both SWH = 36 cm and SWH = 64 cm.

SWH = 36 cm (Figs. 6.17a to d respectively) and also for a SWH = 64 cm (Figs. 6.17e to h respectively), for elevation angles of $\theta_e = 45^\circ$, 60° , 75° , and 86° respectively. On the other hand, the theoretical roughness values corresponding to the half of the coherent reflectivity decaying factor (Eqn. 6.4) are ~ 1.75 cm, ~ 1.5 cm, ~ 1.25 cm, and ~ 1.25 for elevation angles of $\theta_e = 45^\circ$, 60° , 75° , and 86° respectively. Therefore, an experimental correction term P could be derived from the ratio of the empirically-derived (Figure 6.17) to the theoretical small scale surface roughness values (Table 6.5). This term is introduced to estimate the effective small scale roughness $\sigma_{\text{eff}} = \sigma / P$. The difference between the effective small scale roughness and the theoretical values is higher for lower elevation angles, as a factor of ~ 4.1 and ~ 2.5 for elevation angles of $\theta_e = 45^\circ$ and $\theta_e = 86^\circ$ respectively.

Table 6.5. Theoretical and experimental small scale roughness values, and correction term for SWH = 36 cm, and 64 cm for $\theta_e = 45^\circ$, 60° , 75° , and 86° .

θ_e (degrees)	45°	60°	75°	86°
Theoretical small scale roughness	1.75	1.5	1.25	1.25
Experimental small scale roughness (SWH = 36 cm)	7.2	4.4	3.1	3.1
Experimental small scale roughness (SWH = 64 cm)	7.2	4.4	3.1	3.1
Correction Term P (SWH = 36 cm)	4.1	2.9	2.5	2.5
Correction Term P (SWH = 64 cm)	4.1	2.9	2.5	2.5

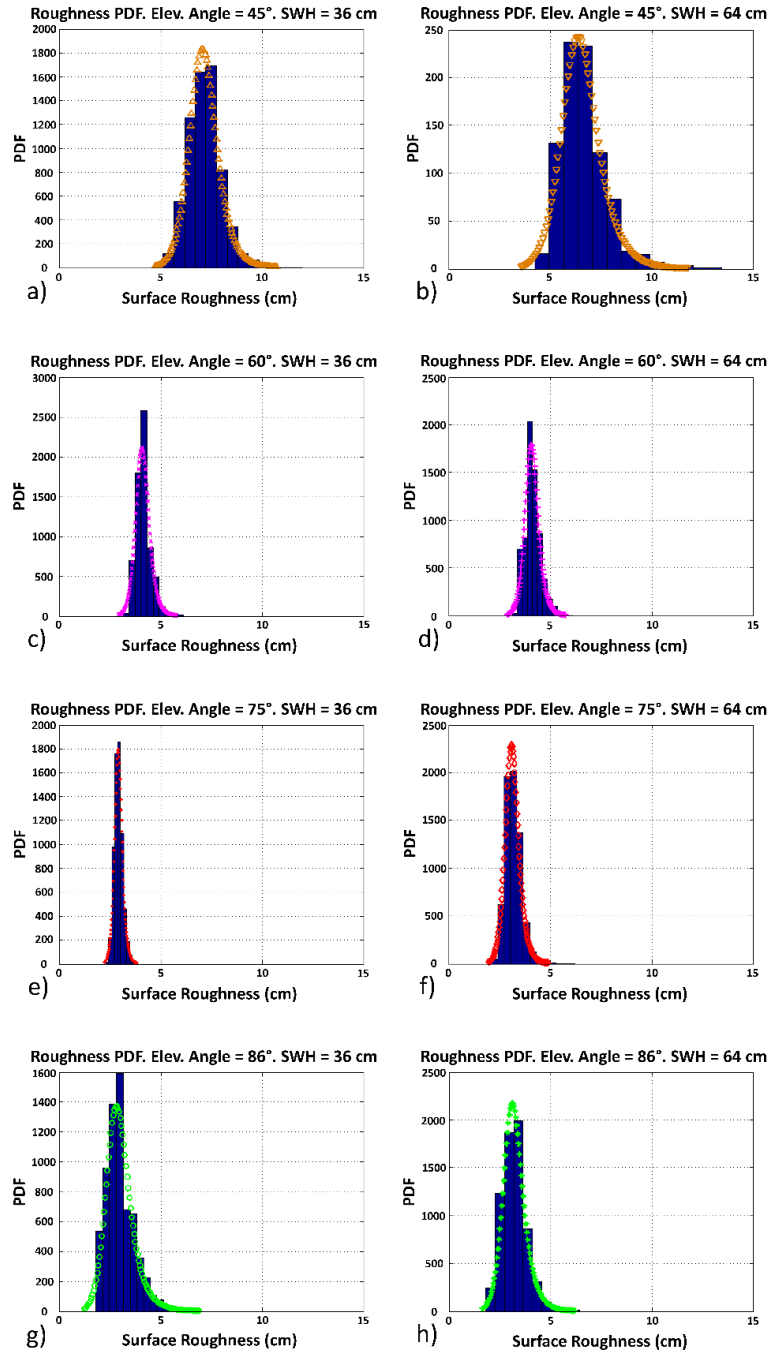


Fig. 6.17. Theoretical log-logistic PDF approximation to the small scale surface roughness distributions for an elevation angle of (a,b) $\theta_e = 45^\circ$, (c,d) $\theta_e = 60^\circ$, (e,f) $\theta_e = 75^\circ$, (g,h) $\theta_e = 86^\circ$; for (a,c,e,g) SWH = 36 cm and (b,d,f,h) for SWH = 64 cm. Note: The distributions of the small scale surface roughness have been derived using the standard deviation of the signal before retracking.

6.4 Final discussions

First results show the feasibility of the PYCARO instrument operated in closed-loop mode for "sea" waves monitoring for long-term local sea level and wave monitoring. The correlation of the GNSS-R derived "sea" waves and the ground truth data show a dependence with the elevation angle and the SWH. The experiment in the CIEM wave channel provided a unique opportunity to demonstrate the wave monitoring capabilities using closed-loop GNSS-R techniques as opposed to open-loop ones, which require an a priori approximated knowledge of the reflecting surface to perform the waveform tracking. In this work, the coherent scattering over the small scale 1-D mechanically-driven waves has been evaluated. It has been found a lower value of the effective small scale roughness as compared to the real water surface. The feasibility of local sea level monitoring using coherently reflected GPS C/A signals under large roughness conditions will also require a dedicated field experiment and further theoretical studies, but the application of GNSS-R to perform local sea level determination with the required precision for altimetric calibrations [86] is already promising.

6.5 Conclusions

A low altitude GNSS-R like experiment has been performed in a controlled scenario in the CIEM wave channel at the premises of the Civil Engineering School of the UPC-BarcelonaTech using synthetic GPS data to mimic a realistic scenario. Two different water surface states with a SWH = 36 cm and 64 cm have been simulated for GPS "satellites" at elevation angles of $\theta_e = 45^\circ, 60^\circ, 75^\circ$, and 86° . The size of the scattering cells during the coherent integration time ($T_c = 20$ ms) increases for larger scale surface roughness (SWH) and for decreasing elevation angles. The cell main axis is 0.22 m for a SWH = 36 cm and $\theta_e = 86^\circ$ and 1.36 m for a SWH = 64 cm and $\theta_e = 45^\circ$. The Pearson's linear correlation coefficients of the bistatically-derived SSH with the wave gauge data are: 0.78, 0.85, and 0.81 for a SWH = 36 cm and 0.34, 0.74, and 0.72 for a SWH = 64 cm, respectively for transmitters elevation angles of $\theta_e = 60^\circ, 75^\circ$, and 86° , respectively. The ratio of the coherent-to-incoherent

components of the scattered field after retracking was evaluated using a re-constructed field approach. In order to improve the statistical significance of the results a 30 min long observation was acquired for each configuration. The ratio of the coherent-to-incoherent components as seen by the PYCARO reflectometer for a SWH = 36 cm is approximately ~ 1 in the range from $\theta_e = 60^\circ$ to $\theta_e = 86^\circ$. As an independent scientific observable, the phase standard deviation of the GPS signals before retracking was computed during the experiment. Using these measurements an estimation of the “facets” roughness (small scale waves) was derived. Then, an empirical correction term to estimate the effective small scale roughness was inferred comparing the experimental small scale surface roughness data with those provided by the coherent reflectivity model derived under the KM Scalar Approximation. It depends on the satellite elevation angle, and is as large as $P \sim 4.1$ for $\theta_e = 45^\circ$. The lower value of the effective small scale roughness at L1 as compared to the real water surface means that the scattering surface as seen by the GNSS-R instrument is smoother. This work has shown the feasibility of “low-cost”²¹ GNSS-R techniques to perform local tides and “sea” waves determination using the coherently reflected GPS reflected signals in off-shore applications.

²¹ “Low-cost” as compared to the deployment and maintenance of coastal oceanographic buoys and sea tide gauges.

7

7. ESA AIRBORNE FLIGHTS OVER THE BALTIC SEA

7.1 Introduction

The success of Global Navigation Satellite Systems Reflectometry (GNSS-R) technique for ocean altimetry [2, 3] will rely on its feasibility to measure the Sea Surface Height (SSH) and its changes, with enough precision and accuracy, at improved spatial and temporal resolutions, as compared to traditional radar altimetry [105]. This advantage in terms of spatio-temporal sampling is due to the multi-static configuration allowing to perform measurements over many points along directions away from the nadir. At present, the ultimate influence of the different GNSS-R parameters in the achievable precision and accuracy is still being analyzing. The impact of different noise sources, as well as the theoretical height precision expectations, and the corrections of the different bias terms must be correlated with results obtained in a real scenario. This work presents the results of two ESA-sponsored air-borne experiments carried out in the Baltic Sea on June and November 2011 using conventional GNSS-R with the Global Positioning System (GPS) L1 C/A code only.

Section 7.2 presents the work methodology. The conventional GNSS-R complex cross-correlation technique is stated, as well as its impact on the theoretical height precision once the altimetric tracking point is identified.

Then, in Section 7.3, the conditions of both air-borne experiments are summarized as a starting point to evaluate the results obtained. These results depend on the techniques used to identify the specular point delay in the reflected waveform, and to perform the different delay corrections to derive the geometric delay. Also, the geometric model assumed for the scenario determines the accuracy of the altimetric range.

Section 7.4 analyzes the feasibility of the conventional GNSS-R technique by comparing the experimental precision achieved with the one expected by theoretical approximations. Then, the relative accuracy is shown by comparing it with traditional radar altimetry data provided by Jason-2. At the end of this Section it will be demonstrated that the achievable accuracy is enough to detect geoid undulation changes, by observing the derivative of the relative SSH.

Finally, Section 7.5 summarizes the main results of this study.

7.2 Altimetric performance

This Section provides the theoretical framework required for the analysis of the altimetric performance of the experimental results.

7.2.1 Conventional GNSS-R or complex cross-correlation technique using the clean code replica approach

The technique employed to extract the incoming codes from the direct and the reflected signals is to perform the complex cross-correlations between each of them and a locally-generated clean replica of the transmitted GPS codes. As a result, direct and reflected waveforms are obtained. This processing allows to obtain their relative delay. Hereafter, this theoretical discussion focuses on the reflected signal. In this case only the down-looking (or the up-looking in case of the direct signal) chain is affected by thermal noise²² providing a cleaner waveform than in the “interferometric” GNSS-R technique.

The reflected signal v_r is first band-pass filtered and down-converted at a non-zero intermediate frequency. Then, in the GPS Open-Loop Differential Real-Time Receiver (GOLD-RTR) case [57], the down-converted signal is counter-rotated using a counter-rotation phase model to remove the frequency of the signal. Finally, the remaining signal is ready for cross-correlation with the replica v_{replica} over a coherent integration time T_c . After this, the power of the correlator output $Y(\tau, f)$ at lag “ τ ”, and frequency “ f ” is obtained, and accumulated incoherently over N_{inc} samples.

If the reflected signal v_r is represented as a sum of the signal $s_r(t)$ and the thermal noise $n_r(t)$, the cross-correlation output at a frequency “ f ” can be represented as [95]:

²² Actually, in the case of the scattered signal the measured cross-correlation or “waveform” is also affected by speckle noise.

$$\begin{aligned}
Y(\tau, f) &= \int_{-\frac{T_c}{2}}^{\frac{T_c}{2}} v_r(t') v_{\text{replica}}^*(t' - \tau) dt' = \int_{-\frac{T_c}{2}}^{\frac{T_c}{2}} s_r(t') v_{\text{replica}}^*(t' - \tau) dt' + \\
&+ \int_{-\frac{T_c}{2}}^{\frac{T_c}{2}} n_r(t') v_{\text{replica}}^*(t' - \tau) dt' = Y_S(\tau, f) + Y_N(\tau, f).
\end{aligned} \tag{7.1}$$

Then, the average power at the correlator output is given by the the sum of two terms [95]:

$$\left\langle |Y(\tau, f)|^2 \right\rangle = \left\langle |Y_S(\tau, f)|^2 \right\rangle + \left\langle |Y_N(\tau, f)|^2 \right\rangle, \tag{7.2}$$

where $Y_S(\tau, f)$ is the cross-correlated signal power, and $Y_N(\tau, f)$ is the cross-correlated noise power.

The Signal-to-Noise Ratio for the cGNSS-R case (SNR_{cr}) is then given by:

$$\text{SNR}_{\text{cr}}(\tau, f) = \frac{\left\langle |Y_S(\tau, f)|^2 \right\rangle}{\left\langle |Y_N(\tau, f)|^2 \right\rangle} = \frac{T_c [P_R(\tau, f) * |WAF(\tau, f)|^2]}{k T_{\text{Nr}}}, \tag{7.3}$$

where f is the Doppler frequency, P_R is the total reflected power received in the antenna beam at the input of the cross-correlator, WAF is the Woodward ambiguity function of the GPS signal, $k = 1.3 \cdot 10^{-23}$ J/K is the Boltzmann constant, and T_{Nr} is the equivalent noise temperature of the down-looking chain [3].

The average power is a function of the delay τ between the reflected and the locally-replicated codes and the Doppler frequency f . Its graphical representation is called Delay Doppler Map. After the restriction of one degree of freedom the output power is a function of the delay or the Doppler frequency, being the obtained functions called waveforms. The analysis of the delay is required to perform altimetry. Therefore, the averaged waveforms are represented as a function of the average signal power of constant Doppler points and their corresponding SNR_{cr} :

$$\begin{aligned}\left\langle \left| Y(\tau, f = \text{cte}) \right|^2 \right\rangle &= \left\langle \left| Y_S(\tau, f = \text{cte}) \right|^2 \right\rangle + \left\langle \left| Y_N(\tau, f = \text{cte}) \right|^2 \right\rangle \\ &= \left\langle \left| Y_S(\tau, f = \text{cte}) \right|^2 \right\rangle \left(1 + \frac{1}{\text{SNR}_{\text{cr}}(\tau, f = \text{cte})} \right).\end{aligned}\quad (7.4)$$

7.2.2 Altimetric tracking point

In an ideal case, in absence of noise, the reflected waveform corresponding to the point of specular reflection²³ can be formulated as [16]:

$$\begin{aligned}w(\tau) &= \left\langle \left| Y_S(\tau, f = 0) \right|^2 \right\rangle = \\ &= \frac{P_t}{(4\pi)^2} \frac{\lambda^2}{4\pi} T_c^2 \iint \frac{G_t(\bar{\rho}) G_r(\bar{\rho}) |S(\Delta f(\bar{\rho}))|^2 \Lambda^2[(R_0 + R)/c + \Delta\tau]}{R_t^2 R_r^2} \sigma^0(\bar{\rho}) d^2\bar{\rho},\end{aligned}\quad (7.5)$$

where $\bar{\rho}$ is the spatial integration variable, P_t is the transmitted power, λ is the electromagnetic wavelength of the signal, $G_r(\bar{\rho})$ and $G_t(\bar{\rho})$ are the power gain of the receiving and the transmitting antenna respectively, $\sigma^0(\bar{\rho})$ is the normalized bistatic radar cross-section of the sea surface, R_t and R_r are the distances from the transmitter and the receiver to the point $\bar{\rho}$, $S(\Delta f(\bar{\rho}))$ is the sinc-exponential function:

$$S(\Delta f(\bar{\rho})) = \frac{\sin(\pi \Delta f(\bar{\rho}) T_c)}{\pi \Delta f(\bar{\rho}) T_c} \exp(-j\pi T_c), \quad (7.6)$$

and Λ is approximately the triangle function:

$$\Lambda(\tau) = \begin{cases} 1 - \frac{|\tau|}{\tau_c}, & \text{if } |\tau| < \tau_c, \\ 0, & \text{otherwise} \end{cases}, \quad (7.7)$$

where τ_c is the chip length, which is approximately equal to 1 μs for the C/A code (actually 1 ms/1,023). A simplification of (Eqn. 7.5) can be written as the convolution product [56]:

$$w(\tau) = p(\tau) * \Lambda^2(\tau), \quad (7.8)$$

²³ It has been assigned $f = 0$ to the point of specular reflection.

where $p(\tau)$ is the power per unit of delay, and represents the contribution to the waveform of the points with a delay τ .

It has been demonstrated [79, 81] that, for an ideal case (infinite bandwidth receiver) the delay corresponding to the maximum derivative of the reflected waveform is equal to the delay corresponding to the specular reflection (altimetric tracking point). However, for a band-limited receiver, the waveform is filtered and this filtering [106] introduces a bias in the position of the specular reflection point. This bias has a systematic instrument related component, that can be in principle calibrated, and a component dependent on the sea state, [45], a sort of electromagnetic bias that is not yet fully understood at L-band and for a bistatic configuration.

In a real scenario a more complete analysis must be performed. It is required to include considerations related to a finite sampling interval of the waveforms in the receiver, and different sources of noise: thermal noise (additive), speckle noise²⁴ (multiplicative), and processing noise due to errors in the way the signals are processed. In such situation a correction term b_{spec} appears [79]. This error is due to the large coherent integration time which causes a spatial filtering of the power scattered off the sea surface [3].

Additionally, other biases must be corrected for. For example, not all the scattering elements equally contribute to the radar return, since valleys of waves tend to reflect GPS pulses better than crests. Thus, the centroid of the mean reflecting surface is shifted away from the mean sea level towards the valleys of the waves. If the sea state is rougher, this bias will be larger, then reducing the accuracy of the GNSS-R altimetry products. This shift is the electromagnetic bias that causes an overestimation in the SSH measurement, and it is well understood in classical nadir-looking altimetry, but little is known in bistatic configurations at L-band. In an air-borne scenario, the ionosphere affects both direct and reflected signals in the same way.

²⁴ Speckle is a source of noise that involves diffuse scattering from rough surfaces. If the ocean is reasonably rough with respect to the incoming GPS signal wavelength, the different heights and orientations of the waves over the glistening zone will randomly shift the phases of the GPS signals. Some of these paths will interfere destructively and others will interfere constructively, as a consequence, the signal power level will fluctuate randomly at the antenna input. From this, it can be derived that the Signal-to-Noise Ratio (SNR) of the reflected signal is severely affected by the sea state. To mitigate this effect, incoherent averaging of consecutive uncorrelated signals must to be performed [45].

Therefore, the relative delay between them is independent of the bias induced by the ionosphere. In case of a space-borne platform, such as the planned PARIS-IoD mission [3], the reflected signal is seriously affected by the ionosphere, while the direct signal only marginally (depending ultimately on the platform height). Therefore, in this scenario it is required to compensate this delay, but not in an air-borne one.

7.2.3 Expected achievable height precision

Few models have been developed to predict the height precision. Each one drives the analysis from different hypothesis. The first code range precision model was proposed by Lowe et al. [25]. Martín et al. [106] used a new one based on the Cramer-Rao Bound (CRB) approach. The CRB method allows to predict the optimum behavior in stochastic problems which can be described by a probability density function.

A simpler model is introduced here, since it allows to analyze the height precision as a function of different parameters involved in GNSS-R scenario such as the Signal-to-Noise-Ratio (SNR), the speckle noise²⁵, the observation geometry, and the auto-correlation properties of GPS signals [50].

The standard deviation σ_R of the total received waveform power is dependent on the SNR_{cr} , and as it is shown in Eqn. 7.9, it decreases as a function of the number of incoherent averaging N_{inc} [35, pp. 492]:

$$\sigma_R = \frac{\langle |Y(\tau)|^2 \rangle}{\sqrt{N_{\text{inc}}}} = \frac{\langle |Y_S(\tau)|^2 \rangle}{\sqrt{N_{\text{inc}}}} \left(1 + \frac{1}{\text{SNR}_{\text{cr}}(\tau)} \right), \quad (7.9)$$

being the noise power standard deviation:

$$\sigma_N = \frac{\langle |Y_S(\tau)|^2 \rangle}{\sqrt{N_{\text{inc}}}} \left(\frac{1}{\text{SNR}_{\text{cr}}(\tau)} \right). \quad (7.10)$$

²⁵ Speckle noise is also correlated between consecutive correlation lags, due to the width of the ACF and the sampling frequency and from waveform to waveform being more correlated where the amplitude is larger (up to 7 consecutive WFs), less correlated where the amplitude is smaller, and uncorrelated where the dominant noise term is the thermal noise [46].

If the signal and the noise are uncorrelated, the standard deviation of the signal power, becomes then [35, pp. 493]:

$$\sigma_S = \sqrt{\sigma_R^2 + \sigma_N^2} = \frac{\langle |Y_S(\tau)|^2 \rangle}{\sqrt{N_{\text{inc}}}} \sqrt{\left(1 + \frac{1}{\text{SNR}_{\text{cr}}(\tau)}\right)^2 + \left(\frac{1}{\text{SNR}_{\text{cr}}(\tau)}\right)^2}. \quad (7.11)$$

In order to obtain the standard deviation of the height estimation it is first required to estimate the delay error σ_d (position of the waveform's peak derivative) associated to the presence of noise.

In the ideal case of an infinite bandwidth receiver the altimetric tracking point is the point of maximum derivative of the power waveform [79]. Under this hypothesis, the height precision (σ_h) can be expressed as follows:

$$\sigma_h = \frac{c\sigma_d}{2\sin\theta_e} = \frac{c\langle |Y_S(\tau)|^2 \rangle}{2\langle |Y_S(\tau)|^2 \rangle' \sin\theta_e} \frac{1}{\sqrt{N_{\text{inc}}}} \sqrt{\left(1 + \frac{1}{\text{SNR}_{\text{cr}}(\tau)}\right)^2 + \left(\frac{1}{\text{SNR}_{\text{cr}}(\tau)}\right)^2}, \quad (7.12)$$

where c is the speed of light in the vacuum or air, and θ_e is the local elevation angle at the specular point.

Note that, to achieve a high precision, a high SNR_{cr} is required. The height precision is also inversely proportional to the slope of the power waveform at the tracking point. The waveform slope, in turn, increases with the signal bandwidth, therefore the P code should improve the height precision, as compared to the achievable one using the C/A code. This model has been previously employed [3, 50, 79, 107] to analyze the expected achievable height precision using different techniques: conventional GNSS-R in which the received signal is cross-correlated with a local replica of the transmitted signal, and “interferometric” GNSS-R in which direct and reflected signals are cross-correlated. In this work it will be used to assess its performance against experimental data (Section 7.4.1).

7.3. Experiment description

This Section describes the experiment set-up used during both air-borne experiments over the Baltic Sea and introduces the altimetric scenario. The information here is useful to properly understand the results of this Chapter.

7.3.1 Experimental set-up



Fig. 7.1. Skyvan Short SC-7 (Laboratory of Space Technology) at the Helsinki airport.

Two airborne experiments have been carried out using the IEEC/ICE-CSIC GOLD-RTR [50] in the Gulf of Finland, in the vicinity of Helsinki, with the Aalto University's research Skyvan Short SC-7 (Fig. 7.1). These airborne experiments were sponsored by the European Space Agency to test the new "interferometric" GNSS-R techniques, with a modified version of the GOLD-RTR instrument named PIR-A (PARIS Interferometric Receiver-Airborne) [60, 65, 66].

The first flight took place on June 21st, 2011. One part of the trajectory consisted of several overpasses over the estuary of the Kymi River with smooth and calm water at a flight altitude $h = 150$ m. The other part consisted of two overpasses over open sea, the first one at $h = 500$ m, and the second one at $h = 350$ m (Fig. 7.2a). In this first experiment, GPS Antcom[®] omnidirectional antennas [75, pp.118] were used for both

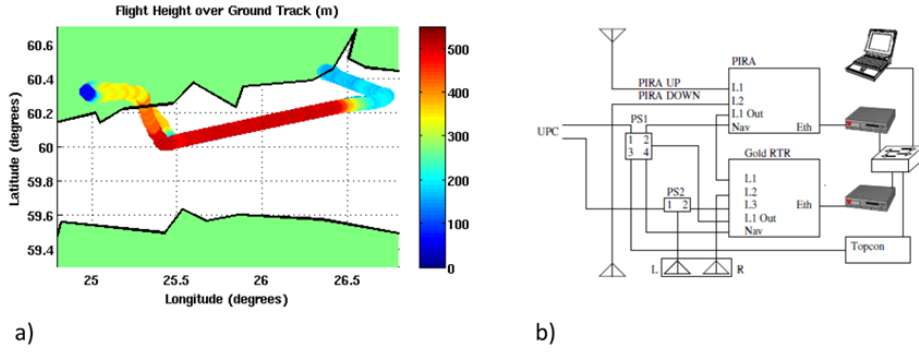


Fig. 7.2. (a) Trajectory of the Skyvan during the first experiment. (b) First flight instrumentation scheme. Note: PS 1, 2 are the power splitters 1 and 2, Topcon is a GPS receiver, and Eth is an Ethernet connection [108].

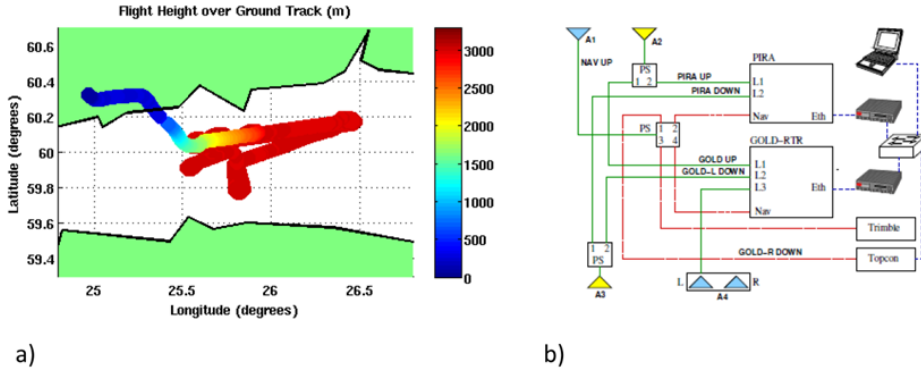


Fig. 7.3. (a) Trajectory of the Skyvan during the second experiment. (b) Second flight instrumentation scheme. Note: PS are the power splitters, Topcon and Trimble are GPS receivers, and Eth is an Ethernet connection [108].

up and down-looking signals, using right-hand and left-hand circular polarizations respectively (Fig. 7.2b).

The second experiment was performed on November 11th, 2011. The trajectory was composed by several overpasses over open sea at $h = 3,000$ m (Fig. 7.3a). In this flight, high gain ($G > 15$ dB) GPS Antcom[®] directional zenith and nadir-looking antennas were used (Fig. 7.3b) to compensate the lower SNR at higher altitudes, required by the new “interferometric” GNSS-R technique. The antennas were attached to the fuselage, and there was no steering mechanism. Therefore, only the signals from the high elevation satellites (within the antenna beamwidth) were

analyzed. Higher temporal and spatial resolution can be achieved by increasing the number of GPS satellites tracked. However, the SNR would decrease, and only a steerable antenna can compensate for this loss.

7.3.2 Altimetric scenario

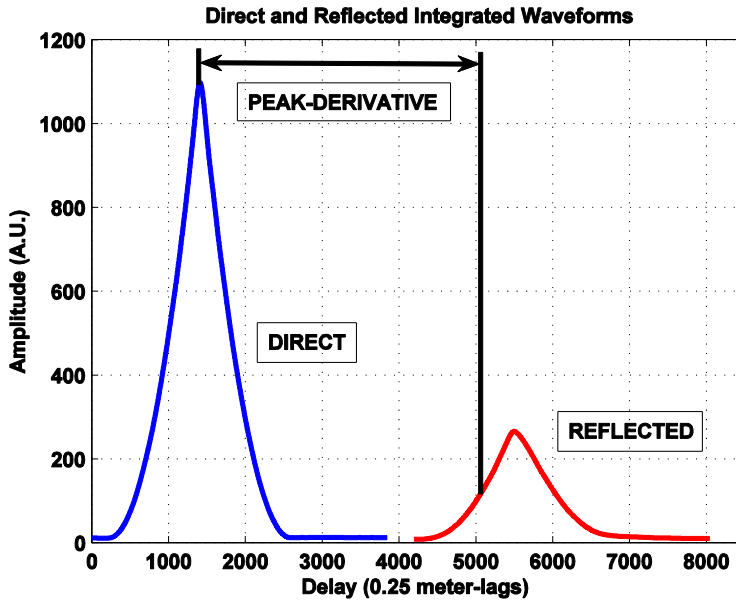


Fig. 7.4. Sample direct and reflected integrated waveforms during the first flight [$T_c = 1$ ms and $N_{inc} = 1,000$].

The GOLD-RTR collects the direct GPS signals and the ones reflected over the sea surface, and correlates each of them against a clean replica of the C/A code. The receiver has ten correlation channels. Each channel contains 64 single-lag correlators in order to provide 64-lag waveforms at approximately 50 ns (≈ 15 m) spacing, which is too large as compared to the expected height precision. To solve it, an optimum re-sampling and interpolation of the resulting 3,840-lag waveforms were performed. As a result, the direct and the reflected waveforms were obtained (Fig. 7.4). The coherent integration time during both flights was set to be the same allowing

intercomparison of both data sets and as low as $T_c = 1$ ms because the coherence time for the first flight and for high elevation angles is less than 2 ms as per Eqn. 4 in [109].

In the present work the point of maximum derivative of reflected waveform is taken as the specular reflection point [79]. Then, in addition to the uncorrected electromagnetic bias b_{EM} [81], the effect of band-limited receiver b_{spec} [79, 106, 110] is present in our assumptions. In order to extract the geometric distance between the reflected and the direct paths ρ_{geo} , biases caused by the antenna's offset vector (different position of the up- and down-looking antennas), and the atmospheric delay have to be corrected. Once the geometric delay has been measured, assuming parallel direct and reflected propagation directions, and a flat surface, the experimental height between the up-looking antenna and the sea surface can be calculated as:

$$H = \frac{\rho_{geo}}{2\sin\theta_e} + b_{spec} + b_{EM}. \quad (7.13)$$

Finally, in order to extract the SSH, H must be subtracted from the GPS measured up-looking antenna altitude H_{WGS84} relative to the WGS 84 surface. Then, the ultimate accuracy of the GNSS-R technique is determined by the inherent error of the measurement:

$$SSH_{measured} = H_{WGS84} - H. \quad (7.14)$$

The lack of an absolute calibration of these uncertainties experiments limits the absolute accuracy analysis of both airborne. However the goal of both experiments was to test the precision of the conventional GNSS-R technique and the feasibility to derive the Relative Mean Dynamic Topography (RMDT).

7.4 Results

The presentation, the description and the discussion of the experimental results is performed in this Section. Additional theoretical details and the comparison with previous air-borne campaigns help the interpretation of the results.

7.4.1 Reliability of the theoretical model for height precision estimation

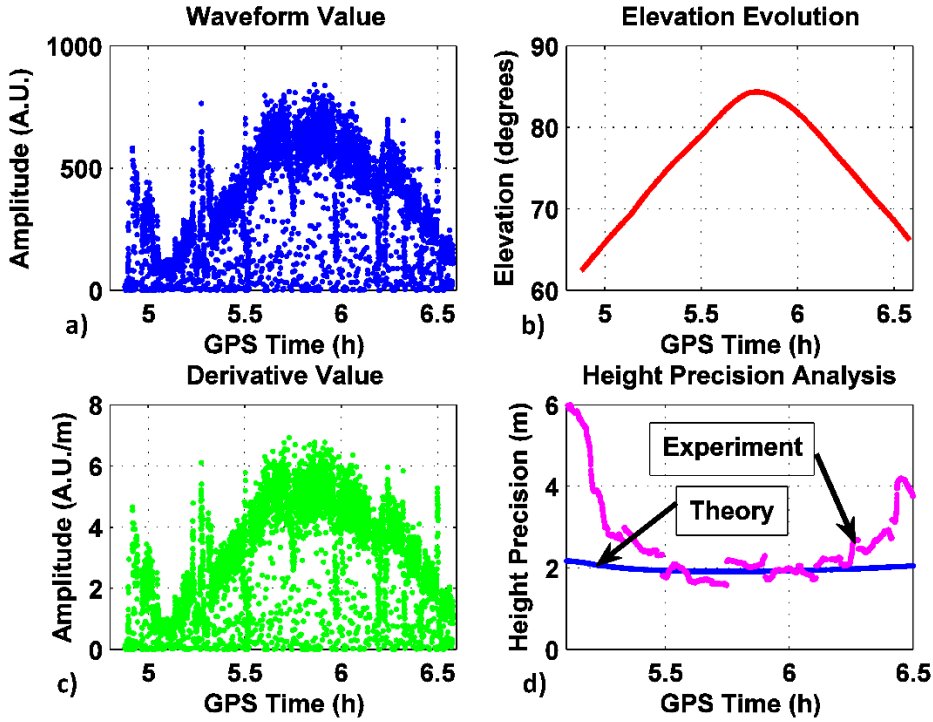


Fig. 7.5. (a) Reflected waveform values at the point of maximum derivative. (b) Elevation angle of the satellite PRN12 as function of the GPS time. (c) Reflected waveform derivative values at the point of maximum derivative. (d) Validation of the theoretical precision expectation with real data from the second air-borne experiment. Note: from GPS Time from ~ 5.35 h to ~ 6.35 h the elevation angles are larger than 75° .

Due to the wider Auto-Correlation-Function (ACF), and the lack of thermal noise in the clean replica signal (conventional GNSS-R technique) the SNR_{cr} is high. Otherwise, the incoherent integration time should be increased (Eqn. 7.12), and higher antenna gains would be required. On the other hand, increasing the incoherent averaging reduces the spatial resolution.

In this situation, an estimation of the height precision for high SNR_{cr} can be derived from a simplified form of Eqn. (7.12) as:

$$\sigma_h \cong \frac{c \langle |Y(\tau)|^2 \rangle}{2 \langle |Y(\tau)|^2 \rangle' \sqrt{N_{inc}} \sin \theta_e}. \quad (7.15)$$

The validity of this model is tested with data from the second aircraft experiment. The waveform value (Fig. 7.5a), as well as the waveform derivative value (Fig. 7.5c) at the point of maximum derivative are found after incoherent integration of 1,000 1-ms waveforms (1 s total integration time), being σ_h on the order of 2 m (Fig. 7.5d). Experimental results diverge from the theoretical ones as the elevation angle decreases. For elevation angles higher than 75° (Fig. 7.5b), the values provided by this model give an estimation within 0.5 m error with respect to the SSH measurements (Fig. 7.5d). As a main conclusion it can be derived that future work is needed to develop more accurate models for lower elevation angles.

7.4.2 Height precision analysis

7.4.2.1 Achieved height precision

The high frequency oscillations of the Skyvan trajectory during both experiments additionally introduce a source of random noise [111]. The Allan's standard deviation [111] of the measured SSH is obtained using:

$$\sigma_{Allan}(T, M) = \sqrt{\frac{1}{2(M-1)} \sum_{i=0}^{M-2} (\bar{y}_{i+1} - \bar{y}_i)^2}. \quad (7.16)$$

In (Eqn. 7.16) T is the sampling period, M is the number of samples being averaged and \bar{y} is the incoherently averaged SSH. The time-difference between adjacent samples was considered fixed in the employed Allan's standard deviation estimator used.

In both flight experiments (Figs. 7.6b,d,f,h) the Allan's standard deviation tends to a constant value, indicating that up to 180 s the obtained height precision is not dominated by this source of random noise.

The precision of the conventional GNSS-R technique (Section 7.2) is evaluated by calculating the standard deviation of the detrended $SSH_{measured}$ to compensate the

aircraft's altitude changes due to atmospheric turbulence. For the analysis of the first flight, the satellite PRN 25 has been selected because of the high elevation angles during the experiment (from 62° to 76°).

For low elevation angles the widely used Kirchhoff model under Geometric Optics approximation [16] fails due to the fact that shadowing and multiple scattering effects have been ignored. Also, the polarization purity of the transmitted GPS signals is better for higher elevation angles²⁶.

The evolution of the height precision with incoherent averaging for the two parts of the first flight is shown in Figs. 7.6a,c. The first part (Fig. 7.6a) was performed over open sea at $h = 500$ m over the reference ellipsoid, being the second part (Fig. 7.6c) at $h = 150$ m. In the first case a 25 cm precision is obtained after 40 s incoherent averaging, which corresponds approximately to an overflight of 3.3 km length (Table 7.1). In the second part (Table 7.2), the height precision is around 28 cm after 40 s incoherent averaging because of the smaller glistening zone, due to lower flight altitude. Note that the lower flight altitude reduces the amount of speckle noise reduction, due to the reduced number of scatters within the antenna footprint.

In the second flight, the experimental height precision increases during the first 100 s of incoherent averaging (Figs. 7.6e,g). The height precision is 31 cm and 6 cm, at 20 s and 100 s averaging, respectively (Table 7.3). During the time period between 5.4 h and 6.6 h the satellite PRN 12 was selected because of the elevation angle ranged from 66° to 85° . Altimetric delays corresponding to aircraft maneuvers have been eliminated. During these periods (5 h, 5.25 h, 6.25 h and 6.5 h), there are sudden reductions [113] of the value of the product of the two antenna gains in the direction of the GPS transmitter and its corresponding specular point. These power losses appear as peaks and dips in the value of the waveforms and their derivatives at the point of maximum derivative (Figs. 7.5a,c).

²⁶ The GPS transmitted signals are right-hand circularly polarized, with an ellipticity at L1 smaller than 1.2 dB within a $\pm 13.8^\circ$ cone around the antenna boresight for block II A satellites, and smaller than 1.8 dB for blocks II R/II R-M/II F/GPS III [112].

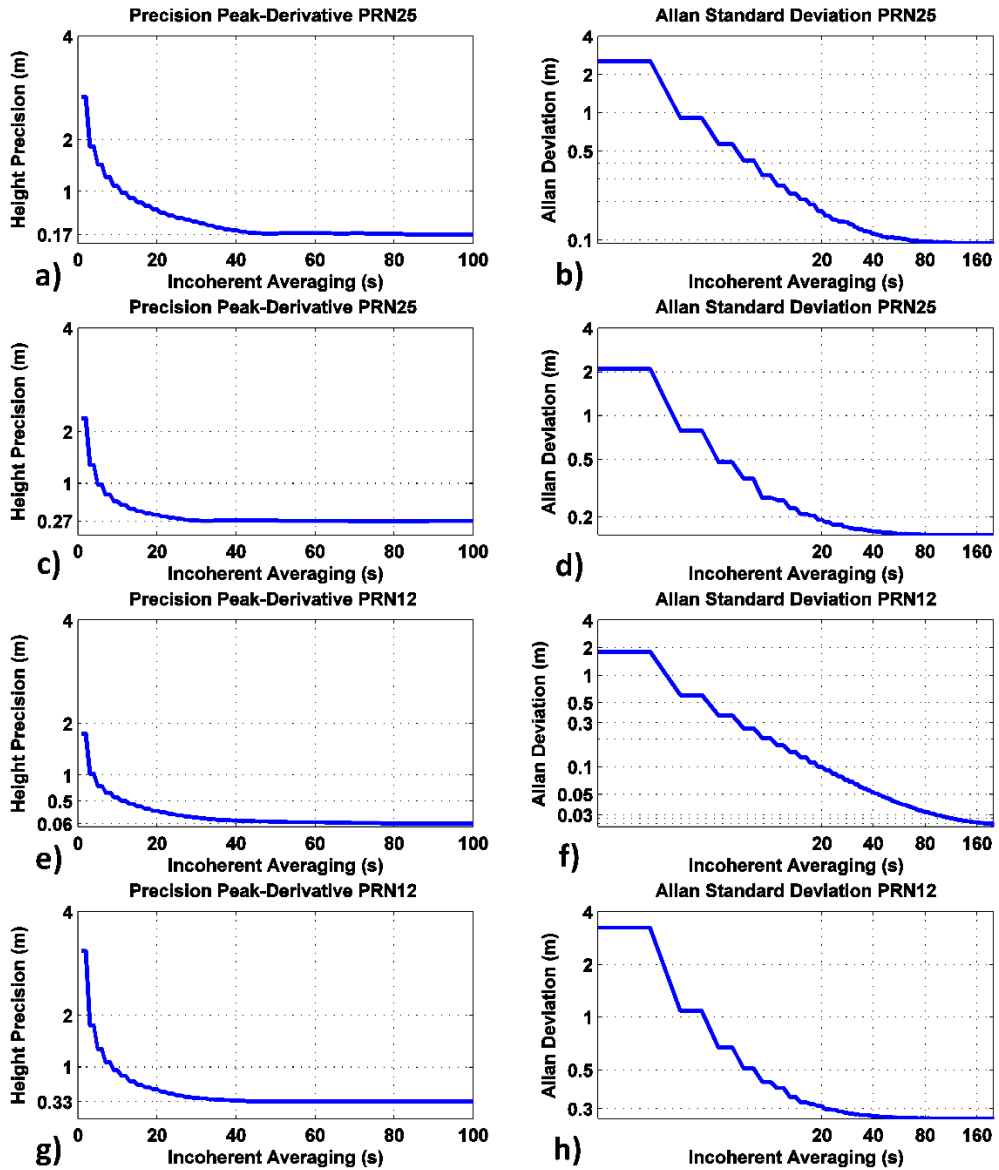


Fig. 7.6. (a) Height precision: $h = 500$ m, θ_e from 73° to 76° , GPS Time from 16.4 h to 16.6 h, $v_{\text{aircraft}} = 302$ km/h. (b) Allan's standard deviation: $h = 500$ m, θ_e from 73° to 76° , GPS Time from 16.4 h to 16.6 h, $v_{\text{aircraft}} = 302$ km/h. (c) Height precision: $h = 150$ m, θ_e from 62° to 66° , GPS Time from 17.5 h to 17.7 h, $v_{\text{aircraft}} = 205$ km/h. (d) Allan's standard deviation: $h = 150$ m, θ_e from 62° to 66° , GPS Time from 17.5 h to 17.7 h, $v_{\text{aircraft}} = 205$ km/h. (e) Height precision: $h = 3,000$ m, θ_e from 66° to 85° , GPS Time from 5.4 h to 6.6 h, $v_{\text{aircraft}} = 237$ km/h. (f) Allan's standard deviation: $h = 3,000$ m, θ_e from 66° to 85° , GPS Time from 5.4 h to 6.6 h, $v_{\text{aircraft}} = 237$ km/h. (g) Height precision: $h = 3,000$ m, θ_e from 70° to 77° , GPS Time from 5.6 h to 6.2 h, $v_{\text{aircraft}} = 237$ km/h. (h) Allan's standard deviation: $h = 3,000$ m, θ_e from 70° to 77° , GPS Time from 5.6 h to 6.2 h, $v_{\text{aircraft}} = 237$ km/h.

Table 7.1. Altimetric precision: $h = 500$ m, θ_e from 73° to 76° , GPS Time from 16.4 h to 16.6 h, $v_{\text{aircraft}} = 302$ km/h (values corresponding to Fig. 7.6a).

Along Track	Incoherent	Precision (m)
Spatial Resolution (km)	Averaging (s)	
0.08	1	2.82
0.8	10	1.15
1.6	20	0.65
2.5	30	0.42
3.3	40	0.25
4.2	50	0.2
5	60	0.2
5.8	70	0.2
6.7	80	0.18
7.2	90	0.17
8	100	0.17

Table 7.2. Altimetric precision: $h = 150$ m, θ_e from 62° to 66° , GPS Time from 17.5 h to 17.7 h, $v_{\text{aircraft}} = 205$ km/h (values corresponding to Fig. 7.6c).

Along Track	Incoherent	Precision (m)
Spatial Resolution (km)	Averaging (s)	
0.05	1	2.26
0.5	10	0.65
1.1	20	0.39
1.7	30	0.28
2.2	40	0.28
2.8	50	0.28
3.4	60	0.27
3.9	70	0.27
4.5	80	0.27
5.1	90	0.27
5.7	100	0.27

Table 7.3. Altimetric precision: $h = 3,000$ m, θ_e from 66° to 85° , GPS Time from 5.4 h to 6.6 h, $v_{\text{aircraft}} = 237$ km/h (values corresponding to Fig. 7.6e).

Along Track	Incoherent	Precision (m)
Spatial Resolution (km)	Averaging (s)	
0.06	1	1.8
0.6	10	0.57
1.3	20	0.31
1.9	30	0.19
2.6	40	0.13
3.3	50	0.1
3.9	60	0.09
4.6	70	0.08
5.3	80	0.07
5.9	90	0.07
6.6	100	0.06

Table 7.4. Altimetric precision: $h = 3,000$ m, θ_e from 70° to 77° , GPS Time from 5.6 h to 6.2 h, $v_{\text{aircraft}} = 237$ km/h (values corresponding to Fig. 7.6g).

Along Track	Incoherent	Precision (m)
Spatial Resolution (km)	Averaging (s)	
0.06	1	3.25
0.6	10	0.94
1.3	20	0.57
1.9	30	0.41
2.6	40	0.36
3.3	50	0.34
3.9	60	0.34
4.6	70	0.34
5.3	80	0.34
5.9	90	0.34
6.6	100	0.33

7.4.2.2 Comparative analysis with other airborne experiments

A comparative analysis of the results obtained during both campaigns in the Gulf of Finland with other air-borne experiments is performed: Platform Harvest [20], and Campaign for validating the Operation of SMOS (CoSMOS) [79].

Conventional GNSS-R altimetry with the P(Y) code was employed during an aircraft experiment performed in January 2001 over the Platform Harvest off the coast of California. In this experiment, the altimetric point position was extracted by fitting the reflected signal to a model. The mean delay precision obtained from two GPS satellites with elevation angles of 55° and 60° was $\text{rms} = 56 \text{ cm}$ [$T_c = 10 \text{ ms}$ and $N_{\text{inc}} = 200$]. The trajectory consisted of 7 passes of 3-4.5 min each so about 60 min of data were collected at a flight altitude of 3,000 m. It was observed that the scatter was stronger at lower aircraft speeds due to the lesser reduction of the speckle²⁷ noise: $\text{rms} = 46 \text{ cm}$ for $v_{\text{aircraft}} = 288 \text{ km/h}$ and $\text{rms} = 64 \text{ cm}$ for $v_{\text{aircraft}} = 180 \text{ km/h}$. After incoherent averaging over 7 km, the speckle was reduced and the achieved delay precision was $\text{rms} = 5.5 \text{ cm}$. Speckle, calculation, and antenna beam pattern model seemed to be the sources of largest systematic errors. The proposed improving methodologies were to fly at higher aircraft altitudes to reduce the speckle, more fully populated geometric parameter space, and more detailed wind-vector retrieval or using external wind-vector measurements.

Data from a previous GOLD-RTR flight experiment are used to make a comparative study with the same receiver. These data were acquired during the CoSMOS campaign [79] performed on April 15th, 2006. The flight was at 3,000 m altitude with a speed $v_{\text{aircraft}} = 270 \text{ km/h}$. Data were collected during 1,900 s for altimetric purposes corresponding to three different satellites at elevation in the angles ranges: 70° to 77° , 45° to 55° , and 35° to 50° . In the first elevation angle range the delay precision achieved was 2.51 m for $T_c = 1 \text{ ms}$, $N_{\text{inc}} = 1,000$, and 6 cm for $T_c = 1 \text{ ms}$,

²⁷ The correlation time between consecutive waveforms depends with the square root of the flight altitude. Therefore, at higher altitudes, speckle is more correlated and averaging is not as effective in reducing the variance of the observations. However, at higher flight altitudes, the number of scatterers in the glistening zone is larger than at low flight altitudes, and the signal fluctuation is less important.

$N_{\text{inc}} = 1751,000$. In order to compare with the previous results, data from the satellite PRN 12 has been analyzed at a similar elevation angle range from 70° to 77° . Our expected results (Figs. 7.6g and 7.6h and Table 7.4) present a delay standard deviation of 6 cm for $T_c = 1$ ms, $N_{\text{inc}} = 1550,000$, which is consistent with the CoSMOS results.

7.4.3. Dependence of the accuracy with the elevation angle

One of the purposes of this study is to analyze the influence of the elevation angle on the accuracy of the measurements using the conventional GNSS-R technique. From the collected data is inferred that the $\text{SSH}_{\text{measured}}$ values are overestimated below elevation angles of $\theta_e = 50^\circ$ (Fig. 7.7), because of the weaker sensitivity to ocean height at lower elevations [81], being severely degraded for elevation angles below 20° . Additionally, the influence of the receiver altitude over the sea surface on the altimetric accuracy must be studied, since the attenuation of the reflected signals in

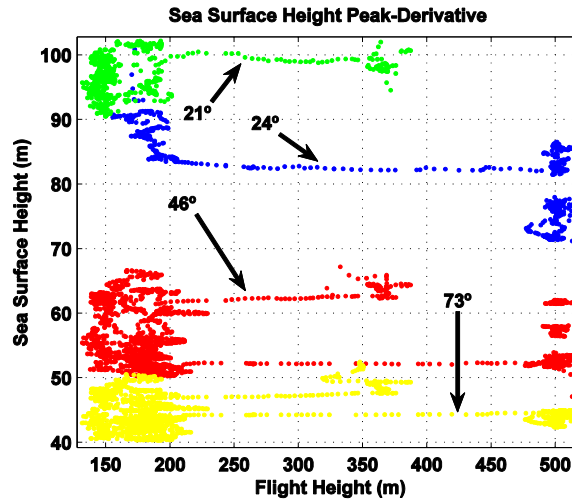


Fig. 7.7. Accuracy analysis considerations with elevation angle and flight height parameters. The mean elevation angle of each GPS satellite is: $\theta_{e,\text{mean}} = 73^\circ$ (yellow), $\theta_{e,\text{mean}} = 46^\circ$ (red), $\theta_{e,\text{mean}} = 24^\circ$ (blue), $\theta_{e,\text{mean}} = 21^\circ$ (green). Note: Dispersion in measurements at the flight range from 150 m to 200 m, at 350 m, and at 500 m, is due to changes in the elevation angle of the GPS satellites during the experiment, since the evolution of the constellation's geometry with time.

the propagation path, as derived from (Eqn. 7.5) might be significant. Experimental results show that for the flight altitude, in the range from 0 to 500 m, no influence has been observed, even for the lowest elevation angles (Fig. 7.7).

7.4.4. Relative mean dynamic topography

In the absence of tides and currents the sea surface shape should be the same as the geoid. Tides modify the mean value of the SSH. However, ocean currents induce fluctuations that change the sea topography. In order to analyze the effect of currents on the sea topography, the relative value of the Sea Level Anomaly (SLA) was extracted from the SSH data provided by GNSS-R. The results obtained were compared to the radar altimetry data which has a much higher precision. More concretely, Jason-2 data [114] were used for this purpose (Table 7.5). Figures 7.8a,b,c,d show that the Relative Mean Dynamic Topography (RMDT) provided by Jason-2 over a complete month around each of the experiments has the same trend as the GNSS-R RMDT measurements. The rms of the RMDT difference between both instruments (Figs. 7.8e,f) is 48 cm for the first flight, and 198 cm for the second flight. The bias of the measured RMDT between Jason-2 and GOLD-RTR is 46 cm for the first flight, and 2 cm for the second flight.

Table 7.5. Jason-2 temporal and spatial data window during both experiments.

Experiment	Track	Day	Time
1	92	01/06/2011	11:56/12:52
1	92	11/06/2011	13:57/14:54
1	92	21/06/2011	15:59/16:55
1	111	02/06/2011	09:47/10:43
1	111	12/06/2011	07:48/08:44
1	111	22/06/2011	05:44/06:40
2	92	07/11/2011	07:35/08:31
2	92	17/11/2011	05:34/06:30
2	92	27/11/2011	03:32/04:29
2	111	08/11/2011	01:23/02:30
2	111	17/11/2011	23:22/00:18
2	111	27/11/2011	21:20/22:17

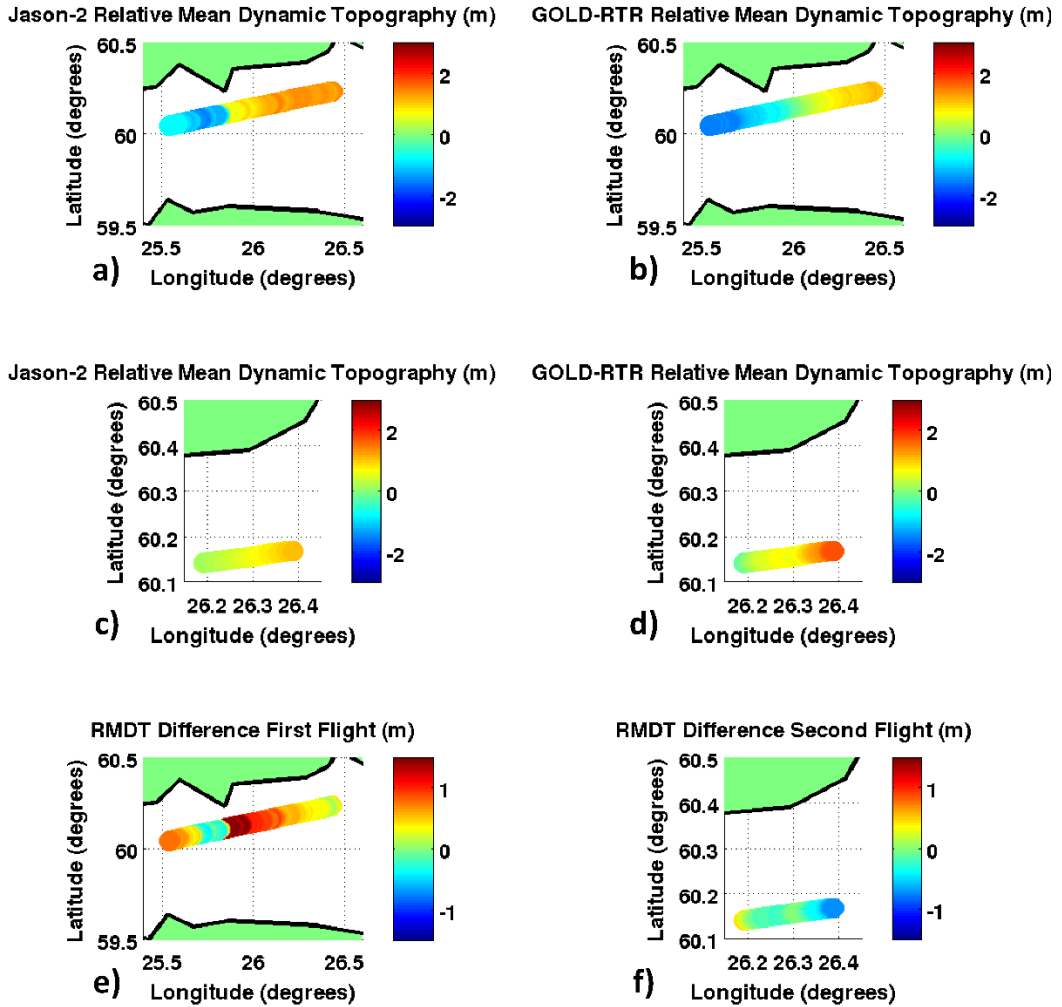


Fig. 7.8. (a) Sea surface topography provided by Jason-2 at the specular point for PRN 25. (b) Sea surface topography provided by GOLD-RTR at the specular point for PRN 25: $h = 500$ m height, θ_e from 73° to 76° , GPS Time from 16.4 h to 16.6 h, $v_{\text{aircraft}} = 302$ km/h. (c) Sea surface topography provided by Jason-2 at the specular point for PRN 12. (d) Sea surface topography provided by GOLD-RTR at the specular point for PRN 12: $h = 3,000$ m, θ_e from 80° to 84° , GPS Time from 5.5 h to 5.7 h, $v_{\text{aircraft}} = 237$ km/h. (e) Difference between sea surface topography measured by Jason-2 and GOLD-RTR at the specular point for PRN 25: $h = 500$ m height, θ_e from 73° to 76° , GPS Time from 16.4 h to 16.6 h, $v_{\text{aircraft}} = 302$ km/h. (f) Difference between sea surface topography measured by Jason-2 and GOLD-RTR at the specular point for PRN 12: $h = 3,000$ m, θ_e from 80° to 84° , GPS Time from 5.5 h to 5.7 h, $v_{\text{aircraft}} = 237$ km/h.

7.4.5 Sea slope measurement

The SSH slope is determined by the geoid undulation. As a consequence, by measuring the slope changes and comparing them with the EGM96 theoretical approximation of the geoid, it is possible to analyze the capability of the presented technique (Section 7.2) for ocean altimetry.

In the time period from 5.5 h to 6 h during the second experiment, the elevation angles were higher than 80° . The geoid undulations along to the track of the aircraft during this period is about 1 m, larger than the precision for 300 s incoherent averaging. As it can be seen in Fig. 7.9 the measured SSH has the same slope than the geoid. The mean value of the difference between geoid undulation and Sea Surface Height (49 cm) was added to the SSH in order to compare the slope of the surface with the geoid. This result shows the capability of the GNSS-R technique to provide not only relative (Section 7.4.4), but also absolute sea slope measurements and its variations with high accuracy.

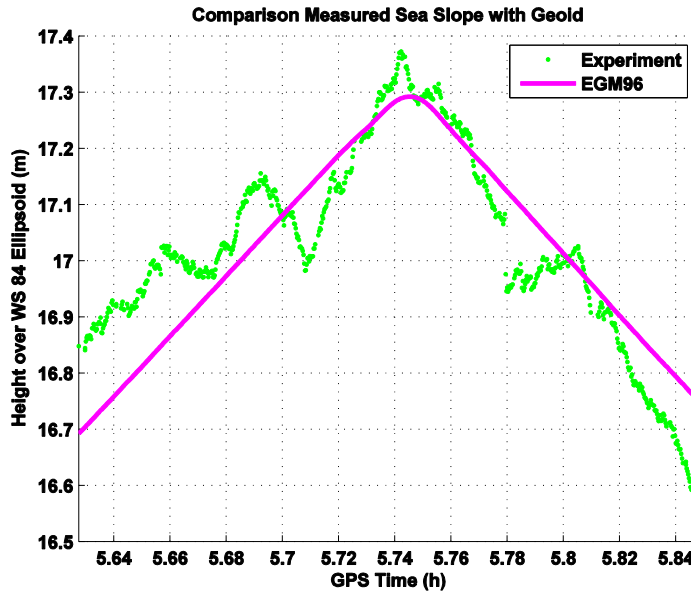


Fig. 7.9. Analysis of the capability of the proposed technique to detect geoid undulation changes: $h = 3,000$ m, θ_e from 82° to 84° , GPS Time from 5.6 h to 5.8 h, $v_{\text{aircraft}} = 237$ km/h.

7.5 Summary and conclusions

This work has first described the conventional GNSS-R technique and the altimetric tracking point employed in the frame of this work has been identified. Then, the height precision model generally accepted by the community has been demonstrated to diverge from experimental results away from the zenith. From this evidence, it can be concluded that future work is needed to develop a valid model which would allow a correct prediction of the performance of GNSS-R systems in a space-borne scenario.

Next, the scenario, the parameters in the two air-borne experiments, the procedure and assumptions used have been presented. In the first experiment, during the flight over the open sea (rough surface) at $h = 500$ m, with satellites at elevation angles from 73° to 76° , the achieved height precision was 2.82 m for 1 s, and 17 cm for 100 s of incoherent averaging time. These results show a greater impact of the sea state than the elevation angle range, since in the first part, at just 1 s of averaging, the height precision is lower despite the large elevation angles. Nonetheless, the height precision after 100 s of averaging is better in the first part because the larger glistening zone due to the higher flight altitude. During the second experiment the flight altitude was fixed at $h = 3,000$ m. Two different elevation angle ranges were selected to analyze its impact on the achievable height precision, in case of same sea state conditions and platform altitude. The height precision was 1.8 m for 1 s, and 6 cm for 100 s of averaging, for satellites at elevation angles from 66° to 85° . However, in case of satellites at elevation angles ranging from 70° to 77° the achieved height precision was 3.25 m for 1 s and 33 cm for 100 s of incoherent averaging time. From these results, it can be concluded that the impact of a 4° lower elevation angle (66° vs 70°) is compensated by a 8° higher maximum elevation angle (77° to 85°), which shows the large impact of the elevation angle on the GNSS-R precision performance. All experiments have used a coherent integration time of $T_c = 1$ ms.

After the achievable height precision analysis, some considerations related to the accuracy have been exposed. If elevation angle of $\theta_e = 50^\circ$ is required to ensure the feasibility of the SSH measurements. Then, the capability of the conventional GNSS-R technique to analyze the effect of currents on the sea topography has been compared with traditional radar altimetry by means of analyzing the Sea Level Anomaly (SLA).

The results from both measurement systems demonstrate a similar trend with a rms of the Relative Mean Dynamic Topography (RMDT) difference of 48 cm for the first flight, and 198 cm for the second flight. Additionally it has been proved that the measured Sea Surface Height (SSH) follows the theoretical one of the geoid. Therefore, the performance of this technique for ocean altimetry validates the feasibility to measure SSH, and its changes, with the required precision and accuracy.

8

8. ESA BEXUS 17: CROSS-POLAR L1 C/A GPS SIGNALS

8.1 Introduction

Newer applications of GNSS-R include wind speed measurements [55, 70], ice altimetry [115], soil moisture and vegetation determination [116]. Several experiments have been carried out to analyze the performance of different GNSS-R techniques: conventional cGNSS-R (GPS L1 CA) (e.g. [56]), interferometric iGNSS-R (GPS L1 CA, P(Y) and M) [69], and reconstructed-code rGNSS-R (GPS L1&L2 P(Y)) [83].

The potential of GNSS-R to provide soil moisture measurements over land was first assessed in 2000 [117]. As compared to GPS reflections over the ocean the main differences identified are in the spatial and temporal variability of the soil dielectric constant, the surface roughness, and the vegetation cover. Over land, the width of the correlated waveform (WF) is much narrower than over the ocean surface, and the variability of the moisture is clearly manifested in the peak power of the WF [117]. In 2008, the multipath signal collected by geodetic GPS receivers was used to infer soil moisture information from the fluctuations of the Signal-to-Noise Ratio (SNR) [118]. In 2009, the Interference Pattern Technique (IPT) was proposed [119] for soil moisture measurements using linear polarization antennas pointing towards the horizontal direction so as to increase the amplitude of the signal that is being degraded by fading noise. Then, the IPT was proposed for vegetation height retrieval [120]. In 2012, a similar technique as [118] was proposed [121] to infer vegetation growth. The retrieval method relied on amplitude changes. In 2009, field experiment results showed the capabilities of GNSS-R polarimetric observations as a remote sensing tool for agricultural applications from ground-based receivers [122, 123] and a simulator was developed to interpret these results [124]. The framework to analyze the coherent scattering over soil was established by Fung and Eom [125], and the scattering as a function on the antenna beamwidth, the incident and scattering angles, and the distance from the antenna to the target was evaluated in [126].

In July 2014 Surrey Satellite Technology Ltd. SSTL's TechDemoSat-1 mission was successfully launched [127]. In addition, at least other four space-borne missions are currently approved or "under-study": National Aeronautics and Space Agency NASA's Cyclone Global Navigation Satellite System (CyGNSS) [48], European

Space Agency ESA's GNSS rEfectometry, Radio Occultation and Scatterometry on-board International Space Station (GEROS-ISS) [128], ESA's PAssive Reflectometry and Interferometry System In-Orbit Demonstrator (PARIS-IoD) [3], and ³Cat-2 [129].

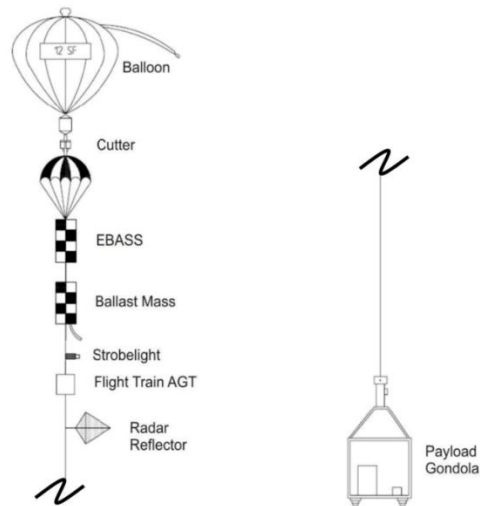
This work presents the results of an experiment carried out in the DLR-SNSB sponsored BEXUS 17 stratospheric balloon over boreal forests North of Sweden on October 10th 2013, as a proof-of-concept of the payload of the ³Cat-2 mission [129]. Section 8.1 describes the experimental set-up. Section 8.2 presents the study of the scattered electromagnetic fields over the boreal forests using experimental data. Section 8.3 analyses the total scattered field. Finally, Section 8.4 summarizes the main results of this study.

8.2 Experimental set-up

The Balloon EXperiments for University Students (BEXUS) program is implemented under a bilateral agency agreement between the German Aerospace Center (DLR) and the Swedish National Space Board (SNSB). The BEXUS 17 stratospheric balloon (Figs. 8.1a,b) launch campaign took place in Esrange Space Center from October 4th to 14th 2013. The launch took place on October 10th at 16 h (Global Positioning System GPS Time), and the flight duration was 6 hours with an apogee of ~ 27,000 m (Fig. 8.2). The trajectory was a single track (Fig. 8.3) from Esrange Space Center (Sweden) to Juujarvi (Finland).



a)



b)

Fig. 8.1. (a) BEXUS stratospheric balloon during take-off at Esrange Space Center. (b) Typical BEXUS configuration: 12,000 m³ balloon, valve, cutter, parachute, Esrange Balloon Service System (EBASS), flight train, Argos GPS and Air Traffic Control (ATC) Transponder (AGT), strobe light, radar reflector, and gondola. Total length of the system is up to 75 m [130].

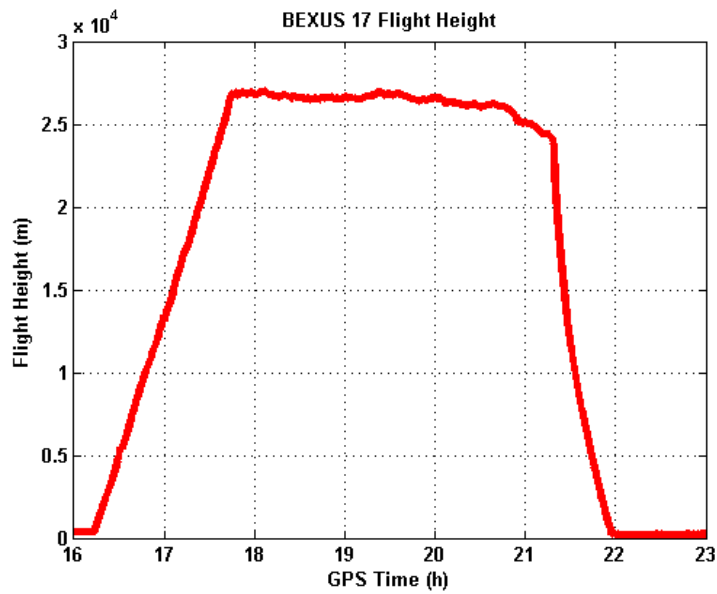


Fig. 8.2. Flight height during the experiment as a function of the GPS Time (10 10 2013).

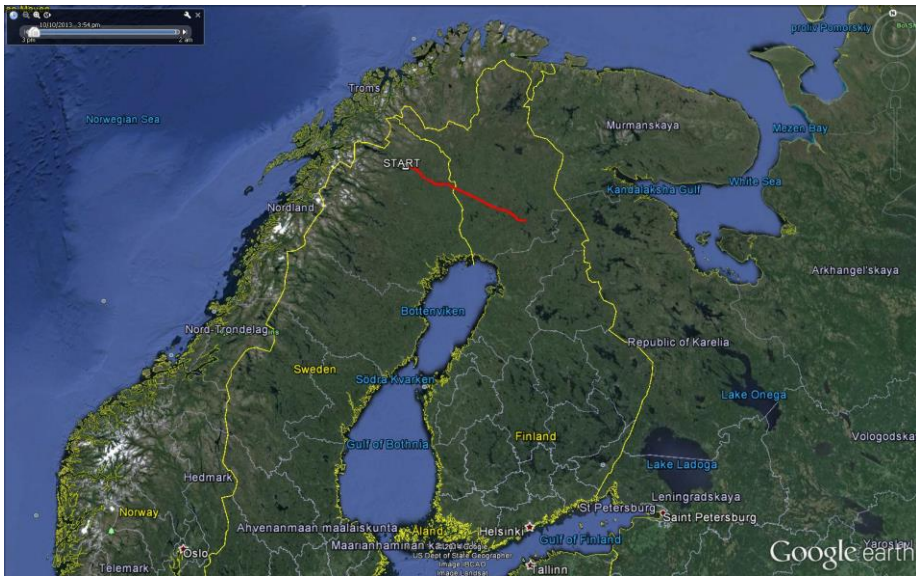


Fig. 8.3. The track of the BEXUS 17 during the experiment. The trajectory was a single track from Esrange Space Center (latitude $67^{\circ} 53'N$, longitude $21^{\circ} 04'E$) to Juujarvi (latitude $66^{\circ} 24' N$, longitude $27^{\circ} 18' E$).

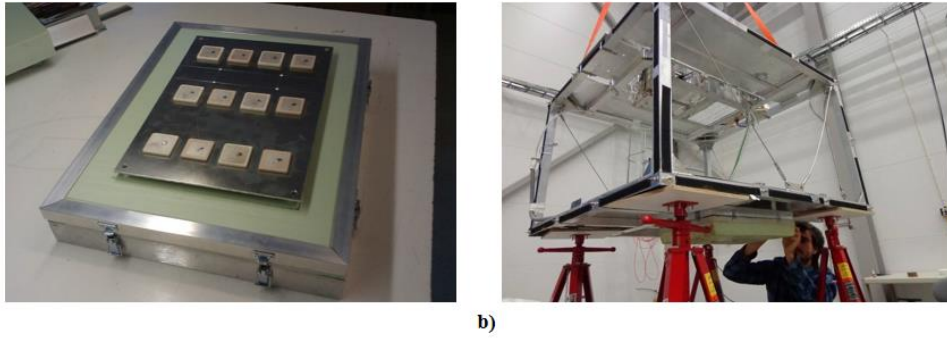


Fig. 8.4. (a) Nadir-looking antenna inside the thermally insulating radome. (b) Image of the thermally insulating radome at the bottom of the gondola.

The experimental set-up was composed of the PYCARO reflectometer (P(Y) & C/A ReflectOmeter) [72], a zenith-looking omnidirectional dual-band (L1, L2) Right Hand Circular Polarized (RHCP) antenna patch to collect the direct GPS signals, a Left Hand Circular Polarized (LHCP) nadir-looking dual-band (L1, L2) antenna array to collect the Earth-reflected signals (Figs. 8.4a,b), three batteries providing up to 100 Wh at low temperatures inside the gondola down to -40°C , and an On Board Computer (OBC) for the experiment management. The nadir-looking antenna was composed of two interleaved arrays (L1 and L2) of 6 elementary antenna patches each. The total gain of the antenna was 13 dB at L1, and 11 dB at L2. The Command and Data Handling System (CDHS) was composed of a Programmable Intelligent Computer (PIC) for housekeeping and scientific data management, communications with the ground station, and data storage in a micro-Secure Digital (SD) card. The collected data were registered in two internal SD memories (PYCARO and microcontroller), and simultaneously they were sent to the ground segment via the E-Link system [130].

8.3 First experimental evaluation of the reflected signals over boreal forests

When an electromagnetic wave impinges from above upon the boundary surface between two semi-infinite media, a portion of the incident energy is scattered towards the upper medium and the rest is transmitted forward into the lower medium [35, pp.

846]. If the lower medium is homogenous the problem in question is a surface-scattering problem. On the other hand, if the lower medium is inhomogeneous (i.e. a mixture of materials of different dielectric properties), the scattering takes place within the volume of the lower medium, and it is referred as volume scattering. Since volume scattering is caused mainly by dielectric discontinuities within a volume and, in general, the spatial locations of discontinuities are random, the scattered waves are expected to be within the volume in all directions. The surface scattering strength is proportional to the relative complex dielectric constant of the lower medium, and the surface roughness. The volume scattering strength is proportional to the dielectric discontinuities inside the medium and the density of the embedded discontinuities, the average dielectric constant of the medium and the geometric size of the inhomogeneities relatives to the incident wavelength.

Forests are perfect examples of volume scattering with scattering elements bounded by the air at the top, and by the soil surface at the bottom. The forward scattering coefficient is governed by the scattering properties of the vegetation elements and the soil surface, as well as the interaction between the canopy and the soil, and the soil with the trunk [35, pp. 863; 40]. Several models describing the backscattering of electromagnetic waves over vegetated surfaces exist: from simple 3-layer models, to models including a continuous medium and a discrete medium characterized by scatterers (e.g. [131]). However, few studies have been performed to evaluate the forward scattering coefficient at L-band and at circular polarization. In the case of GNSS-R bistatic reflections over forest area, a scattering model considering of both the coherent and incoherent fields was proposed [132]. This model predicts the coherent field as the result of the electromagnetic interactions of the GPS signals with the soil, only, attenuated by the vegetation canopy above it. Recently, experimental data over forest biomass from 100 ton/ha to 350 t/ha have been published [133]. As predicted in [132], a lower value of the coherent soil-reflectivity is found for larger vegetation density.

The reflectivity $\Gamma_{\text{RHCP-LHCP}}^{\text{coh}}$ can be estimated as the ratio of the reflected $Y_{\text{r}}^{\text{LHCP}}$ and direct $Y_{\text{d}}^{\text{RHCP}}$ power waveform's peaks, after proper compensation of the noise power floor:

$$\Gamma_{\text{RHCP-LHCP}}^{\text{coh}} = \frac{|\langle \mathbf{Y}_r^{\text{LHCP}} \rangle|^2}{|\langle \mathbf{Y}_d^{\text{RHCP}} \rangle|^2}. \quad (8.1)$$

In Eqn. (8.1), superscripts RHCP and LHCP denote the incident polarization (Right Hand Circular Polarization), and the scattered polarization (Left Hand Circular Polarization), respectively.

The scattering of GNSS signals is originated in an area around the nominal specular point. In general, the scattered field contains both a coherent and an incoherent component in different proportions. The coherent scattering area is limited to the first Fresnel zone. On the other side, the incoherent scattering which is also centered on the nominal specular direction, is limited by an area (glistening zone) much larger than the first Fresnel zone. The incoherent power component is eliminated in the estimation of the reflectivity in Eqn. (8.1) by subtracting to each incoherently averaged waveform's peak the amplitude variance of the complex waveforms' peaks $\sigma_{|\mathbf{Y}_r^{\text{LHCP}}|}^2$ [97, pp. 125]:

$$|\langle \mathbf{Y}_r^{\text{LHCP}} \rangle|^2 = \langle |\mathbf{Y}_r^{\text{LHCP}}|^2 \rangle - \sigma_{|\mathbf{Y}_r^{\text{LHCP}}|}^2. \quad (8.2)$$

Therefore, reflectivity values are associated to the first Fresnel zone. The semi-major axis of the first Fresnel zone r_a from which the coherent reflections are coming, from a flight height of $h \sim 27,000$ m, and for the L1 signal is [93]:

$$r_a = \sqrt{\lambda h / \sin \theta_e + \left(\lambda / 2 \sin \theta_e \right)^2} / \sin \theta_e = 78 \text{ m}, \quad (8.3)$$

where λ is the signal's electromagnetic wavelength, and θ_e is the elevation angle. The diameter of the antenna footprint varied from 1.4 km to 40 km respectively for a flight height from 1,000 m to 27,000 m. Since it is much larger than the size of the first Fresnel zone different reflectivity values were simultaneously measured corresponding to different satellites (different Fresnel zones within the antenna footprint).

In this work, the bistatic coherent reflectivity $\Gamma_{\text{RHCP-LHCP}}^{\text{coh}}$ of boreal forests is experimentally evaluated for the first time to author's knowledge. When analyzing this problem it has to be taken into account that the reflected GNSS signal is significantly strong around the specular direction only, and the power density rapidly

decreases away from it [132]. In [132] the coherent scattering is assumed to come only from the reflected signals over the soil, attenuated by the vegetation canopy. On the other hand, incoherent scattering includes volume scattering from leaves and branches, double bouncing due to the soil and trunk interactions, multiple interactions between vegetation elements, and between the vegetation and the soil, and incoherent scattering from the soil attenuated by the overlapping vegetation canopy. However, coherent effects may appear because the distance between scatterers is comparable to the electromagnetic wavelength [35, pp. 827].

The TORMES (TOpography from Reflectometric Measurements: an Experiment from the Stratosphere) stratospheric experiment was performed North of Sweden from the Esrange Space Center (latitude $67^{\circ} 53' \text{N}$, longitude $21^{\circ} 04' \text{E}$) to Juujarvi (latitude $66^{\circ} 24' \text{N}$, longitude $27^{\circ} 18' \text{E}$). The GPS space segment is divided into six orbital planes with an inclination of $\sim 55^{\circ}$. As a consequence, GNSS-R acquisitions were performed with a maximum elevation angle around 75° , and an average of 5 GPS satellites' could be tracked simultaneously during 3 h each. The PYCARO reflectometer [72, 83] was configured to use the C/A GPS code during this experiment. It measured the direct and the reflected waveforms using a coherent integration time of $T_c = 20$ ms, and an incoherent averaging of $N_{\text{inc}} = 10$ samples. These default parameters were implemented in the automatic mode of the OBDH subsystem, since during the experiment preparation activities it was determined that the Signal-to-Noise Ratio (SNR) increases as a function of the coherent integration time up to 13 dB using $T_c = 20$ ms, as compared to $T_c = 1$ ms. The selection of the number of incoherent averaging samples was a trade-off between the spatial resolution and the noise filtering. To mitigate the effect of noise, incoherent averaging of consecutive uncorrelated signals must be performed. However, the larger the number of incoherently averaged complex waveforms, the lower the spatial resolution. In this experiment, the spatial resolution was very slightly degraded because the low speed of the balloon. Unfortunately, just after take-off the BEXUS E-Link failed and the experiment was operated autonomously during all the flight. As a first step, the 20 ms coherently integrated waveforms (WF) were computed on-board. The reflected GPS signals were multiplied by a locally generated carrier signal and with a 90° phase-shifted signal to generate respectively the in-phase and quadrature components. Then, the Fourier transform of the complex input signal were multiplied with the Fourier

transform of the transmitted Pseudo-Random Noise (PRN) code. The result of the multiplication was transformed into the time domain by an inverse Fourier transform. The WF's were properly aligned to compensate for the GPS satellites motion [134]. Then, they were incoherently averaged ($N_{inc} = 10$) to reduce the effect of the noise.

The PYCARO reflectometer [72, 83] was configured to track the correlation peak of each temporal measurement during this experiment. After the flight, during data processing, the reflection coefficients were computed applying Eqn. 8.1 to the temporal series of data provided by the reflectometer. The temporal evolution of the coherent reflectivity at a flight height of $h \sim 27,000$ m is represented in Fig. 8.5 as a function of the elevation angle θ_e , after compensating for the antenna pattern gain. It can be observed that, as expected, the higher the elevation angles (closer to zenith), the lower values of coherent reflectivity [35, pp.1008].

The boreal forest is characterized by coniferous forests consisting mostly of pines, spruces, and larches. Boreal forests can be described using allometric relationships [135]. In the following, ground truth data, and data provided by air-borne lidar are included as additional information along this work [135]. In Figure 8.6a height vs. biomass from ground measurement plots are shown. The measurements for the two test sites, Krycklan (latitude $64^\circ 10'N$, longitude $20^\circ 01'E$) in green, and Remningstorp (latitude $58^\circ 25'N$, longitude $13^\circ 14'E$) in blue, show a high correlation ($R^2 = 0.75$) and both follow the same allometric relationships [135]:

$$Q = 0.25h_{forest}^2, \quad (8.4)$$

here Q is the biomass [t/ha], and h_{forest} the forest height [m].

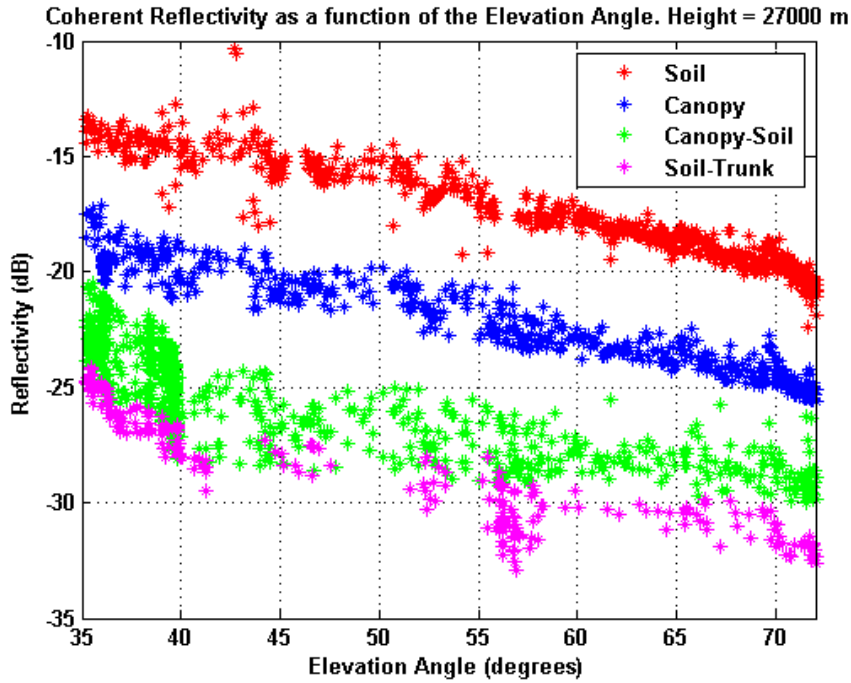


Fig. 8.5. Evolution of the coherent reflectivity over the different scattering contributing media of the forest (soil, canopy, canopy-soil, and soil-trunk) as a function of the elevation angle at a flight height of $h \sim 27,000$ m.

Figure 8.6b shows the height-to-biomass relationship derived from air-borne lidar data for the test site Krycklan. It follows the same allometric relationship as for the ground measurements. Using data provided by NASA (Fig. 8.7), an estimation of the biomass for Krycklan using Eqn. 8.4 is ~ 100 t/ha.

The multi-modal behaviour shown in Fig. 8.5 suggests that the coherent scattering may take place in differentiated scattering media with different scattering properties.

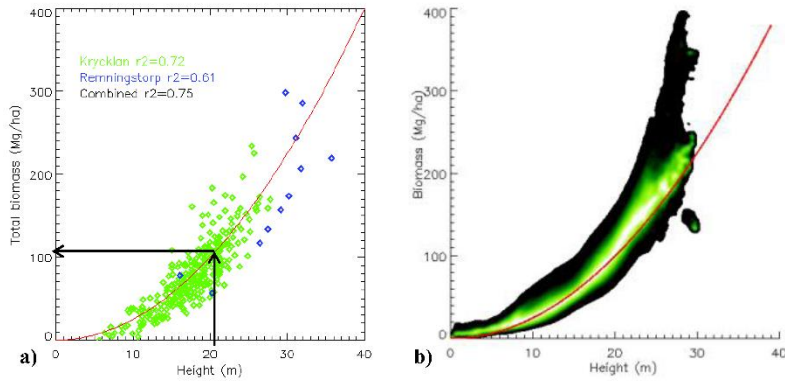


Fig. 8.6. (a) Ground truth plots in Krycklan (green) and Remningstorp (blue). (b) Krycklan site for airborne lidar height vs. air-borne lidar-derived biomass [135].

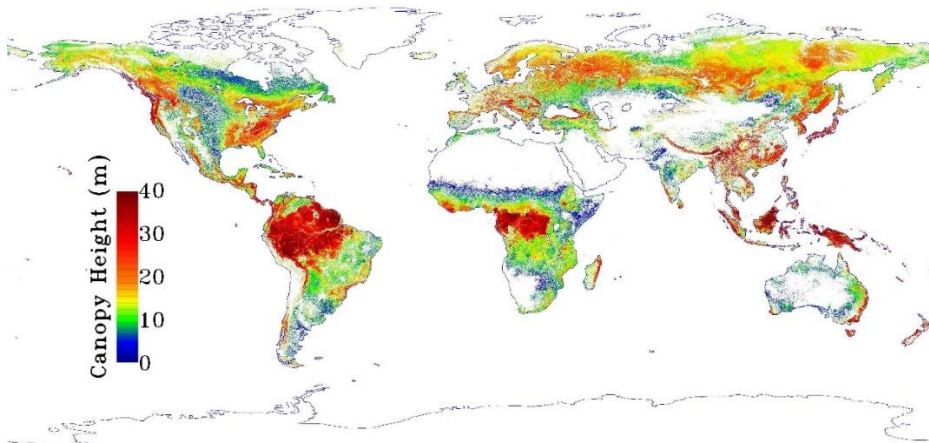


Fig. 8.7. Global map of forest height produced from NASA's ICESAT/GLAS, MODIS, and TRMM sensors [136].

The fluctuations of the coherent reflectivity as derived from the peak of the WF follow four different trends, each one with different levels and relative variations of the reflectivity. Forests are characterized by random variations of the dielectric properties. Different scattering media²⁸ (soil, trunks, branches, leaves) each one with a particular dielectric properties may lead to different reflected power levels of the signals.

²⁸ The terrain type on the flight path was inspected by the authors during a car travel. Actually, Fig. 8.8 shows four-shots of the main scattering type scenarios found in the flight path. These four scenarios appear alternatively on the path.

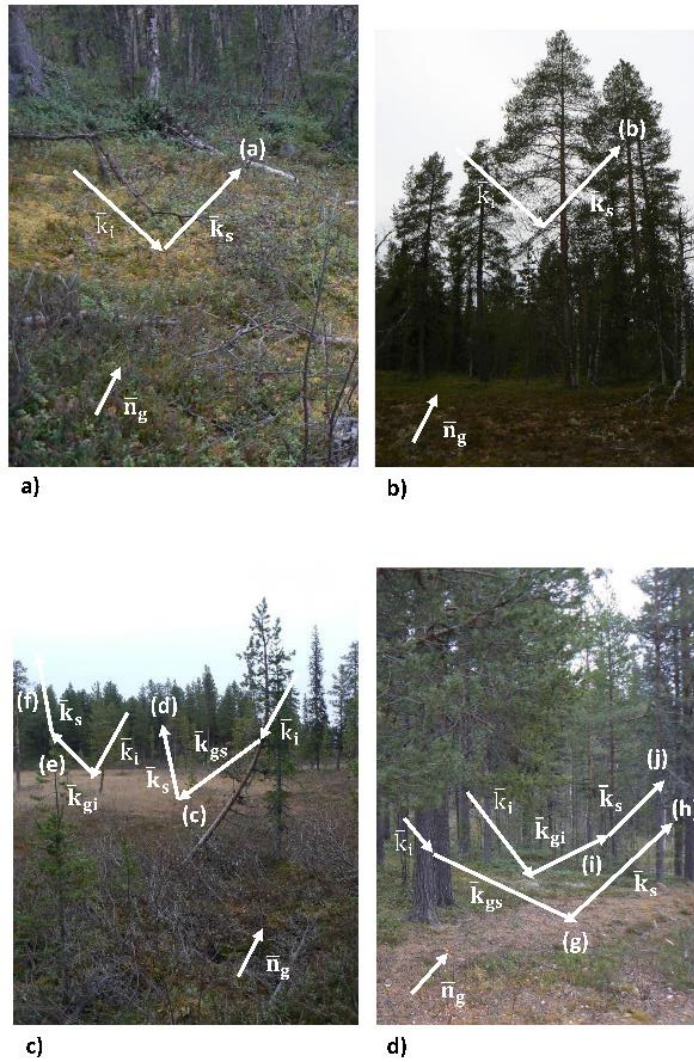


Fig. 8.8. (a) Scattering over the ground surface, (b) direct scattering over the canopy, (c) multiple scattering involving both the soil and the canopy, and (d) multiple scattering involving both the soil and the trunks.

As a consequence of: a) the small size of the coherent scattering area (limited by the first Fresnel zone), b) the different dielectric properties of the forest elements, c) the different levels of signal attenuation due to multiple reflections and the different heights of the scatterers, and d) Wu and Jin [41] suggested that forward scattering of GNSS signals takes place not only over the soil, but also over trees in a multimodal

behaviour, we hypothesize that the different scattering mechanisms are dominating sequentially (Fig. 6.5) over the: Soil (red), and the canopy (blue), and the canopy-soil (green) and the soil-trunk (pink) interactions. This result indicates that coherent scattering is also taking place in the canopy and trunks. Depending upon the vegetation-cover fraction the scattered power may be composed of several contributions. Direct scattering from the soil (Fig. 8.8a) and the canopy (Fig. 8.8b), as well as multiple scattering involving both the soil and the canopy (Fig. 8.8c), and both trunks and the soil (Fig. 8.8d).

Each incoherently averaged WF was composed of several correlation peaks. PYCARO was configured to track the highest peak of each WF. The scattering over the canopy in a multi-modal behaviour produces reflected signals with different delays. Additionally, note that the effect of the topography can produce coherent scattering (under specular condition) from areas (several first Fresnel zones) that do not correspond to the smaller geometric delay. Thus, only the scattering mechanism with the highest power contribution to the total scattered field can be identified at each individual waveform ($T_c = 20$ ms and $N_{inc} = 10$). In addition, the histogram corresponding to the total scattered field over boreal forests at a flight height of $h \sim 27,000$ m and for high elevation angles in the range $\theta_e = [35^\circ, 72^\circ]$ is represented in Fig. 8.9 where four amplitude distributions can be identified depending on the level of coherence of the reflected signal during the flight. These distributions are obtained taking into account the four different types of scattering mechanisms (soil, canopy, canopy-soil, and soil-trunk) considered along this section.

The amount of the coherent reflected power $P_{RHCP-LHCP}^{coh}$ can be obtained applying Eqn. 8.5 with the antennas separated by a distance $R = R_t + R_r$ [126, 137]:

$$P_{RHCP-LHCP}^{coh} = \Gamma_{RHCP-LHCP}^{coh} \frac{P_t \lambda^2 G_t G_r}{(4\pi)^2 (R_t + R_r)^2}, \quad (8.5)$$

where P_t is the power emitted by the GPS satellites, G_t is the gain of the transmitting antenna, G_r is the gain of the receiving antenna.

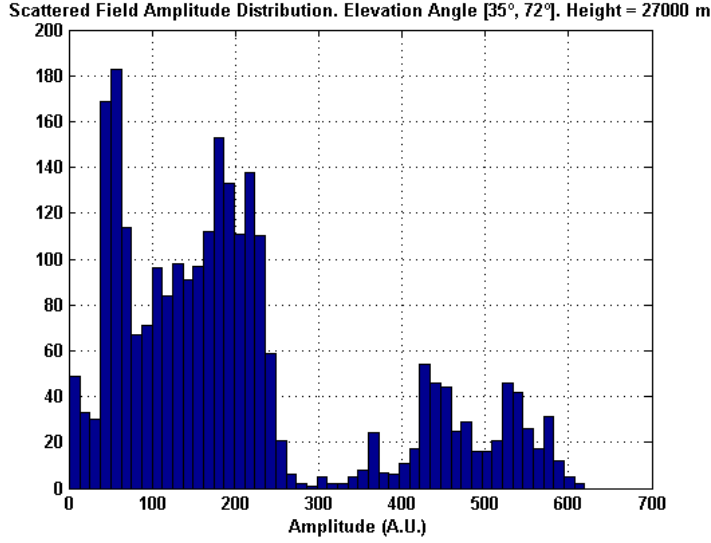


Fig. 8.9. Total scattered field (over boreal forests) amplitude distribution histogram at a flight height of $h \sim 27,000$ m and for an elevation angle in the range $\theta_e = [35^\circ, 72^\circ]$. There are four main peaks (larger number of samples at these four identified amplitude levels): ~ 50 , ~ 190 , ~ 420 , ~ 520 (A.U.).

Since $R_t \gg R_r$, the reflected coherent power is approximately constant:

$$P_{\text{RHCP-LHCP}}^{\text{coh}} \approx \Gamma_{\text{RHCP-LHCP}}^{\text{coh}} \frac{P_t \lambda^2 G_t G_r}{(4\pi)^2 (R_t)^2}. \quad (8.6)$$

On the other hand, the incoherent power can be theoretically described as [124]:

$$P_{\text{RHCP-LHCP}}^{\text{incoh}} = \frac{P_t \lambda^2 T_c^2}{(4\pi)^3} \iint \frac{G_t G_r \Lambda^2(\delta\tau) S^2(\delta f)}{(R_t)^2 (R_r)^2} \sigma_{\text{ri}}^0 dA, \quad (8.7)$$

where Λ is the autocorrelation function of the C/A GPS code, S is the Sinc-exponential function, $\delta\tau$ and δf are the differences between the sampled time delay τ or sampled frequency f , and a reference delay and Doppler frequency, σ_{ri}^0 is the incoherent bistatic radar scattering coefficient, and A is the integration area. The scattered signal may be Doppler-limited if the Doppler filter corresponding to a high coherent integration time up to $T_c = 20$ m is smaller than the first C/A chip size. An analysis has been performed for different elevation angles in the range $\theta_e = [45^\circ, 75^\circ]$ and for different platform heights in the range $h = [1,000, 27,000]$ m using the PAU/PARIS End-to-End Performance Simulator (PEPS). Results show (Fig. 8. 10) that there is only Doppler bandwidth effects for a flight height $h \sim 1,000$ m (Figs.

8.10a,b). For the flight conditions ($h \sim 27,000$ m and scattering over land surfaces) the Earth region contributing to the incoherent component is the first chip iso-delay ellipse which is a function of the autocorrelation function of the different GNSS codes. However, in the case of ocean scattering the spreading of the signal over the surface includes many chips. The area of the first iso-delay ellipse is equal to [96]:

$$A = \pi ab = \frac{2c\tau\pi R_r}{(\sin \theta_e)^2}, \quad (8.8)$$

where a and b are respectively the semi-major and semi-minor axis of the first iso-delay ellipse, c is the speed of light and τ is the chip size of the PRN [96]. Therefore the incoherent reflected power is proportional to $\sim 1/R_r$ vs. the coherent scattering that can be theoretically modelled independently of R_r (Eqn. 8.6). Figure 8.11 shows that the evolution the reflected power as a function of the flight height in the range from $h = 0$ to $h = 20,000$ m is roughly constant for the range of heights involved, since the coherent integration time was set to be $T_c = 20$ ms to limit the incoherent scattering.

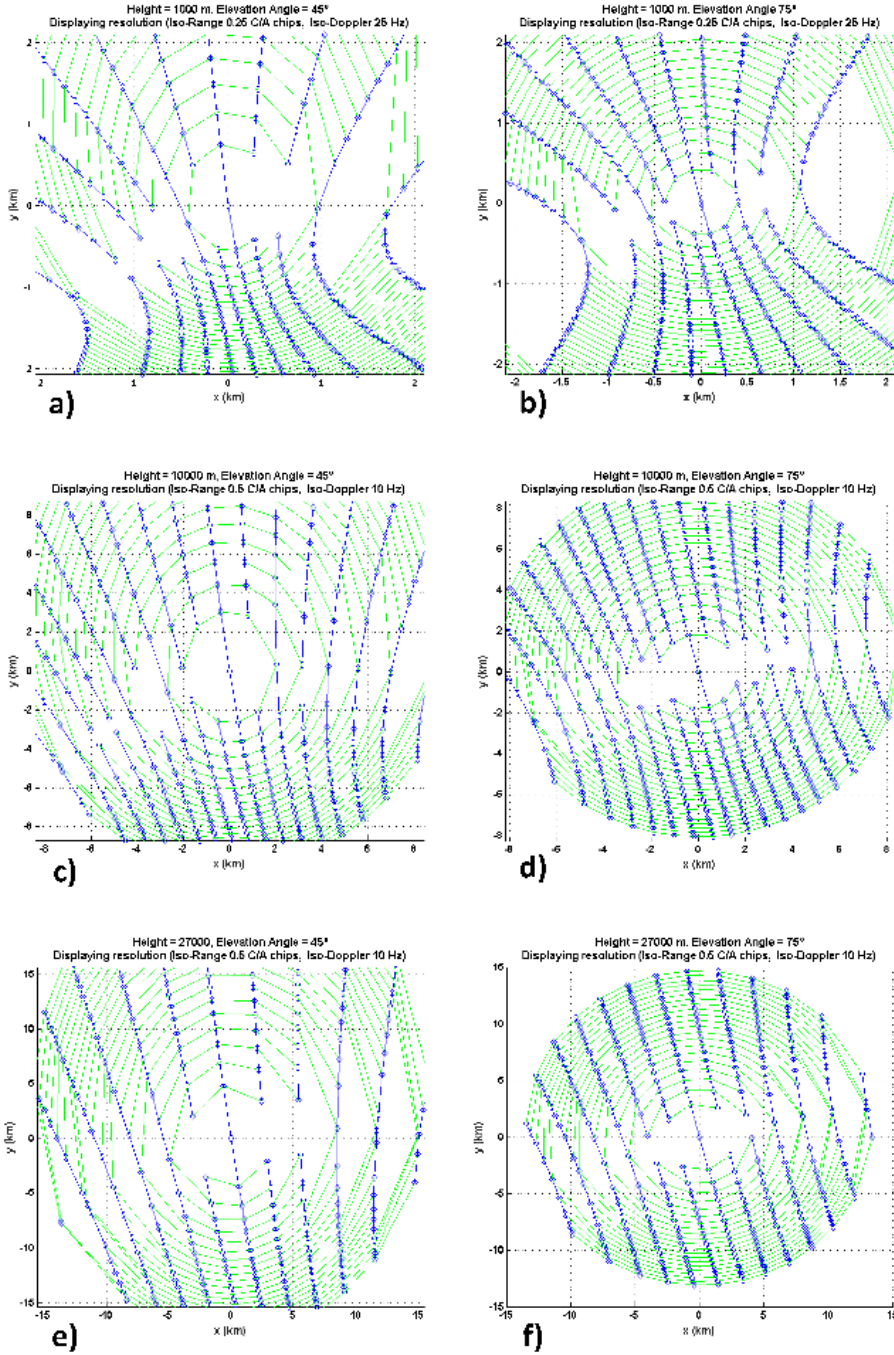


Fig. 8.10. Sample iso-range (green-lines) and iso-Doppler (blue-lines) lines for different flight conditions: a) $h = 1,000$ m and $\theta_e = 45^\circ$, b) $h = 1,000$ m and $\theta_e = 75^\circ$, c) $h = 10,000$ m and $\theta_e = 45^\circ$, d) $h = 10,000$ m and $\theta_e = 75^\circ$, e) $h = 27,000$ m and $\theta_e = 45^\circ$, f) $h = 27,000$ m and $\theta_e = 75^\circ$. Results using the PAU/PARIS End-to-End Performance Simulator (PEPS): Credits by H. Park et al.

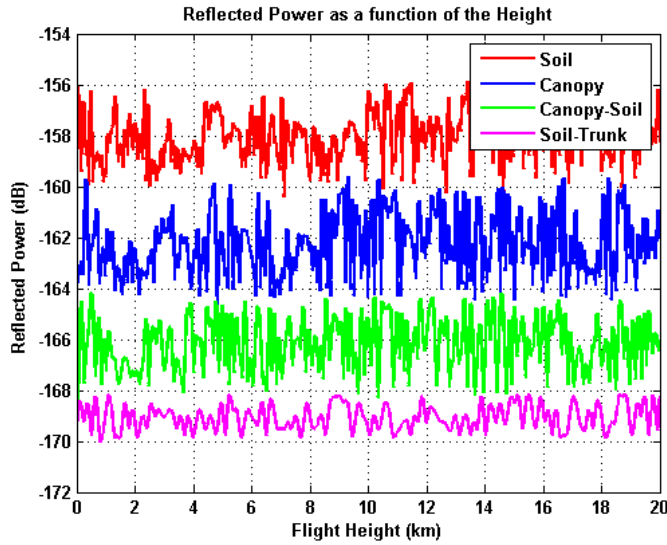


Fig. 8.11. Reflected power evolution as a function of the time, expressed as flight height during the ascending path, and the scattering media: soil, canopy, canopy-soil, and soil-trunk. This figure was derived using the highest peak of the WFs and it shows that the total reflected power is dominated by the coherent component since the evolution is roughly constant as a function of the flight height. Note that the variation of the elevation angle is low since the corresponding satellite is in the region around its maximum elevation angle. This situation is different to that in Fig. 8.9. In there, the variation of the elevation angle is high so that there are large variations of the reflected power.

8.4 First analysis of the total scattered field

In Section 8.3, the reflectivity was analyzed considering the temporal evolution of the scattered signals, finding out just from power considerations that there was a strong coherent component. Now, using the in-phase and the quadrature components, the total scattered field is analyzed. The total scattered field of this configuration of scatterers (~ 15 min long each data set over boreal forest) can be described as a vector sum in the complex plane of the temporal measurements provided by PYCARO. The coherent vs. incoherent scattering analysis is performed using the complete data sets of 15 min each. Instantaneously, during each coherent integration time, the reflected signals are highly coherent [72, 83] and PYCARO was able to track the phase (of the coherent component) of the reflected signal because the coherent integration time was set to be very high $T_c = 20$ ms to limit the incoherent scattering. However, when the complete temporal series of data is taken into account, the resulting reflected signal

(sum of the instantaneous signal vectors) is composed of both, a coherent and incoherent component. The contribution of the four different types of scattering mechanisms (soil, canopy, canopy-soil, and soil-trunk) to the total scattered field are equally distributed in the same region of the complex plane (Fig. 8.12). Figures 8.12a,b,c show the total scattered complex field distribution for three different flight height ranges $h = [0, 5,000]$ m, $h = [20,000, 25,000]$ m and $h \sim 27,000$ m for mid-low elevation angles respectively, and Figs. 8.12d,e,f for high elevation angles. If the scattered complex field described a circle centered around (0, 0), the scattering²⁹ would be completely incoherent. However, the scattered field is displaced from the origin³⁰ by a value α (equal to the mean of the amplitude distribution). The relative weight of the coherent to the incoherent components is quantified by the following parameter B^2 as defined in Section 6.3.3 [97, pp. 126]. Note that B tends to ∞ for a totally coherent field, and it is equal to 0 for a totally incoherent field. The evolution of this parameter for each type of scattering element is represented as a function of the flight height in Fig. 8.13a for high elevation angles in the range $\theta_e = [60^\circ, 70^\circ]$, and in Fig. 8.13b for low elevation angles in the range $\theta_e = [25^\circ, 45^\circ]$, showing that the relative weight is roughly independent of the flight height for a re-constructed scattered field corresponding to an along-track³¹ of ~ 25 km.

The coherent and the incoherent components of the re-constructed field (25,000 m along-track) tend to increase with the flight height (Table 8.1) because the larger noise of the received signals (Fig. 8.12) due to the attitude oscillations of the gondola during the take off. At a flight height in the range $[20,000, 25,000]$ m the scattering area is larger (Table 8.1) which partially mitigates these oscillations, but also note that during this part of the flight the trajectory was much stable being totally stable during the

²⁹ In a general case, the resulting scattered field can be described as the sum of a constant vector and a Hoyt vector which is defined as 2-D Gaussian distribution with mean value zero and variances s_1 and s_2 [97, pp.125].

³⁰ There are two regions displaced $\pm\alpha$ from the center because the phase changes due to the navigation bit changes sign.

³¹ The horizontal speed of the balloon was approximately 100 km/h and the duration of the data set 15 min each.

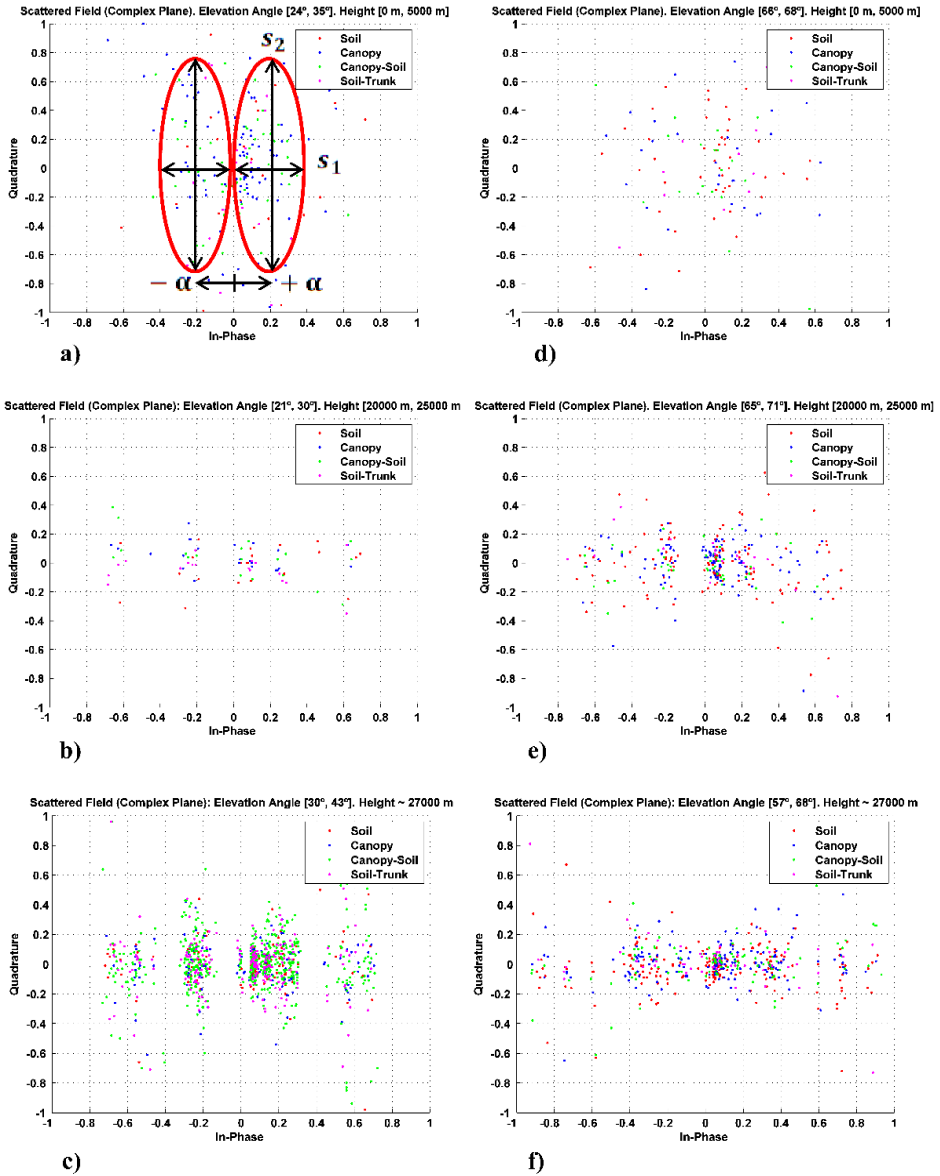


Fig. 8.12. (a) Scattered field complex plane representation for a flight height $h = [0, 5000]$ m, and an elevation angle in the range $\theta_e = [24^\circ, 35^\circ]$. (b) Scattered field complex plane representation for a flight height $h = [20,000, 25,000]$ m, and an elevation angle in the range $\theta_e = [21^\circ, 30^\circ]$. (c) Scattered field complex plane representation for a flight height $h \sim 27,000$ m, and an elevation angle in the range $\theta_e = [30^\circ, 43^\circ]$. (d) Scattered field complex plane representation for a flight height $h = [0, 5000]$ m, and an elevation angle in the range $\theta_e = [66^\circ, 68^\circ]$. (e) Scattered field complex plane representation for a flight height $h = [20,000, 25,000]$ m, and an elevation angle in the range $\theta_e = [65^\circ, 71^\circ]$. (f) Scattered field complex plane representation for a flight height $h \sim 27,000$ m, and an elevation angle in the range $\theta_e = [57^\circ, 68^\circ]$.

Table 8.1. Amount of coherent scattering and incoherent scattering, asymmetry factor and residual phase std. deviation over soil, canopy, canopy-soil, and soil-trunk as a function of the flight height and the elevation angle.

	Cluster 1 (red)	Cluster 2 (blue)	Cluster 3 (green)	Cluster 4 (pink)
h = [0, 5,000] m, $\theta_e = [65^\circ, 70^\circ]$				
Coherent Scattering: α^2 (A.U.)	32,761	54,756	20,449	44,944
Incoherent Scattering: $s_1 + s_2$ (A.U.)	51,650	73,021	37,837	58,642
Asymmetry Factor: $K = s_1 / s_2$	4.1	5.3	4.1	6.1
Residual Phase Std. (degrees)	24.7	14.4	22	8.8
h = [0, 5,000] m, $\theta_e = [30^\circ, 35^\circ]$				
Coherent Scattering: α^2 (A.U.)	43,264	33,124	29,929	49,729
Incoherent Scattering: $s_1 + s_2$ (A.U.)	73,021	52,432	44,234	81,917
Asymmetry Factor: $K = s_1 / s_2$	3.7	2.8	4.4	26
Residual Phase Std. (degrees)	18.7	25.5	18.9	2.8
h = [20,000, 25,000] m, $\theta_e = [65^\circ, 70^\circ]$				
Coherent Scattering: α^2 (A.U.)	34,969	41,616	33,856	29,929
Incoherent Scattering: $s_1 + s_2$ (A.U.)	56,813	67,796	58,685	46,369
Asymmetry Factor: $K = s_1 / s_2$	18.3	18.5	22	17.9
Residual Phase Std. (degrees)	9	12.4	15.7	8.4
h = [20,000, 25,000] m, $\theta_e = [30^\circ, 35^\circ]$				
Coherent Scattering: α^2 (A.U.)	54,756	45,639	33,124	75,076
Incoherent Scattering: $s_1 + s_2$ (A.U.)	86,557	72,410	121,248	107,648
Asymmetry Factor: $K = s_1 / s_2$	26.7	38.4	29	41
Residual Phase Std. (degrees)	6.6	13	5.4	1.6

float phase with an apogee of $\sim 27,000$ m. Note that this effect³² is only visible in the re-constructed field because during the coherent integration time the orientation of the gondola is practically frozen (Section 8.3). From Fig. 8.12, it is clear that the clusters

³² Flight data provided by SSC computed on-board the balloon. Vertical speed of the balloon during the float phase was smaller than 1 m/s.

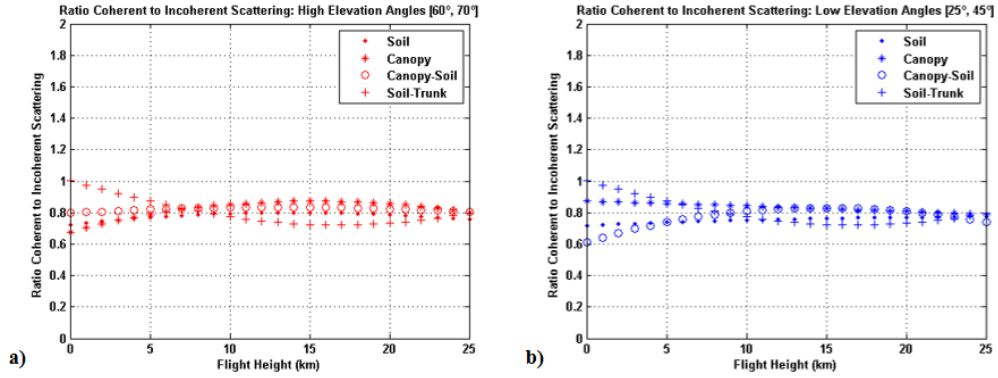


Fig. 8.13. (a) Evolution of the ratio of the coherent to incoherent scattering as a function of the flight height and for an elevation angle in the range $\theta_e = [60^\circ, 70^\circ]$. (b) Evolution of the weight of the coherent to incoherent scattering as a function of the flight height and for an elevation angle in the range $\theta_e = [25^\circ, 45^\circ]$.

of points are better defined in Figs. 8.12c,f than in Figs. 8.12a,d. This behavior is evaluated using the asymmetry factor defined as:

$$K = \frac{s_1}{s_2}. \quad (8.9)$$

It is observed that the asymmetry factor of each forest contribution increases with the flight height, being larger in case of low elevation angles (Table 8.1). It means that the phase is less noisier at a flight height of $h = [20,000, 25,000]$ m than in the range $h = [0, 5,000]$ m, which explains the clustered behavior (Figs. 8.12c,f). In particular, the asymmetry factor increment from the ascend to the float phase is in the range $K = [15, 35]$ A.U. for lower elevation angles, while for high elevation angles is in the range $K = [12, 18]$ A.U. (Table 8.1). The phase information is retrieved from the coherent component of the scattered field. Additionally, it can be stated that the effect of the amplitude noise is larger than the effect of the phase noise since the asymmetry factor is larger than 1 in all cases. The multi-modal behavior due to the scattering over different types of scatterers creates fluctuations in the amplitude of the signal, being larger than the phase noise.

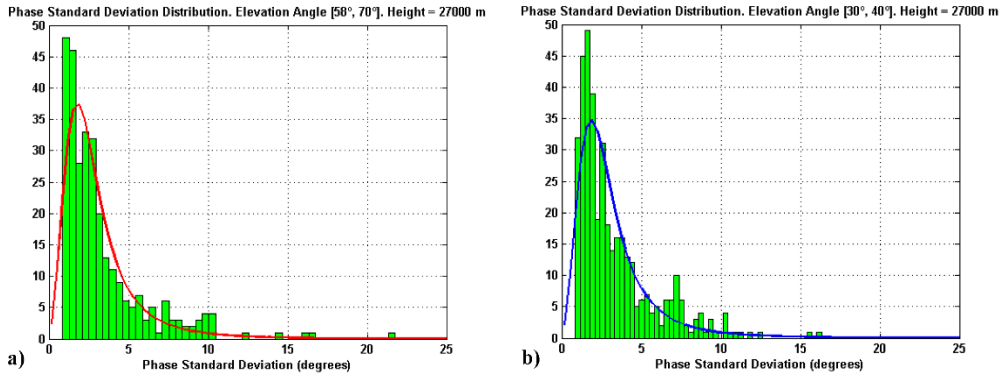


Fig. 8.14. (a) Carrier phase standard deviation distribution for a flight height of $h \sim 27,000$ m and an elevation angle $\theta_e = [58^\circ, 70^\circ]$. (b) Carrier phase standard deviation distribution for a flight height of $h \sim 27,000$ m and an elevation angle $\theta_e = [30^\circ, 40^\circ]$.

The distributions of the reflected WF peak phase ($T_c = 20$ ms, number of incoherent averaging samples $N_{inc} = 10$) as measured by PYCARO before the GPS signal is retracked are represented in Figs. 8.14a,b respectively for high and mid-low elevation angles, and for a flight height of $h \sim 27,000$ m. These distributions are fitted by log-logistic PDF's. It has been reported that in foliage environment, log-logistics PDF's can provide a more accurate fitting of the amplitude of multipath impulse responses other than log-normal, Weibull, and Rayleigh models for narrowband signals [104]. The Kolmogorov-Smirnov test was used to perform a goodness of fit test. This test rejected the null hypothesis that the phase comes from a Weibull, Rayleigh and log-logistic distributions at a 9%, 6% and 3% of the significance level respectively. The log-logistic distribution for this particular set of data is the more accurate one in agreement with [104]. The Maximum Likelihood Estimates (MLE's) for the parameters are: mean $\mu = 2.47^\circ$, and scale parameter $\beta = 1.48$; and mean $\mu = 2.57^\circ$, and scale parameter $\beta = 1.48$, respectively for high $[58^\circ, 70^\circ]$, and low $[30^\circ, 40^\circ]$, elevation angles.

Increasing the flight height reduces the phase noise (Table 8.1) of consecutives samples after signal retracking. The retracking strategy implemented in the PYCARO reflectometer tends to align the sum of the in-phase and quadrature components of the scattered field with the in-phase axis, and switches 180° during each data bit reversal. The purpose of this retracking strategy was to properly align the WFs before the

incoherent averaging was performed [134]. The coherently integrated WFs need to be aligned to compensate the GPS satellites motion. This motion induces a change in the delay difference of the direct and the reflected waveforms during the incoherent averaging. The performance of a space-borne GNSS-R altimeter is seriously degraded without alignment of the waveform samples [134]. Thus, Figs. 8.12 and 8.13 deal, with the phase after demodulation as provided by the lock-loop mechanism implemented to perform the retracking of the waveforms.

8.5 Summary and conclusions

This work has described the first-ever to authors' knowledge GNSS-R stratospheric experiment over land surfaces. The BEXUS 17 stratospheric flight trajectory was a single track from Esrange Space Center (latitude $67^{\circ} 53' \text{N}$, longitude $21^{\circ} 04' \text{E}$) to Juujarvi (latitude $66^{\circ} 24' \text{N}$, longitude $27^{\circ} 18' \text{E}$), with an apogee around $\sim 27,000 \text{ m}$ and the float phase of 4 h. The outdoor temperature during the flight reached -67°C , however the environmental conditions in North Sweden during the complete launch campaign were relatively warm, and no ice cover over the ground was found. During this flight, contributions from 4 different scattering sources over boreal forest have been observed, coming from the soil, the canopy, and the interactions canopy-soil and soil-trunks. It is found that the coherent reflectivity decreases from $\sim -15 \text{ dB}$ to $\sim -21 \text{ dB}$ (for the soil), from $\sim -19 \text{ dB}$ to $\sim -25 \text{ dB}$ (for the canopy), from $\sim -22 \text{ dB}$ to $\sim -30 \text{ dB}$ (for the canopy-soil), and from $\sim -25 \text{ dB}$ to $\sim -33 \text{ dB}$ (for the soil-trunk), when the elevation angle θ_e increases from 35° to 72° . The reflected power is nearly independent on the flight height which evidences a strong coherent component for a very high coherent integration time $T_c = 20 \text{ ms}$. These empirical results show that the scattering over the forest elements occurs in a clear multi-modal manner.

9

9. ESA BEXUS 19: MULTI-CONSTELLATION, DUAL-BAND AND DUAL-POLARIZATION SIGNALS

9.1 Introduction

In 2012 and 2013 two ground-based low-altitude experiments using the Galileo E1/E5a/E5b signals [138], and the GLONASS L1 composite signal [139] have been performed over a lake and from a pier over the North Sea, respectively.

Boreal forests cover approximately 15 % of Earth's land surface. Mapping boreal biomass is a key-factor to study the carbon cycle. ESA's BIOMASS mission for example will focus in this variable using a P-band SAR (e.g. [140]). Some studies have shown the potential of GNSS-R to measure forest biomass [132]. At present, UK TechDemoSat-1 [141], NASA GyGNSS mission [142], ESA's GNSS rEfectometry, Radio Occultation and Scatterometry experiment on-board the International Space Station (GEROS-ISS) [128], ESA's Passive Reflectometry and Interferometry System In-Orbit Demonstrator (PARIS-IoD) [3], and UPC's ³Cat-2 6U CubeSat [143] include GNSS-R payloads.

A scattering model considering both the coherent and incoherent scattered fields was proposed in [132]. This model predicts the coherent field as the result of the electromagnetic interactions of the GNSS signals with the soil only, attenuated by the vegetation canopy above it. In [133] experimental data over forest biomass from 100 t/ha to 350 t/ha using GPS signals was reported. As predicted in [132], a lower value of the coherent soil-reflectivity is found for larger vegetation density. The coherent scattering over a rough soil including antenna pattern effects was studied in [125], and applied later to the GNSS-R case for vegetation-covered soils [126]. More recently, a different approach has been proposed that states that the forward scattering coefficient is governed by the scattering properties of the vegetation elements and the soil surface, as well as by the interaction between the canopy and the soil, and the soil with the trunks [40, 41].

This work presents the first ever GNSS-R dual-frequency (L1 and L2), multi-constellation (GPS and GLONASS, and for E1 Galileo) observations over boreal forests, from a stratospheric balloon using the PYCARO reflectometer in closed-loop mode. The study is performed using data from the float phase of the flight ($h \sim 27,000$ m), and with GNSS satellites at a high elevation angle in the range $\theta_e = [45^\circ, 70^\circ]$. Section 9.2 describes the set-up used in this experiment carried out North of Sweden

on October 8th, 2014 on-board the ESA-sponsored BEXUS 19 stratospheric balloon. Section 9.3 describes the theoretical framework. Section 9.4 describes the experimental results. Finally, Section 9.5 summarizes the main results of this study.

9.2 Experimental set-up

The BEXUS program is implemented under a bilateral agency agreement between the German Aerospace Center (DLR), and the Swedish National Space Board (SNSB). The BEXUS 19 stratospheric balloon (Fig. 9.1) launch campaign took place in Esrange Space Center from October 3th to 13th, 2014. The launch took place on October 8th, 2014 at 18 h (GPS Time), and the flight duration was 4 hours with an apogee of $\sim 27,000$ m. The trajectory was a single track from Esrange Space Center (latitude $67^{\circ} 53'N$, longitude $21^{\circ} 04'E$) to the Finland Lapland (latitude $68^{\circ} 04'N$, longitude $25^{\circ} 81'E$) over boreal forests with a density ~ 100 t/ha, and a tree height of ~ 20 m.

The experimental set-up (see Appendix A) was composed of the PYCARO rGNSS-R instrument (P(Y) & C/A ReflectOmeter) [72, 83], both a dual-band (L1, L2) and dual-polarization³³ (RHCP and LHCP) zenith-looking patch antenna to collect the direct GNSS signals, and a nadir-looking antenna array to collect the Earth-reflected signals (Fig. 9.2), an On Board Computer (OBC) for the experiment management, and an active thermal control, since the outside temperature went down to $-70^{\circ}C$. The nadir-looking antenna was composed of 6 elementary antenna patches (Fig. 9.2). The total gain of the antenna was 12.9 dB at L1-LHCP, 13.3 dB at L1-RHCP, 11.6 dB at L2-LHCP and 11.6 dB at L2-RHCP. The Command and Data Handling System (CDHS) was composed of a Commercial Off-The-Shelf (COTS) microcontroller for housekeeping and scientific data management, communications with the ground station, and data storage in a micro-SD. The collected data were registered in two internal SD memories (PYCARO and microcontroller), and they were simultaneously sent to the ground segment via the E-Link system [130].

³³ In this study only Left Hand Circular Polarization (LHCP) reflected signals are presented.

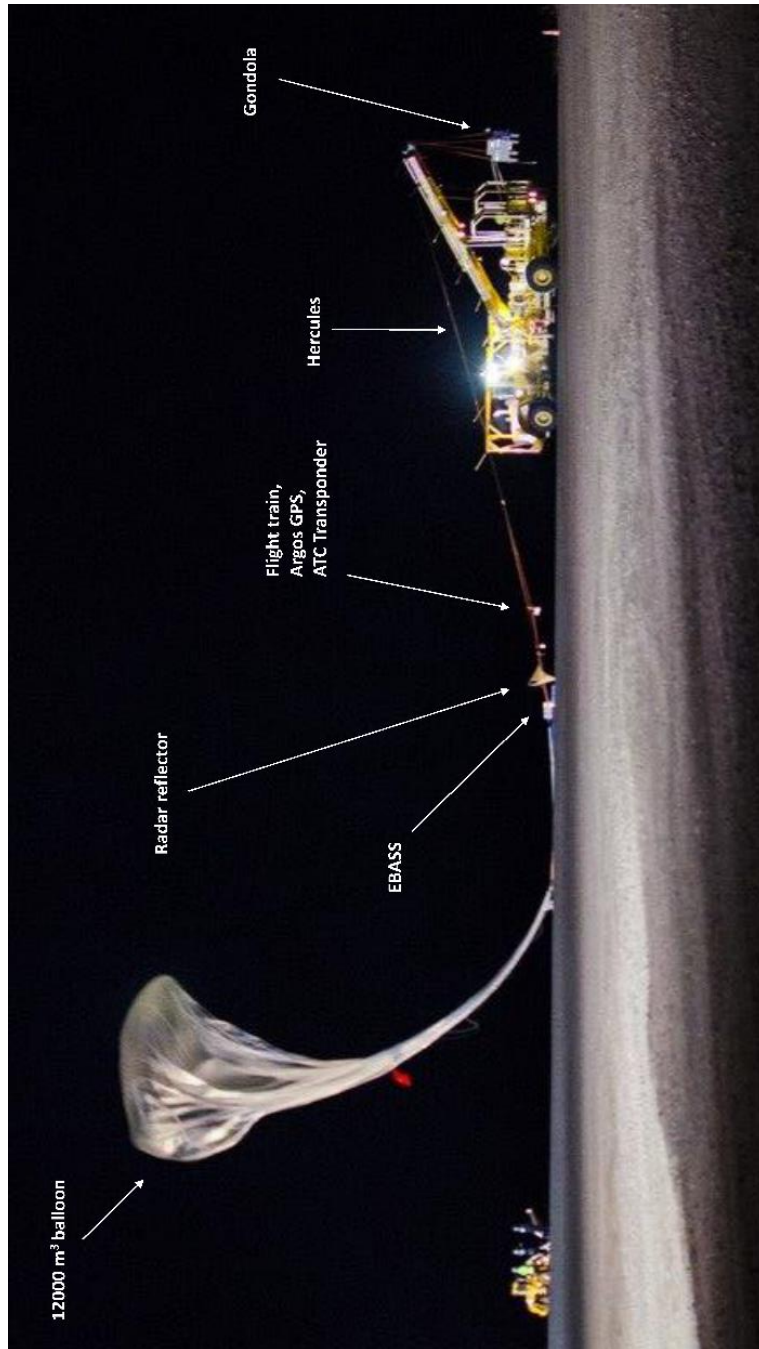


Fig. 9.1. BEXUS 19 stratospheric balloon during take-off at Esrange Space Center. Typical BEXUS configuration: 12,000 m³ balloon, valve, cutter, parachute, Esrange Balloon Service System (EBASS), flight train, Argos GPS and Air Traffic Control (ATC) transponder (AGT), strobe light, radar reflector, and gondola. Total length of the system is up to 75 m [130]. Photo Credits: SNSB-K. Dannenberg.

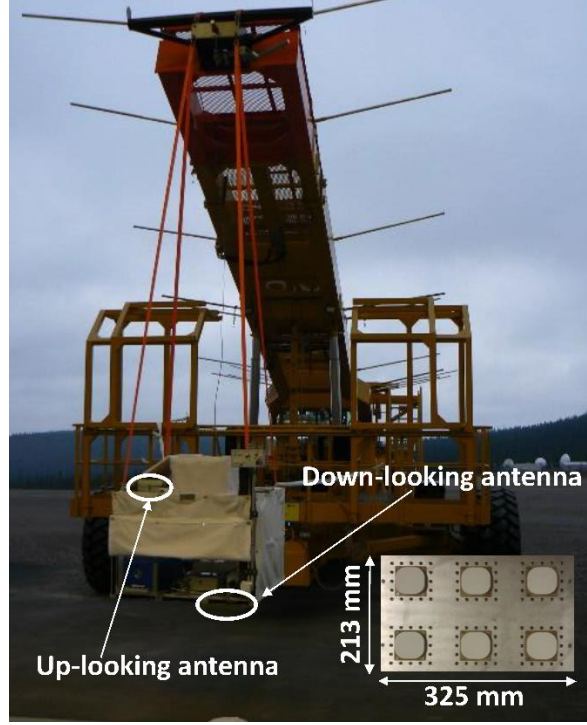


Fig. 9.2. Up-looking patch antenna and down-looking antenna array inside the thermally insulating radomes on-board the BEXUS 19 gondola.

9.3 Theoretical framework

The GNSS-Reflectometer used is the PYCARO instrument operated in closed-loop mode with delay and phase tracking loops activated that uses the cGNSS-R technique for the open-access codes, and the rGNSS-R one for the encrypted codes. The complex cross-correlation waveform of the direct signal is proportional to the electromagnetic field reaching the instrument as [144]:

$$Y_d(\tau, f_c) \propto T_c \cdot WAF(\tau, f_c) \approx T_c \cdot ACF(\tau) \frac{\sin(\pi f_c T_c)}{\pi f_c T_c} e^{-j\pi f_c T_c}, \quad (9.1)$$

where τ is the delay of the signal from the transmitter to the receiver, f_c is the carrier frequency of the direct electromagnetic signal, T_c is the coherent integration time, WAF is the well known Woodward Ambiguity Function, $ACF(\tau)$ is the Auto-Correlation Function of the code, and $j = \sqrt{-1}$ is the imaginary unit.

The complex waveform associated to the field scattered by an ensemble of scatterers such as soil, and trunks, branches and leaves of a forest will consist of the sum of a finite number of WAFs each one affected by a complex weight ($a_m = |a_m|e^{j\phi_m}$) that accounts for the scattering amplitude of the electromagnetic field, delayed by a delay $\delta\tau_m$ and affected by a Doppler shift δf_m :

$$\begin{aligned} Y_r(\tau, f_{c,sp}) &= T_c \sum_{m=1}^M |a_m| e^{j\phi_m} \cdot \text{WAF}(\tau + \delta\tau_m, f_{c,sp} + \delta f_m) \approx \\ &\approx T_c \sum_{m=1}^M |a_m| e^{j\phi_m} \cdot \text{ACF}(\tau + \delta\tau_m) \frac{\sin(\pi(f_{c,sp} + \delta f_m)T_c)}{\pi(f_{c,sp} + \delta f_m)T_c} e^{-j\pi(f_{c,sp} + \delta f_m)T_c}, \end{aligned} \quad (9.2)$$

where $f_{c,sp}$ is the Doppler shift of the electromagnetic signal reflected at the nominal specular point. Actually Eqn. (9.2) can be understood as the discrete version of the integrated form in [16]. A detailed analysis of the cross-correlation properties ($\text{ACF}(\tau)$ in Eqn. 9.1) of different navigation signals is provided in [145]. The main parameters of these signals are summarized in Table 9.1.

The phase difference before retracking ($\delta\Psi_n$) between the peak amplitude of the direct and the reflected complex waveforms at time t_n is used to infer the geometric delay $\rho_{\text{geo},n}$ as:

$$\rho_{\text{geo},n} = \frac{\lambda \delta\Psi_n}{2\pi}, \quad (9.3)$$

where λ is the signal electromagnetic wavelength. Height³⁴ changes δh_n of the center of phase of the scatterers (soil, trunks, branches and leaves) that contribute to the peak of the amplitude of the complex reflected waveform $Y_r(\tau, f_c)$ are related to the difference of the geometric delays $\delta\rho_{\text{geo},n}$ between two consecutive samples as [24]:

$$\delta h_n = \frac{\delta\rho_{\text{geo},n}}{2 \sin \theta_e} = \frac{\rho_{\text{geo},n} - \rho_{\text{geo},n-1}}{2 \sin \theta_e}, \quad (9.4)$$

where θ_e is the elevation angle. Finally, since we are using differential measurements with a period defined by the coherent integration time of the waveforms (T_c), the

³⁴ Precise flight trajectory provided by SSC computed using a GPS receiver on-board the balloon, and small platform height variations were compensated for. Vertical speed of the balloon during the float phase was smaller than 1 m/s, which prevented phase jumps.

phase delays introduced by the atmosphere are implicitly cancelled out because they can be assumed to be constant during these short periods of time.

GPS satellites' motion and receiver's motion as well induce a change in the delay, and the phase difference of the waveforms. The PYCARO reflectometer compensates these changes to perform the coherent and incoherent averaging. In addition to the phase of the peak of the reflected waveforms before retracking $Y_r(\tau_{\text{Peak}}, f_{c,\text{Peak}})$ one important scientific observable is the phase Ω_n of the peak of the complex reflected waveforms after being retracked, to center the tracking delay and Doppler windows.

9.4 Experimental results

The experimental results derived from the BEXUS 19 flight that are presented here confirm the multi-modal scattering behaviour observed during the previous BEXUS 17 experiment. A detailed analysis and discussion is provided along this Section.

9.4.1 Analysis of the coherent-to-incoherent scattering ratio

The total scattered field of the GNSS signals during the float phase of the flight can be described as the vector sum of the different contributions (complex waveforms peaks) in the complex plane. The ratio of the coherent and incoherent scattering components is analyzed using a data set of ~ 2 h, which corresponds to a flight height of $h \sim 27,000$ m (Table 9.1). The reflected complex waveforms were tracked using a Delay Locked Loop (DLL), and a Phase Locked Loop (PLL). The optimum parameters are provided in Table 9.2, and were found empirically by changing PYCARO's configuration in real time during the experiment thanks to the E-Link.

Forests are characterized by random variations of the dielectric properties. The scattered field during the coherent integration time T_c can be described as the sum of random vectors with phases ϕ_m , and amplitudes a_m (Eqn. 9.2). The total scattered fields during the float phase corresponding to GPS (Figs. 9.3a,c-forests and 9.3b,d-lakes), GLONASS (Figs. 9.3e-forests and 9.3f-lakes), and Galileo (Figs. 9.3g-forests

and 9.3h-lakes) are represented in the complex plane for elevation angles in the range $\theta_e = [45^\circ, 70^\circ]$. In Figs. 9.3a,b and 9.3e,f there are two regions displaced by $\pm|\langle Y_{r,\text{Peak}} \rangle|$ (mean of the amplitude distribution) from the center of the complex plane for both the GPS L1 C/A and GLONASS L2 C/A signals, because of the phase changes associated to the navigation bit. GPS L2 C (Figs. 9.3c,d), and Galileo E1 BC (Figs. 9.3g,h) are the so-called data-less channels or pilot channels. The tracking of the code is done coherently because no data bit is present. The complex plane representation is then centered in a region displaced $+\langle Y_{r,\text{Peak}} \rangle$ from the center. These I/Q scatter plots show how the behaviour changes depending on the scattering surface: from poorly coherent over boreal forests, to a highly coherent over lakes. The relative weight of the coherent-to-incoherent components is quantified by the following ratio [97, pp. 126]:

$$B^2 = \frac{|\langle Y_r \rangle|^2}{\sigma_{\text{Real}}^2 + \sigma_{\text{Im}}^2}, \quad (9.5)$$

where $|\langle Y_r \rangle|^2$ is the mean of the power distribution, and σ_{Real}^2 and σ_{Im}^2 are the variances of the real and imaginary components of the complex cross-correlation waveforms peak after retracking.

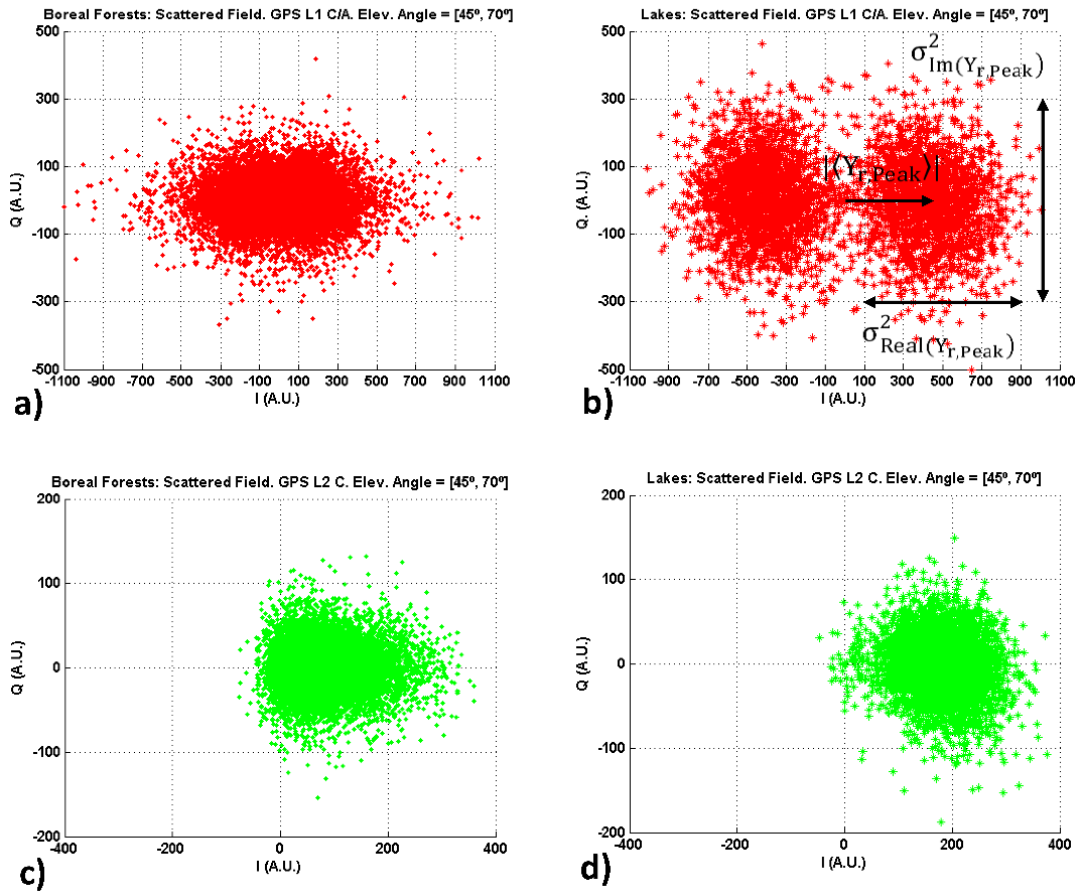


Fig. 9.3. Scattered complex field (peak of the complex waveform, T_c from Table 9.2, no incoherent averaging) for an elevation angle of $\theta_e = [45^\circ, 70^\circ]$ and a flight height $h \sim 27,000$ m. GPS L1 C/A (a) boreal forests and (b) lakes (b), GPS L2 C (c) boreal forests and (d) lakes.

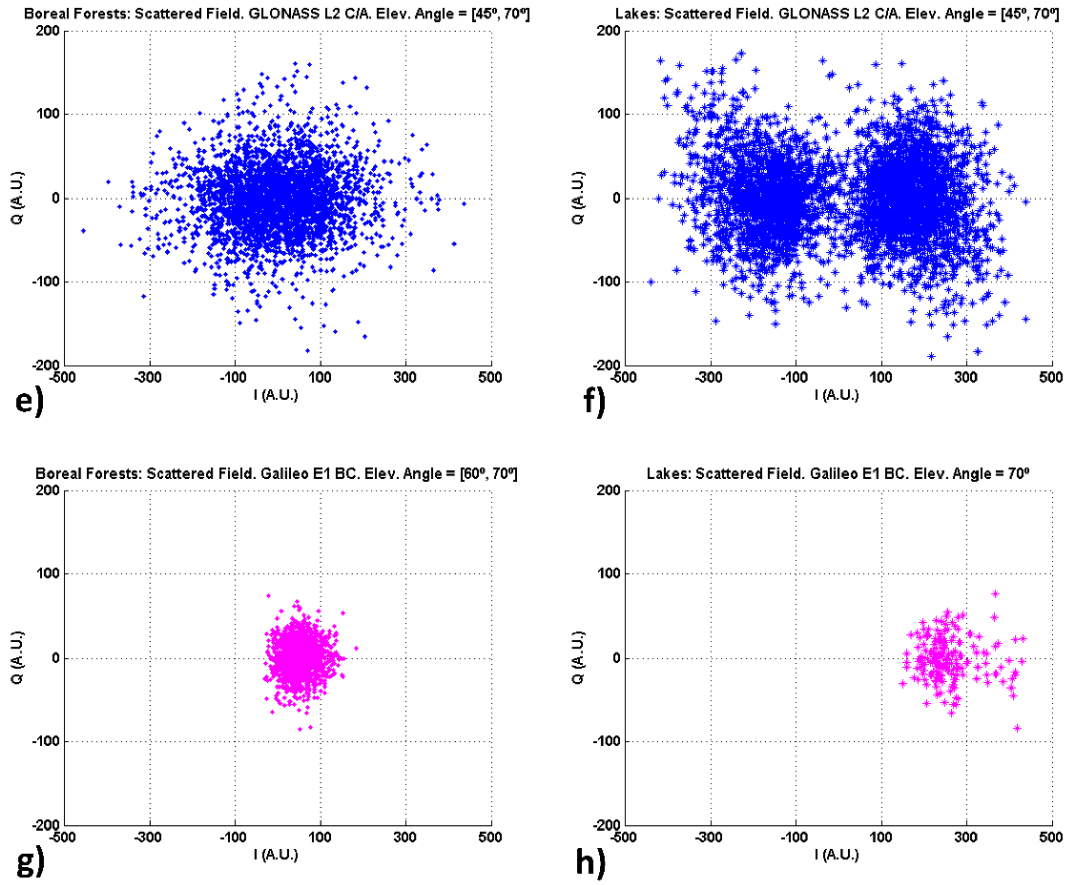


Fig. 9.3. Scattered complex field (peak of the complex waveform, T_c from Table 9.2, no incoherent averaging) for an elevation angle of $\theta_e = [45^\circ, 70^\circ]$ and a flight height $h \sim 27,000$ m. GLONASS L2 C/A (e) boreal forests and (f) lakes, and Galileo E1 BC (g) boreal forests and (h) lakes.

Table 9.1. Amount of coherent and incoherent scattering, reflected phase oscillations std. deviation over boreal forests and lakes as a function of the elevation angle for: GPS, GLONASS and Galileo signals at a flight height of $h \sim 27,000$ m.

	L1 C/A FORESTS	L2 C FORESTS	L1 C/A LAKES	L2 C LAKES
GPS, h ≈ 27,000 m, θ _e = [45°, 70°]				
Coherent Scattering: $\left \langle Y_{r,Peak} \rangle\right ^2$ (A.U.)	33,782	6,037	199,090	33,015
Incoherent Scattering: $\sigma^2_{Real(Y_{r,Peak})} + \sigma^2_{Im(Y_{r,Peak})}$ (A.U.)	16,888+4,178	3,102+622	32,569+15,363	2,910+1,238
Ratio B ²	1.6	1.6	4.1	7.9
Reflected Phase Oscillations Std. (degrees)	30	27	20.7	12.5
	L1 C/A FORESTS	L2 C/A FORESTS	L1 C/A LAKES	L2 C/A LAKES
GLONASS, h ≈ 27,000 m, θ _e = [45°, 70°]				
Coherent Scattering: $\left \langle Y_{r,Peak} \rangle\right ^2$ (A.U.)	x	9,761	x	32,508
Incoherent Scattering: $\sigma^2_{Real(Y_{r,Peak})} + \sigma^2_{Im(Y_{r,Peak})}$ (A.U.)	x	4,610+1,686	x	5,847+2,439
Ratio B ²	x	1.5	x	3.9
Reflected Phase Oscillations Std. (degrees)	x	35	x	19.8
	E1 BC FORESTS		E1 BC LAKES	
Galileo, h ≈ 27,000 m, θ _e = [60°, 70°]				
Coherent Scattering: $\left \langle Y_{r,Peak} \rangle\right ^2$ (A.U.)	3,434	x	68,069	x
Incoherent Scattering: $\sigma^2_{Real(Y_{r,Peak})} + \sigma^2_{Im(Y_{r,Peak})}$ (A.U.)	1,208+423	x	3,477+658	x
Ratio B ²	2.1	x	16.5	x
Reflected Phase Oscillations Std. (degrees)	28.2	x	5.7	x

Table 9.2. Optimum delay and phase locked loop parameters used during the float phase of the experiment for GPS [146], GLONASS [147, 148], and Galileo signals [149].

GNSS code	T_c^{PLL} (ms)	B^{PLL} (Hz)	T_c^{DLL} (ms)	N_{inc}^{DLL} (complex waveforms)	B^{DLL} (Hz)
GPS L1 C/A	10	15	20	1	0.01
GPS L2 P(Y)	10	15	20	1	0.01
GPS L1 P(Y)	10	15	20	1	0.01
GPS L2 C [146]	10	15	20	1	0.01
GLONASS L1 C/A [147]	10	15	10	2	0.01
GLONASS L2 C/A [147]	10	15	10	2	0.01
GLONASS L2 P [148]	4	15	4	5	0.01
Galileo E1 BC [149]	4	15	4	5	0.01

This definition is equivalent to that used in Section 6.3.3 but here we use this expression to show more clearly the impact of Table 9.2. Note that B tends to ∞ for a totally coherent field, and it is equal to 0 for a totally incoherent field. If the scatter plot was centered around (0, 0), the scattering would be completely incoherent. However, the scattered field is clearly displaced from the origin by a value equal to the mean of the amplitude distribution.

Over boreal forests, the ratio B^2 (Table 9.1) shows the presence of a coherent component which is $B^2 \sim 1.5$ for GPS and GLONASS signals for elevation angles in the range $\theta_e = [45^\circ, 70^\circ]$, and it is ~ 2.1 for Galileo signals for elevation angles in the range $\theta_e = [60^\circ, 70^\circ]$. This value is slightly different for the different codes because of the different scattering properties of the forested areas at the time of signal acquisition (different tracks and time periods), and slightly different elevation angles.

On the other side, over lakes the ratio B^2 is much higher, up to 16.5 for Galileo signals, and in the range [3.9, 7.9] for GPS and GLONASS. Additionally, the standard deviation of the phase at the peak of the complex waveforms after retracking is in the range $[27^\circ, 35^\circ]$ over boreal forests, and $[5.7^\circ, 20.7^\circ]$ over lakes. This value is lower ($\sim 3^\circ$ for GPS L1 C/A over forests and $\sim 8^\circ$ for GPS L2 C over lakes) at L2 as compared to the L1 measurements. One reason is that the effective roughness is lower, as the signal wavelength is larger ($\lambda_{L1} = 19$ cm and $\lambda_{L2} = 24$ cm). The amount of Galileo signals collected along the flight were significant lower than the GPS and GLONASS ones, due to the lesser number of satellites, and to the fact that the CBOC modulation and the steeper ACF translate into a higher filtering of the coherent scattered signals and a lower SNR.

9.4.2 Scattering properties over boreal forests

The coherent scattering over boreal forests (soil, trunks, branches, and leaves) is now studied using the signatures in the phase Ψ_n of the peak of the complex waveforms before retracking ($Y_{r,Peak}$). The information contained in the unwrapped phase is translated into height fluctuations of the scatterers using Eqn. 9.4. The distributions of these height and post coherent-correlation SNR fluctuations over boreal forests are represented for the different signals: GPS L1 C/A (Figs. 9.4a,b), GPS L2 C (Figs. 9.4c,d), GLONASS L2 C (Figs. 9.4e,f), and Galileo (Figs. 9.4g,h). The SNR decreases with increasing values of the receiver bandwidth (4 MHz GPS L1 C/A, 6 MHz GPS L2 C, 19 MHz GLONASS L2 C/A, and 24 MHz Galileo E1 BC). For GPS and GLONASS, the maximum value of the estimated SNR is ~ 39 dB GPS L1 C/A, 32 dB GPS L2 C, and ~ 26 dB GLONASS L2 C/A, and the variation is in a range of $\sim [24, 27]$ dB which can be attributed to the different ground-tracks of the specular reflection points. The height fluctuations exhibit a multi-modal behaviour and are as high as ± 10 m for GPS and GLONASS. However, for the Galileo signals, due to the larger bandwidth and the lower SNR ($SNR < 14$ dB) only the strongest reflections are tracked, those coming from the soil, therefore height fluctuations are usually much

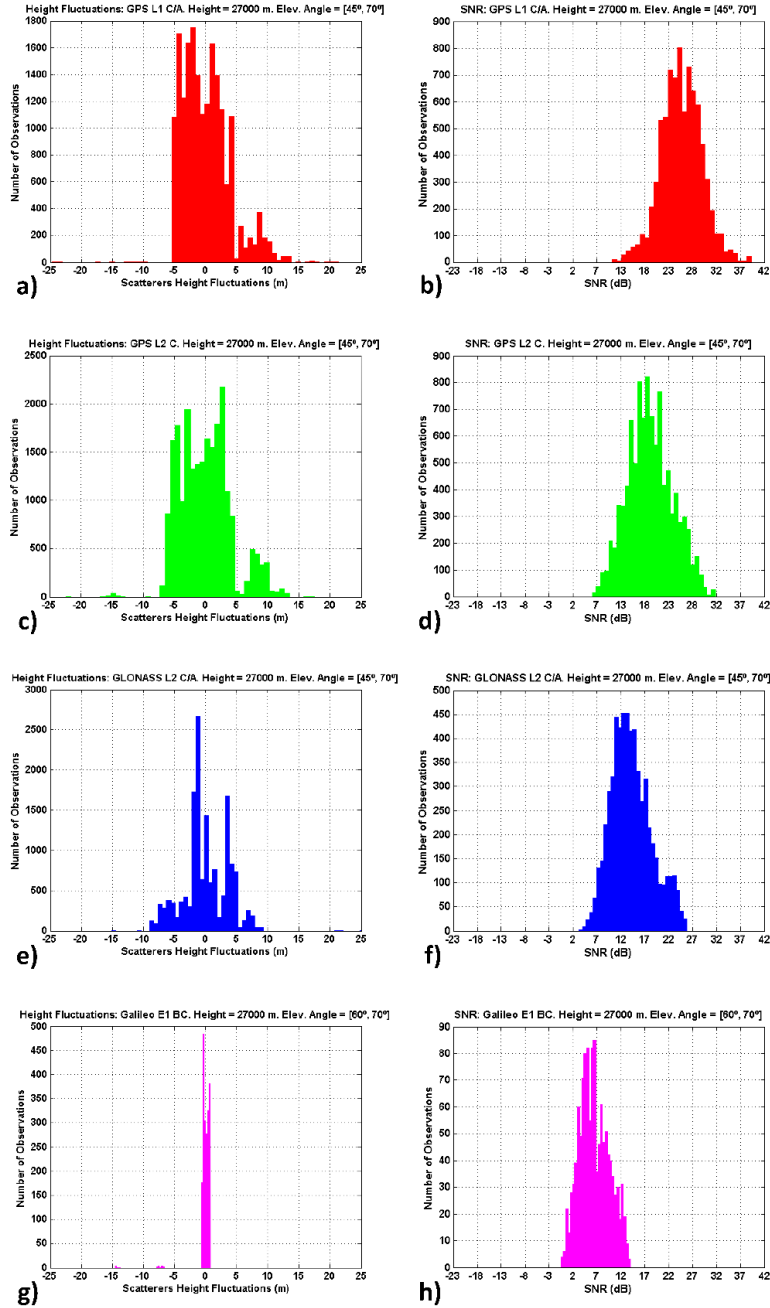


Fig. 9.4. Height fluctuations of the scatterers and post coherent-correlation SNR over boreal forests for an elevation angle $\theta_e = [45^\circ, 70^\circ]$ and a flight height $h \sim 27,000$ m. (a,b) GPS L1 C/A boreal forests, (c,d) GPS L2 C boreal forests, (e,f) GLONASS L2 C/A boreal forests, and (g,h) Galileo E1 BC boreal forests.

smaller (~ 0.5 m) except for a peak of ~ -7 m. These empirical results suggest that coherent scattering is taking place not only over the soil (higher SNR because the higher reflectivity, and lower height dispersion), but also over the trees which produces a multi-modal behavior with clearly differentiated levels of SNR which may include multiple reflections involving canopy and soil as suggested in [40].

Now, taking into account the non-stationarity of the phase after retracking (Figs. 9.5a,b) due to the random distribution of the scatterers, an analysis in the time-frequency domain is performed. Spectrograms are used to further study the phase fluctuations of the reflected GNSS signals. GLONASS L2 CA (Figs. 9.5a,c) and GPS L2 C (Figs. 9.5b,d) signals over lakes and boreal forest are considered to illustrate the analysis showing randomly distributed energy peaks. It is found that there is a surface scattering both over lakes (Fig. 9.5c) and forested areas (Fig. 9.5d) determined by the main and smoother scattering media: water and land surfaces, respectively. Additionally, there are some peaks localized in particular Doppler values (Fig. 9.5c) with higher power level, equal in magnitude to the surface scattering over boreal forests. This is due to the effect of specularly reflected signals over land regions inside the first Fresnel zone at time of signal acquisition. On the other side, the spectral pattern over forested areas also shows regions with very high power peak which appear simultaneously in time, an indication that scattering is taking place at different heights simultaneously (trunks, branches...). The largest phase fluctuations are associated with these power peaks. The phase evolution in the spatial domain (Figs. 9.5a,b) is superposed with the time-frequency analysis (Figs. 9.5c,d) showing that the large phase fluctuations correlate well with this multi-modal frequency clusters in the spectrograms.

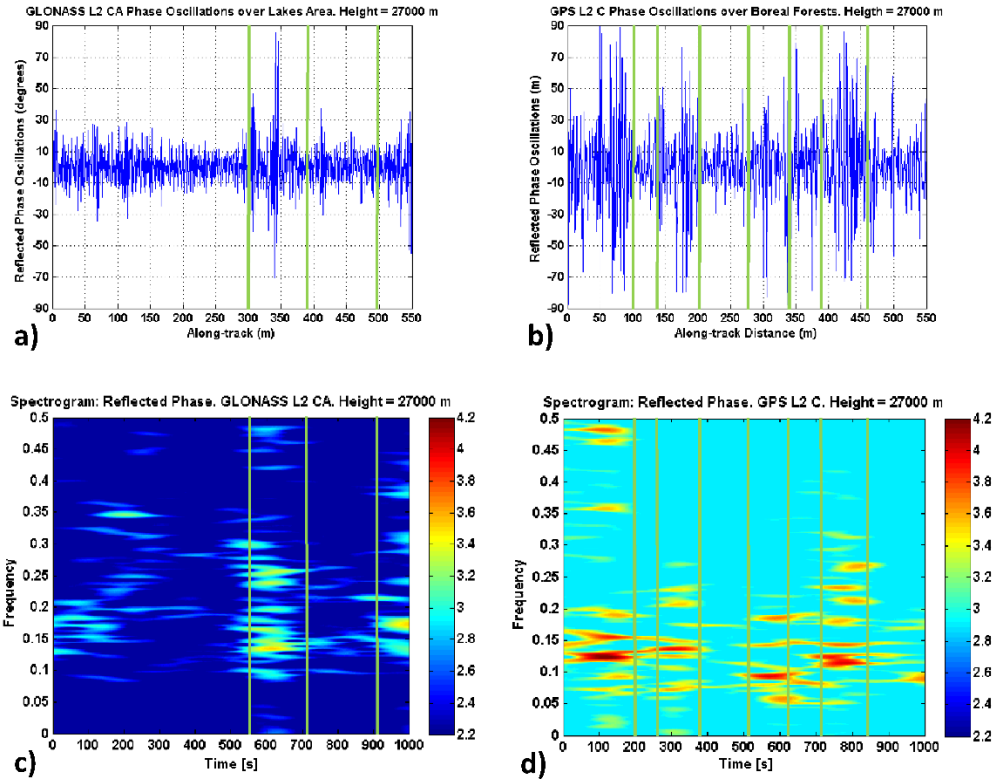


Fig. 9.5. Along-track reflected phase oscillations and spectrograms for (a) and (c): GLONASS L2 CA (boreal forests), and for (b) and (d) GPS L2 C (lakes areas), respectively.

9.4.3 Reflectivity maps

The cross-polar reflectivity $\Gamma_{\text{RHCP-LHCP}}$ is estimated as the ratio of the reflected ($Y_{\text{r}}^{\text{LHCP}}$) and direct ($Y_{\text{d}}^{\text{RHCP}}$) power waveforms peaks, after proper compensation of the noise power floor and the antenna gains (nadir and zenith-looking) as a function of the elevation angle:

$$\Gamma_{\text{RHCP-LHCP}} = \frac{\langle |Y_{\text{r}}^{\text{LHCP}}|^2 \rangle}{\langle |Y_{\text{d}}^{\text{RHCP}}|^2 \rangle}. \quad (9.6)$$

In Eqn. 9.6, RHCP and LHCP denote the incident polarization (Right Hand Circular Polarization), and the scattered polarization (Left Hand Circular Polarization),

Table 9.3. Semi-major axis of the first chip iso-delay ellipse, semi-major axis of the first Fresnel zone at different elevation angles ($\theta_e = 45^\circ$ and $\theta_e = 70^\circ$) for GPS, GLONASS and Galileo signals.

GNSS code	Semi-major axis first chip ellipse (m) $\theta_e = 70^\circ$	Semi-major axis first Fresnel zone (m) $\theta_e = 70^\circ$	Semi-major axis first chip ellipse (m) $\theta_e = 45^\circ$	Semi-major axis first Fresnel zone (m) $\theta_e = 45^\circ$
GPS L1 C/A	4,366	78	6,689	120
GPS L2 P(Y)	1,380	88	2,115	135
GPS L1 P(Y)	1,380	78	2,115	120
GPS L2 C	6,175	88	9,460	135
GLONASS L1 C/A	6,175	78	9,460	120
GLONASS L2 C/A	6,175	88	9,460	135
GLONASS L2 P	x	88	x	135
Galileo E1 BC	4,366	78	6,689	120

respectively. The correlation parameters in the computation of the waveforms are important for the evaluation of the results. The DLL and the PLL coherent integration times (T_c^{DLL} and T_c^{PLL}), the number of incoherent averaging samples (N_{inc}^{DLL}), and the DLL and PLL bandwidths (B^{DLL} and B^{PLL}) are included in Table 9.2. The PLL coherent integration time was set to be 10 ms for all the codes³⁵, and the $B^{PLL} = 15$ Hz to tolerate abrupt phase changes due to the scattering process over boreal forests. The DLL coherent integration time (T_c^{DLL}) was set to be equal to the navigation data bit period for each code [146-149], because during the experiment preparation activities it was determined that the SNR increased as a function of the coherent integration time up to 13 dB for $T_c^{PLL} = 20$ ms. The DLL optimum bandwidth was set empirically during the experiment to be $B^{DLL} = 0.01$ Hz to stabilize the frequency after getting locked. After the estimation of the reflectivity values, the specular points were geolocalized over Google Maps for the sake of a simpler data interpretation. The orbit parameters of the GNSS satellites were obtained from the ephemerides as provided by an on-board positioning receiver, while the

³⁵ GLONASS L2 P [148] and Galileo E1 BC [149] codes were limited by their navigation data bit period (4 ms).

PYCARO trajectory was determined using the on-board receiver. Before the evaluation of the results, some theoretical considerations about the reflectivity estimation algorithms are commented. The reflectivity values as estimated using Eqn. 9.6, introduce a dependency with the platform height through the WAF in $Y_{r,Peak}$ (Eqn. 9.2), due to the different sizes of the scattering area, which is translated into different power levels of the reflected signals [67]. For the flight conditions ($h \sim 27,000$ m and scattering over land surfaces), the Earth region contributing to the incoherent component is the first chip iso-delay ellipse which is a function of the ACF of the different GNSS codes. On the other side, the area contributing to the coherent component is limited by the first Fresnel zone, which actually depends on the signal wavelength. These values are summarized in Table 9.3.

Figures 9.6 and 9.7 show the reflectivity values using GPS, GLONASS and Galileo signals. cGNSS-R was used for computation of the waveforms using GPS L1 C/A (Fig. 9.6a), GPS L2 C (Fig. 9.6b), GLONASS L1 C/A (Fig. 9.7a), GLONASS L2 C/A (Fig. 9.7b), GLONASS L2 P (Fig. 9.7c), and Galileo E1 BC (Fig. 9.7d), while rGNSS-R for GPS L1 P(Y) and L2 P(Y) (Figs. 9.6c,d). The reflectivity values are as high as -2 dB over lakes. On the other side, they show large fluctuations from -3 dB to -25 dB, over boreal forests. When using cGNSS-R, the reflectivity shows a similar behavior for the different codes of each GNSS system. The coherent component, the one actually tracked by PYCARO, is coming from an area equal to the first Fresnel zone. Therefore, although the WAF spreads the signal over areas of different size, $\Gamma_{RHCP-LHCP}$ follows the same trend independently of the code and the signal wavelength. Finally, the rGNSS-R is evaluated successfully for first time over forested areas, despite the high dispersion of the signal induced by the scattering media. Reflectivity values are ~ 10 dB below those obtained by cGNSS-R because of the squaring losses of the P(Y) code correlation technique implemented in PYCARO, which exhibits a non-linear dependence with the SNR of the incoming signal [72, 83]: the lower the SNR, the larger the squaring losses [74].

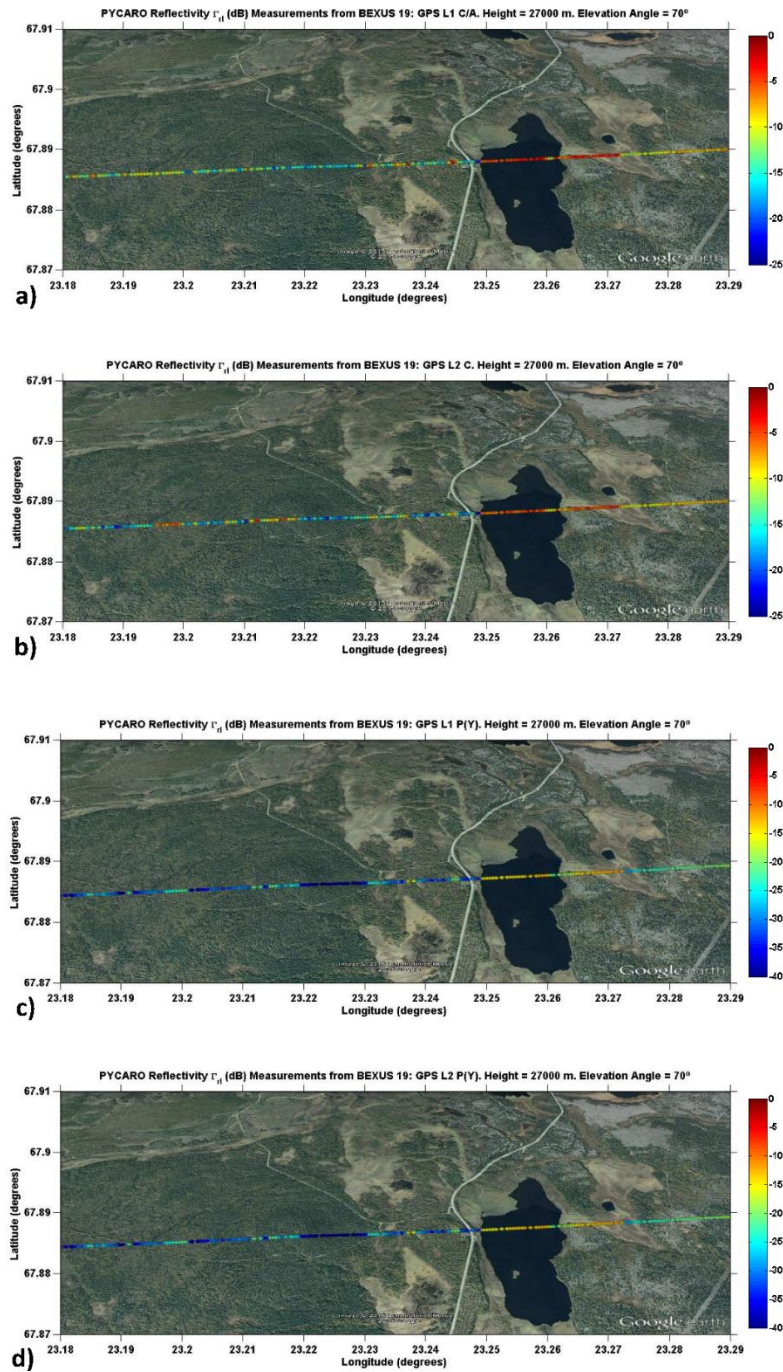


Fig. 9.6. Cross-polar reflectivity maps (LHCP-reflected) geolocated over the nominal specular points over boreals forests and lakes for GPS signals: (a) L1 C/A, (b) L2 C, (c) L1 P(Y), and (d) L2 P(Y).

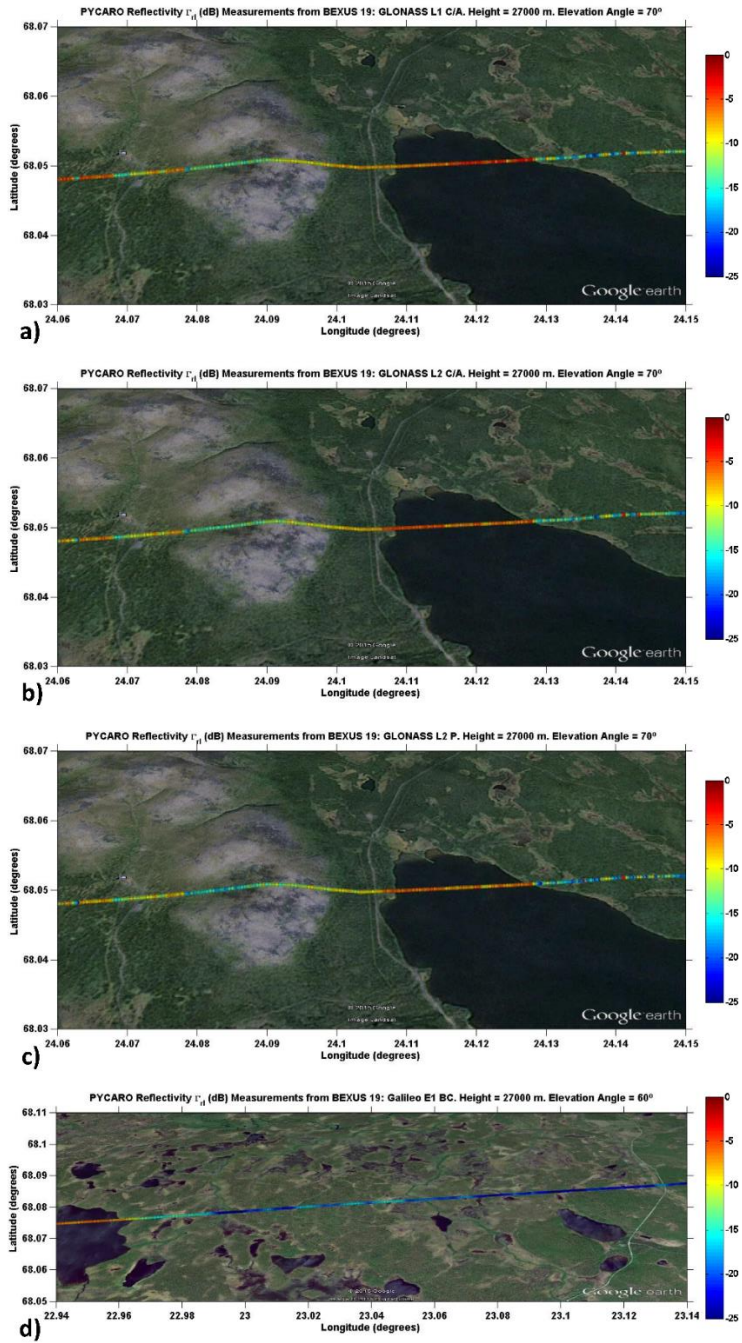


Fig. 9.7. Cross-polar reflectivity maps (LHCP-reflected) geolocated over the nominal specular points over boreal forests and lakes for GLONASS signals: (a) L1 C/A, (b) L2 C/A, (c) L2 P, and (d) Galileo E1 BC signals.

9.5 Summary and conclusions

This work has presented the first dual-frequency GNSS-R observations using GPS, GLONASS, and Galileo E1 BC signals, collected from a stratospheric balloon experiment performed North of Sweden using the PYCARO reflectometer. LHCP reflected signals were collected with an antenna array of ~ 13 dB gain at L1 and ~ 12 dB gain at L2. Results show the feasibility of tracking the coherent component of the scattering over boreal forests and lakes even from high altitude platforms. The coherent-to-incoherent ratio of the scattered signals for high elevation angles $\theta_e = [45^\circ, 70^\circ]$ is found to be ~ 1.5 over boreal forests, while over lakes it is in the range $[3.9, 7.9]$ for GPS and GLONASS, and it is high up to 16.5 for Galileo signals. The CBOC modulation and the steeper ACF of the Galileo signals translate into a higher filtering of the coherent scattered signals so that only highly coherent signals were tracked. This is the reason that explains the higher value of the coherent-to-incoherent ratio for Galileo signals. The height distribution of the scatterers has been derived from the fluctuations of the phase of the complex waveforms peak, which range from ± 10 m to the submeter level. Reflectivity values are highly variable from -3 dB to -25 dB, as derived using cGNSS-R. Reflectivity maps derived from the different codes of each GNSS system are highly similar despite the different power spreading over the scattering media induced by the different ACFs. Actually, the coherent component provides the highest power contribution to the peak of the complex waveforms. As a consequence, the fluctuations of the signal power depend only on an area equal to the first Fresnel zone for a rough scattering media. Additionally, the rGNSS-R technique has been successfully tested. PYCARO was able to reconstruct the GPS P(Y) code despite the large dispersion of the signal after the scattering over the boreal forests. As a main conclusion, the analysis of the GNSS-R complex waveforms shows a coherent multi-modal contribution after the signal scattering over forested regions. The performance of GNSS-R in terms of spatio-temporal sampling will benefit when future GNSS constellations will be fully operational. Geophysical parameters retrieval over high latitude targets (in particular, biomass monitoring) will take advantage of the relatively high orbital inclination (from 55° to 65°) of the navigation systems.

10

10. ESA BEXUS 19: FIRST GNSS-R MULTI-CONSTELLATION POLARIMETRIC MEASUREMENTS AT DUAL-BAND

10.1 Introduction

The use of GNSS-R polarimetry over land was first proposed in 2000 for soil moisture monitoring [150]. Later, theoretical simulations were carried out to evaluate the performance of GNSS-R polarimetric measurements for biomass monitoring [132]. Coherent and incoherent scattering were considered in the simulations. In particular, the coherent electromagnetic field was modeled as the reflection of the GNSS signals over the soil, attenuated by the vegetation above it. In this work [132] it was stated that the coherent component of the co-polar reflected signal is 30 dB lower than the cross-polar one. The incoherent component is dominant for co-polar signatures and for a biomass density larger than 50 t/ha, while the coherent component is the highest for cross-polar signals up to 200 t/ha. Later, an experimental study [133] showed that the co-polar coherent reflectivity is roughly constant for biomass densities from 100 t/ha to 350 t/ha, and for elevation angles in the range $\theta_e = [50^\circ, 80^\circ]$. On the other hand, the cross-polar component is shown to be reduced approximately ~ 5 dB. Recently, a different approach has proposed that the forward scattering coefficient is governed by the scattering properties of the vegetation elements and the soil surface, as well as by the interaction between the canopy and the soil, and the soil with the trunks [41]. In this study, the total cross- and the co-polar scattering coefficients are shown to be respectively $\sim [-8, 8]$ dB, and $\sim [-2, -15]$ dB for elevation angles in the range $\theta_e = [10^\circ, 80^\circ]$.

This work presents the first-ever measurements of dual polarization GNSS-R signatures using data from a stratospheric balloon experiment. Section 10.2 presents the experimental results obtained with the P(Y) and C/A ReflectOmeter (PYCARO) and their interpretation. Section 10.3 provides the final discussions, and conclusions are included in Section 10.4.

10.2 Polarimetric measurements over boreal forests and lakes

During the BEXUS 19 experiment the PYCARO reflectometer was operated in closed-loop mode with delay and phase tracking loops activated. It uses cGNSS-R technique to process the open-access codes, and the rGNSS-R one for the encrypted codes. The polarimetric study is performed using two different observables: the polarimetric ratio [150], and the polarimetric phase [151] using the measurements provided by the phase tracking loop. The polarization ratio is more sensitive to soil dielectric properties and can cancel roughness effects although it does not do so perfectly for arbitrary scattering media. It is defined as the ratio of the cross- over the co-polar reflectivities $\Gamma_{\text{RHCP-LHCP}} / \Gamma_{\text{RHCP-RHCP}}$, and it is estimated as the ratio of peak of the reflected power waveform at LHCP over the peak of the reflected power waveform at RHCP, after proper compensation of the noise power floor and the antenna radiation pattern [150]:

$$\frac{\Gamma_{\text{RHCP-LHCP}}}{\Gamma_{\text{RHCP-RHCP}}} = \frac{|\langle Y_r^{\text{LHCP}} \rangle|^2}{|\langle Y_r^{\text{RHCP}} \rangle|^2}. \quad (10.1)$$

Note that the noise power floor of the reflected waveforms has to be subtracted to the reflected power waveform to obtain the power of the signal itself. Additionally, the different gain of the antenna array at LHCP (12.9 dB at L1-LHCP and 11.6 at L2-LHCP) and RHCP (13.3 dB at L1-RHCP and 11.6 dB at L2-RHCP) have to be compensated by subtracting the antenna gain to the reflected signal power. Once the effect of the noise and the antenna have been compensated, the incoherent power component is omitted in the reflectivity, as obtained using Eqn. 10.1, by subtracting to each incoherently averaged waveform's peak the amplitude variance of the complex waveforms' peaks [97, pp. 125]:

$$|\langle Y_r \rangle|^2 = \langle |Y_r|^2 \rangle - \sigma_{|Y_r|}^2. \quad (10.2)$$

Thus, reflectivity values are associated to the first Fresnel zone. The semi-major axis of the first Fresnel zone during the float phase of the flight and for an elevation angle $\theta_e = 70^\circ$ is: GPS L1 C/A (78 m), GPS L2 P(Y) (88 m), GPS L1 P(Y) (78 m), GPS L2 Civilian C (88 m), GLONASS L1 C/A (78 m), GLONASS L2 C/A (88 m), GLONASS L2 P (88 m) and Galileo E1 BC (78 m). Additionally, the difference of

the unwrapped phases of the complex waveforms peak at LHCP Ψ_n^{LHCP} and RHCP Ψ_n^{RHCP} can be used. This phase has two terms; one induced during the scattering process, which is roughly constant at high elevation angles (e.g., $\theta_e \geq 60^\circ$), and another one due to the propagation. As compared to the polarimetric ratio the main advantage is that the phase difference between the RHCP and LHCP signals can be modeled independently of the elevation angle [151].

After compensation of the first term (using as a first approximation a flat soil model) the phase difference $\delta\Psi_n$ between the peak amplitude of the LHCP and the RHCP reflected complex waveforms at time t_n can be used to infer the geometric delay difference $\rho_{\text{geo},n}$ as:

$$\rho_{\text{geo},n} = \frac{\lambda \delta\Psi_n}{2\pi}, \quad (10.3)$$

where λ is the signal wavelength. Height differences h_n of the center of phase of the scatterers at LHCP and RHCP are related to the geometric delay difference $\rho_{\text{geo},n}$ as:

$$h_n = \frac{\rho_{\text{geo},n}}{2 \sin \theta_e}. \quad (10.4)$$

It is found that the mean of the polarimetric phase corresponding to GPS, GLONASS and Galileo signals over boreal forests is in the range from approximate -1.4 m to -9.6 m, which suggests that the phase center of the reflected signals at LHCP is higher than the one at RHCP, that is the scattering process takes place over the canopy and the soil [40]. The trajectory of the balloon was provided by Swedish Space Corporation (SSC) using a GPS receiver on-board, and small platform height variations were compensated for. Note that the vertical speed of the gondola during the float phase was smaller than 1 m/s, which prevented phase jumps. Single reflections (from RHCP to LHCP) are mainly due to interactions with the upper scatterers on the forests. On the other side, signals collected at RHCP involve multiple scattering soil-leaves and soil-branches (first from RHCP to LHCP and then from LHCP to RHCP). This is the reason that explains that the polarimetric phase has negative values (Eqn. 10.4).

Figures 10.1 and 10.2 show the first-ever maps of the polarimetric ratio using dual-band multi-constellation signals over boreal forests and lakes. The polarimetric ratio was provided over lakes and boreal forests to give a more complete information and

description of the polarimetric properties in the GNSS-R case for different types of scattering media. In Figure 2 there are two different color scales to show a general overview of the polarimetric ratio and also the sensitivity of the technique over boreal forests as it can be seen in the embedded scales. For this study, the elevation angle of the selected satellites was $\theta_e = 70^\circ$ for GPS and GLONASS, and $\theta_e = 60^\circ$ for Galileo. This selection was made because for lower elevation angles the performance of the technique was degraded due to the high directivity of the down-looking antenna array. The maps correspond to different ground tracks. The polarimetric ratio values at the specular reflection points were geolocated and represented over the Earth's surface using Google Maps for simpler interpretation. The ephemerides as provided by an on-board positioning receiver were used to derive the orbit parameters of the GNSS satellites, while the PYCARO trajectory was measured by the on-board receiver. cGNSS-R was used for data acquisition of GPS L1 C/A (Fig. 10.1a), GPS L2 C (Fig. 10.1b), GLONASS L1 C/A (Fig. 10.2a), GLONASS L2 C/A (Fig. 10.2b), GLONASS L2 P (Fig. 10.2c) and Galileo E1 BC (Fig. 10.2d) signals, while rGNSS-R for GPS L1 P(Y) (Fig. 10.1c) and GPS L2 P(Y) (Fig. 10.1d). The mean polarimetric ratio (PR) for GPS L1 C/A signals is ~ 8 dB and ~ 4.2 dB over lakes and boreal forests, respectively (Table 10.1). Additionally, it is found that for the so-called data-less signal GPS L2 C the ratio is, respectively, ~ 12.7 dB and ~ 8.1 dB over lakes and boreal forests. The reason that explains the higher values of PR of GPS L2 C as compared to GPS L1 C/A signals is that the depolarization of the direct signal (Table 10.2) is higher for L1 C/A than for L2 C signals ($\text{SNR}_{\text{GPS,L1C/A,LHCP}} = 13$ dB and $\text{SNR}_{\text{GPS,L2C,LHCP}} = 3$ dB), so that the ratio $\Gamma_{\text{RHCP-LHCP}} / \Gamma_{\text{RHCP-RHCP}}$ (Eqn. 10.1) is larger in the first case. As it can be appreciated in Table 10.2, the Signal-to-Noise Ratio (SNR) values of the direct signals at LHCP are higher for L1 than for L2. This empirical evidence shows that the degree of depolarization is lower for GPS L2 C signals.

Table 10.1. Mean polarimetric ratio over forests and lakes for GPS (L1 C/A, L2 C, L1 P(Y) and L2 P(Y)), GLONASS (L1 C/A, L2 C/A and L2 P) and Galileo (E1 BC) signals during the float phase of BEXUS 19 flight.

GNSS code	Elevation Angle (degrees)	PR (dB)	
		Forests	Lakes
GPS L1 C/A	$\theta_e \sim 70^\circ$	4.2	8
GPS L2 P(Y)	$\theta_e \sim 70^\circ$	14.6	20.4
GPS L1 P(Y)	$\theta_e \sim 70^\circ$	14.6	20.4
GPS L2 C	$\theta_e \sim 70^\circ$	8.1	12.7
GLONASS L1 C/A	$\theta_e \sim 70^\circ$	6.7	8.2
GLONASS L2 C/A	$\theta_e \sim 70^\circ$	6.3	x
GLONASS L2 P	$\theta_e \sim 70^\circ$	6.3	x
Galileo E1 BC	$\theta_e \sim 60^\circ$	4.1	x

Table 10.2. Signal-to-Noise Ratio at RHCP y LHCP of the direct GPS (L1 C/A, L2 C, L1 P(Y) and L2 P(Y)), GLONASS (L1 C/A, L2 C/A and L2 P) and Galileo (E1 BC) signals as function of the elevation angle during the float phase of BEXUS 19 flight.

GNSS code	SNR _{RHCP} (dB)	SNR _{LHCP} (dB)	SNR _{RHCP} (dB)	SNR _{LHCP} (dB)	SNR _{RHCP} (dB)	SNR _{LHCP} (dB)	SNR _{RHCP} (dB)	SNR _{LHCP} (dB)
	$\theta_e \sim 70^\circ$	$\theta_e \sim 70^\circ$	$\theta_e \sim 60^\circ$	$\theta_e \sim 60^\circ$	$\theta_e \sim 50^\circ$	$\theta_e \sim 50^\circ$	$\theta_e \sim 40^\circ$	$\theta_e \sim 40^\circ$
GPS L1 C/A	34	13	33	23	32	23	30	23
GPS L2 P(Y)	19	x	16	x	13	x	10	x
GPS L1 P(Y)	19	x	16	x	13	x	10	x
GPS L2 C	28	3	25	3	23	8	21	8
GLONASS L1 C/A	31	12	31	18	29	25	21	15
GLONASS L2 C/A	16	x	16	x	20	x	20	x
GLONASS L2 P	12	x	12	x	16	x	16	x
Galileo E1 BC	15	x	14	x	13	x	11	x

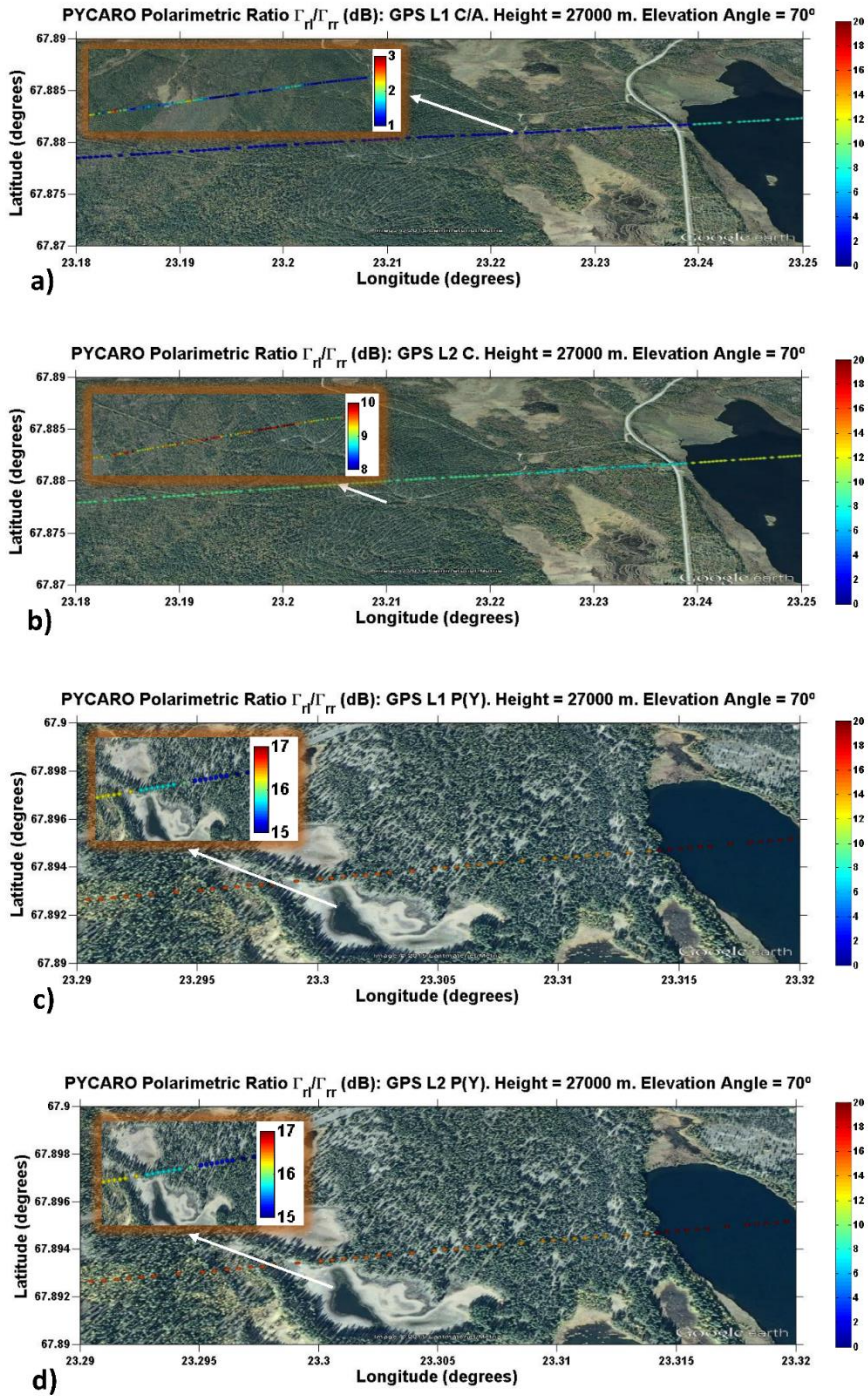


Fig. 10.1 Measured polarimetric ratios for a flight height of $\sim 27,000$ m and an elevation angle $\theta_e = 70^\circ$ for (a) GPS L1 C/A, (b) GPS L2 C, (c) GPS L1 P(Y), and (d) GPS L2 P(Y).

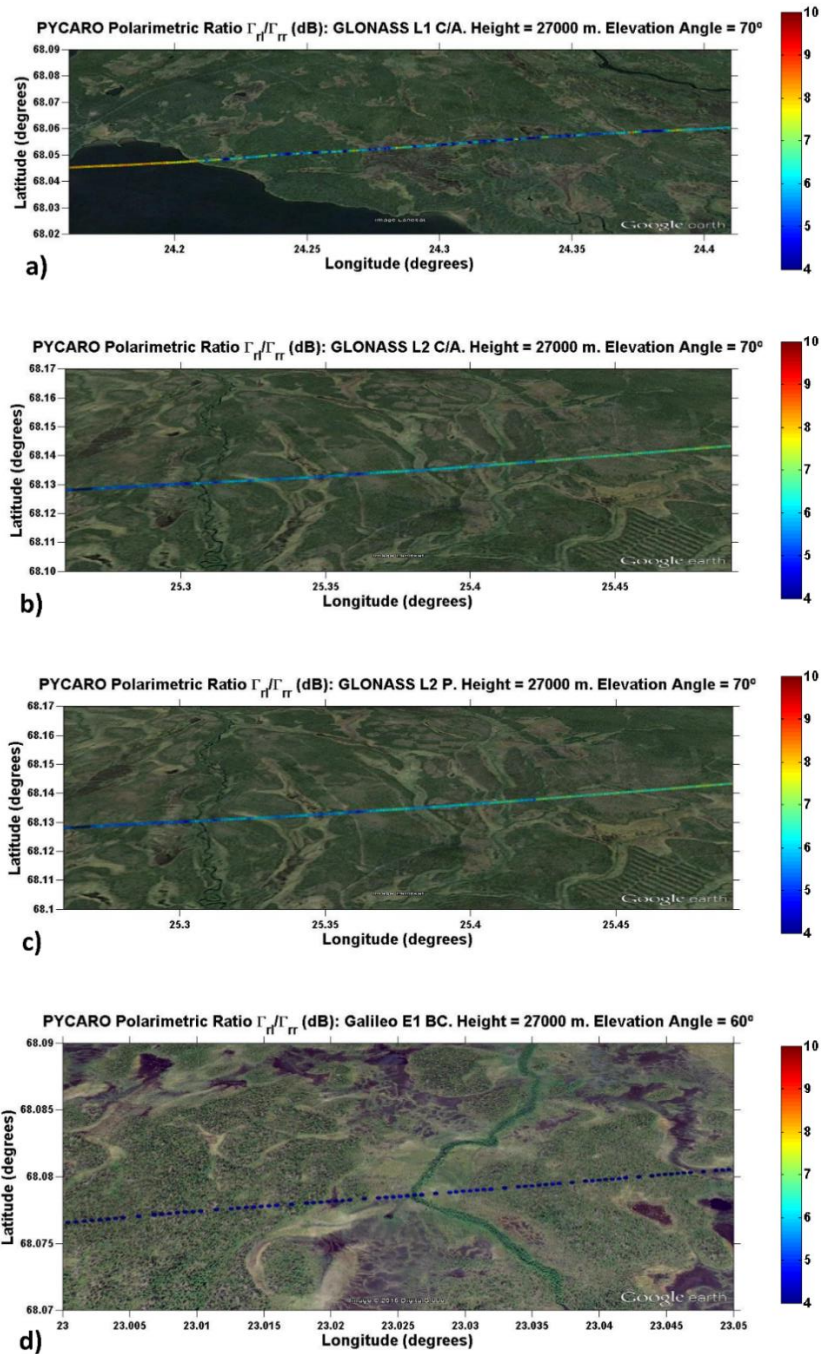


Fig. 10.2. Measured polarimetric ratios for a flight height of $\sim 27,000$ m and an elevation angle $\theta_e = 70^\circ$ for (a) GLONASS L1 C/A, (b) GLONASS L2 C/A, (c) GLONASS L2 P; and for an elevation angle $\theta_e = 60^\circ$ for (d) Galileo E1 BC.

The rGNSS-R is evaluated successfully for first time over forests, despite the large dispersion of the signal induced by the scattering media. The polarimetric ratio is larger as compared to the GPS L1 C/A signals, with a value ~ 20.4 dB and ~ 14.6 dB over lakes and boreal forests respectively. It is worth to point out some considerations about the squaring losses of the P(Y) code correlation technique implemented in PYCARO (rGNSS-R). They have a non-linear dependence with the SNR of the received signal [72, 83]: the lower the SNR, the larger the squaring losses [74]. Therefore, the polarimetric ratio as derived from the P(Y) code is higher because of the SNR of the collected RHCP signals is lower than the LHCP ones. Additionally the direct P(Y) signal depolarization is much lower as compared to the L1 C/A and the L2 C, which also contributes to a higher PR.

Maps of the mean polarimetric ratio for GLONASS L1 C/A (Fig. 10.2a), L2 C/A (Fig. 10.2b) and L2 P (Fig. 10.2c) are also included. Values over lakes are found to be ~ 8.2 dB for GLONASS L1 C/A signals, in agreement with GPS L1 C/A signals (Tables 10.1 and 10.2) because the corresponding direct signals have a similar level of depolarization, and the lakes scattering properties are the same independently of the track. On the other side, the effect of the different tracks (different forest structure) is manifested in the different values of the polarimetric ratio over forests because the signal depolarization due to the scattering, the propagation and the effect of multiple reflections. However, there were no signal acquisitions over lakes at RHCP for GLONASS L2 C/A and L2 P because the direct signal is found to be highly polarized (Table 10.2). Table 2 shows that there were no signal acquisitions of the direct GLONASS L2 C/A and L2 P signals at LHCP. This is an indication showing that these signals are highly polarized so that the SNR at LHCP is so low that could not be detected by the PYCARO instrument during the flight. This is an important observation for the design of future space-borne missions. On the other side, the following values are found over boreal forests: $PR_{GLONASS,L1CA} \sim 6.7$ dB, $PR_{GLONASS,L2CA} \sim 6.3$ dB and $PR_{GLONASS,L2P} \sim 6.3$ dB. The impact of the forest structure in the total scattered field is theoretically shown in the Section 4.2.3.

In this work, authors use the available ground truth data to interpret the results, but unfortunately there are no ground truth data for each track. The PR for GLONASS L2 C/A and L2 P are found to be equal over the same track because the direct signals were not depolarized (Table 10.2). Finally, it is found that the polarimetric ratio for

Galileo E1 BC over boreal forests for a different track and time of signal acquisition is $PR_{\text{Galileo,E1BC}} \sim 4.1$ dB.

A common characteristic for all the GNSS signals is that the polarimetric ratio is lower over boreal forests ($PR_{\text{GPS,L1CA}} \sim 4.2$ dB, $PR_{\text{GPS,L2C}} \sim 8.1$ dB, $PR_{\text{GPS,P(Y)}} \sim 14.6$ dB, and $PR_{\text{GLONASS,L1CA}} \sim 6.7$ dB) than over lakes ($PR_{\text{GPS,L1CA}} \sim 8$ dB, $PR_{\text{GPS,L2C}} \sim 12.7$ dB, $PR_{\text{GPS,P(Y)}} \sim 20.4$ dB, and $PR_{\text{GLONASS,L1CA}} \sim 8.2$ dB). In this scenario, in addition to depolarization effects due to scattering and propagation through the vegetation, multiple reflections involving canopy–soil and soil–branches increase the amount of co-polar signals in the final scattered field reaching the receiver. This point is supported by simulation results that show that the co-polar signal is dominant in case of multiple reflections for high elevation angles (Figs. 4.4d,e,f).

10.3 Final discussions

The BEXUS 19 stratospheric balloon experiment with an apogee of $\sim 27,000$ m has provided an unique opportunity to study for first time the scattering of GNSS signals over boreal forests. Multi-constellation (GPS, GLONASS and Galileo) reflected signals were collected by the PYCARO instrument at dual-band (L1, L2) and dual-polarization (RHCP, LHCP). The scientific evaluation of this dataset offers the opportunity to evaluate the feasibility of the GNSS-R to perform biomass monitoring which is a key-factor to analyze the carbon cycle. The main added value is the measurement of polarimetric signatures which shows sensitivity over forests and lakes. Additionally, different data acquisition techniques have been used: cGNSS-R for the open-source codes and the novel rGNSS-R for the encrypted P(Y) GPS code. Theoretical simulations of the reflectivity over boreal forests have been performed to help the interpretation of the empirical results. The scattering of the GNSS-R signals takes place over the soil and the canopy but also through multiple reflections involving canopy-soil and soil-branches interactions. This is an important issue that has to be considered to perform biomass monitoring since the vegetation provides a scattered field additionally to the effect of the attenuation on the signals reflected over the soil. Future work should include a study of: a) the potential advantages of the synergy

between both data access techniques, and b) scattering over different types of vegetated soils.

10.4 Conclusions

The polarimetric ratio and the mean polarimetric phase over boreal forests with a biomass density of $\sim 2,700$ trees/ha and for an elevation angle of $\theta_e = 70^\circ$ for GPS and GLONASS and $\theta_e = 60^\circ$ for Galileo vary in the ranges from approximate 2 to 16 dB and from approximate -1.4 to -9.6 m, respectively. This is due to the effect of different tracks, periods of signal acquisition, levels of depolarization of the direct signals and because of the squaring losses of the rGNSS-R. The polarimetric phase is found to be negative, which means that the center of phase of the reflected signals at LHCP is higher in the vertical profile of the forests as compared with RHCP signals. As the main conclusion, GNSS-R has been shown to have sensitivity to perform polarimetric measurements over lakes and boreal forests from a stratospheric balloon flight with an apogee of $\sim 27,000$ m using dual-band multi-constellation signals.

Additionally, a theoretical investigation (Section 4.2) of the different contributions to the total reflectivity over boreal forests has been performed and it is included in Section 4.2.2. A much lower tree density for a biomass density of 100 t/ha (725 trees/ha instead $\sim 2,700$ trees/ha as in [42] for a tree height ~ 20 m) was required to make the simulations feasible; however results can be extrapolated. The scientific evaluation of this study (Table 10.3) offers the opportunity to evaluate the feasibility of the GNSS-R to perform biomass monitoring which is a key-factor to analyze the carbon cycle.

Table 10.3. Summary of the key observation and simulation results.

Experimental Polarimetric Ratio GPS L1 C/A Forests, $\theta_e \sim 70^\circ$	4.2 dB
Experimental Polarimetric Ratio GPS L1 C/A Lakes, $\theta_e \sim 70^\circ$	8 dB
Simulated Polarimetric Ratio branches, 725 trees/ha, $\theta_e \sim 70^\circ$	5 dB
Simulated Polarimetric Ratio leaves 725 trees/ha, $\theta_e \sim 70^\circ$	5 dB
Simulated Polarimetric Ratio soil 725 trees/ha, $\theta_e \sim 70^\circ$	20 dB

PART IV:

**TOWARDS A SPACE-BORNE MULTI-
CONSTELLATION, DUAL-FREQUENCY AND
DUAL-POLARIZATION GNSS-R MISSION**

11

11. ³Cat-2; AN EXPERIMENTAL NANO-SATELLITE FOR GNSS-R EARTH OBSERVATION: MISSION CONCEPT AND ANALYSIS

11.1 Introduction

During the last decades aerospace engineering was focused in the development, design, and manufacturing of mostly large satellites. Nowadays, with advances in microelectronics and computing, following the advances in cell phones technologies many of the functions of a satellite can be implemented in a few integrated circuits. Small satellites are therefore becoming a true alternative for some Earth Observation techniques [152] with reduced dimensions and weight of the spacecrafts and payloads, missions based on small satellites can be conceived, implemented and launched at a reasonable cost. The CubeSat concept [153] was originally devised by Prof. Jordi Puig-Suari at California Polytechnic State University (Cal Poly) and Prof. Bob Twiggs at Stanford University's Space Systems Development Laboratory. CubeSats of one, two or three units (roughly $10 \times 10 \times 10 \text{ cm}^3$, $10 \times 10 \times 20 \text{ cm}^3$, $10 \times 10 \times 30 \text{ cm}^3$ [153]) offer an standard approach to develop pico and nano-satellites, and provided a standard to launch them into space, especially for research groups. In 2011, a second standardization including 6, 12 and 27 units CubeSats was carried out [154]. These architectures have the potential to combine the temporal resolution of GEostationary Orbit (GEO) missions with the spatial resolution of Low Earth Orbit (LEO) missions, thus changing the traditional trade-off in Earth Observation mission design [152]. At present, numerous CubeSats for technology and scientific demonstration, as well as for Earth Observation have already been launched [152]. Even constellations of 3U CubeSats are planned for Optical Earth Observation or for Radio-Occultations [155].

The intrinsic multi-static nature of GNSS-R techniques provides improved spatio-temporal resolution [45]. The first space-borne measurement of an Earth-reflected GPS signal took place during the Space-borne Imaging Radar-C (SIR-C) mission in 1994 [25] using an L-band antenna of $12 \times 2.7 \text{ m}^2$. The collected data helped to estimate the Signal-to-Noise Ratio (SNR) during the preparatory activities of the SAC-C and CHAMP missions. CHAMP collected reflected GPS signals during the GPS radio-occultations operational mode at very low elevation angles [156]. The first space-borne proof-of-concept of GNSS reflectometry from space took place with the data logger on-board the UK-DMC [54]. Samples of the GPS signals reflected over ocean, land and ice were collected, downloaded and processed on-ground. The nadir-

looking antenna was composed of three LHCP GPS patches at L1 (1575.42 MHz), with a total gain at boresight of ~ 12 dB. In June 2014 the UK TechDemoSat-1 from SSTL was launched [157], and at present, at least three other space-borne missions are approved or under-study: the Cyclone Global Navigation Satellite System (CyGNSS) from NASA [142] to be launched in Q4 2016, the PAssive Reflectometry and Interferometry System In-Orbit Demonstrator (PARIS-IoD) from the European Space Agency (ESA) [3] now reincarned in the GNSS rEfectometry Radio Occultation and Scatterometry experiment on-board International Space Station (GEROS-ISS) experiment [128]. The CyGNSS mission consists of a constellation of 8 microsatellites (1470 mm x 430 mm x 200 mm) and it is expected to be launched in 2016. The TechDemoSat-1 is a multi-payload microsatellite (770 mm x 500 mm x 900 mm) including the SGR-ReSI GNSS-R instrument [158], which is the precursor of the CyGNSS payloads. The TET-1 platform was selected for PARIS-IoD (1100 mm x 900 mm x 880 mm). An additional deployable structure should be designed for the accommodation of the antenna array. Table I summarizes the main specifications of the different subsystems for these missions: TechDemoSat-1, CyGNSS and PARIS-IoD. Additionally, Phase A studies have been done to perform GNSS-R using smaller platforms [159]: MicroGem (130 kg), NanoGem (50 kg), and Nano X (50 kg).

This work presents the mission concept and analysis of ³Cat-2: a 6U CubeSat performing multi-constellation, dual-band (L1, L2), and dual-polarization (RHCP, LHCP) GNSS-R to be launched in Q2 2016. The ³Cat-2 mass is ~ 7 kg, the average power generated on-board per orbit period is ~ 6 W and the expected payload data volume is up to ~ 10 MB per day. Section 11.2 describes the scientific objectives, Section 11.3 presents the mission concept, and the architecture of the instrumentation is described in Section 11.4 including a detailed explanation of the different subsystems of the spacecraft. Section 11.5 summarizes the mission analysis. Finally, Section 11.6 summarizes the main results of this study.

Table 11.1. Overview of the most relevant subsystems for TechDemoSat-1, CyGNSS and PARIS-IoD.

	TechDemosat-1	CyGNSS	PARIS-IoD
GNSS-R instrument	SGR-RESI	DMR	(Under development)
ADCS	3-axes (CubeSat technology)	3-axes	3-axes
TT&C	Full-duplex: S-band 400 Mbps Down-link: X-band 400 Mbps	Down-link: S-band 1.25 Mbps (science), S-band 2-64 kbps (housekeeping). Up-link: S-band 125-2k bps	Down-link: X-band 95 Mbps (science), S-band 137.5 kbps (housekeeping). Up-link: S-band 5 bps
Battery	Saft	3 Ahr Li-Ion	NA
Determination	Sun sensors, magnetometers, gyroscopes	Pitch/roll horizon sensors, 3 magnetometers (Precision = 2.1° , $3\text{-}\sigma$)	Star trackers (Precision = 30 arcsec)
Control	Magnetorquers	Pitch momentum wheel (30 mMns @ 5600 rpm, 2 mNm torque) (Precision = 2.3° , $3\text{-}\sigma$), and 3 magnetorquers (1 Am^2 , residual moments $< 0.1\text{ Am}^2$)	Reaction wheels (Precision = 5 arcmin) and magnetorquers
Position	NA	NA	Dual frequency GPS receiver (Accuracy = 0.3 m, $1\text{-}\sigma$)
Thermal	Heaters	Multi-Layer Insulation (MLI), surface finishes, and heaters	Insulation layers, thermal fillers, heaters, and thermistors
Mass	150 kg	17.6 kg	170 kg
Zenith antenna	1 RHCP L1/L2 (1 patch), 2 RHCP L1 (1 patch each one)	1 RHCP L1 (1 patch)	19 RHCP radiators
Nadir antenna	1 LHCP L1/L2 (4 patches), dielectric air	2 LHCP L1 (3 patches each), dielectric air	19 LHCP radiators
Duty cycle	NA	100%	97% (non-eclipse), 75 % (eclipse)
Radiation Total Dose	NA	$> 5\text{krad}$	NA
Solar panels	52 W	Cell eff. (EOL) 28.5 % , 0.22 m^2 , Triple junction (InGaP/InGaAs/Ge)	166 W (After 5 years)
Platform	1 microsatellite	8 separate microsatellites	1 microsatellite (TET-1)

11.2 Mission objectives

The main goals of ³Cat-2 mission are two fold: 1) to explore some new GNSS-R techniques in particular the reconstructed and interferometric ones, and 2) to acquire data over different targets to obtain algorithms to derive geophysical parameters. ³Cat-2 is a modest research and demonstration mission to advance in our understanding of the main state-of-the art techniques for space-borne GNSS-R ocean and ice altimetry and scatterometry for sea state determination, soil moisture measurements, and biomass monitoring. The main mission objectives of ³Cat-2 mission are:

1. To demonstrate the capabilities of nano-satellites for Earth Observation, and in particular those based in the CubeSat standard.
2. To perform an inter-comparison of the achievable altimetric precision using conventional GNSS-R (cGNSS-R), interferometric GNSS-R (iGNSS-R), and reconstructed code GNSS-R (rGNSS-R) [160] for methodology demonstration, error budget validation, and study of the spatio-temporal resolution, and its comparison with data of traditional monostatic radar altimeter data.
3. To evaluate the sensitivity of GNSS-R for sea state determination as a function of the wind speed or sea state conditions.
4. To evaluate the potential application of GNSS-R over land surfaces, and in particular to infer soil moisture and vegetation biomass, with special focus over boreal forests, where other missions (e.g. ESA's BIOMASS mission [140]) will not be able to.
5. To perform an inter-comparison of the GNSS-R scattering properties as a function of the autocorrelation properties of the different available GNSS signals of opportunity (GPS, GLONASS, Galileo and COMPASS). In particular, to map the performance of the different scientific applications as function of the center frequency, receiver bandwidth, signal polarization, access technique, chipping rate, coherent and incoherent integration times and satellite elevation angle.

-
6. To empirically evaluate the coherent-to-incoherent scattering ratio over land, ocean and cryosphere, and
 7. To evaluate the potential synergy between closed- and open-loop correlation techniques [57, 83].

11.3 Mission concept

This Section describes the concept of the ³Cat-2 mission: orbit, platform, payload and in-orbit operations.

11.3.1 Orbit selection

The fundamental mission objective is to collect scattered GNSS signals over land, ocean and cryosphere surface targets in a nadir-looking configuration. The satellite will operate in a Sun-Synchronous Orbit (SSO) with a Local Time of Ascending Node (LTAN) of 00:00 h (AM), and an orbit reference height of ~ 510 km. As it will be shown (Section V) the altitude decay is 3 km and the LTAN increment is 5.5 min in a 3 years extended mission lifetime. Therefore, the orbit is stable and there is no need to use a propulsion subsystem. A 6 days revisit time goal is also achieved with a down-looking antenna array beam-width of 70° .

11.3.2 Platform selection

In GNSS-R the access to the geophysical information is cast in the so-called Delay Doppler Maps (DDMs) [160]. The performance of the scientific objectives depends on the Signal-to-Noise Ratio (SNR) which benefits from a large antenna size.

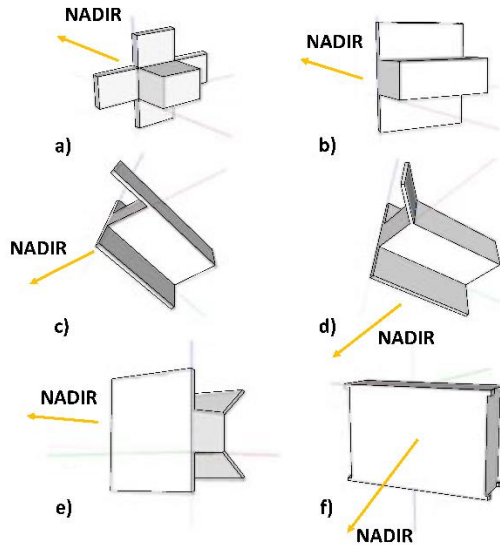


Fig. 11.1. Artist view of the 1U, 2U, and 6U CubeSat configurations considered during the ³Cat-2 mission feasibility study: 1U (a), 2U, (b,c,d,e), 6U (f).

Table 11.2. Key mission requirements.

Orbit	SSO, mean LTAN = 00:00 h AM, $450 < H_{ref} < 650$ km
Revisit Time	12 days
ADCS maximum error	7.5° (3- σ) in nominal mode including guidance, determination and control
Antenna Nadir	Dual frequency (L1, L2) antenna array
Antenna Nadir	Dual polarization (RHCP, LHCP) antenna array
Antenna Nadir	Minimum gain antenna array of 11 dB
Payload duty cycle	Payload duty cycle of at least 10 % orbit period

On the other hand, the ³Cat-2 mission is constrained to a CubeSat platform, which imposes serious constraints to the size of the downlooking antenna, and the size of the solar panels required for power generation. During ³Cat-2 feasibility study (Tables 11.2 and 11.3) several configurations were analyzed from 1U to 6U CubeSat platforms (Fig. 11.1 and Table 11.3). After a careful study, it was found that configurations (e) (using a passive magnetic Attitude Determination and Control System ADCS) and (f) (Earth Centered Inertial ECI velocity alignment with nadir

Table 11.3. Different satellite configurations considered during the feasibility study.

N° U	1	1	1	1	1	1
Configuration	a	a	a	a	a	a
Mass (g)	1,345	1,545	1,345	1,522	1,522	1,522
Generated Power (W)	1.6	2.6	0.9	1.4	0.3	1.3
Attitude Determination and Control System	Passive magnetic	Passive magnetic	Passive magnetic	ECI velocity alignment with nadir constraint	ECI velocity alignment with nadir constraint	Spin about nadir
N° solar cells	8	16	8	8	8	8
N° U	1	2	2	2	2	2
Configuration	a	b	b	b	c	d
Mass (g)	1,522	1,593	1,770	1,770	1,693	1,693
Generated Power (W)	0.3	2.6	2.6	2.5	3.4	3.3
Attitude Determination and Control System	Spin about nadir	Passive magnetic	ECI velocity alignment with nadir constraint	Spin about nadir	Passive magnetic	Passive magnetic
N° solar cells	8	14	14	14	18	18
N° U	2	6	6	6	6	6
Configuration	e	f	f	f	f	f
Mass (g)	2,274	4,100	4,100	4,100	4,100	4,100
Generated Power (W)	5.3	6.6	6.2	6.6	6.6	4.3
Attitude Determination and Control System	Passive magnetic	ECI velocity alignment with nadir constraint	ECI velocity alignment with Sun constraint	ECF velocity alignment with radial constraint	ECF velocity alignment with nadir constraint	Spin about nadir
N° solar cells	30	32	32	32	32	32

or radial constraint ADCS and Earth Centered Fixed ECF velocity alignment with nadir constraint ADCS) satisfy the link and the power budget requirements, although the configuration (e) requires deployable solar panels, and downlooking payload antenna (to be designed). Due to a higher risk the final selected configuration for ³Cat-2 platform was a 6U CubeSat [129, 161], (f) in Fig. 11.1 without any deployables (see Appendix B,C, and D).

11.3.3 Payload

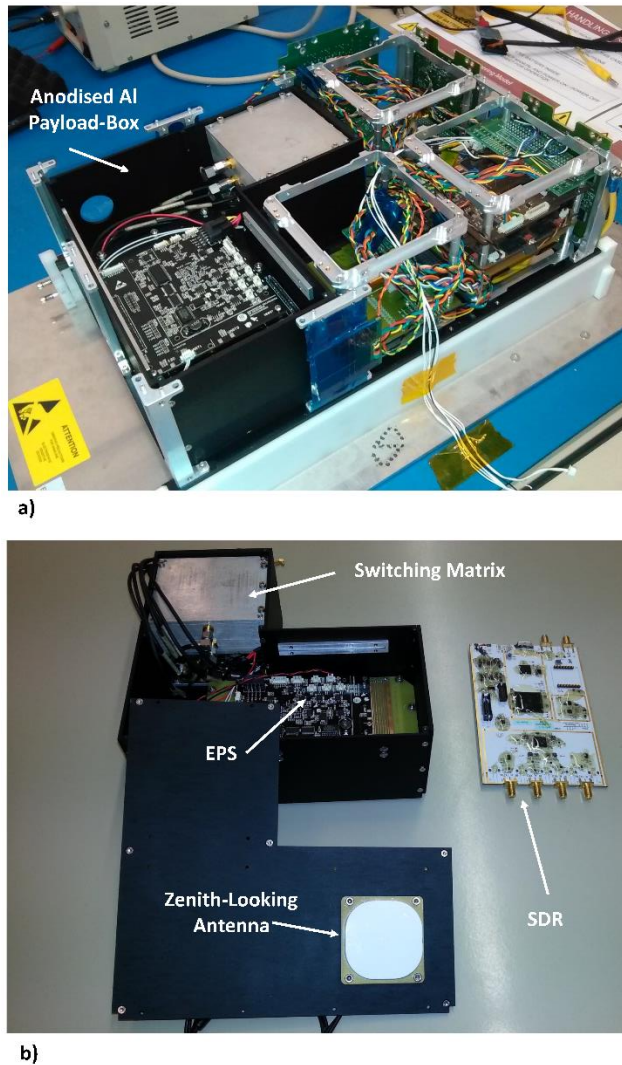
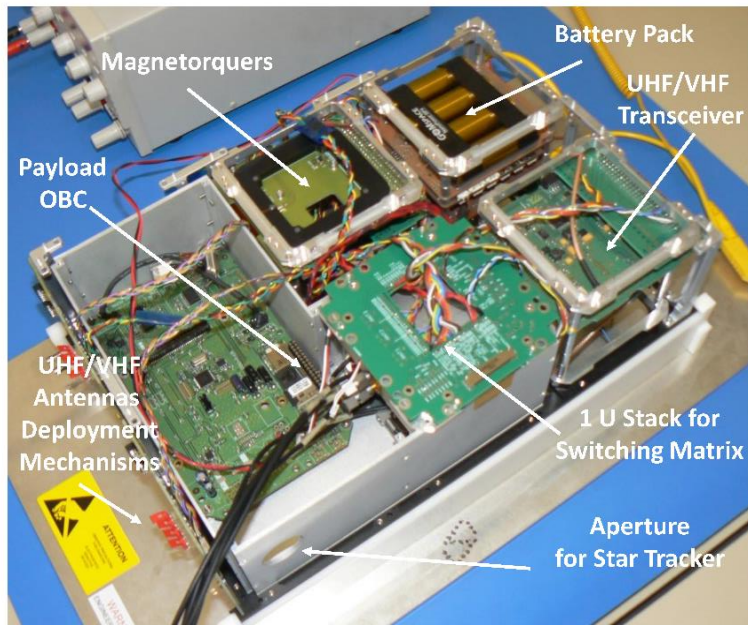
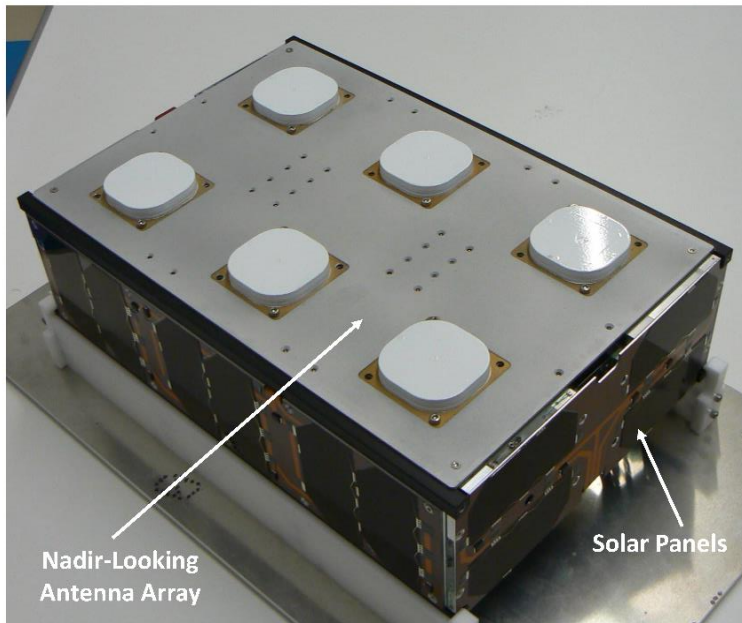


Fig. 11.2. (a) Image of the ³Cat-2 Engineering Model (EM) with the payload inside the 3 mm thickness Al anodised box (in black). (b) Image of the ³Cat-2 Engineering Model (EM) with the payload inside the 3 mm thickness Al anodised box (in black).

The ³Cat-2 payload (Fig. 11.2) is the so-called P(Y) & C/A ReflectOmeter (PYCARO) [83]. It was designed and developed in parallel to the platform and tested in several ground-based, airborne and stratospheric balloon flights field experiments.



a)



b)

Fig. 11.3. (a) Image of the ³Cat-2 EM: Payload OBC, magnetorquers, battery pack, UHF/VHF transceiver, 1U stack for switching matrix, 3 mm width payload Al box (3U stacks), aperture for star tracker, and UHF/VHF antennas deployment mechanisms. (b) Image of the ³Cat-2 EM with the nadir-looking antenna array integrated at the top of the structure.

The definitive proof-of-concept of the payload took place in two ESA-sponsored stratospheric balloon experiments launched from Esrange Space Center (Sweden). The apogee was $\sim 27,000$ m, and PYCARO collected GNSS-R reflections mostly over boreal forests, and some lakes [40, 143]. The ³Cat-2 payload comprises a set of subsystems accommodated on the upper 3U volume of the structure (Fig. 11.3). All of these elements provide the mechanical and electrical interface between the payload and the platform. To reach the mission objectives outlined in Section 11.2, the ³Cat-2 payload must be capable of receiving multiple GNSS reflected signals coming from different directions within a wide angular range. In addition, the signals have to be received with a sufficiently high antenna gain so as to guarantee range measurements, crucial for the first priority mission objective (altimetry). The selected antenna type is a six dual-frequency (L1 and L2) and dual-polarization (RHCP and LHCP) patch array whose output signals combined to form a single high gain beam pointing to the array boresight. In order to optimize the Noise Figure (NF), each element of the antenna array includes a low noise amplifier (LNA), necessary to ensure optimal SNR ($G = 33$ dB, $NF = 2.2$ dB). A switching matrix routes the up/down signals at the appropriate polarization to the payload receiver. The RF signals are converted to baseband before entering the PYCARO back-end in which the different observables for the various applications are obtained. The ³Cat-2 payload consists of the following subsystems:

1. A dual-band (L1, L2), dual-polarization (RHCP, LHCP) zenith-looking antenna patch to collect the direct GNSS signals, and nadir-looking 3×2 patch antenna array (Fig. 11.3b) to collect the Earth-reflected signals. Figure 4 shows the measured antenna patterns at the UPC anechoic chamber [162]. The total gain of the array was 12.9 dB at L1-LHCP, 13.3 dB at L1-RHCP, 11.6 at L2-LHCP and 11.6 dB at L2-RHCP (Fig. 11.4).
2. A dual-channel Software Defined Radio (SDR) that samples data collected from the up and down-looking antennas, both in-phase and quadrature, with 8 bits precision, at a rate of 5 Msamples/s³⁶.

³⁶ This sampling rate is not enough to test the iGNSS-R technique. The directivity of the up-looking antenna is not optimum either, but at least the three GNSS-R techniques (cGNSS-R, iGNSS-R and

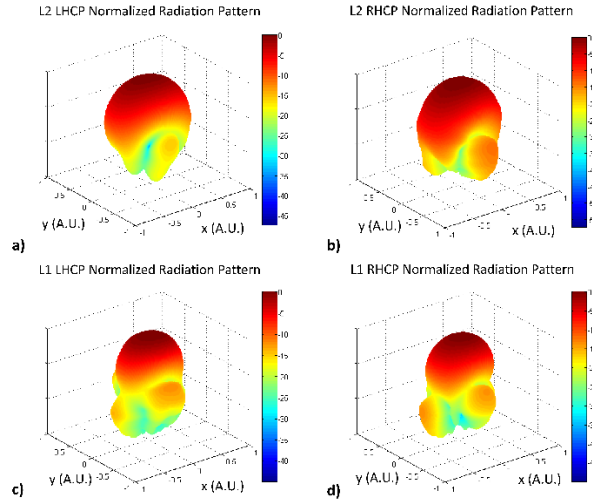


Fig. 11.4. Antenna array radiation patterns and gain values for both frequencies (L1, and L2) and for both polarizations (LHCP and RHCP).

3. A Gumstix Overo IronStorm OBC that manages the payload, configures the SDR and computes the DDMs. This OBC has flight heritage [163], reduced power consumption, and volume. It runs a Linux operative system, the CPU is an ARM Cortex 8 A8 up to 1 GHz, and the RAM is 512 MB. The OBC runs the so-called ³COPS (³Cat-2 Orchestration Payload System) orchestration payload system to perform the complete scheduling of the data handing activities, and to command the payload subsystems (Fig. 11.5).

4. An self-designed EPS for the payload operations using Commercial Off-the-Shelf (COTS) components to allow turning on and off the different payload modules for improved power management.

The complete payload will be embedded into a 3 mm thickness Aluminum anodised box (Fig. 11.2) to keep the effect of the total ionization dose below 10 krad for an extended mission lifetime of 3 years.

rGNSS-R) could be inter-compared in the same conditions. Sampling rate can be increased only if one channel is sampled.

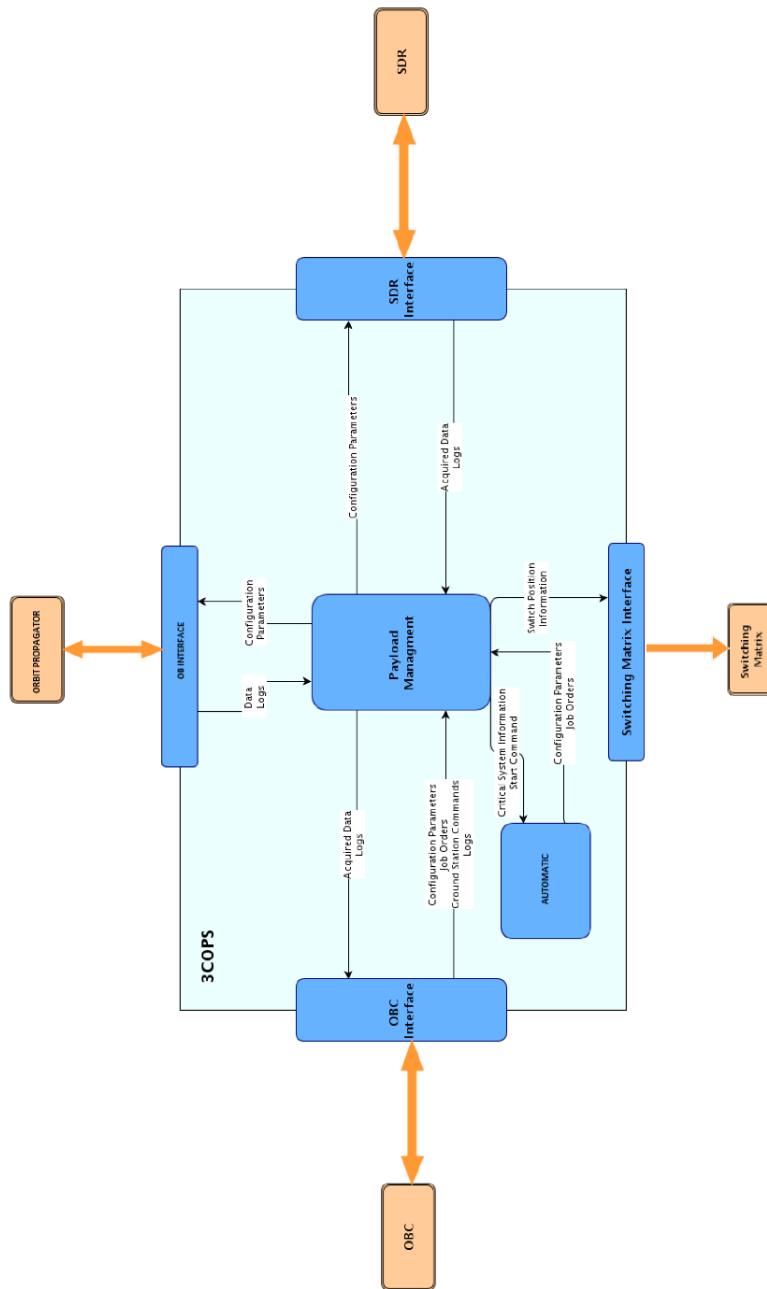


Fig. 11.5. Sketch of the main modules of the ³COPS orchestrator. It identifies the internal modules (Payload Management Module (PMM), Automatic Module (AM) and Log Module (LOG)) and the internal/external interfaces. The orange arrows represent the connections with the payload subsystems, related with hardware interfaces. The grey arrows are related with the internal software interfaces. Image credits Deimos Engenharia.

11.3.4 In-orbit operations

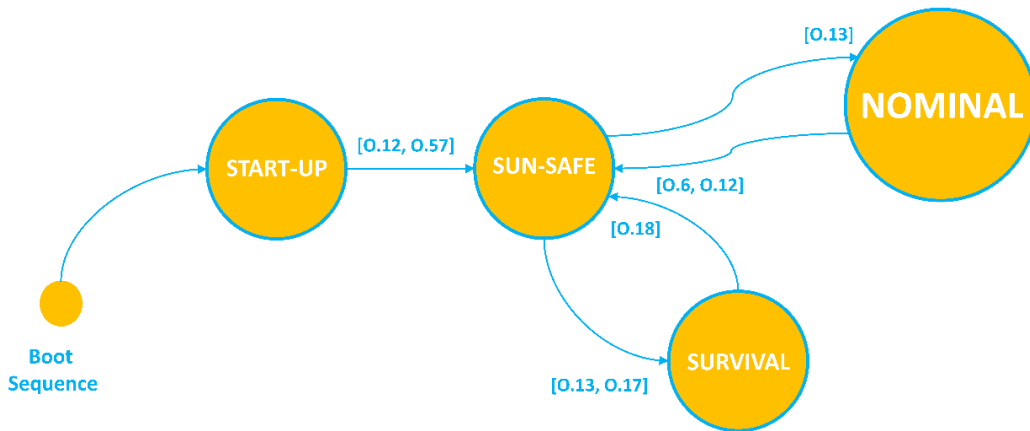


Fig. 11.6. Satellite state diagram. The satellites operational modes are: Start-Up (SU), Sun-Safe (SS), Nominal and Survival. [O.6] The exits of the Nominal mode shall be: a) Exit to SS mode upon SS mode triggers (autonomously), b) exit to SS mode through Ground Station (GS) telecommands, c) exit to Survival mode upon SS mode triggers (autonomously), d) exit to Survival mode through GS telecommands. [O.12] The triggers of the SS mode shall be: a) EPS fault: Battery voltage < 90%, b) ADCS fault: Any failure that endangers power so that battery voltage < 90%., c) CDHS fault. [O.13] The SS mode exist shall be only possible by GS telecommands to: a) Nominal mode, b) Survival mode, c) SU mode. [O.17] The triggers of the Survival mode shall be: a) EPS critical fault: Battery voltage < 80%, b) ADCS critical fault: any failure that endangers power so that battery voltage < 80%, c) CDHS critical fault. [O.18] The Survival mode exist shall only possible to SS mode by GS telecommands. [O.57] The exits of the SU mode shall be: a) exit to Nominal mode upon SU mode triggers (autonomously), b) exit to Nominal mode through GS telecommands, c) exit to SS mode upon SU mode triggers (autonomously), d) exit to SS mode through GS telecommands, e) exit to Survival mode upon SU mode triggers (autonomously), f) exit to Survival mode through GS telecommands.

The planned in-orbit operations will follow the following sequence (Fig. 11.6):

1. Boot sequence.

2. Stat-Up mode: In this mode the Command and Data Handling System (CDHS) is in its nominal mode, the Electrical Power System (EPS) only provides electrical power to the main On Board Computer (OBC), and to the deployment system of the communications antenna. The beacon is activated allowing to track the satellite from ground.

3. Sun-Safe mode: This is the first level of bus contingency operations. The different subsystems are turned-on and checked sequentially from the ground station, the ADCS performs the detumbling, and once rotations have stopped the Sun-tracking to increase the energy storage in the batteries.

4. Nominal mode: The satellite will turn into to this mode if the battery voltage is higher than 90 % of the nominal value, and the platform angular rate is lower than 0.5 °/s. The Nominal mode possess contingency operations for extended loss of communications. In particular, the system is capable to generate automatically scientific data, and store them on-board. On the other side, the ground segment is capable to inhibit any on-board automatic function, and to take full control of the schedule by telecommands, i.e. selection of the satellite operational mode, selection of the payload mode, upload new ADCS configurations, upload configuration files to the payload OBC, to reset the payload, and to downlink the housekeeping and the scientific data.

5. Survival mode: The satellite will switch into this mode if the battery voltage is lower than 80 % of the nominal value and/or if a critical ADCS or on-flight software error is detected. In this mode only sequences of highest priority are executed, and it is only possible to exit this mode by telecommands.

In nominal mode the satellite will perform on-board the data pre-processing, and the downlink of compressed datasets to the ground segment. The compression will be performed using an innovative software called FAPEC [164] developed for the Gaia mission, which achieves lossless compression ratios of ~ 1.5 and lossy compression ratios up to ~ 40 . The P(Y) & C/A Reflectometer (PYCARO) payload [83] will be operated in closed- and open-loop modes, and for cGNSS-R, iGNSS-R and rGNSS-R modes. Dual-band (L1, L2) measurements will be acquired for the ionospheric delay correction in altimetry. Direct and reflected signals will be acquired at dual-polarization (LHCP and RHCP) by switching the up- and down-looking antennas for biomass studies. The payload will also be operated using different (to be optimized during the commissioning phase) configurations (e.g. coherent and incoherent integration times, optimum tracking loop parameters), for each surface target (ocean, land and cryosphere). The criteria for using different payload configuration files is determined by the mission objectives, in particular, the evaluation of: maximum

coherence time over ocean surface, the potential saturation of the reflected signals at L-band over Amazon rain forests (biomass density up to ~ 500 t/ha), coherent-to-incoherent ratio of the scattered field, and dual-band measurements over sea ice to demonstrate ice altimetry. Additionally telecommands will be sent from the ground segment to schedule data collections (latitude and longitude of relevant areas of study).

11.4 Platform subsystems

This Section describes the different subsystems of the satellite. The technical specifications and the design is included.

11.4.1 Mechanical structure

The structure is composed of six 1U PCB stacks and structural brackets (Al 6082) sandwiched between two side frames (Al 6082). The structural brackets provide mechanical strength to the platform as well as mechanical interfaces. The 6U shape (340.5 x 226.3 x 100 mm) is optimum for the dual-band (L1 and L2) 6-patches antenna array. A single-patch antenna is placed in the opposite side for collection of the direct GPS signals. The satellite is configured without moving mechanisms or propulsion subsystem. The only deployable structures are the monopoles used for communications: (2 at UHF, 2 at VHF: nominal and redundant, one at S-band). Two pairs of orthogonal monopoles (Figs. 11.7 and 11.8) with wide antenna beams ensure communications with the ground station even in case of ADCS failure. The avionics is placed in the 3U volume at the bottom of the structure (Fig. 11.3a). The upper 3U

Table 11.4. Technical specifications of the mechanical structure.

Property	Value
Mass	1,200 g
Outside Envelope	100 mm x 227 mm x 341 mm
Thermal Range	[-40, +90] °C
Maximum Supporting Mass	12,000 g

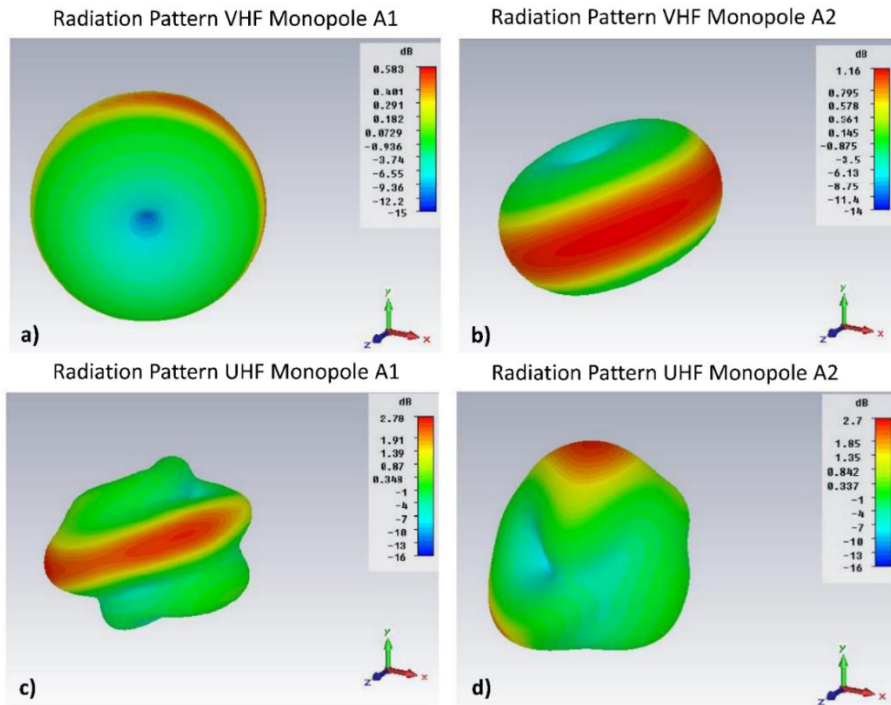


Fig. 11.7. Antenna radiation pattern of the two pairs (UHF-uplink, VHF-downlink) of orthogonal monopoles. Image credits ISIS Space.

volume is dedicated to the PYCARO payload (Fig. 11.2). Primary shear and axial loads are carried by the nano-satellite primary structure, providing full compliance with the dynamic launch vehicle envelope. The thermal control design provides thermal stability and minimizes thermal gradients through surface treatments, but also patch heaters are used to maintain the batteries in their operational temperature range.

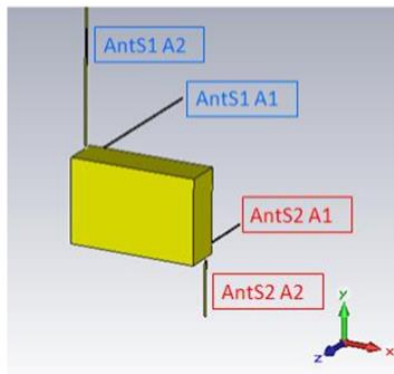


Fig. 11.8. Configuration of the VHF (Ant S1 A1 and Ant S1 A2) and UHF (Ant S2 A1 and AntS2 A2) monopoles in the CubeSat. Image credits ISIS Space.

11.4.2 Telemetry, tracking and command

The scientific data downlink is performed at S-band (2100 MHz), using a Binary Phase Shift Keying (BPSK) modulation, with a data rate up to 115 kbps (Table 11.5). Housekeeping data is downlinked at VHF (145,995 MHz) with a BPSK modulation at a data rate up to 9.6 kbps, while the uplink of telecommands is performed at UHF (437,940 MHz) with a Multiple Frequency Shift Keying (MFSK) modulation, at a data rate up to 1.2 kbps (Tables 11.6 and 11.7). The UHF receiver is always on, and always decoding AX.25 frames. The ground segment is located at UPC premises and includes a 3 m S-band dish, and two dual-polarization UHF/VHF yagi antennas. Telemetry collects and formats at high level the housekeeping and scientific data. These data are stored for later downlink respectively at VHF and S-bands. The storage software controls the data acquisition, recording, and playback of housekeeping and scientific data using respectively 2 GB, and 8 GB on-board memories for data storage. Data storage allows for more than 5 days of continuous scientific operations without downlink, providing significant margin for contingency operations. The Flight Model (FM) includes a second redundant UHF/VHF transceiver as a back-up system in case of failure of the nominal one. Additionally a beacon mode will be used to find and track the satellite (e.g. when the satellite has been ejected from the launch vehicle

Table 11.5. Technical specifications of the S-band transmitter.

Property	Value
Supply Voltage Range	[6.5, 30] V
Downlink Modulation	BPSK, GMSK
Transmitter Frequency Range	[2,100, 2,500] MHz
Frequency Accuracy	± 10 kHz
Transmit Power	Up 28 dBm average
Mass	62 g
Envelope	Format PC/104, width 15 mm
Downlink Rate	Up to 100 kbps
Power Consumption	3.5 W

Table 11.6. Technical specifications of the UHF/VHF transceiver.

Property	Value
Supply Voltage Range	[6.5, 12.5] V
Power Consumption	1.55 W (transmitter on), 0.2 W (receiver on)
Transmitter Frequency Range	[140, 150] MHz
Receiver Frequency Range	[430, 440] MHz
Transmit Power	22 dBm average
Mass	90 g
Envelope	Format PC/104, thickness 15 mm
Downlink Rate	9,600 baud
Uplink Rate	1,200 baud
Downlink Modulation	BPSK
Uplink Modulation	Both AFSK and MFSK must be supported

Table 11.7. Technical specifications of the UHF/VHF antennas.

Property	Value
RF Impedance	50 Ohm
Max RF Power	2 W
Frequency Range	[10, 13] MHz bandwidth within [130, 500] MHz
Mass	100 g
Envelope: (l x w x h)	98 mm 98 mm x 7 mm
Qualified Operational Temperature Range	[-20, +60] °C

Storage Temperature Range	[-50, +85] °C (Relative Humidity (RH) < 60%)
Supply Voltage Range	[3, 3.6] V (3.3 V nominal)
Typical Current Consumption	9 mA at 20 °C
Antenna Return Loss at Resonance Frequency	-10 dB

or when the satellite is in Sun-safe state). It will be active during all the satellite operations without requiring intervention of any other subsystems.

11.4.3 Attitude determination and control system

The total ADCS error (guidance, navigation and control) shall be lower than 7.5° ($3\text{-}\sigma$). The ADCS uses a 3-axis magnetorquer system [165] providing 0.2 Am^2 of nominal magnetic dipole per actuator. The combination of two torque rods (0.2 W of actuation power) with a flat air core torquer (0.57 W) reduces the required volume and provides equal magnetic moments in all the three dimensions (Table 11.8). The necessary condition for power optimality of a control law is that the magnetic moment lies on a 2-dimensional manifold perpendicular to the geomagnetic field vector. The attitude determination strategy includes (one) 3-axes gyroscope, (two) 3-axes magnetometer, and (six) photodiodes located each side of the platform.

The ADCS has three primary states of operation: detumbling, Sun-tracking, and nadir-pointing (nominal mode). The detumbling is performed after separation from the CubeSat deployer, and for anomaly recovery if the rotation rate overpass $0.5 \text{ }^\circ/\text{s}$.

The detumbling states uses a B-dot algorithm to drive magnetic dipole moments opposed to the rate of change of the magnetic vector (both measured in body coordinates). It only uses the sensed magnetic field to determine a rough attitude. The satellite changes to nadir acquisition once the body rates are damped if the battery state is high enough ($> 90 \%$).

During scientific observations, the satellite motion can be regarded as in the vicinity of the reference. Thus an application of a linear model of the satellite equations of motion is selected [166]. Multiple sensors of different types can be used to update the

estimated state vector [167]. When a low accuracy measurement is used to update the state vector, it will be weighted lower than a predicted model. On the other side, when a high accuracy measurement is used to update the state vector, it will be weighted much more heavily than the predicted model. The result is an estimation that when properly implemented can provide more an accurate state estimation then the direct measurements alone. In order to cope with different sensors producing data at different rates for the Extended Kalman Filter (EKF) [168] superposition of the updates is used [169] because it linearizes the propagation and updates equations about the current state estimate [167]. This technique consists of updating the gain, error covariance, and state error vector with each successively available measurement. The EKF will propagate the estimated state and covariance matrix until the next measurement or set of measurements are available. This also significantly reduces the OBC requirements because just a 3×3 matrix inverse is required instead of a $3n \times 3n$ matrix needed to compute a gain matrix [168]. The EKF used is based in the work done by Tuthill [167]. This EKF creates an accurate attitude estimation using the sensors selected for the ³Cat-2, but also the performance will be appropriate to be implemented in the OBC.

Computation of the infinite and finite horizon attitude controllers are not optimum to be implemented in a real-time OBC. A simple constant gain attitude controller is selected. The design algorithm replaces the time varying parameters of the satellite by its averaged values evaluated over a period of one orbit. A Linear Quadratic Regulator (LQR) is used for the constant gain controller design. The system is linear, time invariant and controllable thus a control law can be based on the solution of the steady state Riccati equation [166].

Table 11.8. Technical specifications of the magnetorquers.

Property	Value
Actuation Level	[0.2, 0.4] Am ²
Supply Voltage	5 V
Mass	200 g
Envelope	Format PC/104, thickness 17 mm
Power Consumption	[1, 2] W/Am ²
Qualified Operational Temperature Range	[-40, +70] °C
Storage Temperature Range	[-50, +85] °C, (RH < 60%)
Nominal Magnetic Dipole (per actuator)	0.2 Am ²
Actuation Power (rods)	0.2 W
Actuation Power (air core)	0.57 W
Temperature Sensor Current Consumption	150 uA

11.4.4 Command and data handling system

The Command and Data Handling System (CDHS) computer is based on an 40 MHz clock speed ARM7 embedded processor with a memory of 2 MB static RAM, 4 MB flash memory (data storage), 4 MB flash memory (code storage), and a 2 GB microSD card (Table 11.9). The system operates the FreeRTOS real-time operating system. Modularity and reusability are valuable software architectural goals achieved using a star architecture. All payload processing is provided by a Gumstix Iron Storm (see Section 11.3.3) running Linux because of the wide support and documentation available, and the existing software packets that are tested and that can be reused.

Table 11.9. Technical specifications of the platform OBC.

Property
32-bit ARM7 RISC CPU
Compatible with FreeRTOS and eCos realtime operating systems
Clock speed: [8, 40] MHz
2MB Static RAM
4MB Data Storage (Flash Memory)
4MB Code Storage (Flash Memory)
2GB Micro-SD card support
104-pin bus connector
1 CAN bus interface
1 I2C interface
1 USART interface
Real Time Clock (RTC) with backup power for at least 60 minutes without external power.
Temperature sensors
3-Axes magneto-resistive sensor
3 Pulse Width Modulation (PWM) bidirectional output from 3.3 to 5 V / ± 3 A
1 SPI interface to e.g. gyroscopes, etc
Power monitor/power-on reset
3.3 V single supply voltage
Operating temperature tolerance: [-10, +85] °C
Dimensions: Format PC/104, thickness 10 mm
Mass: 60 g

11.4.5 Electrical power system

The Electrical Power System (EPS) [170] can perform the Li-Ion battery (29 Wh) charging without interrupting scientific data acquisition (Tables 11.10 and 11.11). The outer satellite surface is covered by GaAs solar panels (Table 11.12) except in the nadir-looking side where the antenna array is located (Fig. 11.3b).

Table 11.10. Technical specifications of the EPS.

Property	Value
Power Consumption	250 mW
Supply Voltage	3.3 V
Charge Current	1,250 mA typ. (2,500 mA max.)
Discharge Current	500 mA typ. (3,750 mA max.)
Mass without Batteries	105 g
Mass with Batteries	200 g
Envelope	Format PC/104, thickness 26 mm
Regulated Power Buses	3.3 V at 5 A and 5 V at 4 A
Input Power Capacity	Up to 30 W

Table 11.11. Technical specifications of the additional battery pack.

Property	Value
Capacity	5,200 mAh
Output Voltage Range	[6.0, 8.4] V
Nominal Discharge Current	38,480 mA
Charge Current	2,600 mA typ. (5,200 mA max)
Mass	240 g
Envelope	Format PC/104, thickness 23 mm

Table 11.12. Technical specifications of the solar panels.

Property	Value
Total Power Delivered	36.8 W
Supply Voltage	3.3 V
Cell Material	GaAs
Cell Efficiency	28%
Cover Glass	QioptiQ
Interconnector	Invar Silver plated
Total Mass	800 g
Qualified Operational Temperature Range	[-40, +125] °C

The top panel also provides space to locate a single patch GPS antenna ($52 \times 54 \text{ mm}^2$), (Fig. 11.2b). The GaAs-cell efficiency is 28%, and the average efficiency of the input converter is 93%. There are three individual photovoltaic input channels each having its own Maximum Power Point Tracking (MPPT). This enables the voltage to be set independently on all panels thus capturing the exact maximum power point at all illuminated cells. Finally it worth to point out that there are three regulated power buses of 3.3 V, 5V, and 6V for the payload and other satellite subsystems.

11.5 Mission analysis

This Section presents the mission analysis. The main results regarding the orbit evolution, coverage, debris, and mission budgets are described.

11.5.1 Orbit evolution analysis

The launch campaign of the ³Cat-2 is scheduled for the second quarter of 2016. ³Cat-2 nominal orbit is Sun-Synchronous (SSO) with a Local Time of Ascending Node (LTAN) of 00:00 h (baseline), and an orbit height of $H_{\text{ref}} = 510 \text{ km}$. The orbit evolution analysis is performed for an orbit height range of $H_{\text{ref}} = [510, 613] \text{ km}$ and takes into account the atmospheric drag (Jachhia-Bowmann model [171]), the solar activity [172], the Earth's gravity up to J4 zonal harmonic (NASA-MSFC-MSAFE geomagnetic activity [173]; EIGEN-GL04C Earth's gravity model [174]), and perturbations by third bodies (Sun and Moon).

The ³Cat-2 effective drag area for GNSS-R operations is $A_{\text{eff}} = 0.0226 \text{ mm}^2$ (equal to the smallest CubeSat surface), while for GNSS-RO (secondary mission objective) is $A_{\text{eff}} = 0.0771 \text{ mm}^2$ (equal to a cross-section of $226.3 \text{ mm} \times 340.5 \text{ mm}$). To complete the CubeSat configuration, the mass is considered in the analysis. It is in the

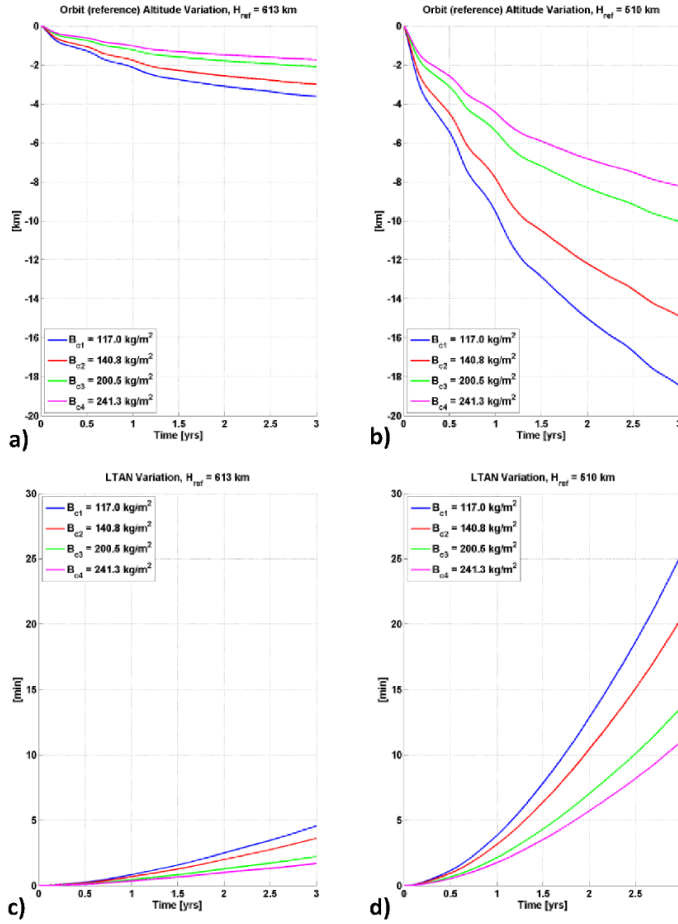


Fig. 11.9. Orbit evolution analysis as a function of the ballistic coefficient and the lifetime: Variation of the orbit mean altitude for a) $H_{\text{ref}} = 510 \text{ km}$, and b) $H_{\text{ref}} = 613 \text{ km}$. Mean LTAN variations for c) $H_{\text{ref}} = 510 \text{ km}$, and d) $H_{\text{ref}} = 613 \text{ km}$. Image credits Deimos Space.

range $m = [7, 12] \text{ kg}$. The analysis is performed as a function of the ballistic coefficient B_c as:

$$B_c = \frac{m}{A_{\text{eff}} C_D}, \quad (11.1)$$

where C_D is the drag coefficient. Two effective drag areas have been used, the first equal to the smallest surface and the second equal to the smallest surface increases by

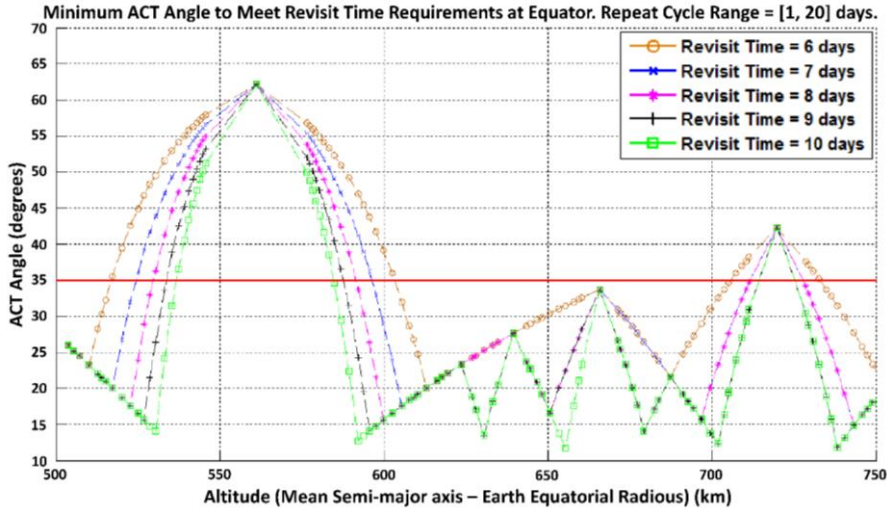


Fig. 11.10. Maximum across-track angle required for global coverage from 6 to 10 days of revisit time as a function of the reference orbit altitude. Image credits Deimos Space.

its 20% to account for transition from GNSS-R (nominal mode) to GNSS-RO (secondary mode) operations. Results show that even in the most critical case ($B_c = 117.17 \text{ kg/m}^2$ and an altitude $H_{\text{ref}} = 510 \text{ km}$) the altitude decay is $\sim 10 \text{ km}$ (Figs. 11.9a,b) and the LTAN increment (Figs. 11.9c,d) is just $\sim 4 \text{ min}$ in a 1 year time period. Therefore, the orbit is stable and there is no need to use a propulsion subsystem.

GNSS-R coverage mission requirements have been evaluated using the baseline nominal orbit. Figure 11.10 shows the across-track angle required to achieve the goal of global coverage within a revisit time from 6 to 10 days as a function of the orbit altitude in the range $H_{\text{ref}} = [500, 750] \text{ km}$. SSOs with a Repeat Cycle³⁷ (RC) of 20 days or less have been considered. There is a range $H_{\text{ref}} = [536, 584] \text{ km}$ with very short RC orbits and large revisit time. In this altitude range there are no orbits that enable the fulfillment of the coverage requirement with an across-track angle of 35° imposed by the nadir-looking antenna array beam-width. If the injection orbital

³⁷ Orbits with larger RC provide a better compromise between the temporal sampling (revisit time) and the spatial sampling (coverage grid).

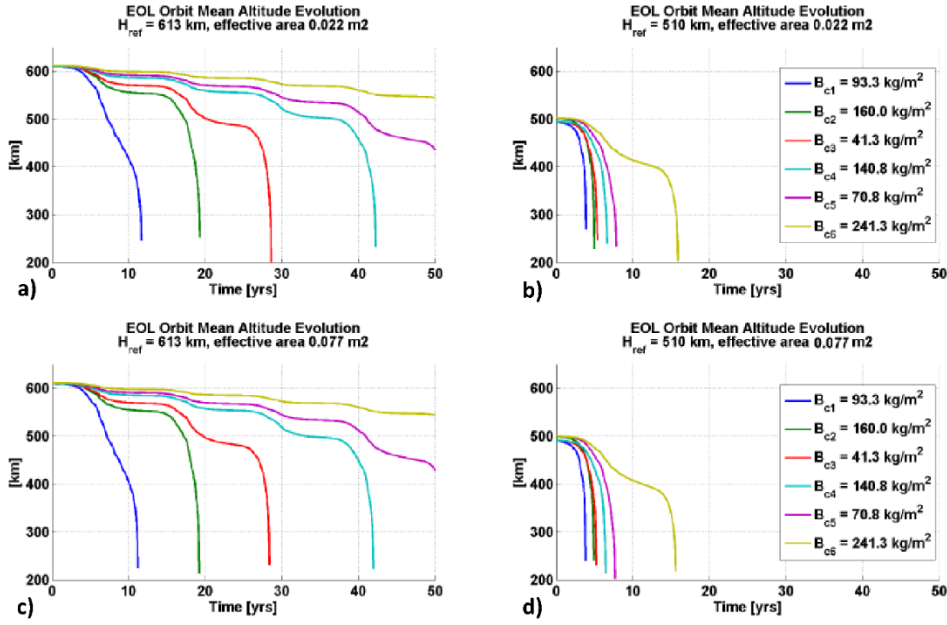


Fig. 11.11 End-Of-Life (EOL) orbit mean altitude decay for a) $H_{ref} = 613$ km, and $A_{eff} = 0.022 \text{ m}^2$, b) $H_{ref} = 510$ km and $A_{eff} = 0.022 \text{ m}^2$, c) $H_{ref} = 613$ km, and $A_{eff} = 0.077 \text{ m}^2$, and d) $H_{ref} = 510$ km and $A_{eff} = 0.077 \text{ m}^2$. Image credits Deimos Space.

altitude is in the range $H_{ref} = 510$ km, the operational orbit does not cross the exclusion range for revisit time ≤ 10 days. These results show that the main mission objective (GNSS-R) is satisfied with at least 12 days of revisit time with a down-looking antenna array beam-width of 70° . Furthermore, if the orbit altitude is maintained in the nominal range during the mission lifetime, even a revisit time of 6 days can be achieved.

The satellite does not use a propulsion subsystem, therefore it is required to check whether it performs a natural un-controlled re-entry within 25 years timeframe. Solar and geomagnetic activity models are chosen so that they represent a conservative scenario. The $^3\text{Cat-2}$ configuration for the End-Of-Life (EOL) disposal is assumed to be defined by a tumbling satellite. EOL simulations have been performed with three cross-sections corresponding to the satellite surfaces (0.0226 , 0.0341 and 0.0771 m^2). Figure 11.11 shows the orbit mean altitude profiles over the EOL simulation time for the considered ballistic coefficient (Eqn. 11.1) and orbit altitudes. The lower

reference altitude ($H_{\text{ref}} = 510 \text{ km}$) allows to comply with the space debris mitigation standards for any value of the satellite ballistic coefficient. In fact, the re-entry time is well below the 25 years specified by the standards [175].

11.5.2 Mission budgets

The selected ³Cat-2 configuration satisfies the mass (Table 11.13), power (Tables 11.14 and 11.15) link (Tables 11.16, 11.17, and 11.18) and data (Table 11.19) budgets. In this Section these mission budgets are described.

The EPS provides, stores, distributes, and controls the spacecraft electrical power. The most important sizing requirements are the demands for average and peak electrical power and the orbital parameters. It is required to identify the electrical power loads for the mission operations at the Beginning-Of-Life (BOL), and at the End-Of-Life (EOL). The power that the solar arrays shall provide during a complete orbit is calculated as:

$$P_{\text{sa}} = \frac{\left(\frac{P_e T_e}{X_e} + \frac{P_d T_d}{X_d} \right)}{T_d}, \quad (11.2)$$

where the subscripts *e* and *d* denote eclipse and daylight. P_e and P_d are power requirements, T_e and T_d are the lengths of eclipse and daylight periods per orbit, X_e and X_d are the efficiency of the paths from the solar arrays through the batteries to the loads and the path directly from the arrays to the loads respectively. The efficiency values for the daylight and the eclipse depend on the power regulation: direct energy transfer ($X_e = 0.65$ and $X_d = 0.85$) or MPPT ($X_e = 0.6$ and $X_d = 0.8$).

Additionally to the efficiency of paths from the solar arrays to the batteries, the inherent degradation due to design, the physical temperature of the array and shadowing of cells, have to be considered. For many missions, the EOL power demands must be reduced to compensate for solar array performance degradation. The ³Cat-2 has been designed for a nominal operational life of 1 year. A 2% of degradation per year (ξ) due to thermal cycling, in/out eclipses, micrometeoroid strikes and

radiation has been considered during the design process [176]. Then, the EOL power generated on-board is derived as:

$$P_{EOL} = P_{BOL} (1 - \xi)^n, \quad (11.3)$$

where P_{BOL} is the BOL array's power per unit area, and n is the number of years in orbit. The mean effective area $A_{sa,eff}$ required for the mission is calculated as:

$$A_{sa,eff} = \frac{P_{sa}}{P_{EOL}} = 0.0258 \text{ m}^2 \quad (11.4)$$

This value is lower than the mean effective area of the CubeSat (0.0312 m^2) as derived using Systems Tool Kit (STK). Additionally, the EOL power margins using GaAs solar cells of 28% of efficiency and for a payload duty cycle of the 15 % of the orbit period are 1585 W and 1100 W respectively for an orbit without ground station access and for an orbit with one ground station access (Table 11.14 and 11.15). Therefore the CubeSat configuration satisfied the power requirements of the mission.

Table 11.13. Mass budget.

Subsystem	Mass (g)	Margin (%)	Total Mass (g)
ADCS	194	5	204
CDHS	530	5	586
Mechanical	1160	10	1276
Payload	1200	10	1320
Antennas	1000	10	1100
Power	1265	5	1328
TT&C	349	5	366
Thermal	25	5	26
Subtotal	5723	483	6206
System Margin	x	10	620
Total	x	x	6826

Table 11.14. Power budget without ground station access.

Subsystem	Peak time (%)	Average (mW)
ADCS	25	200
CDHS	100	368
Mechanical	0	0
Payload	15	1200
Antennas	15	150
Power	100	250
TT&C	0	0
Thermal	0	0
Average Power Consumed	x	2168
Efficiency Losses	x	910
Degradation (1 year of life)	x	1127
Total Average Power Consumed	x	4205
Average Power Generated	x	5790
Margin	x	1585

Table 11.15. Power budget with 1 ground station access.

Subsystem	Peak time (%)	Average (mW)
ADCS	25	200
CDHS	100	368
Mechanical	0	0
Payload	15	1200
Antennas	15	150
Power	100	250
TT&C	6	312
Thermal	0	0
Average Power Consumed	x	2480
Efficiency Losses	x	1041
Degradation (1 year of life)	x	1289
Total Average Power Consumed	x	4810
Average Power Generated	x	5910
Margin	x	1100

The link equation used to size the data link of a communications system is:

$$\frac{E_b}{N_0} = \frac{P_t L_t G_t L_s L_a G_r}{k T_s D R}, \quad (11.5)$$

where E_b / N_0 is the ratio of the received energy per bit to noise density, P_t is the transmitter power, L_t is the transmitter-to-antenna line loss, G_t is the transmit antenna gain, L_s is the space loss, L_a is the transmission path loss, G_r is the receiver antenna gain, k is the Boltzmann constant, T_s is the system noise temperature, and $D R$ is the data rate.

The simulated radiation patterns of the VHF monopoles (Ant S1 A1 and Ant S1 A2) and UHF monopoles (Ant S2 A1 and AntS2 A2) are shown in Fig. 11.7. The peak transmit antenna gain is: 0.58 dB (Ant S1 A1), 1.16 dB (Ant S1 A2), 2.78 dB (Ant S2 A1) and 2.7 dB (AntS2 A2). For the simulations it is assumed a maximum antenna pointing error of 30°. The free space path loss is calculated as:

$$L_s = 147.55 - 20 \log(S) - 20 \log(f), \quad (11.6)$$

where S is the distance from the ground station and the satellite and f is the transmitted frequency. It is considered the satellite with an elevation angle of 15°. The system noise temperature, the required bit energy to noise ratio, the transmitter line loss and implementation loss are estimated as per [176]. The margins for housekeeping, scientific data and telecommands are 8.4 dB (Table 11.16), 4.9 dB (Table 11.17) and 32 dB (Table 11.18) respectively considering a high ADCS error of 30°. In nominal conditions, the margins should be higher up to 4.5 dB more.

Table 11.16. Link budget: Down-link telemetry.

DOWNLINK TELEMETRY	Symbol	Units	Source	Value
Frequency	f	MHz	Defined	146
Transmitter Power	P_t	dBW	Data	-8
Transmitter Line Loss	L_t	dB	Estimated	-1
Peak Transmit Antenna Gain	G_t	dB	Data	0.5
Effect. Isotropic Radiated Power	EIRP	dB	$P_t + G_t + L_t$	-8.5
Transmitter antenna half power beamwidth	θ_t	deg	Calculated	80
Transmitter antenna pointing error	e_t	deg	Estimated	30
Transmitter antenna pointing loss	L_{pt}	dB	$-12(e_t / \theta_t)$	-4.5
Free Space Path Loss	L_s	dB	Calculated	-143.5
Polarization Loss	L_a	dB	Estimated	-3
Receiver Antenna Peak Gain	G_r	dB	Data	12.3
System Noise Temperature	T_s	K	Estimated	1,295
Data Rate	DR	bps	Defined	5,000
Bit Energy/Noise Ratio	E_b/N_0	dB	Calculated	14.4
Bit Error Rate	BER	-	Defined	0.01
Required Bit Energy/Noise Ratio	E_b/N_0	dBHz	BPSK	4
Implementation Loss	-	dB	Estimated	-2
Margin	-	dB	Calculated	8.4

Table 11.17. Link budget: Down-link scientific data.

DOWNLINK PAYLOAD	Symbol	Units	Source	Value
Frequency	f	MHz	Defined	2,100
Transmitter Power	P_t	dBW	Data	-2
Transmitter Line Loss	L_t	dB	Estimated	-1
Peak Transmit Antenna Gain	G_t	dB	Data	5
Effect. Isotropic Radiated Power	EIRP	dB	$P_t + G_t + L_t$	3
Transmitter antenna half power beamwidth	θ_t	deg	Calculated	80
Transmitter antenna pointing error	e_t	deg	Estimated	30
Transmitter antenna pointing loss	L_{pt}	dB	$-12(e_t / \theta_t)$	-4.5
Free Space Path Loss	L_s	dB	Calculated	-166.7
Polarization Loss	L_a	dB	Estimated	-3
Receiver Antenna Peak Gain	G_r	dB	Data	31.5
System Noise Temperature	T_s	K	Estimated	1,800
Data Rate	DR	bps	Defined	50,000
Bit Energy/Noise Ratio	E_b/N_0	dB	Calculated	10.9
Bit Error Rate	BER	-	Defined	0.01
Required	E_b/N_0	dBHz	BPSK or GMSK	4
Implementation Loss	-	dB	Estimate	-2
Margin	-	dB	Calculated	4.9

Table 11.18. Link budget: Up-link telecommands.

UPLINK TELECOMMANDS	Symbol	Units	Source	Value
Frequency	f	MHz	Defined	438
Transmitter Power	P_t	dBW	Data	20
Transmitter Line Loss	L_t	dB	Estimated	-1
Peak Transmit Antenna Gain	G_t	dB	Unknown	12.3
Effect. Isotropic Radiated Power	EIRP	dB	$P_t + G_t + L_t$	31.3
Receiver antenna half power beamwidth	θ_t	deg	Calculated	80
Receiver antenna pointing error	e_t	deg	Estimated	30
Receiver antenna pointing loss	L_{pt}	dB	$12(e_t / \theta_t)$	-4.5
Free Space Path Loss	L_s	dB	Calculated	-153.1
Polarization Loss	L_a	dB	Estimated	-3
Receiver Antenna Peak Gain	G_r	dB	Data	2.7
System Noise Temperature	T_s	K	Estimated	375
Data Rate	DR	bps	Defined	1,200
Bit Energy/Noise Ratio	E_b/N_0	dB	Calculated	50
Bit Error Rate	BER	-	Defined	0.00001
Required Bit Energy/Noise Ratio	E_b/N_0	dBHz	AFSK or MFSK	13
Implementation Loss	-	dB	Estimated	-2
Margin	-	dB	Calculated	32

Table 11.19. Data budget of the ³Cat-2 (ADCS error free).

Ground Station Contact Time (min/day)	20
VHF Downlink Rate (kbps)	9.6
Downlink Volume (MB/day)	1.4
S Band Downlink Rate (kbps)	70
Housekeeping Data (MB/day)	10.5
Expected Payload Data Volume (MB/day)	11.9
Uplink Rate (kbps)	1.2
Uplink Volume (MB/day)	0.18

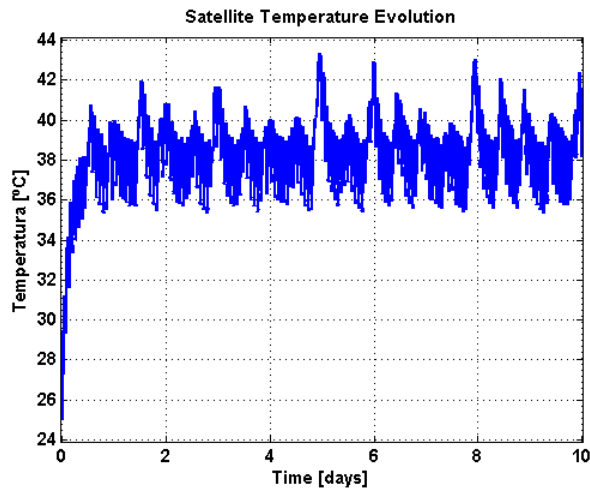


Fig.11.12. Satellite temperature evolution as a function of the time.

³Cat-2 operations will be controlled using an ad-hoc designed ground station located at UPC premises. It is located at Building D3 of UPC Campus Nord (latitude: 41° 23' 20" North; longitude: 2° 6' 43" East; altitude: 175 meters), Barcelona (Spain). A mean of 20 minutes of communications with the CubeSat per day will be possible taking into account the 15° of minimum elevation angle constraint imposed by the Collserola mountains at the East of the city. In acse of ADCS error free condicions, it will be possible to downlink ~ 1.2 MB of housekeeping data and ~ 11.9 MB of payload data

per day. On the other side the maximum uplink volume will be ~ 0.18 MB per day (Table 11.19).

Finally, a thermal evaluation is performed for the ³Cat-2 configuration using an ad-hoc mission simulation tool [177]. The input parameters in the simulation were the emittance (0.85 for solar panels, 0.77 for Al chasis), the absorbance (0.92 for solar panels, 0.5 for Al chasis), the Sun radiation power ($1,400 \text{ W/m}^2$) and the Earth albedo (average value 0.3 [178]). Results (Fig. 11.12) show that the in-orbit CubeSat temperature fluctuates in the range $[36, 44]^\circ\text{C}$, being the initial temperature set to 25°C . This temperature range allows to operate the satellite in nominal conditions.

11.6 Discussions and conclusions

³Cat-2 is a 6U CubeSat demonstration mission for Earth Observation using GNSS-R. The ADCS approach is similar to that used in TechDemosat-1 (Sun and magnetic field sensors for attitude determination, and 3-axes magnetorquer to control the platform's attitude) aiming at a pointing accuracy of 7.5° ($3\text{-}\sigma$), needed for the antenna pattern correction in scatterometry measurements. The payload duty cycle will be up to $\sim 15\%$, and the expected data volume up to ~ 10 MB per day, which will be downloaded to the UPC ground station using a S-band scientific data downlink up to 115 kbps. ³Cat-2 payload has been designed with a 3×2 dual-band (L1, L2) and dual-polarization (LHCP, RHCP) patch antenna array to perform GNSS-R measurements over the ocean, land and cryosphere using multi-constellation signals (GPS, GLONASS, Galileo and COMPASS). The key point towards a more effective integration campaign has been a simple, modular and robust design and the fact that the payload and the platform have been validated independently each other. The evaluation of the achievable performances (both for altimetry and scatterometry) vs. payload parameters will provide useful information for upcoming missions and experiments (e.g. Geros-ISS). ³Cat-2 aims also at providing scientifically valuable data in a very cost-effective manner which may open the door to future constellations of GNSS-R instruments.

12

12. CONCLUSIONS AND FUTURE RESEARCH LINES

12.1 Summary and conclusions

Global Navigation Satellite Systems Reflectometry (GNSS-R) is a multi-static radar using navigation signals as signals of opportunity. It provides wide-swath and improved spatio-temporal sampling over current space-borne missions. The lack of experimental datasets from space covering signals from multiple constellations (GPS, GLONASS, Galileo and COMPASS) at dual-band (L1 and L2) and dual-polarization (Right and Left Hand Circular Polarization: RHCP and LHCP), over the ocean, land and cryosphere remains a bottleneck to further develop these techniques. ³Cat-2 is a 6 units (3 x 2 elementary blocks of 10 x 10 x 10 cm³) CubeSat mission aiming to explore fundamental issues towards an improvement in the understanding of the bistatic scattering properties of different targets. Since geolocalization of the specific reflection points is determined by the geometry only, a moderate pointing accuracy is still required to correct for the antenna pattern in scatterometry measurements. ³Cat-2 launch is foreseen for the second quarter of 2016 into a Sun-Synchronous orbit of 510 km height using a Long March II D rocket.

This Ph. D. Thesis represents the main contributions to the development of the ³Cat-2 GNSS-R Earth Observation mission (a 6U CubeSat) including a novel type of GNSS-R technique: the reconstructed one. The desing, developement and validation of the PYCARO payload (closed and open-loop operational modes) have been carried out in parallel to the design and development of the platform, and a number of ground-based, air-borne and stratospheric balloon experiments to validate the technique and to optimize the instrument. Both operational modes will be tested from space. The proof-of-concept of the closep-loop mode from a high speed and high altitude platform is strongly interesting since the results could open the door to the development of new scattering models in the GNSS-R community.

In particular, the main contributions of this Ph. D. Thesis are:

- A novel dual-band Global Navigation Satellite Systems Reflectometer (GNSS-R) that uses the P(Y) and C/A signals scattered over the sea surface to perform highly precise altimetric measurements (PYCARO) has been designed. PYCARO uses a closed-loop receiver with delay and Doppler

tracking loops that uses the so-called conventional GNSS-R technique for the GPS C/A code and the reconstructed GNSS-R technique for the P(Y) code.

- The first proof-of-concept of PYCARO was performed during two different ground-based field experiments over a dam and over the sea under different surface's roughness conditions. The analysis of the altimetric performance shows that the results obtained using the P(Y) code improve by a factor between 1.4 and 2.4 as compared to the results obtained using the C/A code, respectively, for high and mid-low satellite's elevation angles.
- The scattering of GNSS signals over a water surface has been studied when the receiver is at low height, as for GNSS-R coastal altimetry applications. The precise determination of the local sea level and wave state from the coast can provide useful altimetry and wave information as “dry” tide and wave gauges. In order to test this concept an experiment has been conducted at the Canal d'Investigació i Experimentació Marítima (CIEM) wave channel for two synthetic “sea” states. After retracking of the scattered GPS signals, the coherent and incoherent components have been studied. To reproduce the transmitted GPS signals indoors, a SMU 200 A Rohde and Schwarz signal generator was used. It has been found that, despite the ratio of the coherent and incoherent components being ~ 1 , the coherent component is strong enough that it can be tracked. The coherent component comes from clusters of points on the surface that approximately satisfy the specular reflection conditions (“roughed facet”). The Pearson's linear correlation coefficients of the derived “sea” surface height with the wave gauge data are: 0.78, 0.85 and 0.81 for a SWH = 36 cm and 0.34, 0.74, and 0.72 for a SWH = 64 cm, respectively, for transmitter elevation angles of $\theta_e = 60^\circ$, 75° and 86° , respectively. Finally, the rms phase of the received signal before the retracking processing was used to estimate the effective rms surface height of the ‘facets’, where the waves get scattered. It is found to be between 2.5- and 4.1-times smaller than the theoretical values corresponding to the half of the coherent reflectivity decaying factor.

-
- Two ESA-sponsored airborne experiments were performed to test the precision and the relative accuracy of the conventional Global Navigation Satellite Systems Reflectometry (GNSS-R) technique employing only the C/A code are presented. The first and the second experiments demonstrated, respectively, a 17 cm precision for a 500 m flight altitude with a 8 km along-track spatial resolution, and a 6 cm precision for a 3,000 m flight altitude with a 6.6 km along-track spatial resolution. In both, the Relative Mean Dynamic Topography (RMDT) was compared with results derived from traditional radar altimetry provided by Jason-2. The rms of the RMDT difference between both measurement systems was 48 cm for the first flight, and 198 cm for the second flight. During the second flight, the feasibility of the proposed technique to measure the sea slopes was also demonstrated by superposing over the aircraft ground track the measured sea surface height with the geoid undulations, about 1 meter.
 - The empirical results of a GNSS-R experiment on-board the ESA-sponsored BEXUS 17 stratospheric balloon campaign performed North of Sweden over boreal forests showed that the power of the reflected signals is nearly independent of the platform height for a high coherent integration time $T_c = 20$ ms. This experimental evidence shows a strong coherent component in the forward scattered signal, as compared to the incoherent one, that can allow to be tracked. The bistatic coherent reflectivity was also evaluated as a function of the elevation angle showing a decrease of ~ 6 dB when the elevation angle increases from 35° to 70° . The received power presented a clearly multi-modal behavior, which also suggested that the coherent scattering component may be taking place in the different forest elements: soil, canopy, and through multiple reflections canopy-soil and soil-trunk. This experiment provided the first GNSS-R dataset over boreal forests. The evaluation of these results can be useful for the feasibility study of this technique to perform biomass monitoring which is a key-factor to analyze the carbon cycle over boreal forests.
 - An improved version of the PYCARO payload was tested in October 2014 for the second time during the ESA-sponsored BEXUS 19. This work achieved the first ever dual-frequency, multi-constellation GNSS-R observations over

boreal forests and lakes using GPS, GLONASS and Galileo signals. The coherent-to-incoherent scattering ratio over boreal forests was found to be as large as ~ 1.5 , while over lakes it was as high as 16.5 due to the specular nature of the scattering over the flat water bodies. The scatterers' height fluctuations measured using the phase of the peak of the reflected complex waveforms range from ± 10 m, to the submetric level. Finally, reflectivity maps using the different GNSS codes were presented using the conventional GNSS-R for the open-access codes, and the reconstructed GNSS-R for the encrypted ones. The coherence of the reflected signal was found to be high enough to allow the PYCARO instrument to reconstruct the P(Y) code.

- The first-ever dual-frequency multi-constellation GNSS-R dual polarization measurements over boreal forests and lakes were obtained from the stratosphere during the BEXUS 19 using the PYCARO reflectometer operated in closed-loop mode. The interpretation of the experimental results has been complemented with dual-polarization simulations of the reflectivity using a well-established bistatic scattering model. The simulated cross- (reflected LHCP), and co-polar (reflected RHCP) reflectivities were evaluated for the soil, the canopy, and the canopy-soil interactions for three different biomass densities: 725 trees/ha, 150 trees/ha, and 72 trees/ha. For elevation angles larger than the Brewster angle it is found that the cross-polar signal is dominant when just single reflections over the forests are evaluated, while in the case of multiple reflections the co-polar signal becomes the largest one. Maps of the polarimetric ratio for L1 and L2 GPS and GLONASS, and for E1 Galileo signals are derived from the float phase at $\sim 27,000$ m height, and the specular points are geolocalized on the Earth's surface. Polarimetric ratio maps over boreal forests are shown to be in the range $\sim [2, 16]$ dB for the different GNSS codes. The polarimetric phase is in the range $[-1.4, -9.6]$ m which seems to indicate that the LHCP phase center is located at a higher height of the forests as compared to the RHCP signals. This result suggests that the scattering is taking place not only over the soil, but over the different forests elements as well.
- Finally, a unified GNSS-R model is proposed: There are two different methods to evaluate the specular reflection over rough surfaces [180]: the

Physical Optics approach and the Geometric Optics approach. The analysis of the radiance diagrams of Beckmann-Spizzichino (Physical Optics) and Torrance-Sparrow (Geometric Optics) concluded [180] that a unified surface reflectance model should be composed of three reflection components: the diffuse lobe, specular lobe and specular spike. The diffuse lobe accounts for the internal scattering mechanism and it is distributed in upper half space. The specular lobe represents single reflections and it spreads over a region around the specular direction and has off-specular peaks for large surface roughness values. Finally, the specular spike represents mirror-like reflection, it is the largest contribution for smooth surfaces, and it is only significant in a small region around the specular direction.

In general, the scattered electromagnetic field contains both a coherent and an incoherent component in different proportions. The bistatic scattering coefficient $\sigma_{\text{RHCP-LHCP}}^0$ consists of a coherent component $\sigma_{\text{RHCP-LHCP}}^{0,\text{coh}}$ and an incoherent component $\sigma_{\text{RHCP-LHCP}}^{0,\text{incoh}}$ [27, pp. 200], where incoh and coh represent incoherent and coherent components, and RHCP and LHCP represent the incident polarization (Right Hand Circular Polarization), and the scattered polarization (Left Hand Circular Polarization) respectively. Therefore the main fundamental scientific observable in the GNSS-R case, the so-called reflected power waveform is composed of an incoherent and a coherent contribution:

$$\left\langle |Y_{\text{ref}}|^2 \right\rangle = \left\langle |Y_{\text{ref},\text{incoh}}|^2 \right\rangle + \left\langle |Y_{\text{ref},\text{coh}}|^2 \right\rangle. \quad (12.1)$$

The results of the BEXUS 17 and 19 stratospheric flights demonstrated that a coherent component exists after the scattering over rough surfaces and canopy [40, 181]; and in the conclusion to this dissertation an unified model of the waveform is introduced. In 2013, the BEXUS 17 [40] additionally showed for the first time in the GNSS-R community that the coherent reflected power is roughly independent of the platform height. This experimental evidence triggers the need to develop a model to integrate it in an unified waveform model. The extension of the work of Fung et al. [125] to the bistatic case with the antennas separated a distance equal to $R_{\text{t0}} + R_{\text{0rc}}$ describes correctly this empirical evidence since in the GNSS-R case the distance from the transmitter

to the scattering area R_{t0} is much larger than the distance from the scattering area to the receiver R_{orc} . Therefore the model of the reflected power waveform under the unified framework should be formally expressed as:

$$\begin{aligned} \langle |Y_{\text{ref}}|^2 \rangle &= \langle |Y_{\text{ref, incoh}}|^2 \rangle + \langle |Y_{\text{ref, coh}}|^2 \rangle = \\ &= \frac{P_t \lambda^2 T_c^2}{(4\pi)^3} \iint G_t G_{rc} \text{ACF}^2(\delta\tau) S^2(\delta f) \\ &= \left[\frac{\sigma_{\text{RCHP-LHCP}}^{0, \text{incoh}}}{(R_{t0})^2 (R_{orc})^2} + \frac{\sigma_{\text{RCHP-LHCP}}^{0, \text{coh}}}{(R_{t0} + R_{orc})^2} \right] dA, \end{aligned} \quad (12.2)$$

where P_t is the power emitted by the GNSS satellites, λ is the electromagnetic wavelength, T_c is the coherent integration time, G_t is the gain of the transmitting antenna, G_{rc} is the gain of the receiving antenna, ACF is the auto-correlation function of the GNSS codes, S is the sinc-exponential function, $\delta\tau$ and δf are the differences between the sampled time delay τ or sampled frequency f and a reference delay and Doppler frequency, and A is the scattering area. The bistatic incoherent scattering coefficient is approximated as [150]:

$$\sigma_{\text{RCHP-LHCP}}^{0, \text{incoh}} \propto |\mathfrak{R}|^2 \text{PDF}, \quad (12.3)$$

where \mathfrak{R} is the Fresnel reflection coefficient, and PDF is the probability density function of the surface's slopes. On the other side, the bistatic coherent scattering coefficient taking into account the antenna pattern and the sphericity of the wavefront can be approximated for high elevation angles, typical in the GNSS-R case, as [125]:

$$\sigma_{\text{RCHP-LHCP}}^{0, \text{coh}} = \frac{|\mathfrak{R}|^2}{\left(\frac{1}{k^2 R_{t0}^2 \beta_0^2} + \frac{\beta_0^2}{4} \right)} e^{-4k^2 \sigma^2}, \quad (12.4)$$

where β_0 is the one-sided beamwidth of the transmitting antenna, σ is standard deviation of the surface height, and k is the wavenumber.

12.2 Future research lines

Future research activities should include:

- The analysis of the coherent-to-incoherent ratio from LEO observations. This work now can be started using the extensive data set of TechDemoSat-1
- Further evaluation of the scattering mechanisms over boreal forests using experimental data and theoretical simulations.
- The intercomparison of the different GNSS-R techniques, mainly cGNSS-R, iGNSS-R and rGNSS-R.
- The intercomparison of the space-borne data sets obtained from the ³Cat-2 with those provided by UK TechdemoSat-1, CyGNSS and GEROSS-ISS. Different data access techniques, GNSS-R instruments, orbital parameters and down-looking antenna gain should be considered to derive properly the conclusions.
- The evaluation of the potential use of nano-satellites constellations for Earth Remote Sensing.
- The development of deployable antenna arrays for nano-satellites to increase the antenna directivity.
- The improvement of payload duty-cycles by exploring novel hardware and software approaches.

12.3 List of Publications

Journal Papers

1. **H. Carreno-Luengo**, and A. Camps, “Unified GNSS-R Scattering Framework”, Submitted to IEEE Electronics Letters, 2015.
2. **H. Carreno-Luengo**, A. Camps, A. Amèzaga, D. Vidal, J.F. Munoz, R. Olivé, J. Carola, N. Catarino, M. Hagenfeldt, P. Palomo, and S. Cornara, “³Cat-2: A Nano-Satellite Earth Observation Mission for GNSS-R Concept Exploration”, Submitted to IEEE Journal of Selected Topics in Applied Earth Observations and Remote Sensing, 2015.
3. **H. Carreno-Luengo**, A. Amèzaga, D. Vidal, R. Olivé, J.F. Munoz, and A. Camps, “First Polarimetric GNSS-R Measurements from a Stratospheric Flight and Coherent Reflectivity Simulations over Boreal Forests”, MDPI Remote Sensing, vol. 7, no. 10, pp. 13120-13138, 2015.
4. **H. Carreno-Luengo**, and A. Camps, “First Dual-Band Multi-Constellation GNSS-R Scatterometry Experiment over Boreal Forests from a Stratospheric Balloon”, Accepted to IEEE Journal of Selected Topics in Applied Earth Observations and Remote Sensing, 2015.
5. **H. Carreno-Luengo**, A. Camps, J. Querol, and G. Forte, “First Results of a GNSS-R Experiment from a Stratospheric Balloon over Boreal Forests”, Accepted to IEEE Transactions of Geoscience and Remote Sensing, 2015.
6. **H. Carreno-Luengo**, and A. Camps, “Empirical Results of a Surface Level GNSS-R Experiment in a Wave Channel”, MDPI Remote Sensing, vol. 7, no. 6, pp. 7471-7493, 2015.
7. **H. Carreno-Luengo**, A. Camps, I. Ramos-Pérez, and A. Rius, “Experimental Evaluation of GNSS-Reflectometry Altimetric Precision Using the P(Y) and C/A Signals”, IEEE Journal of Selected Topics in Applied Earth Observations and Remote Sensing, vol. 7, no. 5, pp. 1493 -1500, 2014.
8. **H. Carreno-Luengo**, H. Park, A. Camps, F. Fabra, and A. Rius, “GNSS-R Derived Centimetric Sea Topography: An Airborne Experiment Demonstration”, IEEE Journal of Selected Topics in Applied Earth Observations and Remote Sensing, vol. 6, no. 3, pp. 1468 -1478, 2013.

Conference Papers

1. **H. Carreno-Luengo**, A. Amèzaga, A. Bolet, D. Vidal, J. Jané, J.F. Munoz, R. Olivé, A. Camps, J. Carola, N. Catarino, M. Hagenfeldt, P. Palomo, and S. Cornara, "Cat-2: A 6U Cubesat-based Multi-Constellation, Dual-Polarization, and Dual-Frequency GNSS-R and GNSS-RO Experimental Mission", Proceedings of the 2015 IEEE International Geoscience and Remote Sensing Symposium, pp. 5115-5118, Milan, Italy.
2. **H. Carreno-Luengo**, A. Amèzaga, A. Bolet, D. Vidal, J. Jané, J.F. Munoz, R. Olivé, and A. Camps, "Multi-Constellation, Dual-Polarization, and Dual-Frequency GNSS-R Stratospheric Balloon Experiment Over Boreal Forests", Proceedings of the 2015 IEEE International Geoscience and Remote Sensing Symposium, pp. 5107-5110, Milan, Italy.
3. **H. Carreno-Luengo**, A. Camps, J. Querol, G. Forte, R. Onrubia and R. Díez, "A Stratospheric Balloon GNSS-R Experiment: The Cat-2 Project in DLR/SNSB BEXUS", Proceedings of the 2014 IEEE International Geoscience and Remote Sensing Symposium, pp. 3626-3629, Quebec, Canada, July 2014.
4. **H. Carreno-Luengo**, A. Camps, R. Jové, A. Alonso-Arroyo, R. Olivé, A. Amèzaga, D. Vidal, J. F. Munoz, "The Cat-2 Project: GNSS-R In-Orbit Demonstrator for Earth Observation", Proceedings of the 2014 ESA Small Satellites, Systems & Service Symposium, Mallorca, Spain, May 2014.
5. **H. Carreno-Luengo**, and A. Camps, "A GNSS-R Experiment over Wave Channel Surface", Proceedings of the 2013 IEEE International Geoscience and Remote Sensing Symposium, pp. 366-369, Melbourne, Australia, July 2013.
6. **H. Carreno-Luengo**, A. Camps, I. Ramos-Pérez, G. Forte, R. Onrubia and R. Díez, "Cat-2: A P(Y) and C/A GNSS-R Experimental Nano-Satellite Mission", Proceedings of the 2013 IEEE International Geoscience and Remote Sensing Symposium, pp. 843-846, Melbourne, Australia, July 2013.
7. **H. Carreno-Luengo**, A. Camps, I. Ramos-Pérez, A. Rius, "Pycaro's Instrument Proof of Concept", Proceedings of the 2012 Workshop on

Reflectometry using GNSS and Other Signals of Opportunity (GNSS+R 2012), Purdue University, IN, USA, October, 2012.

8. **H. Carreno-Luengo**, H. Park, A. Camps, F. Fabra, and A. Rius, "Submeter Ocean Altimetry with GPS L1 C/A Signal", Proceedings of the 2012 IEEE International Geoscience and Remote Sensing Symposium, pp. 7071-7074, Munich, Germany, July 2012.

12.4 Participation in relevant projects

1. PI of TORMES-UPC team on-board ESA BEXUS 17, 2013-2014.
2. PI of TORMES-UPC team on-board ESA BEXUS 19, 2014-2015.
3. Team member of the UPC subproject "European GNSS-R Environmental Monitoring" (E-GEM), grant no FP7-607126-E-GEM, 2013-2016.
4. Team member of the UPC subproject "Aplicaciones avanzadas en radio ocultaciones y dispersometría utilizando señales GNSS y otras señales de oportunidad" of the Spanish Ministerio de Ciencia e Innovación (MICINN), grant no AYA2011-29183-C02-01, 2011.

A

APPENDIX A: BEXUS EXPERIMENT SET-UP

A.1 Experiment description

A.1.1 Experiment set-up

The key subsystems of the TORMES 2.0 payload (Fig. A.1) were the antenna array (Fig. A.2), the Software Defined Radio (SDR) and the Signal Processing Unit (SPU). The antenna array provided access to the GNSS signals in a way to achieve as many TORMES 2.0 mission objectives as possible. The SPU included the required signal processing techniques to produce the observables corresponding to the different scientific applications. To achieve nadir and limb access simultaneously, in addition to the down-looking antenna array, an omnidirectional antenna had to point to limb. The up-looking omnidirectional antenna (Fig. A.3) had to provide the GNSS signals to the PPD receiver. Figure A-1 presents the TORMES 2.0 payload high level block diagram.

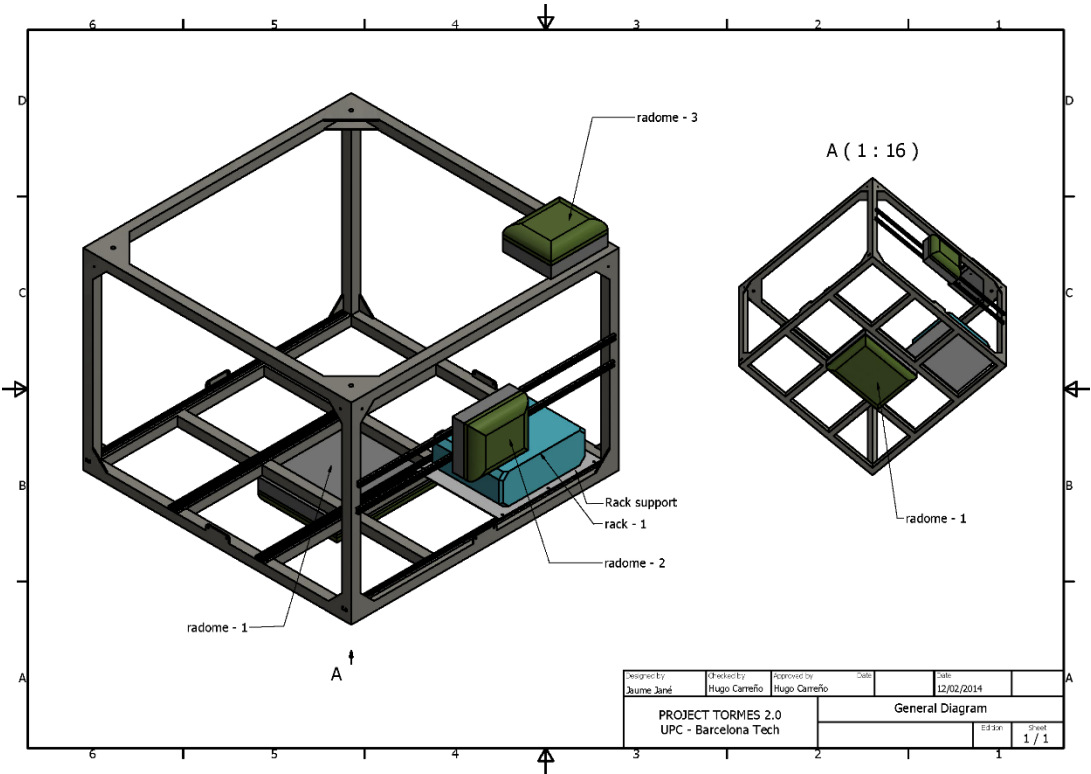


Fig. A.1. TORMES 2.0 placement in the M-Egon gondola.

A.2 Experiment interfaces

A.2.1 Mechanical

- The rack-1 containing the electronics (377 mm x 310 mm x 119 mm) was attached to an aluminum plate (378 mm x 336 mm x 3 mm) by means of two pairs of bolts/nuts (self-locking nyloc)/washers M6 (Fig. A.4). The plate was attached to the rails of the gondola by means of two series of two bolts/nuts (self-locking nyloc) /washers M6.
- The radome-1 (down-looking antenna) was attached to the gondola by two series of two bolts/nuts (self-locking nyloc)/washers M8 (Fig. A.2, Fig. A.5). The antenna was placed at the bottom of the gondola in a nadir-looking position.
- The radome-2 (up-looking antenna) was attached to the gondola by two pairs of bolts/nuts (self-locking nyloc)/washers M5. The plate was placed at the top of the gondola in a zenith-looking position. It was located in one edge of the top of the gondola (Fig. A.3).
- The radome-3 (limb-looking antenna) was attached to one rail by four bolts/nuts (self-locking nyloc)/washers M6. It was placed in the same lateral of the gondola where the racks were attached. It was orientated in a limb-looking position (Fig. A.3). The rail was attached to the gondola by six clamps.
- The three antenna radomes were attached with a safety cable to the gondola.



Fig. A.2. TORMES 2.0 down-looking radome attached to the M-Egon gondola.

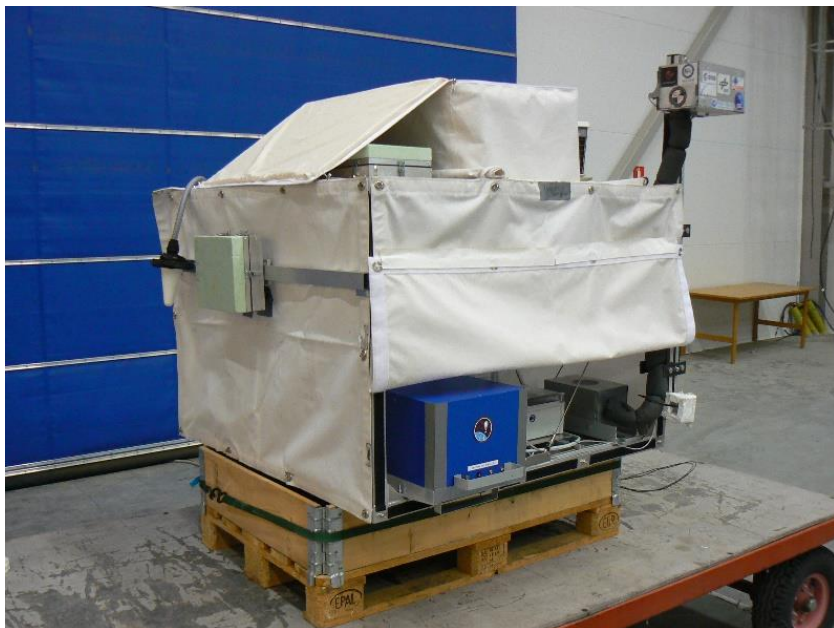


Fig. A.3. TORMES 2.0 up and limb-looking radomes attached to the M-Egon gondola.

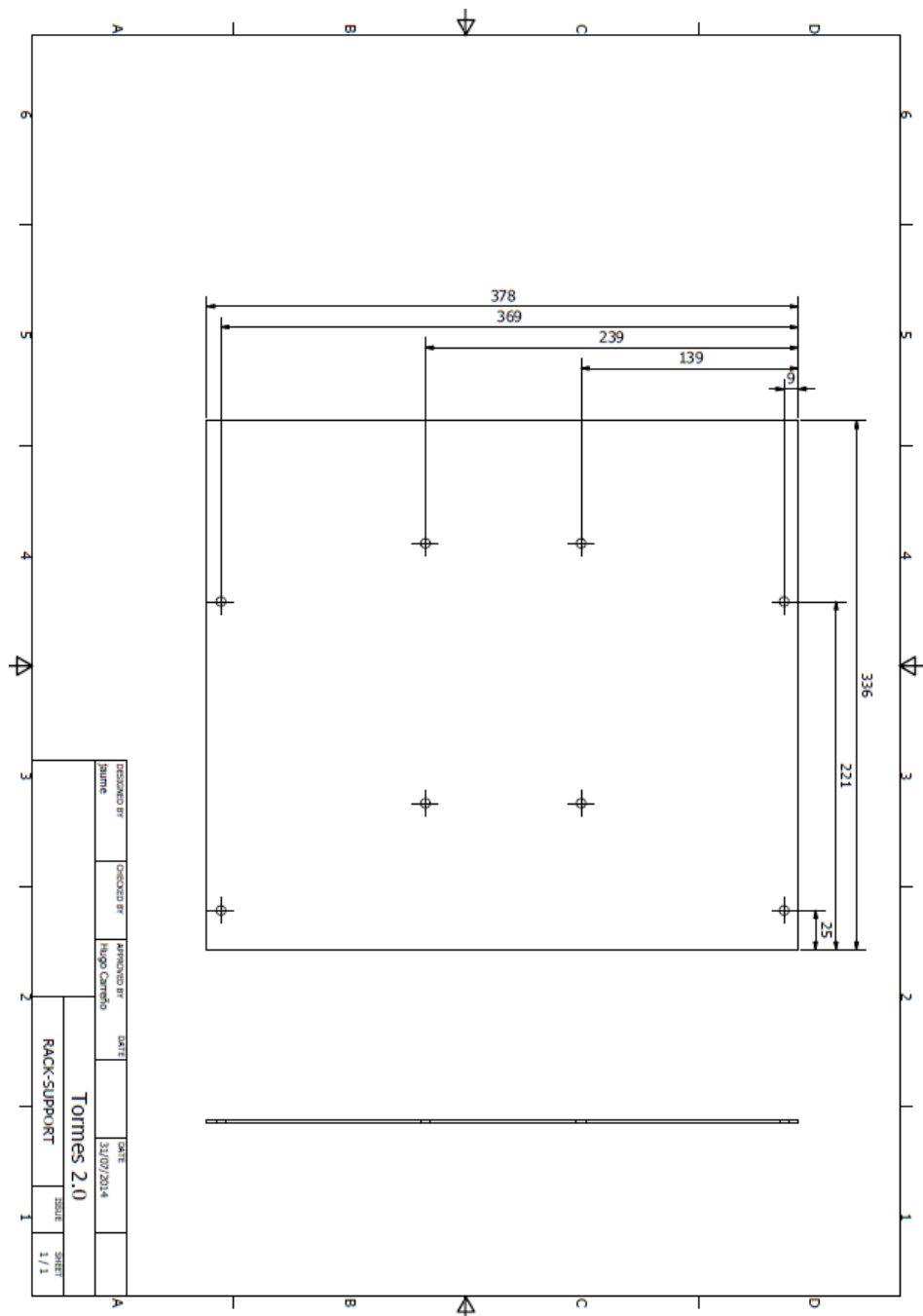


Fig. A.4. Internal interface of the experiment with the gondola.

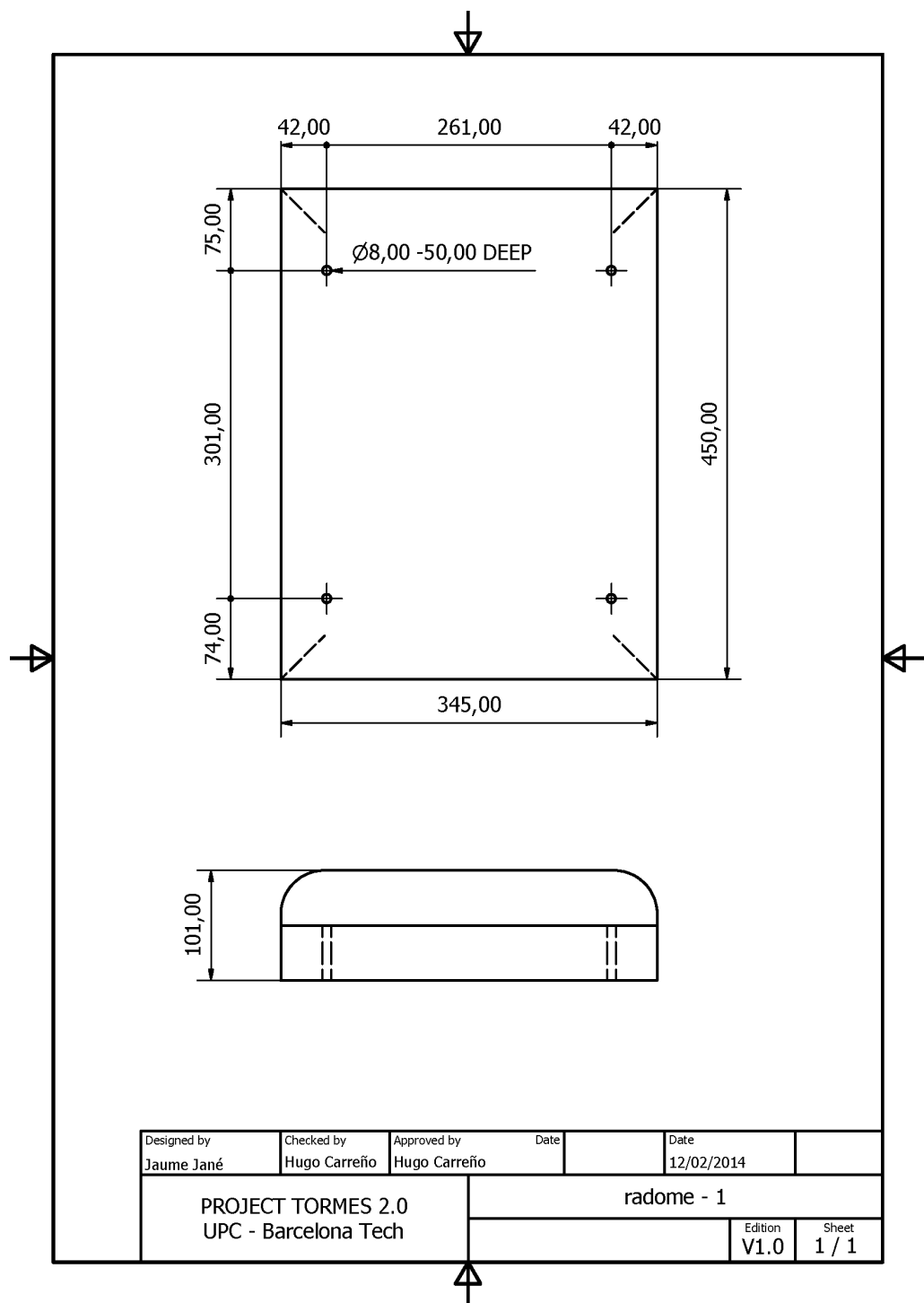


Fig. A-5. Interface of the radome-1 with the gondola.

A.2.2 Electrical

- Collected data were registered using an ATP industrial grade SD 32 GB memory card (PYCARO), and an ATP industrial grade microSD 16 GB memory card (OBC). The experiment was sensitive to other radio frequency sources that have harmonics fall in the frequencies of L1 and L2.
- The limb, up and the down-looking antennas were connected to the rack-1 by means of two Huber&Suhner coaxial cables type EZ_141_CU_TP_COIL. They were selected because of their wide operating temperature range, from -55°C to +125°C.
- The power subsystem: one input from the BEXUS-battery (two batteries connected in parallel) located into the gondola. The electrical connector was one Amphenol MS3112E8-4P.
- The power subsystem: one input from the BEXUS-battery (two batteries connected in parallel) located into the gondola. The electrical connector was one Amphenol MS3112E8-4P.
- The power subsystem: one input from the BEXUS-battery (two batteries connected in parallel) located into the gondola. The electrical connector was one Amphenol MS3112E8-4P.
- Two E-Link connections were required on the experiment.
- Two E-Link connections were required on ground.

A.2.3 Radio frequencies

- One GPS receiver was embedded into the rack. The specifications of the arriving signals are: Frequencies: L1 (1575.42 MHz), L2 (1227.60 MHz); Power: > -150 dBm; modulation: Binary Phase Shift Keying (BPSK).
- The experiment was sensitive to other radio frequency sources that have harmonics fall in the frequencies of L1 and L2.
- The bandwidths were 2.046 MHz for C/A-code L1 and L2C, and 20.46 MHz for P(Y)-code L1 and P(Y) L2.
- The experiment was totally passive (no emitted signal).

A.2.4 Thermal

- External elements: Patch heaters were attached to the antennas ground plane. The antennas were embedded into insulating radomes.

Radome-1: 2 heaters (2 x 1 W).

Radome-2: 1 heater (1 W).

Radome-3: 1 heater (1 W).

- Internal elements: 2 Patch heaters (2 x 1 W) were attached to the aluminium plate close to the SDR and to the switching matrix PCB.
- Position of heaters:

Heater-1 (1 W): Geometric center of the ground plane of the antenna-1.

Heater-2 (1 W): Geometric center of the ground plane of the antenna-2.

Heater-3 (1 W): Geometric center of the ground plane of the antenna-3.

Heater-4 (1 W): Geometric center of the 6:1 combiners (inside radome-1).

Heater-5 (1 W): SDR.

Heater-6 (1 W): Switching Matrix PCB.

A.3 Main experiment components

Table A.1. Technical specifications of the experiment components.

Component	Model	Supplier	Reasons
SD memory	Industrial Grade SD	ATP	Temperature range
microSD memory	Industrial Grade microSD	ATP	Temperature range
Rack-1	Series 110 N° 6	Retex	Mini-rack
Combiner 6:1	ZB6PD-17	Minicircuits	Low insertion loss
Combiner 2:1	GP2S+	Minicircuits	Low insertion loss, small size
Switch	MSWA-2-20+	Minicircuits	Small size, high isolation
Heater (1W)	1EFISI975001	Zoppas	Thermal budget
Temperature sensor	P1K0.232.6W.B.010	IST	Temperature range
GPS patch antenna	Specfic design to UPC	Antcom	Dual frequency L1&L2. Dual Polarization RHCP&LHCP
GPS Receiver	Aster	Septentrio	Low power consumption
E-Link Connector	PCD - RJF21B CODE A	AMPHENOL	EuroLaunch specification
Electric connector	MS3112E8-4P	AMPHENOL	EuroLaunch specification
SDR	USRP B210	Ettus Research	First fully integrated, two-channel USRP device with continuous RF coverage from 70 MHz -6 GHz
IMU	9DOF Razor	Sparkfun	Working experience
OBC	Overo IronStorm +Tobi	Gumstix	USB 2.0 High Speed

Table A.2. Technical specifications of the experiment components.

Component	Size (mm)	Operating Temperature (°C)	Current Status
Microcontroller	105 x 40 x 21	[-30, +85]	Delivered
SD memory	32 x 24 x 2	[-40, +85]	Delivered
microSD memory	15 x 11 x 1	[-40, +85]	Delivered
Rack-1	370 x 310 x 131	[x, +85]	Delivered
Combiner 6:1	89 x 797x 16	[-55, +100]	Delivered
Combiner 2:1	x	[-40, +85]	Delivered
Switch	x	[-40, +85]	Delivered
Heater (1W)	40 x 20	x	Delivered
Temperature sensor	25 x 16 x 1	[-200, +260]	Delivered
GPS patch antenna	54 x 52 x 9.7	[-55, +85]	Delivered
GPS receiver	230 x 100 x 50	[-40, +70]	Delivered
E-Link Connector	N.A.	[-40, +85]	Delivered
Electric Connector	N.A.	x	Delivered
SDR	155 x 97 x 15	[-40, +55]	Delivered
IMU	41 x 28 x 10	[-40, +65]	Delivered
OBC	105 x 40 x 5	[-40, +85]	Delivered

Table A.3. Mass budget.

Component	Amount	Heritage	Margin (%)	Mass (g)
GPS receiver	1	A	5	210
SDR	1	B	10	367
OBC	1	A	5	37
Combiner 6:1	2	A	5	378
Combiner 2:1	1	A	5	178
GPS patches	8	A	5	672
Radome-1	1	A	5	2,000
Radome-2	1	A	5	1,000
Radome-3	1	A	5	1,000
IMU	1	A	5	100
Rack-1	1	A	5	3,000
Aluminium plate	1	A	5	1,000
EPS	1	D	20	200

Harnessing	x	D	20	1,000
Heaters	6	A	5	x
Others	x	A	5	200
Subtotal	x	x	x	11,342
System Margin	x	x	5	1,134
Total	x	x	x	12,476

Table A.4. Experiment summary. Note: The values of the Center Of Gravity (COG) of the different components are referred to a dextro-rotatory Cartesian reference system with origin in the geometric centre of the M-Egon gondola and the x axis orthogonal to one lateral of the gondola.

Experiment mass (g):	Radome-1 (3,100), radome-2 (600), radome-3 (600), rack-1 (4,000), aluminium plate (650), harnessing (1,800), total (10,750).
Experiment dimensions (m):	Radome-1 (0.450 x 0.345 x 0.101), radome-2 (0.248 x 0.210 x 0.105), radome-3 (0.248 x 0.210 x 0.105), rack-1 (0.377 x 0.310 x 0.119)
Experiment footprint area (m²):	0.2669
Experiment volume (m³):	Radome-1 (0.0092), radome-2 (0.003), radome-3 (0.003), rack-1 (0.015),
Experiment expected Center Of Gravity (COG) position (m):	Radome-1 [0,0,-0.47], radome-2 [0.48,0,0], radome-3 [0.32,0.30,0.47], rack-1 [0.24,0,-0.36]

A.4 Mechanical design

Table A.5. External elements and racks attachment summary.

	Radome-1	Radome-2	Radome-3	Rack-1	Rack-to-gondola
Security Factor	10	10	10	10	10
Weight (kg)	5	1	1	4	16
Tensile Strength (N)	10,460	1,948	1,948	-3,920	-15,680
Shear Strength (N)	7,792	2,615	2,615	±1,960	±7,840
Solicitation/Traction (N)	-4,900	±490	-980	25,133	50,266
Solicitation/Shear (N)	±2,450	-980	±490	18,096	36,191
Number Screws	4	4	4	4	8
Metric	M4	M2	M2	M6	M6

A.5 Electronics design

A.5.1 Electrical power system

The aim of this subsystem was to adapt the voltage provided by the BEXUS battery (28 V) to that required by the different subsystems of the TORMES 2.0 payload. The selected internal power switch buck DC-DC regulators (Linear Technology) guaranteed very high efficiency in the range [80, 90] %, had a wide input range [3, 50] V, and had an operational temperature in the range [-40, +125] °C. A PCB with the following requirements was designed and manufactured:

- GPS: 5 V, 5.25 W
- ADS: 3.5 V, 50 mW
- SDR: 6 V, 4.4 W
- OBC: 5 V, 1 W
- Antennas: 3.3 V, 0.92 W
- Switches control: 4 V and 8 V

Some decoupling capacitors (ceramic and tantalum) of different values were added to the inputs and outputs to avoid ripple. The power inductors used were chosen with the minimum DC series resistance (below 0.1 Ω) to keep the maximum efficiency according to datasheets. A large ground plane was created in order to keep a good temperature dissipation. Additionally two PCBs were designed to read the sensors' data and to control the heaters (consisting of 6 equal circuits based on the Fairchild FPF2700 chip to drive the heaters, and control their activation and deactivation through the OBC).

A.6 Thermal design

The role of the thermal control system was to maintain the payload components and subsystems within their required temperature limits during the flight. Temperature ranges (operational and survival) included a lower and an upper limits imposed by the design requirements.

The antennas were located outside of the gondola. The environmental temperature was extremely cold down to -70°C and the operational thermal range of the GPS patch antennas was $[-55, +85]^{\circ}\text{C}$. The antennas should be embedded into insulating radomes to minimize the power consumption of the patch heaters. The width and type of the insulating material as well as the thermal power to be transmitted to the ground plane (that was required to maintain the antennas inside their operational thermal range) was calculated by thermal simulation using ESATAN (Fig. A.7).

The body of each radome was a box manufactured with a 1 mm width aluminium sheet. Inside the box the insulating material (2 cm width depron), the antennas ground plane (aluminium), and the GPS patch antennas were placed. The top of the radome was manufactured with a rectangular aluminium joint, a 4 cm width depron sheet and a fiberglass enclosure providing environmental isolation and structural rigidity. The width of the lateral depron-isolation was 6 cm. In addition, by filling the internal space of the radomes with depron, the amount of residual internal air was minimized, as well as the probability of water condensation. The two pieces of the radomes were joined by means of four pairs of steel junction elements riveted to the aluminum box. Depron was selected as an insulating material because it has low thermal conductivity (0.03 J/kg K) and density (40 kg/m^3).

Attribute: Temperature

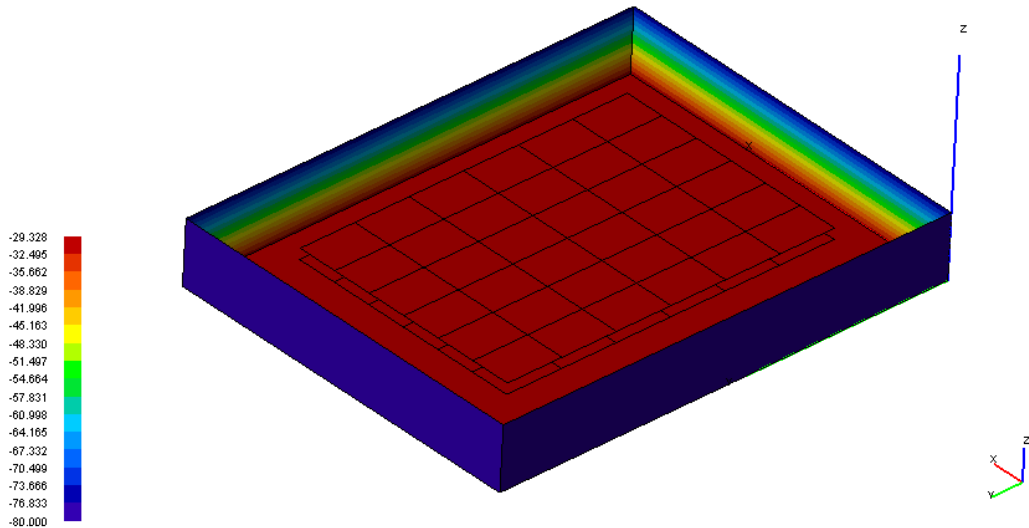


Fig. A.7. View of the results of the achieved temperatures in the down-looking antenna in a steady situation. They have been provided by a finite analysis simulation using the package software ESATAN.

The “patch heater” was selected as heating element. It consists of an electrical resistance element sandwiched between two sheets of flexible electrically insulating material. From the testing campaign and the BEXUS 17 data, the optimum number of patches as well as the minimum amount of thermal power to be transmitted was determined:

- 1 x 1 W RICA patch heater (40 mm x 20 mm) attached to the down-looking ground plane.
- 1 x 1 W RICA patch heater (40 mm x 20 mm) attached to the 6:1 combiners inside the radome-1.
- 1 x 1 W RICA patch heater (40 mm x 20 mm) attached to the up-looking ground plane.
- 1 x 1 W RICA patch heater (40 mm x 20 mm) attached to the limb-looking ground plane.

Usually in space systems the heater system has some sort of switch or control. This typically involves a relay to enable or disable power to the heater, a fuse to protect the vehicle from a short circuit, and, most commonly, a thermostat or solid-state controller to turn the heater on and off at predetermined temperatures. The system selected for this mission was an OBC (Gumstix Iron Strom microcontroller) to monitor temperatures and to turn heaters on and off as appropriate. The selected temperature sensors were:

- 2 x P1K0.232.6W.B.010 temperature sensor PT1000 attached to the down-looking antenna.
- 2 x P1K0.232.6W.B.010 temperature sensor PT1000 attached to the up-looking ground plane.
- 2 x P1K0.232.6W.B.010 temperature sensor PT1000 attached to the limb-looking ground plane.

Additionally an internal thermal control was implemented in rack-1 (electronics):

- 2 x 1 W RICA patch heaters (80 mm x 20 mm) attached to the SDR.
- 2 x P1K0.232.6W.B.010 temperature sensor PT1000 attached to the internal aluminium plane.

Note: As default the outdoor hub was deactivated because of the insulating radomes provide high thermal isolation. Note that TORMES 2.0 included individual radomes for each GPS patch antenna providing an operational temperature range from -55° to +85° even without the external radomes. This strategy allowed to reduce the power consumption and therefore the mass budget (no need for a dedicated battery).

Note: The heaters were manufactured following the ESCC (European Space Components Coordination) No. 4009/002.

Summary:

- Reduction in the amount of outdoor heaters as compared with BEXUS 17.
- TORMES 2.0 antennas had the Low Noise Amplifiers (LNAs) integrated in each single GPS patch. Each pack was already integrated into an individual radome (in addition of the external radome). Therefore there was no requirement of an additional heater for external LNAs. Only the antennas’ ground planes were provided with heaters.
- As a consequence of that TORMES 2.0 had half the number of heaters as compared with the last flight.
- Additionally, using housekeeping data from BEXUS 17 we determined that the thermal simulation provided a conservative value of required amount of heaters.
- Using this improvement, TORMES 2.0 included thermal control also for the internal electronics.

A.7 Power system design

- The power strategy (Fig. A.8 and Table A.6) took as a reference the power budget defined by the power consumption of the different experiment components, the design requirements and the experience during the BEXUS 17 flight. TORMES 2.0 increased the SNR of each RF channel including the LNAs before the 2:1 combiners. This was done using a dedicated antenna package that already integrated the first amplification step. As a consequence, the dedicated 5 W heaters to the LNAs and the combiners were not required. In addition, based on the performance of the system during BEXUS 17, the power dissipated by the heaters was reduced. TORMES 2.0 included a thermal control for the internal elements because the flight was expected to be done during night (colder environment), because of the experience with the E-Link failure during BEXUS 17, and because of the recommendations of the ESA thermal mentor.
- Two BEXUS batteries connected in parallel were required to supply power to the heaters and the rest of the experiment.
- The nominal voltage provided by the BEXUS batteries (or the external power supplied from Hercules which was used until T-40 min) is 28 V. A dedicated EPS was used to properly supply power to the experiment.
- The selected power strategy included one electrical connector (Amphenol MS3112E8-4P) to drive the on-ground activities, the countdown and the flight.

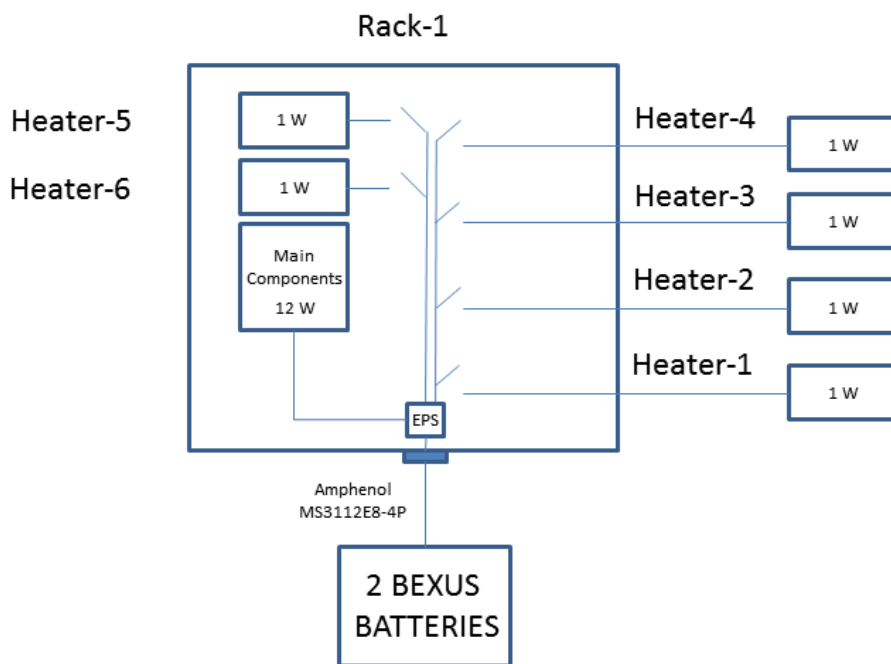


Fig. A.8. Sketch of the power strategy for “on ground” and “flight” configuration. During “on ground” activities the two battery inputs are substituted by external power.

Table A.6. Energy budget.

Component	Current (A)	Consumption (W)	Electric charge (Ah)	Energy (Wh)
Internal heaters	0.25	2.3	0.75 (3 h)	6.1 (3 h)
External heaters	0.48	4.7	0.21 (0.45 h)	2.1 (0.45 h)
GPS	0.045	5.9	0.31 (7 h)	41.3 (7 h)
SDR	0.47	2.9	3.29 (7 h)	20.3 (7 h)
OBC	0.7	3.5	4.9 (7 h)	24.5 (7 h)
Antennas	0.35	1.2	2.45 (7 h)	8.4 (7 h)
ADCS	0.017	0.06	0.12 (7 h)	0.42 (7 h)
Total	2.31	20.6	12	103.1
Estimation Available (minimum -20 °C)	5 (fuse)	35	12	350 (25 V)
Margin (0.85 efficiency included)	2.69	14.4	0	246.88

A.8 Software design

A.8.1 Command and data handling system

System overview

All processing power was provided by a Gumstix Iron Storm, an industrial computer based on ARM. This board was equipped with an Ubuntu Linux distribution running a 2.5.38 Kernel. Ubuntu was preferred instead of different Linux ports for embedded systems due to its wide support and robustness. Embedded operating systems would lead to a greater performance because they are lighter by definition. However, there are other factors to consider when picking an Operating System (OS). The most important one was the time restriction of the project. Developing time was reduced significantly using a widely used OS such as Ubuntu because: a) there are precompiled packages ready for use (such as GNU Radio), b) more recent software packages are available, and c) the community support and available documentation is significantly more extensive. These factors compensate widely the decrease in performance of the final system. Also, it should be noted that the selected on-board computer was a high end product compared to different embedded computers (CPU clock: 800 MHz, 512 MB RAM).

The two interfaces used for debugging were a serial port providing a console, and an Ethernet port along with a SSH server. The last was preferred due to its speed, robustness and easiness of use. The board also included a JTAG connector, although it was unlikely to make use of it since it was used to debug software at a very low level. The system run three processes at the same time (not including the processes that may be related to the OS itself), which was created by a boot sequence program. These three processes were:

- Telecommand management process
- Payload management process
- Housekeeping management process

Boot sequence

Gumstix Iron Storm started its boot sequence (Fig. A.9) when it was powered on, so no special process had to be applied. The very first step was to load uBoot through the bootstrap present in a NAND static memory. uBoot in turn loaded the Linux Kernel. The bootstrap and the uBoot were important in the sense that they had the ability to perform very low level operations such as writing registers and memory directly. From previous experience this was shown to be important for things such as watchdog configuration. A first program run after the Kernel initialization. This program exported the GPIO to the user space, that is, it provided a handler for each one that was necessary. This process also created pipes to provide communication between processes. Finally the three processes were created and started. After these operations were finished, this process blocked.

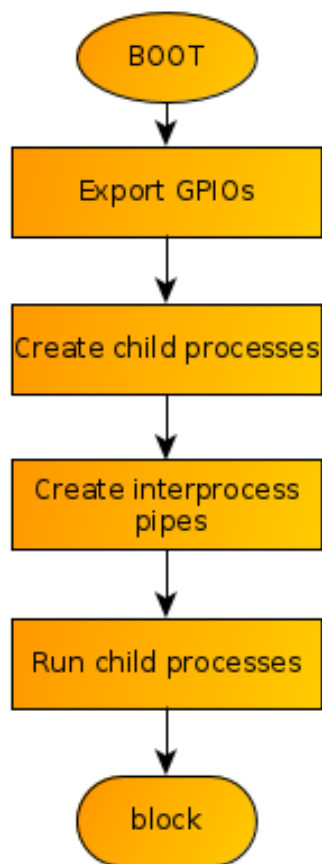


Fig. A.9. Boot sequence process.

Telecommand management process

The telecommand management process (Fig. A.10) analyzed the telecommands sent by the ground station and performed the operations needed in response for each one. The process started by creating transmission and reception (TX and RX) pipes which were used as a way of interfacing the user program with the Ethernet Kernel hardware driver. It was likely that the interface provided by Ubuntu (also a pipe or more commonly called a file in this context) was usable without the need of modifications. The process then proceeded to read a default configuration file and creating a log file in which events related to telecommands were dumped. The next step was to open an User Datagram Protocol (UDP) socket to communicate with the ground station. After the configuration was completed, the thread enters in an infinite loop in which it first read the RX pipe for available data.

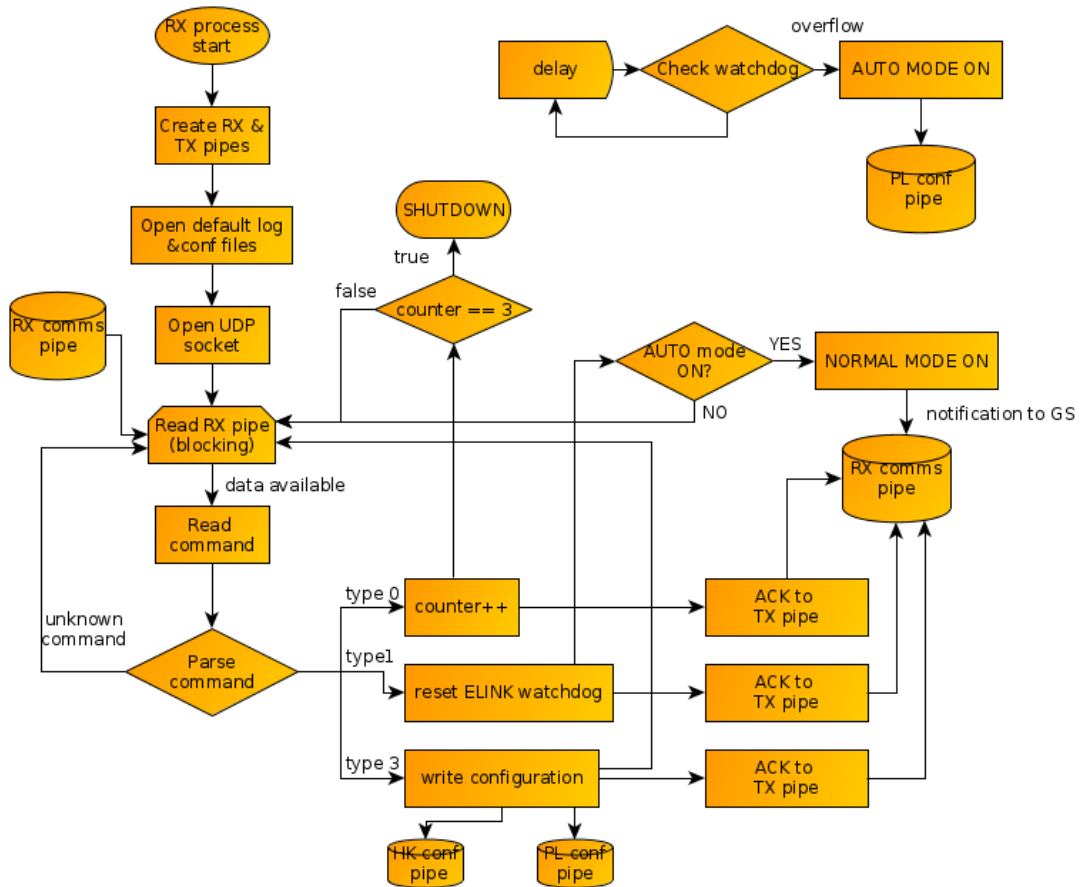


Fig. A.10. Telecommand management process.

The process blocked in case there was no data available and unblocked through an interruption when data arrived. In the event that data were available to be read, the process stored and parsed it in order to extract the needed information. When the type of command was extracted, the process took the specific actions defined for each one and sent an acknowledgement data packet specific for each command to the TX pipe.

A description of each command is here presented:

Type 0 command: This command was used to shutdown the experiment. In order to avoid the fatal event in case the command was sent by error, it had to be transmitted three times before shutdown actually took place.

Type 1 command: This command was used to change the configuration of the experiment.

Pipes were used instead of flags or other simple data structures because they are a very simple way to protect data from concurrency problems. Also, they were useful to save CPU time by blocking and unblocking the process automatically in a simple way instead of polling a variable or blocking and unblocking the process using other methods.

An automatic mode was implemented. First of all, a beacon was sent from the ground station periodically in order to detect a link failure. An automatic mode was started in the case the telecommand process did not receive it after a period of time.

Command structures

The command structure was defined as follows: HEADER COMMAND TYPE PARAM 1 PARAM 2 ... PARAM N

Payload management process

The payload management process acquired data samples from the PYCARO payload. First of all a configuration file was read after the process started. After that, the process started reading a batch of samples generated by the payload. Finally the samples were processed, stored in a microSD card, and sent to the TX comms pipe in order to perform real time measurements in the ground station. The process started by reading the configuration. Note that there was a default configuration file and the input pipe to this process was used to change the configuration at any time.

Housekeeping management process

The housekeeping management process (Fig. A.11) read the state of the sensors. An Analog-to-Digital Converter (ADC) was used to read the temperature sensors. The process started opening a log file in which events related to housekeeping, as well as the data, were dumped. Then a default configuration file was read in case there were no data in the input pipe of the process (exclusively used to change configuration parameters). After the system was set up the process proceeded to read each temperature sensor sequentially by changing the state of a multiplexer connected to these sensors and the ADC. The results were then stored in the log file. This loop repeated at a configurable amount of time, and the data read were only sent to the TX comms pipe at a configurable number of loop iterations in order to save bandwidth.

An automatic mode was meant in case the E-Link failure. An “E-Link watchdog” was implemented and it was meant to look after the proper operation of the link. In case this watchdog was not reset by a special command for a defined period of time, the

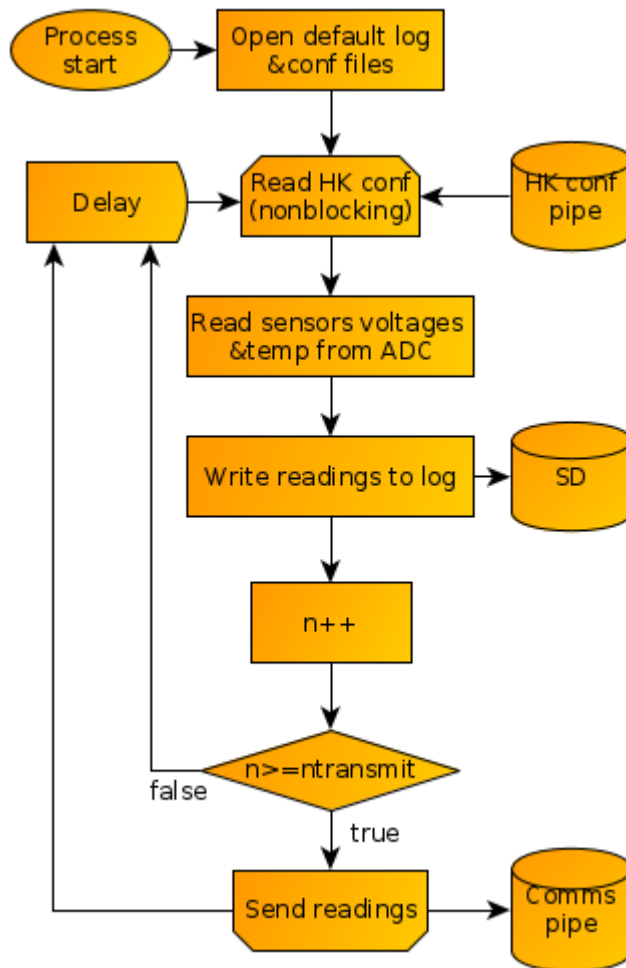


Fig. A.11. Housekeeping management process.

experiment switches to the automatic mode. The switch was performed writing a default configuration to the payload management process.

A.8.2 Ground station

There were two threads of execution dedicated to data reception and sending (Fig. A.12). Received data were displayed graphically in different ways depending on their type. Temperatures and voltages were displayed versus time. Finally, the Graphical Unit Interface (GUI) should display buttons used to send the implemented commands. The implementation was done using GNURadio as it allowed a very short developing time, including the GUI.

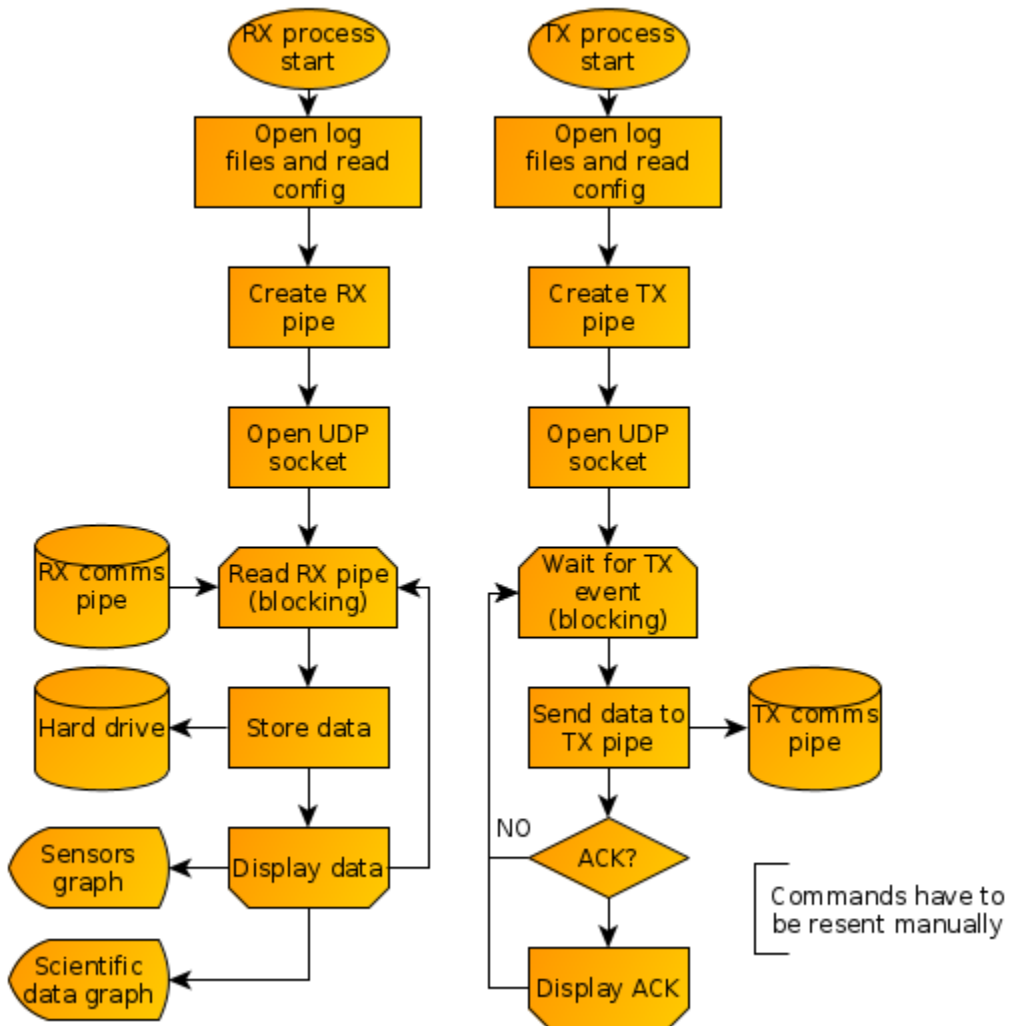


Fig. A.12. Ground Station (GS) process.

A.9 Attitude determination system

The razor IMU 9-dof board had the capability to capture different on-flight data which were used to compute the attitude: a 3-axes gyroscope (ITG-3200) to determine the angular velocity and a 3-axes magnetometer (HMC5883L) to measure the Earth magnetic field. All the outputs were controlled by the OBC which was programmed for data management, gyroscopes drift correction and calibration for all the sensors. The flow diagram of the Attitude Determination System (ADS) followed this sequence (Fig. A.13):

1. Get the data.
2. Get the GPS data (Latitude and longitude).
3. Compute the IGRF.
4. Compute the attitude algorithm using the QUEST solution.

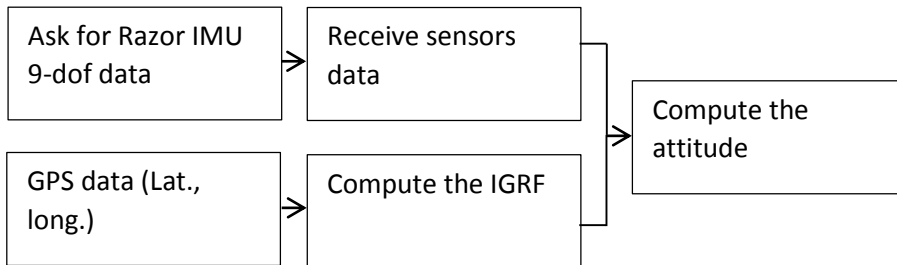


Fig. A.13. Attitude Determination System (ADS) flow diagram.

A.10 Testing plan

The experiment testing campaign was performed following the flow diagrams shown in this section (Figs. A.14-A.16). The payload and the platform were developed separately and they were tested also separately. After this, they were integrated and a health check was performed. After that, the thermal-vacuum and vibration tests were performed to verify the corresponding requirements. Finally, the bench was performed.

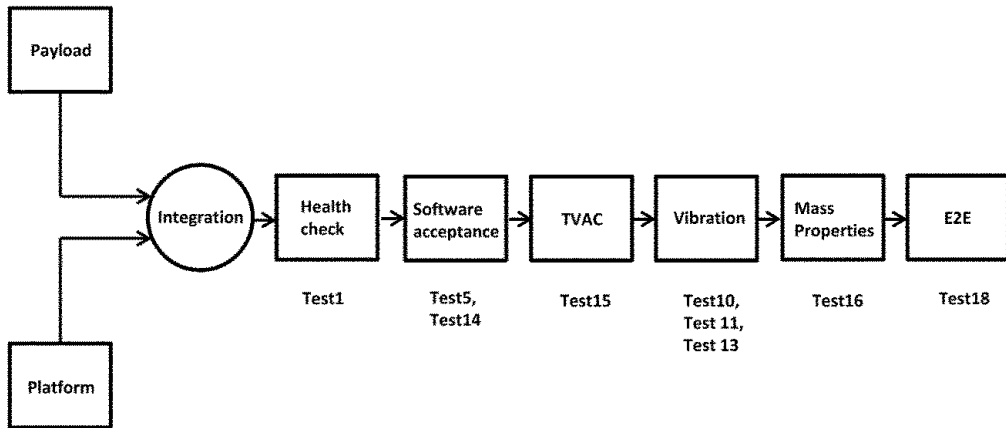


Fig. A.14. Flow of the testing campaign for the complete experiment set-up.

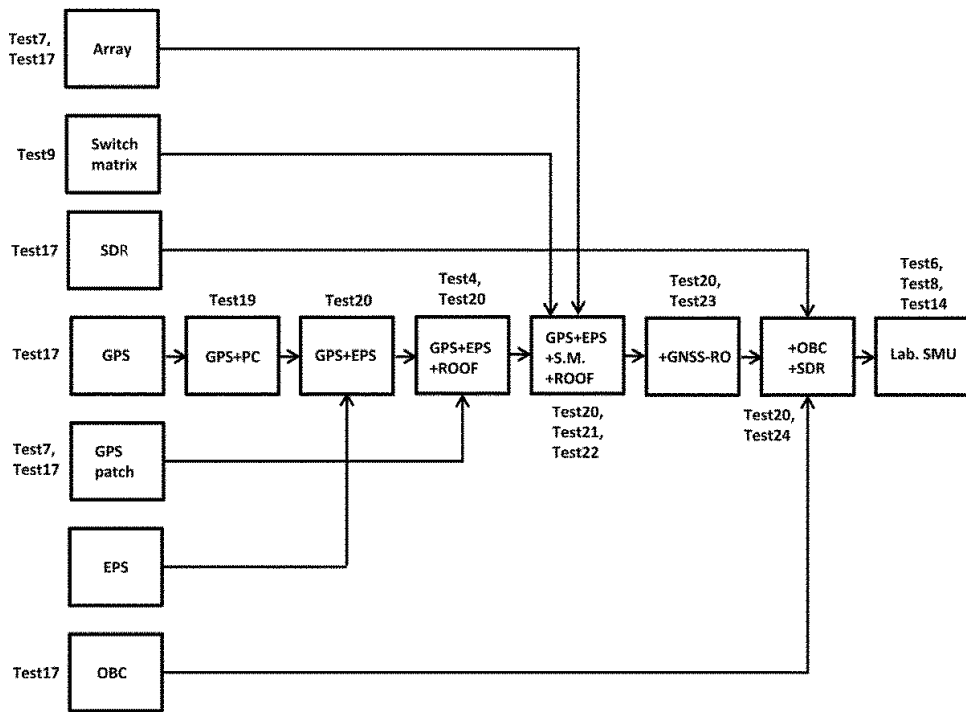


Fig. A.15. Flow of the testing campaign for the payload.

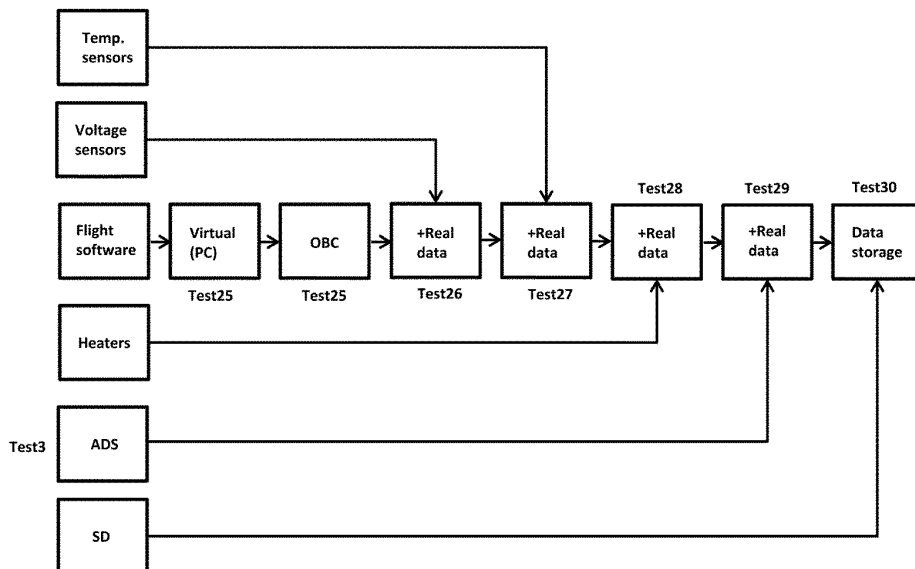


Fig. A.16. Schedule of the testing campaign for the platform.

Tests results:

- Each subsystem was separately tested. During the analysis some minor modifications were included in the ground station; Some “extra” intelligence was transferred to the ground segment to operate the “manual” mode. On the other side the automatic mode operations were performed nominally.
- The mass properties (weight) were characterized. The total mass of the complete experiment set-up was 10.7 kg.
- The thermal-vacuum tests were performed for the external and internal experiment components.
 - a) The radomes provided high thermal isolation so that the external heaters needed to be turned on 45 min for a flight duration of 6 h.
 - b) The energy budget was proper to provide enough energy to guarantee the thermal control of the internal electronics for a flight duration of 6 h.
 - c) The PCBs were covered with epoxy to protect the electronics components of the vacuum. This was verified in the thermal-vacuum chamber.
- The mechanical integrity of the experiment was verified: Shock, random and sinusoidal test in the shake table.
- The technical and scientific requirements were verified testing the PYCARO instrument from a roof at the UPC premises and in a field experiment (Costa del Garraf, Barcelona, Spain).
- The SMU 200 A GPS signal generator was used to properly tune the PYCARO parameters so that the default configuration in the automatic mode guaranteed the collection of scientifically valuable data.
- The antenna array and the GPS patches were characterized in the UPC anechoic chamber. The gain of the array verified the requirements so that the attenuation of the GPS signals in the scattering process could be compensated. This guaranteed the collection of the Earth-reflected GPS-signals during the experiment.
- The antenna array’ secondary lobes did not introduce the direct GPS signals in the correlation channels of the OBC. This was tested in a roof at the UPC premises using absorbent material.

A.11 Launch campaign preparation

Table A.7. Preparations and test activities at Esrange Space Center.

	Activity	Description	Required	Member	Duration (h)
DAY 0					
Action 1	Coordination of the preparation activities.	Pre-flight activities coordination with GranaSAT.	Conversation: (a) ADS calibration and data. (b) To cover GranaSAT external structure with neoprene.	H. Carreno-Luengo	1
DAY 1					
Action 1			Set-up verification after the travel to Esrange Space Center from Barcelona.	H. Carreno-Luengo (PYCARO), A. Amèzaga (OBC), R.Olivé (SDR-OBC), J.F. Munoz (RF), D.Vidal (IMU)	4
DAY 2					
Action1	Set-up verification (before attachment to the gondola).				5
1.1	Antennas and racks connections.	Antennas outdoor placement.	Photography.	J.F. Munoz	0.5
1.2	Mechanical mounting.	Mounting	Photography.	D. Vidal	0.5
1.3.1	PYCARO ³⁸ .	To check correlation channels.	Scientific data measurement.	H. Carreno-Luengo, R. Olivé	2
1.3.2	(CDHS, EPS, ADS, Thermal) ³⁹	To check the different subsystems.	Housekeeping data measurement.	A. Amèzaga, J.F. Munoz, D. Vidal	2
Action 2	Ground equipment installation.				1
2.1	Laptop.	Installation	Photography.	H. Carreno-Luengo, J.F. Munoz	1
Action 3	Electrical Check-Out				1.2
3.1	Power supply connections.	Power connections.	Photography.	A. Amèzaga	0.3
3.2	Mechanical connections.	Mechanical connections.	Photography.	D. Vidal	0.3
3.3	E-Link communication.	To verify E-Link.	Measurement.	J.F. Munoz	0.3

³⁸ PYCARO (P(Y) & C/A ReflectOmeter) was tested at Esrange. Two coaxial cables were used, and the two antennas were placed outside to collect the GNSS signals (H. Carreno-Luengo, R. Olivé).

³⁹ All the subsystems (CDHS, EPS, Thermal, ADS) were turned on when performing the previous test and data were collected. The collected data (housekeeping data) were analyzed to ensure a fully operational experimental set-up: Temperatures, voltages (A. Amèzaga), data storage (J.F. Munoz), attitude (D. Vidal).

<hr/>					
Action 4	Interference test.				1
4.1	Data processing and identification of potential interferences when all experiments are turned on.		Measurement.	H. Carreno-Luengo, R. Olivé	0.5
4.2	System performance with real GNSS signals.	Gondola raise up and open door.	Measurement.	H. Carreno-Luengo, R. Olivé	0.5
Action 5	ADS calibration.				1
5.1	ADS calibration.	To rotate the gondola and to calibrate the IMU. All the experiments shall be turned on in operational mode.	Measurement.	D. Vidal	1
DAY 3					
Action 1	Flight Compatibility Test (Gondola).				5.5
1.1.1	PYCARO ⁴⁰	Check correlation channels and test (Requirement D.5).	Measurement and photography.	H. Carreno-Luengo, R. Olivé	1.5
1.1.2	(OBDH, EPS, Thermal, ADS, TT&C) ⁴¹ .	Check all subsystems.	Measurement and photography.	A. Amèzaga, J.F. Munoz, D. Vidal	1.5
1.1.3	E-Link verification.	Verification of the communications between the experiment and the ground station.	Measurement and photography.	A. Amèzaga, J.F. Munoz	1.5
1.2	Interference analysis.	Team meeting to comment all the measurements and analysis of potential interferences. To give and change information with all the teams and Eurolaunch.		Team	1
Action 2	Flight Readiness Review.				2

⁴⁰ PYCARO (P(Y) & C/A ReflectOmeter) was tested when installed in the gondola. The test was performed in both direct & reflected correlation channels, (H. Carreno-Luengo, R. Olivé).

⁴¹ All the subsystems (CDHS, EPS, Thermal, ADS, TT&C) were turned on when performing the previous test. Housekeeping data were analyzed to ensure a fully operational experimental set-up: Temperatures, voltages (A. Amèzaga), E-Link communication, data storage (J.F. Munoz), attitude (D. Vidal).

2.1	Status report meeting.	H. Carreno-Luengo	1
2.2	Data processing and interference analysis.	H. Carreno-Luengo	1
DAY 4			
Action 1	1 st launch opportunity.		1
1.1	Status report.	H. Carreno-Luengo	1
DAYS 5-10	Possible launches.		

Table A.8. Timeline for countdown and flight.

Time	Operation	Member
T-4H00	Visual inspection of the external mounted elements.	J.F. Munoz
T-4H00	Visual inspection of the internal mounted elements.	D. Vidal
T-4H00	Checking mechanical integrity of the radomes.	A. Amézaga
T-4H00	Checking mechanical integrity of PYCARO.	H. Carreno-Luengo, R. Olivé
T-3H45	Checking RF and electrical connections.	J.F. Munoz
T-3H30	External power supply connection.	A. Amézaga
T-3H30	Operational test 1.1 ⁴² .	H. Carreno-Luengo, R. Olivé
T-2H30	Operational test 1.2 ⁴³ . During the sweet-spot tests it is required to book the possibility to have access to the gondola (H. Carreno-Luengo) in case of no nominal operations.	A. Amézaga, J. F. Munoz, D. Vidal, H. Carreno-Luengo
0H00	Start recording data.	J.F. Munoz
[0H00,T+TBD]	Payload and housekeeping data monitoring.	H. Carreno-Luengo, R. Olivé
T+TBD	To stop communications, to store and to close all the files.	J. F. Munoz
T+TBD	End of mission (recovery).	NA

⁴² PYCARO (P(Y) & C/A ReflectOmeter) was tested during countdown. The test was performed in both direct & reflected correlation channels with the direct GNSS signals. Therefore, it was not required to have the gondola lifted (H. Carreno-Luengo, R. Olivé).

⁴³ All the subsystems (CDHS, EPS, Thermal, ADS, TT&C) were turned on when performing the previous test and data were collected. The collected data (including payload data and housekeeping data) were analyzed to ensure a fully operational experimental set-up: Temperatures, voltages (A. Amézaga), E-Link communication, data storage (J.F. Munoz), and attitude (D. Vidal).

B

APPENDIX B: $^3\text{Cat-2}$ REQUIREMENTS AND CONSTRAINTS

The ³Cat-2 mission requirements (M = Mission, O = Operational, S = System, SB = Subsystem, E = Environmental) and constraints (C) are included here:

M.1 The system shall collect the Earth-reflected GNSS signals.

M.2 The system shall collect the direct GNSS signals.

M.3 The mission shall provide the direct and the Earth-reflected conventional and interferometric “open-loop” waveforms.

M.4 The mission shall provide the direct and the Earth-reflected conventional and reconstructed-code “closed-loop” waveforms.

M.5 The direct “open-loop” conventional waveforms shall be provided using the L1 C/A GPS code, the B1I Beidou code, and the E1 BC Galileo code. These waveforms shall be provided at RHCP.

M.6 The Earth-reflected “open-loop” conventional waveforms shall be provided using the L1 C/A GPS code, the B1I Beidou code, and the E1 BC Galileo code. These waveforms shall be provided at LHCP.

M.7 The direct “closed-loop” conventional waveforms shall be computed using the L1 C/A and L2 C GPS codes, the L1 C/A, L2 C/A and L2 P GLONASS codes, and the E1 BC Galileo code. These waveforms shall be provided at both LHCP, and RHCP.

M.8 The Earth-reflected “closed-loop” conventional waveforms shall be computed using the L1 C/A and L2 C GPS codes, the L1 C/A, L2 C/A, and L2 P GLONASS codes, and the E1 BC Galileo code. These waveforms shall be provided at both LHCP and RHCP.

M.9 The direct “open-loop” interferometric waveforms shall be provided using as much bandwidth of the GPS signals at L1 and L2 as possible, and preferable the full bandwidth. These waveforms shall be provided at RHCP.

M.10 The Earth-reflected “open-loop” interferometric waveforms shall be provided as much bandwidth of the GPS signals at L1 and L2 as possible, and preferable the full bandwidth. These waveforms shall be provided at LHCP.

M.11 The direct “closed-loop” reconstructed-code waveforms shall be provided using the P(Y) GPS code at L1 and L2. These waveforms shall be provided at both LHCP and RHCP.

M.12 The Earth-reflected “closed-loop” reconstructed-code waveforms shall be provided using the P(Y) GPS code at L1 and L2. These waveforms shall be provided at both LHCP and RHCP.

M.13 The system shall determine the attitude of the satellite and control it as required to achieve the primary scientific goals.

M.14 The waveforms’ coherent integration time shall be adjustable to be optimized.

M.15 The Phase Lock Loop (PLL) parameters (bandwidth and pre-detection time) shall be adjustable.

M.16 The Delay Lock Loop (DLL) parameters (bandwidth and pre-detection time) shall be adjustable.

M.17 The Earth-reflected GNSS signals shall be collected with an antenna (antenna-1) of at least 12 dB of gain.

M.18 The Earth-reflected GNSS signals shall be collected with a dual-band (L1 and L2) and dual-polarization (RHCP and LHCP) antenna (antenna-1).

M.19 The direct GNSS signals shall be collected with an omnidirectional antenna (hemispherical) (antenna-2).

M.20 The direct GNSS signals shall be collected with a dual-band (L1 and L2) and dual-polarization (RHCP and LHCP) antenna (antenna-2).

M.21 The Earth-fixed position on any nominal specular point on the geographical grid on the Earth ellipsoid to which reconstructed altimetric values are assigned to shall be known with an accuracy better than 10 km. Only the specular point within the Field Of View (FOV) shall be considered for this requirement.

M.22 To provide Sea Surface Height (SSH) over the World Geodetic System (WGS) 84 ellipsoid in at least 2 points (with a goal of 3 points) over the ocean simultaneously.

M.23 Altimetric products shall be provided with an accuracy of at least 1 m.

M.24 The position of the satellite shall be determined during the nominal mode of the mission with an accuracy of at least 0.5 m.

M.25 Altimetric products shall be provided with a precision of at least 1 m (1- σ).

M.26 The spatial resolution of the main mission objective shall be at least:

a) “Open-loop” mode: 100 km x 10 km (along x across track)

b) “Closed-loop” mode: 7 km x 300 m (along x across track)

M.27 The main mission objective (GNSS-R) shall be satisfied with a revisit time within 12 days.

M.28 The Signal-to-Noise Ratio std. RF channel noise shall be less than 1 dB.

M.48 The RF channels shall be equalized.

M.30 The default coherent integration time shall be 1 ms in both “open-loop” and “close-loop” measurements.

M.31 The coherent integration time scanning in “open-loop” measurements shall be: 1 ms, 3.2 ms and 6.55 ms.

M.32 The coherent integration time scanning in “closed-loop” measurements shall be done in steps of 1 ms, from 1 ms to 20 ms.

M.33 The default PLL bandwidth shall be 1 Hz.

M.34 The PLL bandwidth scanning shall be performed in steps of 1 Hz, from 1 Hz to 15 Hz.

M.35 The default DLL bandwidth shall be 1 Hz.

M.36 The DLL bandwidth scanning shall be performed at: 0.01 Hz, 0.1 Hz, 1 Hz and 10 Hz.

M.37 The default PLL pre-detection time shall be 10 ms.

M.38 The PLL pre-detection time scanning shall be performed in steps of 1 ms from 1 ms to 10 ms.

M.39 The default DLL pre-detection time shall be 20 ms.

M.40 The DLL pre-detection time scanning shall be performed in steps of 1 ms from 1 ms to 20 ms.

M.41 The system should collect the GNSS signals after atmospheric bending.

M.42 The atmospheric signal bending should be measured in “closed-loop” using GPS signals (L1 C/A, L2C and L1&L2 P(Y)), GLONASS signals (L1 C/A, L2 C/A, and L2 P), and Galileo signals (E1 BC). These observables shall be provided at both LHCP and RHCP.

M.43 The GNSS signals after atmospheric bending should be collected with an antenna (antenna-1) of at least 12 dB of gain.

M.44 The GNSS signals after atmospheric bounding should be collected with a dual-band (L1 and L2) and dual-polarization (RHCP and LHCP) antenna (antenna-1).

M. 46 The system should determine the attitude of the satellite and control it as required to achieve the secondary scientific goals.

M. 47 The FOV of the antennas shall be free of structures that could cause multipath.

M.49 The instrument shall consist of a P(Y) and C/A ReflectOmeter (PYCARO).

M.50 PYCARO shall include a structure for a nadir/limb-looking antenna array (antenna-1), and a zenith-looking omnidirectional antenna (antenna-2), and

M.51 PYCARO shall include a Software Defined Radio (SDR),

M.52 PYCARO shall include an on-board microcontroller, and

M.53 PYCARO shall include a dedicated PCB to perform the operational modes changes.

M.54 The radiation-sensitive elements of the payload shall be properly insulated.

M.55 The secondary payload is an experimental magnetometer that will be provided by IEEC for the future Evolved Laser Interferometer Space Antenna (eLISA) mission.

M.56 The secondary payload shall satisfy the constraints imposed by the main scientific objectives of the mission.

M.57 The sampling rate shall be at least 1 Hz.

M.58 The duration of the nominal operational mission lifetime shall be at least 1 year.

M.59 The satellite shall operate in the designated orbit: SSO, mean LTAN = 00:00 AM, $650 \text{ km} > H_{\text{ref}} > 450 \text{ km}$.

O.1 The system shall have four operational modes: Start-Up (SU), Nominal, Survival and Sun-Safe (SS).

O.56 The SU mode shall be the first mode after boot sequence.

O.57 The exits of the SU mode shall be: a) Exit to Nominal mode upon SU mode triggers (autonomously), b) exit to Nominal mode through Ground Station (GS) telecommands, c) exit to SS mode upon SU mode triggers (autonomously), d) exit to SS mode through GS telecommands, e) exit to Survival mode upon SU mode triggers (autonomously), and f) exit to Survival mode through GS telecommands.

O.58 In SU mode: PYCARO payload (off), CDHS (nominal), ADCS (off), EPS (all power service powered on), TT&C (on-command receivable).

O.2 The Nominal mode shall be the scientific mode of the system.

O.3 In Nominal mode, the microprocessor shall auto-trigger a transition to one of the contingency modes.

O.4 The Nominal mode shall possess contingency operations for extended loss of communications. The system shall be capable to generate scientific data and to store them. An on-board scheduler shall orchestrate the periods when the payload has to be turned on.

O.5 In Nominal mode: PYCARO payload (nominal), C&DH (nominal), ADCS (nominal), EPS (all power service powered on), TT&C (on-command receivable).

O.6 The exits of the Nominal mode shall be: a) Exit to SS mode upon SS mode triggers (autonomously), b) exit to SS mode through GS telecommands, c) exit to Survival mode upon SS mode triggers (autonomously), d) exit to Survival mode through GS telecommands.

O.7 The SS mode shall be the first level of bus contingency operations.

O.59 The first turn-on sequence shall be done in SS mode by GS telecommands.

O.8 In SS mode the satellite is pointed in a solar inertial orientation to provide long term autonomous operations.

O.9 In SS mode only sequences of highest priority shall be executed.

O.10 The SS mode shall possess contingency operations for extended loss of communications.

O.11 In SS mode: PYCARO payload (off), CDHS (nominal), ADCS (2 axis Sun track), EPS (reduced power mode), TT&C (on command receivable).

O.12 The triggers of the SS mode shall be: a) EPS fault: battery voltage < 90%, b) ADCS fault: any failure that endangers power so that battery voltage < 90%, c) CDHS fault.

O.13 The SS mode exits shall be only possible by GS telecommands to: a) Nominal mode, b) Survival mode, c) SU mode.

O.14 In Survival mode only the critical bus functionality shall be maintained to provide power and communications.

O.15 In Survival mode only sequences of highest priority shall be executed.

O.55 In Survival mode the satellite is pointed in a solar inertial orientation to provide long term autonomous operations.

O.16 In Survival mode: PYCARO payload (off), CDHS (nominal), ADCS (2 axis Sun track), EPS (only power critical services), TT&C (on command receivable, power demand reduced).

O.17 The triggers of the Survival mode shall be: a) EPS critical fault: battery voltage < 80%, b) ADCS critical fault: any failure that endangers power so that battery voltage < 80%, and c) CDHS critical fault.

O.18 The Survival mode exist shall only possible to SS mode by GS telecommands.

O.19 Altimetry shall be performed using the PYCARO payload based on the “open-loop” conventional and the interferometric GNSS-R principles (cGNSS-R and iGNSS-R).

O.20 Altimetry in “open-loop” mode shall be performed using the collected Earth-reflected GNSS signals in LHCP.

O.21 Altimetry shall be performed using the PYCARO payload based on the “closed-loop” conventional and the reconstructed-code GNSS-R principles (cGNSS-R and rGNSS-R).

O.22 Altimetry in “closed-loop” mode shall be performed using the collected Earth-reflected GNSS signals in LHCP and RHCP.

O.23 Scatterometry shall be performed using the PYCARO payload based on the “open-loop” conventional and the interferometric GNSS-R principles (cGNSS-R and iGNSS-R).

O.24 Scatterometry in “open-loop” mode shall be performed using the collected Earth-reflected GNSS signals in LHCP.

O.25 Scatterometry shall be performed using the PYCARO payload based on the “closed-loop” conventional and the reconstructed-code GNSS-R principles (cGNSS-R and rGNSS-R).

O.26 Scatterometry in “closed-loop” mode shall be performed using the collected Earth-reflected GNSS signals in both polarizations LHCP and RHCP.

O.27 Soil moisture measurements shall be performed using the PYCARO payload based on the “open-loop” conventional and the interferometric GNSS-R principles (cGNSS-R and iGNSS-R).

O.28 Soil moisture measurements in “open-loop” mode shall be performed using the collected Earth-reflected GNSS signals in LHCP.

O.29 Soil moisture measurements shall be performed using the PYCARO payload based on the “closed-loop” conventional and the reconstructed-code GNSS-R principles (cGNSS-R and rGNSS-R).

O.30 Soil moisture measurements in “closed-loop” shall be performed using the collected Earth-reflected GNSS signals in LHCP and RHCP.

O.31 Biomass monitoring shall be performed using the PYCARO payload based on the “open-loop” conventional and the interferometric GNSS-R principles (cGNSS-R and iGNSS-R).

O.32 Biomass monitoring in “open-loop” mode shall be performed using the collected Earth-reflected GNSS signals in LHCP.

O.33 Biomass monitoring shall be performed using the PYCARO payload based on the “closed-loop” conventional and the reconstructed-code GNSS-R principles (cGNSS-R and rGNSS-R).

O.34 Biomass monitoring in “closed-loop” mode shall be performed using the collected Earth-reflected GNSS signals in LHCP and RHCP.

O.35 Cryosphere studies shall be performed using the PYCARO payload based on the “open-loop” conventional and the interferometric GNSS-R principles (cGNSS-R and iGNSS-R).

O.36 Cryosphere studies in “open-loop” mode shall be performed using the collected Earth-reflected GNSS signals in LHCP.

O.37 Cryosphere studies shall be performed using the PYCARO payload based on the “closed-loop” conventional and the reconstructed-code GNSS-R principles (cGNSS-R and rGNSS-R).

O.38 Cryosphere studies in “closed-loop” mode shall be performed using the collected Earth-reflected GNSS signals in LHCP and RHCP.

O.39 GPS Radio-Occultations should be performed using the PYCARO payload based on the “closed-loop” conventional and the reconstructed-code GNSS-R principles (cGNSS-R and rGNSS-R).

O.40 GPS Radio-Occultations should be performed using the collected GNSS signals after atmospheric bending in both polarizations LHCP and RHCP.

O.41 The scientific data time and operational mode stamps shall be located in the packet headers.

O.42 The system shall support uplink telecommands from the GS to enter in any operational mode at any time during the mission.

O.43 The system shall support uplink telecommands from the GS to set the PYCARO payload parameters.

O.44 The GS shall have the capability of activating any PYCARO payload function on-board.

O.45 The GS shall have the capability to inhibit any on-board automatic function and to take further control by GS telecommands.

O.46 The GS shall be able to enable or disable automatic on board reconfigurations.

O.47 The system shall be able to operate autonomously.

O.48 In case of failure the system shall provide information to detect when and where it took place.

O.49 On-board monitoring shall guarantee the good health of on-board hardware and software for both platform and payload.

O.50 Four conditions shall be met in order to trigger a fault response: a) Fault test must be enabled, b) fault test must be failing, c) fault must be mapped to preplanned response, and d) fault response must be enabled. Faults can only be cleared through GS telecommand after root cause of fault has been determined and corrected.

O.51 Qualification, protoflight and acceptance testing campaigns shall be performed so that safety is ensured.

O.52 Modularity shall be used during the design process.

O.53 The functionality of the satellite shall be able to be tested on-ground.

O.54 The functionality of each subsystem shall be able to be tested on-ground.

O.60 The boot sequence shall be done autonomously after 40 min after cubesat deployment.

O.61 The deployment of the VHF/UHF antenna shall be done autonomously after boot sequence.

O.62 The payload operational procedure shall follow the followings steps (O.63-O-72):

O.63 1) To turn on the payload-OBC and the PPR as per payload-scheduler (reflectometry events).

O.64 2) Upload to the PPR the GNSS-R configuration and switching matrix state (1,1).

O.65 3) 50% of the duty cycle in this configuration during each orbit.

O.66 4) Upload to the PPR the GNSS configuration and switching matrix state (0,0). Additionally, at this time the SDR shall be turned on.

O.67 5) 50% of the duty cycle in this configuration during each orbit.

O.68 The GNSS-R default configuration shall be: Automatic Gain Control AGC (on), SNR mask (lowest), multipath (off), smoothing (off), elev. Mask (30°), ionosphere (off), RAIM (off), Position Velocity and Time PVT mode (rover and standalone), troposphere (off).

O.69 The GNSS default configuration shall be: AGC (on), SNR mask (lowest), multipath (off), smoothing (off), elev. Mask (-20), ionosphere (off), RAIM (off), PVT mode (rover and standalone), troposphere (off).

O.70 Each orbit, the PLL and the DLL parameters shall be modified as per M.34, M.36, M.38, and M.40 for the complete definition of the “closed-loop” GNSS-R configuration.

O.71 Each orbit, the coherent integration time shall be modified as per M.30 and M.31 for the complete definition of the “open-loop” GNSS-R configuration.

O.72 The last PVT set computed during each orbit shall be translated into a Two Line Element set (TLE).

S.2 The satellite shall operate in the thermal ambient imposed by the orbit and all the operational modes.

S.3 Redundancy shall be ensured, especially where there are safety or failure risks.

S.4 At equipment / unit level, the following design maturity mass margins shall be applied: a) > 5% for “Off-The-Shelf” items (ECSS Category: A/B), b) > 10% for “Off-The-Shelf” items requiring minor modifications (ECSS Category: C), and c) > 20% for new designed / developed items, or items requiring major modifications or re-design (ECSS Category: D).

S.5 At equipment / unit level and for conventional electronic units, the following design maturity power margins shall be applied: a) > 5% for “Off-The-Shelf” items (ECSS Category: A/B), b) > 10% for “Off-The-Shelf” items requiring minor modifications (ECSS Category: C), and c) > 20% for new designed / developed items, or items requiring major modifications or re-design (ECSS Category: D).

S.6 The antenna-1 shall be placed in 3Ux2U side (-Z Body CS)

S.7 The antenna-2 shall be placed in 3Ux2U side (+Z Body CS)

S.22 The satellite shall survive transport to the launch site.

S.23 The satellite shall survive the environmental conditions during long storage periods at the launch site.

S.24 The payload shall be accommodated inside the structure into a maximum volume of 3U stacks with "L" shape.

SB.1 All electronic assemblies and electronic circuit boards should be conformally coated.

SB.2 All Remove Before Flight (RBF) items shall be identified by a bright red label of at least four square centimeters in area containing the words “Remove Before Flight” or “Remove Before Launch” and the name of the satellite printed in large white capital letters.

SB.3 The Thermal Control System (TCS) shall be achieved by passive elements.

SB.4 The TCS shall include sensors to allow temperature monitoring.

SB.5 The satellite shall maintain all the electronic components within the operational temperature range while in operation and within survival temperature range at all other times after deployment.

SB.6 The satellite shall survive within the temperature range of -10°C to $+50^{\circ}\text{C}$ from the time of launch until its deployment from the deployment system.

SB.8 The satellite shall use the reference frame as shown in Fig. B.1 such that it will be in line with the reference frame of the deployment system.

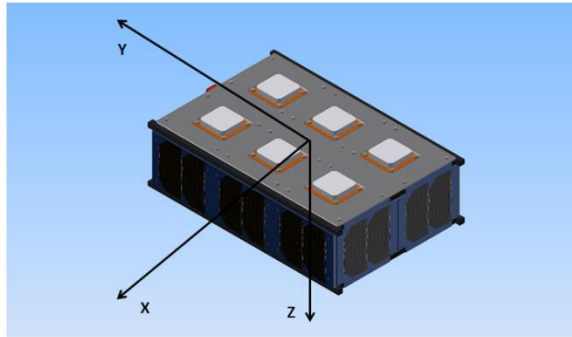


Fig. B.1. Body reference frame.

SB.9 In launch configuration the satellite shall fit entirely within the extended volume dimensions.

SB.10 After integration into the deployer, the satellite shall only require access, for any purpose, through the access hatches in the door of the deployer.

SB.11 The satellite center of gravity shall be located within a sphere of 20 mm diameter, centered on the satellite geometric center.

SB.12 The structure shall provide attachment and support for all other subsystems during on ground operations, and during flight phase and under all natural and induced environments.

SB.13 Mounting interfaces shall allow for easy maintenance, mounting and dismounting.

SB.15 The satellite shall provide sufficient power at the appropriate voltage, either by solar array generation or battery, to meet the power requirements of all satellite subsystems in all modes of operation.

SB.16 The EPS shall be capable of continuous operation with changing loads as required by the mission operations.

SB.17 The EPS shall provide housekeeping information to support monitoring.

SB.18 The EPS shall accept supply from external sources during ground operations.

SB.19 The satellite shall be powered off during the entire launch and until it is deployed from the deployment system.

SB.20 A dedicated EPS shall be used for the payload.

SB.21 The TT&C system shall have two redundant full duplex VHF/UHF transceivers, two (+Z, -X; Body CS) VHF monopole antenna, two (+Z, +X; Body CS) UHF monopole antenna, one S-band transceiver, and one (+Y, Body CS) S-band monopole antenna.

SB.22 The TT&C system shall verify uplink and downlink link budgets to satisfy the mission objectives.

SB.23 The telecommand uplink shall be performed at UHF with a baud rate up to 1,200 bps.

SB.24 The housekeeping data downlink should be performed at VHF with a baud rate up to 9,600 bps.

SB.25 The housekeeping data downlink shall be guaranteed at VHF with a minimum baud rate of 1,200 bps.

SB.26 The scientific data downlink should be performed at S-band with a baud rate up to 115,000 bps.

SB.27 The scientific data downlink shall be guaranteed at S-band with a minimum baud rate of 40,000 bps.

SB.28 Telecommand and telemetry data rates shall be satisfied with minimum margins as defined in ECSS-E-50-05A.

SB.29 The TT&C subsystem shall be fully compatible with the GS at the Universitat Politècnica de Catalunya and the IEEC's GS at the Svalbard island.

SB.30 The ADCS shall include on-board hardware and software items required to determine the ³Cat-2 attitude and its rate of change during all mission phases.

SB.31 The major hardware constituents shall be: 1 three-axes magnetorquer, 6 sun-sensors, 1 three-axes gyroscope, and 1 three-axes magnetic sensor.

SB.32 The location of these actuators in the satellite shall account for: a) the platform asymmetry and principal axes of inertia, and b) the requirements of maneuver in each axis of the body reference frame.

SB.14 The ADCS shall be calibrated with 10-times better accuracy than the pointing requirements. The structure shall guarantee the required alignment between system references, payload and sensors with a maximum error of 1°.

SB.78 The ADCS shall point the antenna-1 in counter-velocity during the radio-occultations measurements.

SB.79 The ADCS shall point the antenna-1 to nadir during the altimetry, scatterometry, soil moisture, biomass measurements, and cryosphere studies.

SB.140 The ADCS shall transform the measurement data into vector measurements, describing the direction of the Sun and the Earth's magnetic field, to be used in the attitude determination.

SB.33 The ADCS shall have 4 modes: SU, Normal (nadir), SS, and Survival.

SB.34 The ADCS should have the Normal (limb) mode and the Slew mode.

SB.36 The ADCS should operate from low (equator) to high latitude (polar regions) targets over the Earth.

SB.110 The ADCS pointing accuracy (guidance error + knowledge error + control error) shall be better than 7.5° (3-σ) in three-axes in the payload coordinate frame to achieve the main scientific goal.

SB.48 In Nominal (nadir) mode the determination accuracy shall be at least 2.5° (3-σ), in three-axes and in real-time.

SB.49 In Nominal (nadir) mode the determination range shall be inside 30° around nadir.

SB.50 In Nominal (nadir) mode the control accuracy shall be at least 2.5° ($3\text{-}\sigma$), in three-axes and in real-time.

SB.51 In Nominal (nadir) mode the control range shall be inside 30° around nadir.

SB.54 In Nominal (nadir) mode the setting time control shall be less than 4 h.

SB.146 The ADCS shall be in Nominal (nadir) mode during the downlink of the scientific data.

SB.55 In Nominal (limb) mode the determination accuracy should be at least 2.5° ($1\text{-}\sigma$), in three-axes and in real-time.

SB.56 In Nominal (limb) mode the determination range should be inside 30° around limb.

SB.57 In Nominal (limb) mode the control accuracy should be at least 2.5° ($1\text{-}\sigma$), in three-axes and in real-time.

SB.58 In Nominal (limb) mode the control range should be inside 30° around limb.

SB.61 In Nominal (limb) mode the setting time control should be less than 4 h.

SB.118 In Nominal (nadir) mode the guidance accuracy shall be at least 2.5° ($3\text{-}\sigma$).

SB.119 In Nominal (limb) mode the guidance accuracy should be at least 2.5° ($1\text{-}\sigma$).

SB.62 In Slew mode the maximum angular rate shall be less than $0.1^\circ/\text{s}$.

SB.69 In SS mode the determination accuracy shall be at least 10° ($1\text{-}\sigma$), in three-axes and in real-time.

SB.70 In SS mode the determination range shall include all possible attitudes.

SB.71 In SS mode the control accuracy shall be at least 20° ($1\text{-}\sigma$), in three-axes and in real-time.

SB.72 In SS mode the control range shall include all possible attitudes.

SB.75 In SS mode the setting time control shall be less than 4 h.

SB.111 In Survival mode the determination accuracy shall be at least 10° ($1\text{-}\sigma$), in three-axes and in real-time.

SB.112 In Survival mode the determination range shall include all possible attitudes.

SB.113 In Survival mode the control accuracy shall be at least 20° ($1\text{-}\sigma$), in three-axes and in real-time.

SB.114 In Survival mode the control range shall include all possible attitudes.

SB.117 In Survival mode the setting time control shall be less than 4 h.

SB.38 The photodiodes measurement shall be transformed to a unit norm Sun vector in the body reference frame.

SB.137 Data sampled from the photodiodes shall be calibrated to compensate for different photosensitivities of the sensors.

SB.120 The maximum measurement error of each photodiode, including measurement errors and misalignment from mounting, shall be lower than 4° .

SB.123 A temperature coefficient shall be determined for the photodiodes, to be used for temperature compensation purposes.

SB.136 Data sampled from the temperature sensors shall be converted to temperature values.

SB.122 The maximum measurement error of the temperature sensors shall be sufficiently low to ensure requirement SB.120. The temperature interval to measure is determined according to the same requirement.

SB.143 An on-board Sun model shall determine the direction to the Sun in the Earth Centered Inertial (ECI) frame with a maximum error less than 1° ($1-\sigma$).

SB.139 Gyroscope data shall be calibrated.

SB.40 The gyroscopes noise performance shall be: a) bias instability less than $15^\circ/\text{h}$, and b) Angular Random Walk (ARW) less than $20 \text{ deg./h}^{1/2}$.

SB.125 The maximum measurement error of the gyroscope, including measurement errors and misalignment from mounting, shall be lower than the required angular rate knowledge ($0.1^\circ/\text{s}$).

SB.138 Magnetometers data shall be calibrated.

SB.121 The maximum measurement error of the magnetometers, including measurement errors and misalignment from mounting, shall be lower than 1° .

SB.124 Calibration procedures shall be performed for the magnetometer, when integrated in engineering and flight model, in order to reduce effects of misalignment and magnetic distortions, this should be done to fulfill requirement SB.121.

SB.142 An on-board magnetic field model shall determine the direction of the magnetic field in the satellite position with a rms error less than 1° ($1-\sigma$).

SB.128 The ADCS-thread running on the OBC shall be executed periodically in intervals of 1 second.

SB.129 The ADCS-thread shall via I2C bus request, receive and save housekeeping data including sensor readings and current measurements from the coils.

SB.130 It shall be possible to save new TLE for use in the orbit model.

SB.141 The satellite shall have knowledge of the position in the ECI frame by using an on-board orbit model, which includes updated TLE sets (uploaded from GS or on-board generated). The error of the orbit model using a one hour old TLE shall not exceed 10 km of position.

SB.131 It shall be possible to perform an Inertial Measurement Unit (IMU) power cycling and transducers reset.

SB.132 It shall be possible to upload six new calibration factors for the photodiodes.

SB.133 It shall be possible to upload the calibration factors for the magnetometers' axes (scaling and offsets).

SB.201 It shall be possible to upload the calibration factors for the gyroscope's axes (scaling and offsets).

SB.144 An albedo correction shall compensate for the fact that the measured Sun vector includes the light of Earth albedo.

SB.134 It shall be possible to switch off the albedo correction algorithm.

SB.135 It shall be possible to update the sunlight threshold value to determine if the satellite is in eclipse.

SB.80 The major constituent of the CDHS shall be an embedded microcontroller.

SB.93 The microcontroller shall be compatible with Real Time Operating Systems (RTOS).

SB.94 The platform and the payload modules shall have the same CDHS.

SB.81 The CDHS shall provide all the functionality required for telemetry, acquisition and processing.

SB.82 The CDHS shall provide all the functionality required for telecommand, decoding and processing.

SB.83 The CDHS shall be in charge of the overall monitoring, commanding and controlling of all platform operations.

SB.84 The CDHS shall perform autonomous failure detection, isolation and recovery of all platform subsystems.

SB.85 The CDHS shall acquire all satellite housekeeping and payload data.

SB.86 The CDHS shall guarantee the good health of on-board hardware and software for both platform and payload.

SB.87 The CDHS shall allow for simultaneous data collection, downlink and uplink.

SB.89 The CDHS shall provide time and operational modes stamping.

SB.90 The CDHS shall acquire all system housekeeping and payload data.

SB.91 The CDHS shall operate automatically with minimum ground intervention, including its own initialization.

SB.96 The CDHS shall provide sufficient data storage capacity based on two solid state mass memories (payload and platform) to collect all data generated on-board without contact with the GSs during 5 days.

SB.95 The platform and the payload data mass memory data storage systems capacity shall be designed with at least a 50% margin.

SB.100 On-board software for the execution of vital operational procedures, including boot procedures, shall be stored in a non-volatile memory such that a default configuration is always available in the event of anomalies. This default configuration shall be transferred automatically into a working memory upon switch on of the on-board computer.

SB.101 It shall be possible to replace this default configuration totally or partially with software uplinked from ground.

SB.102 The on-board software shall be designed in a layered structure so that software maintenance (before and during flight) is confined to the upper application layer.

SB.103 The on-board software shall be structured in a modular way using high level language.

SB.104 Any embedded software shall be identified.

SB.105 If software is reused from previous projects, it shall be possible to test it when integrated in its new environment.

SB.106 Safety critical software (e.g. safe mode, bootstrap, etc.) shall be designed, integrated, tested and validated independently from the rest of the software.

SB.107 In-flight modification of embedded software shall be possible.

SB.108 The ground segment shall be capable of planning and controlling the mission and of operating the satellite under all expected conditions.

SB.109 The ground segment shall be capable of acquiring all the experiment data using the TT&C Earth Terminal at Universitat Politècnica de Catalunya and the IEEC terminal at the Svalbard Island.

SB.126 The OBC interfacing the ADCS sensors shall sample the sensors data from three sensors types.

SB.127 The OBC shall interface ADCS actuators and execute control algorithms.

E.1 ³Cat-2 shall be compatible with a dedicated launch on the Launch Vehicle (LV).

E.2 ³Cat-2 shall be compatible with the interface requirements on the satellite from the launcher, as defined in the LV ICD of the launcher authority. In this respect the launcher performance, injection accuracy, kinematic conditions at separation, launcher induced environment, dynamics, acoustics, thermal, cleanliness and interfaces to the facilities at the launch site shall be considered.

E.3 The satellite shall pass the acceleration (quasi-static) test as per Table A.1.

Table B.1. Acceleration characteristics.

Characteristic	Qualification [g]	Acceptance [g]
Test	Yes	Yes
Axial {LRF}	+ 8	+ 8
Lateral {LRF}	+ 2	+ 2
Test time	5 [min]	5 [min]

E.4 The satellite shall pass a resonance survey test, the characteristics of which are stated in Table B.2 (TBD) and the lowest natural frequency of the FM of the satellite shall be > 20 Hz.

E.5 The satellite shall pass the sinusoidal vibration test as per Table B.3.

Table B.3. Sine vibration test characteristics.

Characteristic		Qualification	Acceptance
Test		Required	Required
Directions	{BRF}	X, Y, Z	X, Y, Z
Profile	Frequency range [Hz]	Amplitude [g]	Amplitude [g]
	5 – 8	7.03 [mm] (0-peak)	4.69 [mm] (0-peak)
	8 – 21	1.8	1.2
	21 – 27	1.0 [mm] (0-peak)	0.68 [mm] (0-peak)
	27 – 100	3.0	2.0
Scan Rate		2 [oct/min]	4 [oct/min]

E.6 The satellite shall pass the random vibration test as per Table B.4.

Table B.4. Random vibration test characteristics.

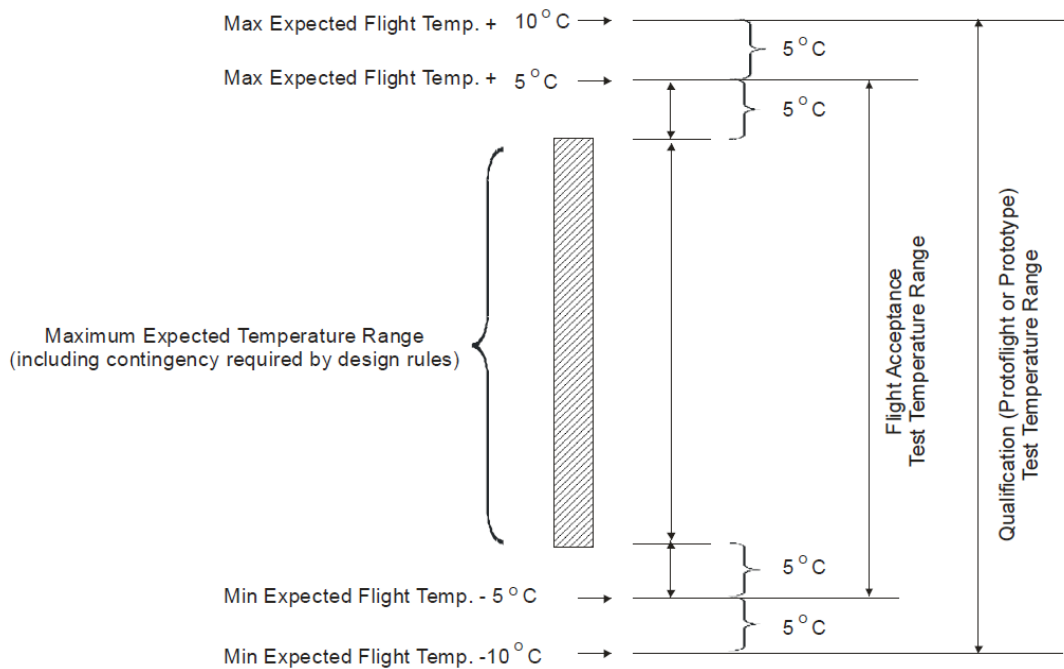
Characteristic		Qualification	Acceptance
Test		Required	Required
Directions	{BRF}	X, Y, Z	X, Y, Z
Profile	Frequency range [Hz]	Amplitude [g ² /Hz]	Amplitude [g ² /Hz]
	20 – 150	+3 [dB/oct]	+3 [dB/oct]
	150 – 280	0.08	0.04
	280 – 320	0.3	0.15
	320 – 380	0.2	0.1
	380 – 850	0.1	0.05
	850 – 1000	0.04	0.02
	1000 – 2000	0.01	0.005
RMS acceleration		10.16 [g]	7.19 [g]
Duration		120 [sec/axis]	60 [sec/axis]

E.7 The satellite shall pass the shock test as per Table B.5.

Table B.5. Shock vibration test characteristics.

Characteristic		Qualification	Acceptance
Test		Yes	No
Profile	Frequency range [Hz]	Shock acceleration response spectrum value [g]	Shock acceleration response spectrum value [g]
	100 – 500	12 [dB/oct]	12 [dB/oct]
	500 – 5000	1000	1000

E.8 The satellite shall pass the thermal-vacuum tests with a qualification temperature margin of no less than 10°C above the “flight” maximum operating temperature and 10°C below the “flight “ minimum operating temperature shall be used in establishing test temperatures. The margins for acceptance testing of previously qualified hardware may be reduced to 5°C, as long as testing to these levels does not preclude protoflight test levels from being achieved at higher levels of assembly.



E.9 Temperature cycling: The minimum number of thermal-vacuum temperature cycles for the payload, subsystem/instrument, and component levels of assembly are as follows (TBD by launcher).

E.10 The minimum temperature dwell times shall be as follows (TBD by launcher).

E.11 The chamber pressure after the electrical discharge checks are conducted shall be less than 10^{-5} mbar during 24 h.

E.12 The payload interface definition shall account for the constraints imposed by the 6U CubeSat structure.

E.13 The payload interface definition shall account for the constraints imposed by the avionics of the 6U CubeSat.

E.14 The payload interface definition shall account for the constraints imposed by the cubesat deployer.

C.1 The mission objectives shall be satisfied using a CubeSat platform.

C.2 The budget.

C.3 The environmental disturbances: Aerodynamic torque, gravity gradient, solar radiation pressure torque, magnetic torque.

C.4 The technical specifications of the different subsystems acquired to ISIS (<http://www.isispace.nl/cms/>) and GOMSPACE (<http://gomspace.com/index.php?p=products>).

C

APPENDIX C: ³Cat-2 REQUIREMENTS TRACEABILITY MATRIX

Table C.1. Requirements Traceability Matrix (RTM).

Req ID	Assoc Req ID
M.1	M.13, M.17, M.18, M.29, O.42, O.43, O.44, O.45, O.46, O.47, S.6, S.7, S.8, S.9, S.11, SB.33, SB.79
M.2	M.19, M.20, S.7, S.9, S.11
M.3	M.28, M.29, M.30
M.4	M.15, M.16, M.28, M.29, M.30-M.40
M.5	M.19, M.20, S.7, S.11
M.6	M.17, M.18, S.6, S.7, S.11
M.7	M.19, M.20, S.7, S.11
M.8	M.17, M.18, S.6, S.7, S.11
M.9	M.19, M.20, S.7, S.11
M.10	M.17, M.18, S.6, S.7, S.11
M.11	M.19, M.20, S.7, S.11
M.12	M.17, M.18, S.6, S.7, S.11
M.13	M.30, M.31, M.32, SB.33, SB.34, SB.35
M.14	M.15, M.16, M.31, M.32
M.15	M.33, M.34, M.37, M.38
M.16	M.35, M.36, M.39, M.40
M.17	
M.18	
M.19	
M.20	
M.21	
M.22	
M.23	
M.24	
M.25	
M.26	
M.27	S.21
M.28	
M.30	
M.31	
M.34	
M.36	
M.38	
M.40	
M.41	SB.34, SB.78
M.42	M.43, M.44
M.43	
M.44	
M.46	
M.47	
M.48	SB.21
M.49	E.12-E.21 E.22, C.4
M.50	S.13, S.14, S.15
M.51	
M.52	
M.53	
M.54	
M.55	
M.56	
M.57	
M.58	
M.59	M.1, SB.145
O.1	SB.23
O.2	
O.3	
O.4	
O.5	
O.6	SB.21, SB.22
O.7	
O.8	
O.9	
O.10	
O.11	
O.12	SB.17, SB.20

O.13	SB.21, SB.22
O.14	
O.15	
O.16	
O.17	SB.17, SB.20
O.18	SB.21, SB.22
O.19	M.1-M.16, M.23, M.24, M.25, S.2, S.19, S.21, O.41, O.47, O.49, SB.15, SB.16, SB.36
O.20	M.1-M.16, M.23, M.24, M.25, S.2, S.19, S.21, O.41, O.47, O.49, SB.15, SB.16, SB.36
O.21	M.1-M.16, M.23, M.24, M.25, S.2, S.19, S.21, O.41, O.47, O.49, SB.15, SB.16, SB.36
O.22	M.1-M.16, M.16, S.2, S.19, S.21, O.41, O.47, O.49, SB.15, SB.16, SB.36
O.23	M.1-M.16, M.16, S.2, S.19, S.21, O.41, O.47, O.49, SB.15, SB.16, SB.36
O.24	M.1-M.16, M.16, S.2, S.19, S.21, O.41, O.47, O.49, SB.15, SB.16, SB.36
O.25	M.1-M.16, M.16, S.2, S.19, S.21, O.41, O.47, O.49, SB.15, SB.16, SB.36
O.26	M.1-M.16, M.16, S.2, S.19, S.21, O.41, O.47, O.49, SB.15, SB.16, SB.36
O.27	M.1-M.16, M.16, S.2, S.19, S.21, O.41, O.47, O.49, SB.15, SB.16, SB.36
O.28	M.1-M.16, M.16, S.2, S.19, S.21, O.41, O.47, O.49, SB.15, SB.16, SB.36
O.29	M.1-M.16, M.16, S.2, S.19, S.21, O.41, O.47, O.49, SB.15, SB.16, SB.36
O.30	M.1-M.16, M.16, S.2, S.19, S.21, O.41, O.47, O.49, SB.15, SB.16, SB.36
O.31	M.1-M.16, M.16, S.2, S.19, S.21, O.41, O.47, O.49, SB.15, SB.16, SB.36
O.32	M.1-M.16, M.16, S.2, S.19, S.21, O.41, O.47, O.49, SB.15, SB.16, SB.36
O.33	M.1-M.16, M.16, S.2, S.19, S.21, O.41, O.47, O.49, SB.15, SB.16, SB.36
O.34	M.1-M.16, M.16, S.2, S.19, S.21, O.41, O.47, O.49, SB.15, SB.16, SB.36
O.35	M.1-M.16, M.16, S.2, S.19, S.21, O.41, O.47, O.49, SB.15, SB.16, SB.36
O.36	M.1-M.16, M.16, S.2, S.19, S.21, O.41, O.47, O.49, SB.15, SB.16, SB.36
O.37	M.1-M.16, M.16, S.2, S.19, S.21, O.41, O.47, O.49, SB.15, SB.16, SB.36
O.38	M.1-M.16, M.16, S.2, S.19, S.21, O.41, O.47, O.49, SB.15, SB.16, SB.36
O.39	
O.40	
O.41	
O.42	SB.21, SB.22, SB.81, SB.82, SB.87, SB.91, SB.94, SB.101, SB.107, SB.102
O.43	SB.21, SB.22
O.44	SB.21, SB.22, SB.108, SB.109
O.45	SB.21, SB.22, SB.108, SB.109
O.46	SB.21, SB.22
O.47	SB.81, SB.83, SB.84, SB.85, SB.86, SB.88, SB.89, SB.90, SB.94-SB.99
O.48	
O.49	O.1-O.18
O.50	
O.51	
O.52	
O.53	
O.54	
O.55	
O.56	
O.57	
O.58	
O.59	
O.60	
O.61	SB.86, SB.168-SB.171, SB.189
O.62	M.1
O.63	M.1
O.64	M.1
O.65	M.1
O.66	M.1
O.67	M.1
O.68	M.1
O.69	M.1
O.70	M.1
O.71	M.1
O.72	M.1
S.2	SB.3, SB.4, SB.5
S.3	SB.21
S.4	
S.5	
S.6	
S.7	
S.22	

S.23	SB.6
S.24	
SB.1	
SB.2	
SB.3	
SB.4	
SB.5	E.8-E.11, E.22
SB.6	
SB.7	
SB.8	
SB.9	E.2, E.22
SB.10	E.2, E.22
SB.11	
SB.12	E.3-E.7, E.22
SB.13	
SB.14	
SB.15	
SB.16	
SB.17	
SB.18	
SB.19	
SB.20	
SB.21	
SB.22	SB.23-SB.29
SB.23	O.1
SB.24	
SB.25	
SB.26	
SB.27	
SB.28	
SB.29	
SB.30	
SB.31	
SB.32	
SB.33	SB.41-SB.54, SB.62-SB.76
SB.34	SB.55-SB.61
SB.36	
SB.38	
SB.39	
SB.40	
SB.48	M.1, M.17, O.12
SB.49	M.1, M.17, O.12
SB.50	M.1, M.17, O.12
SB.51	M.1, M.17, O.12
SB.54	M.1, M.17, O.12
SB.55	M.1, M.21, O.12
SB.56	O.12
SB.57	O.12
SB.58	O.12
SB.61	O.12
SB.62	
SB.69	
SB.70	
SB.71	
SB.72	
SB.75	
SB.78	M.41
SB.79	M.1
SB.80	
SB.81	SB.100-SB.107
SB.82	SB.100-SB.107
SB.83	SB.100-SB.107
SB.84	SB.100-SB.107
SB.85	SB.100-SB.107
SB.86	SB.100-SB.107
SB.87	SB.100-SB.107
SB.89	SB.100-SB.107

SB.91	SB.100-SB.107
SB.93	SB.100-SB.107
SB.94	SB.100-SB.107
SB.95	SB.100-SB.107
SB.96	SB.100-SB.107
SB.97	SB.100-SB.107
SB.100	
SB.101	M.1, SB.110
SB.102	
SB.103	
SB.104	
SB.105	
SB.106	
SB.107	M.1, SB.110
SB.108	
SB.109	
SB.110	SB.14, SB.37-SB.40, C.3
SB.111	
SB.112	
SB.113	
SB.114	
SB.117	
SB.118	
SB.119	
SB.120	SB.48, SB.69, SB.111
SB.121	SB.48, SB.69, SB.111
SB.122	SB.48, SB.69, SB.111, S.120
SB.123	SB.48, SB.69, SB.111, S.120
SB.124	SB.121
SB.125	SB.48, SB.69, SB.111
SB.126	SB.48, SB.69, SB.111
SB.127	SB.50, SB.58, SB.71, SB.113
SB.128	
SB.129	
SB.130	M.1
SB.131	SB.48, SB.69, SB.111
SB.132	SB.48, SB.69, SB.111
SB.133	SB.48, SB.69, SB.111
SB.134	SB.48, SB.69, SB.111
SB.135	SB.48, SB.69, SB.111
SB.136	
SB.137	
SB.138	
SB.139	
SB.140	
SB.141	M.1, SB.48, SB.69, SB.111
SB.142	SB.48, SB.69, SB.111
SB.143	SB.48, SB.69, SB.111
SB.144	SB.48, SB.69, SB.111
SB.146	SB.22
SB.147	
SB.148	
SB.149	M.1, O.1
SB.150	
SB.151	
SB.152	
SB.153	
SB.154	
SB.155	O.19-O.40
SB.156	
SB.157	M.1, O.1
SB.158	SB.81,SB.82,SB.83
SB.159	SB.81,SB.82,SB.83
SB.160	
SB.161	SB.81,SB.82,SB.83
SB.162	SB.81,SB.82,SB.83
SB.163	SB.81,SB.82,SB.83

SB.164	SB.81,SB.82,SB.83
SB.165	
SB.166	SB.81,SB.82,SB.83
SB.167	M.1,SB.81,SB.82,SB.83,SB.110
SB.168	M.1, SB.110
SB.169	M.1
SB.170	M.1, SB.110
SB.171	M.1, SB.110,SB.168,SB.169,SB.170
SB.172	M.1, SB.110,SB.168,SB.169,SB.170
SB.173	M.1, SB.110,SB.168,SB.169,SB.170
SB.174	SB.84,SB.86,SB.91,SB.110
SB.175	M.1, SB.110,SB.86
SB.176	
SB.177	
SB.178	
SB.179	
SB.180	
SB.181	SB.86
SB.182	SB.168-SB.171
SB.183	
SB.184	SB.86
SB.185	SB.86
SB.186	SB.86
SB.187	
SB.188	
SB.189	
SB.190	SB.86, SB.168-SB.171
SB.191	M.1
SB.192	
SB.193	
SB.194	
SB.195	SB.81-SB.91
SB.196	SB.81-SB.91
SB.197	SB.81-SB.91
SB.198	SB.81-SB.91
SB.199	
SB.200	
E.1	
E.2	
E.3	
E.4	
E.5	
E.6	
E.7	
E.8	
E.9	
E.10	
E.11	
E.12	
E.13	
E.14	
C.1	
C.2	
C.3	
C.4	

D

APPENDIX D: ³Cat-2 RISK REGISTER

A risk register is a risk management tool commonly used in risk management and regulatory compliance. The risk register of the ³Cat-2 mission is included in this appendix:

Risk ID

TC – technical/implementation
 MS – mission (operational performance)
 SF – safety
 VE – vehicle
 PE – personnel
 EN – environmental

Probability (P)

A. Minimum – Almost impossible to occur
 B. Low – Small chance to occur
 C. Medium – Reasonable chance to occur
 D. High – Quite likely to occur
 E. Maximum – Certain to occur, maybe more than once

Severity (S)

1. Negligible – Minimal or no impact
 2. Significant – Leads to reduced experiment performance
 3. Major – Leads to failure of subsystem or loss of flight data
 4. Critical – Leads to experiment failure or creates minor health hazards
 5. Catastrophic – Leads to termination of the project, damage to the vehicle or injury to personnel

Table D.1. Risk Register.

ID	Risk (& consequence if not obvious)	P	S	P x S	Action
TC10	Detect a bug in the software in flight.	B	4	Low	Requires a possibility to upload new software in flight. Extensive testing.
TC40	Part of solar panel fails.	A	3	Very Low	Reduce the operational duty cycle. Oversize the solar panel.
TC60	Battery health decreases rapidly.	B	4	Low	Reduce the operation duty cycle. Monitor the usage of the battery. Oversize the battery capacity.
TC70	Delay in knowing what orbit will be used.	A	4	Very Low	Design for the worst case.
TC80	Delay of the launch leading to long storage period (damaging environmental conditions).	C	4	Medium	Make sure it is stored in a controlled environment.
TC90	Error in the TLE at beginning of life.	B	3	Low	Use other TLE source. Make sure the satellite remains safe for a number of days without ground station contact.
TC110	GPS patch failure.	D	4	High	Radiation pattern characterization. Change in operational platform pointing.
TC120	Issues with polarisation switches.	D	4	High	Use the default state.

TC130	Issues with the payload computer.	D	4	High	Operation using GS telecommands directly using Nanomind.
TC140	Nanomind-Gumstix interface.	B	3	Low	Reset communications using GS telecommands.
TC150	Error reflectometry scheduler.	B	3	Low	Operation using GS telecommands.
TC160	Error payload EPS power bus.	B	3	Low	Re-schedule automatic mode using GS telecommands.
TC170	SDR acquisition error.	C	2	Low	Reset SDR.
TC180	SDR parameters error.	C	3	Low	To test payload performance using GS telecommands. To re-schedule automatic mode.
TC190	Error DSP.	B	2	Low	DDM computation using BEXUS software.
TC200	Error data compression.	B	4	High	Re-schedule automatic mode using GS telecommands. To reduce the amounts of targets.
TC240	ADCS issues in the transition from GNSS-R and GNSS-RO.	C	1	Very Low	To re-schedule satellite operations depending on the scientific results. Re-schedule automatic mode using GS telecommands.
TC250	COTS IMU failure.	C	4	Medium	Re-schedule MEKF weighting of the available sensors. Simulations have to be performed for analysis. Scientific targets on Earth could change if required.
TC260	Operational mode is found to be un-useful.	A	2	Very Low	a) To re-schedule the automatic control. b) NO changes. GS telecommands could introduce higher risk.
TC270	Vehicle attitude leading to the lost of GS communications.	C	1	Very Low	Two orthogonal monopoles.
TC280	Error S-band transmitter (scientific data downlink).	B	3	Low	To use VHF back-up transceiver. Re-schedule automatic mode using GS telecommands. To reduce the amounts of targets.
TC290	Error VHF nominal transceiver (HK downlink).	B	2	Very Low	To use back-up transceiver.
TC300	Error UHF nominal transceiver (GS telecommands).	B	2	Very Low	To use back-up transceiver.
TC310	Error nominal and back-up telemetry mode.	A	4	Very Low	Reduce HK downlink using the beacon mode.
TC320	Error S-Band transmitter and both nominal and back-up VHF transceiver.	A	4	Very Low	Reduce data downlink using the beacon mode. To define a basic scientific-kit to be compressed for downlink.
TC330	Wrong GS telecommands.	C	5	High	A command file validator to ensure the authenticity of uplinked files.
TC350	SD card failure.	C	4	Medium	GS telecommand to change the future data storage location from the SD card to the data Flash memory.

TC360	Code flash memory failure.	B	3	Low	GS telecommand to change the future data storage location from the code flash memory to the data flash memory. Further analysis is required.
TC370	Effect of radiation.	C	5	High	Payload embedded into a 3 mm thickness Al box.
TC380	Effect of radiation.	C	5	High	Redundancy flight software (code flash memory and SD card). Validation of the flight software executable on the CDHS before it is executed after launch.
TC390	Processor lockup.	C	5	High	Periodically reset the watchdog timer by changing the input state at a regular interval faster than the timeout period.
TC400	On-flight errors.	C	5	High	To define an error data-base and the actions the satellite should take to resolve the error.
TC410	Data transfer resources between the GS and the satellite.	B	3	Low	Binary commands instead of C++ string commands.
TC420	Sun sensor transducer off.	D	5	Very High	ADCS can work with magnetometers and gyroscope.
TC430	Sun sensor transducer saturation.	D	5	Very High	ADCS can work with magnetometers and gyroscope.
TC440	Sun sensor electronics failure.	D	5	Very High	ADCS can work with magnetometers and gyroscope.
TC450	Magnetometer transducer off.	D	4	High	Two 3-axes magnetometers to be used. To detect failure. Sensor out of loop. Mitigation actions to be performed after loosing a total of 2 parallel-axes. Operational: Go to SS mode. Perform magnetometer power cycling and transducer reset. If not successful, turn off magnetometer and return to nadir pointing with Sun sensors and gyroscope (a drift rotation around Sun vector is expected). Design: Autonomous mode transition is required if (unstable) payload pointing yields risk of power loss. Implement attitude determination and control with Sun sensors and gyroscope.
TC460	Magnetometer transducer saturation.	D	4	High	Two 3-axis magnetometers to be used. To detect failure. Sensor out of loop. Mitigation actions to be performed after loosing a total of 2 parallel-axis. Operational: Go to SS mode. Perform magnetometer power cycling and transducer reset. If not successful, turn off magnetometer and return to nadir pointing with Sun sensors and gyroscope (a drift rotation around Sun vector is expected). Design: Autonomous mode transition is required if (unstable) payload pointing yields risk of power loss. Implement attitude determination and control with Sun sensors and gyroscope.
TC470	Magnetometer electronics failure.	D	4	High	Two 3-axes magnetometers to be used. To detect failure. Sensor out of loop. Mitigation actions to be performed after loosing a total of 2 parallel-axes. Design: Split electronics in 3 branches. If not possible, same as magnetometer transducer.
TC480	Gyroscope transducer off.	B	4	Low	Operational mitigation actions to be implemented in on-flight software: Go to SS mode. Perform gyroscope power cycling and transducer reset. If not

					successful, turn off gyroscope and return to nadir pointing with Sun sensors and magnetometer (an increase in attitude control jitter is expected due to noisier angular velocity estimation). To be validated by review of the design. Testing is not feasible.
TC490	Gyroscope transducer saturation.	B	5	Medium	Operational mitigation actions (same as gyroscope transducer off) to be implemented in on-flight software. To be validated by review of the design. Testing is not feasible.
TC500	Gyroscope electronics failure.	B	4	Low	Operational mitigation actions (same as gyroscope transducer off) to be implemented in on-flight software. To be validated by review of the design. Testing is not feasible.
TC510	Magnetorquer axis off.	B	5	Low	The ADCS performance with 2-axes (1 magnetorquer axis failure) to be checked by testing. If mission requirements can not be achieved no actions (Design: autonomous detection of failure and autonomous transition to SS mode are required. If power continues dropping go to Survival mode. To detect failure, use magnetometer measurements and compare with commands. Include additional magnetorquer bar in a direction diagonal to nominal magnetorquers bars) will be implemented. Loss of mission.
TC520	Magnetorquer axis saturation.	B	5	Low	The ADCS performance with 2-axes (1 magnetorquer axis failure) to be checked by testing. If mission requirements can not be achieved no actions (Design: autonomous detection of failure and autonomous transition to SS mode are required. If power continues dropping go to Survival mode. To detect failure, use magnetometer measurements and compare with commands. Include additional magnetorquer bar in a direction diagonal to nominal magnetorquers bars) will be implemented. Loss of mission.
TC530	Magnetorquer electronics failure.	B	5	Low	The ADCS performance with 2-axes (1 magnetorquer axis failure) to be checked by testing. If mission requirements can not be achieved no actions (Design: Split electronics in 4 branches (3 nominal + 1 redundant) will be implemented. Loss of mission.
TC540	TLE propagation and attitude guidance failure.	C	4	Medium	Testing of functional requirements not feasible. Operational requirements and mitigation actions to be tested. Mitigation actions (Operational: Switch to SS mode. Wait for ground intervention to fix the problem)
TC550	Sun sensors processing failure.	C	5	High	Mitigation actions. Design: Simple and robust algorithms. Test this feature extensively in whole design lifecycle, simulating the failures and checking correct system response. Autonomy is required to overcome this failure. See Sun sensors transducers failures.
TC560	Magnetometer processing failure.	C	4	Medium	To detect failure. Sensor out of loop. Not critical severity. Mitigation actions to be performed after loosing a total of 2 parallel-axes.

TC570	Gyroscope processing failure.	C	4	Medium	Operational mitigation actions (same as gyroscope electronics failure) to be implemented in on-flight software. To be validated by review of the design. Testing is not feasible as described in the document.
TC580	Magnetorquer command distribution failure.	C	5	High	Mitigation actions. Design: Simple and robust algorithms. Test this feature extensively in whole design lifecycle, simulating the failures and checking correct system response. Autonomy is required to overcome this failure. See magnetorquers axis failures.
TC590	Sun acquisition and survival modes attitude determination failure.	D	5	Very High	Mitigation actions. Design: Simple and robust algorithms. Test this feature extensively in whole design lifecycle, simulating the failures and checking correct system response.
TC600	Nominal and Slew modes attitude determination failure.	D	4	High	Mitigation actions. Operational: Go to SS mode. Wait for ground intervention to fix the problem.
TC610	Sun acquisition and survival modes control failure.	D	5	Very High	Mitigation actions. Design: Simple and robust algorithms. Test this feature extensively in whole design lifecycle, simulating the failures and checking correct system response.
TC620	Nominal and slew modes attitude control failure.	D	4	High	Mitigation actions. Operational: Go to SS mode. Wait for ground intervention to fix the problem.

Bibliography

- [1] L.L. Fu, D. Alsdorf, R. Morrow, E. Rodriguez, and Mognard, “SWOT: The Surface Water and Ocean Topography Mission: wide-swath altimetric measurement of water elevation on earth”, NASA JPL, 2012.
- [2] M. Martín-Neira, “A PAssive Reflectometry and Interferometry System (PARIS): application to ocean altimetry”, ESA J., vol. 17, pp. 331-355, 1993.
- [3] M. Martín-Neira, S. D’Addio, C. Buck, N. Floury, and R. Prieto-Cerdeira, “The PARIS ocean altimeter in-orbit demonstrator”, IEEE Transactions on Geoscience and Remote Sensing, vol. 49, no. 6, pp. 2209-2237, 2011.
- [4] TOPEX/Poseidon. Ocean surface Topography from Space: missions. Available online: <http://sealevel.jpl.nasa.gov/missions/> (accessed on 12 10 2015).
- [5] Jason-1. Ocean surface Topography from Space: missions. Available online: <http://sealevel.jpl.nasa.gov/missions/> (accessed on 12 10 2015).
- [6] Jason-2. Ocean surface Topography from Space: missions. Available online: <http://sealevel.jpl.nasa.gov/missions/> (accessed on 12 10 2015).
- [7] ERS-1 and -2. ESA Operational Earth Observation Missions. Available online: <https://earth.esa.int/web/guest/missions/esa-operational-eo-missions> (accessed on 12 10 2015).
- [8] Envisat. ESA Operational Earth Observation Missions. Available online: <https://earth.esa.int/web/guest/missions/esa-operational-eo-missions> (accessed on 12 10 2015).
- [9] A.R. Robinson, Eddies in Marine Science, Springer-Verlag: Weinheim, Germany, 1983.
- [10] M.G. Scharffenberg, and D. Stammer, “Seasonal variations of the large-scale geostrophic flow field and eddy kinetic energy inferred from the TOPEX/Poseidon and Jason-1 tandem mission data”, Journal of Geophysical Research, vol. 115, C2, 2010.

-
- [11] Mullard Space Science Laboratory, In Proceedings Consultative Meeting Imaging Altimeter Requirements Tech., 1990.
- [12] Alenia, “Final report for the constellation of pulse limited nadir looking radar altimeters”, ESTEC, Noordwijk, The Netherlands, IAB/FR/ALS/001, Contract 9370/91, 1992.
- [13] GFZ German Research Center for Geosciences. Available online: <http://www.gfz-potsdam.de/portal/gfz/Struktur/Departments/Department+1/sec11> (accessed on 12 10 2015).
- [14] J.C. Auber, A. Bibaut, and J.M. Rigal, “Characterization of multipath on land and sea at GPS frequencies”, in Proceedings of the 7th Institute of Navigation GPS Conference, pp. 1155-1171, 1004.
- [15] G. Picardi, R. Seu, S. Sorge, and M. Martín-Neira, “Bistatic model of ocean scattering”, IEEE Transactions on Antennas Propagation, vol. 46, no. 10, pp. 1531-1541, 1998.
- [16] V.U. Zavorotny, and A.G. Voronovich, “Scattering of GPS signals from the ocean with wind remote sensing application”, IEEE Transactions on Geoscience and Remote Sensing, vol. 38, no. 2, pp. 951-964, 2000.
- [17] A.K. Fung, C. Zuffada, and C.Y. Hsieh, “Incoherent bistatic scattering from the sea surface at L-band”, IEEE Transactions on Geoscience and Remote Sensing, vol. 39, no.5, pp. 1006-1012, 2001.
- [18] R.N. Treuhaft, S.T. Lowe, C. Zuffada, and Y. Chao, “2-cm GPS altimetry over Crater lake”, Geophysical Research Letters, vol. 28, no. 23, pp. 4343-4346, 2001.
- [19] H. Carreno-Luengo, Ph. D. Thesis proposal, Universitat Politècnica de Catalunya, Barcelona, Spain, 2012.
- [20] S.T. Lowe, C. Zuffada, Y. Chao, P. Kroger, and L.E. Young, “5-cm precision aircraft ocean altimetry using GPS reflections”, Geophysical Research Letters, vol. 29, no. 10, pp. 13-1–13-4, 2002.

-
- [21] A. Rius, J.M. Aparicio, E. Cardellach, M. Martín-Neira, and B. Chapron, “Sea surface state measured using GPS reflected signals”, *Geophysical Research Letters*, vol. 29, no. 23, pp. 37-1–37-4, 2002.
- [22] G. Ruffini, F. Soulat, M. Caparrini, O. Germain, and M. Martín-Neira, “The eddy experiment: accurate GNSS-R ocean altimetry from low altitude aircraft”, *Geophysical Research Letters*, vol. 31, no. 12, L12306, 2004.
- [23] B. Wilmhoff, F. Lalezari, V. Zavorotny, and E. Walsh, “GPS ocean altimetry from aircraft using the P(Y) code signal”, in *Proceedings of the 2007 IEEE International Geoscience and Remote Sensing Symposium*, pp. 5093-5096, Barcelona, Spain, July 2007.
- [24] H. Carreno-Luengo, H. Park, A. Camps, F. Fabra, and A. Rius, “GNSS-R derived centimetric sea topography: an airborne experiment demonstration”, *IEEE Journal of Selected Topics in Applied Earth Observations and Remote Sensing*, vol.6, n.3, pp. 1468-1478, 2013.
- [25] S.T. Lowe, J.L. LaBrecque, C. Zuffada, L.J. Romans, L.E. Young, G.A. Hajj, “First spaceborne observation of an Earth-reflected GPS signal”, *Radio Science*, vol. 37, no.1, pp. 7-1–7-28, 2002.
- [26] J.A. Ávila Rodríguez, *On Generalized Signal Waveforms for Satellite Navigation*, Ph.D. Dissertation, Universität der Bundeswehr München zur Erlangung des akademischen Grades eines, 2008. Available online: <http://dnb.info/1066345600/34> (accessed on 10 11 2015).
- [27] F.T. Ulaby, and D.G. Long, *Microwave Radar and Radiometric Remote Sensing*, The University of Michigan Press: Ann Arbor, MI, USA, 2014; pp. 167, 168, 170, 171, 175, 200, 252, 257, 423, 427.
- [28] P. Addabbo, S. D’Addio, M. di Bisceglie, C. Galdi, and G. Giangregorio, “Simulation of stochastic GNSS-R waveforms based on a novel time-varying sea scattering model”, in *Proceedings of the 2014 IEEE International Geoscience and Remote Sensing Symposium*, pp. 3794-3797, Quebec, Canada, July 2014.

-
- [29] A. Martínez-Vazquez, *Emisividad Polarimétrica del Terreno: Efecto de la Vegetación*, M.St. Thesis, Universitat Politècnica de Catalunya, Barcelona, Spain, 2001.
- [30] I. Ledesma-Galera, *Estudio Experimental del Comportamiento Radiométrico de las Superficies Naturales*, M.St. Thesis, Universitat Politècnica de Catalunya, Barcelona, Spain, 2002.
- [31] A. Martínez-Vazquez, A. Camps, J.M. López-Sanchez, M. Vall-llosera, and A. Monerris, “Numerical Simulation of the full-polarimetric emissivity of vines and comparison with experimental data”, *MDPI Remote Sensing*, vol. 1, no. 3, pp. 300-317, 2009.
- [32] B.J. Choudhury, T.J. Schmugge, A. Chang, R.W. Newton, “Effect of surface roughness on the microwave emission from soils”, *Journal Geophysical Research*, vol. 84, no. C9, pp. 5699-5706, 1979.
- [33] L. Yi-Cheng, and K. Sarabandi, “A Monte Carlo coherent scattering model for forest canopies using fractal-generated trees”, *IEEE Transactions on Geoscience and Remote Sensing*, vol. 37, no. 1, pp. 440-451, 1999.
- [34] L. Tsang, J.A. Kong, and R.T. Shin, *Theory of Microwave Remote Sensing*, Wiley Interscience: New York, NY, USA, 1985.
- [35] F.T. Ulaby, R.K. Moore, and A.K. Fung, *Microwave Remote Sensing: Active and Passive; Volume II: Radar Remote Sensing and Surface Scattering and Emission Theory*, Addison-Wesley: Reading, MA, USA, 1982; pp. 492, 493, 827, 846, 863, 1008, 1540-1541.
- [36] L. Yi-Cheng, and K. Sarabandi, “Electromagnetic scattering model for a tree trunk above a tilted ground plane”, *IEEE Transactions on Geoscience and Remote Sensing*, vol. 33, no. 4, pp. 1063-1700, 1995.
- [37] M.A. Karam, A.K. Fung, and Y.M.M. Antar, “Electromagnetic wave scattering from some vegetation samples”, *IEEE Transactions on Geoscience and Remote Sensing*, vol. 26, no. 6, pp. 799-808, 1998.

-
- [38] A. Lindenmayer, "Developmental algorithms for multicellular organisms: A survey of L-systems," *Journal Theoretical Biology*, vol. 54, pp. 3-22, 1975.
- [39] P. Prusinkiewicz and A. Lindenmayer, *The Algorithmic Beauty of Plants*, Springer-Verlag: New York, NY, USA, 1990.
- [40] H. Carreno-Luengo, A. Camps, J. Querol, G. Forte, R. Díez and R. Onrubia, "First results of a GNSS-R experiment from a stratospheric balloon over boreal forests", Accepted to *IEEE Transactions on Geoscience and Remote Sensing*, 2015.
- [41] X. Wu, and S. Jin, "GPS-Reflectometry: forest canopies polarization scattering properties and modelling", *Advances in Space Research*, vol. 54, no. 5, pp. 863-870, 2014.
- [42] M.L. Imhoff, "Radar backscattering and biomass saturation: ramifications for global biomass inventory", *IEEE Transactions on Geoscience and Remote Sensing*, vol. 33, no.2, pp. 511-518, 1995.
- [43] N. Rodríguez-Alvarez, A. Camps, M. Vall-llosera, X. Bosch-Lluís, A. Monerris, I. Ramos-Pérez, E. Valencia, J.F. Marchán-Hernandez, J. Martinez-Fernandez, G. Baroncini-Turricchia, C. Pérez-Gutiérrez, and N. Sánchez, "Land geophysical parameters retrieval using the interference pattern GNSS-R technique", *IEEE Transactions on Geoscience and Remote Sensing*, vol. 49, no.1, pp. 71-84, 2011.
- [44] C.D. Hall, and R.A. Cordey, "Multistatic Scatterometry", in *Proceedings of the 1988 IEEE International Geoscience and Remote Sensing Symposium*, pp. 561,562, Edinburgh, UK, September 1988.
- [45] A. Camps, H. Park, E. Valencia, D. Pascual, F. Martín, A. Rius, S. Ribó, J. Benito, A. Andrés-Beivide, P. Saameno, G. Staton, M. Martín-Neira, S. D'Addio, P. Willemsen, "Optimization and performance analysis of interferometric GNSS-R altimeters: application to the PARIS IoD mission", *IEEE Journal of Selected Topics in Applied Earth Observation and Remote Sensing*, vol. 7, no. 5, pp. 1436-1451, 2014.
- [46] A. Camps, F. Martín, H. Park, E. Valencia, A. Rius, and S. D'Addio, "Interferometric GNSS-R achievable altimetric performance and compression/denoising using the wavelet transform: an experimental study", in

Proceedings of the 2012 IEEE International Geoscience and Remote Sensing Symposium, pp. 7512-7515, Munich, Germany, July 2012.

[47] S. D’Addio, F. Martín, H. Park, A. Camps, and M. Martín-Neira, “Height precision prediction of the PARIS in orbit demonstrator based on Cramer-Rao bound analysis”, in Proceedings of the 2012 IEEE International Geoscience and Remote Sensing Symposium, pp. 7063-7066, Munich, Germany, July 2012.

[48] S.R. Christopher, S. Gleason, Z. Jelenak, S. Katzberg, A. Ridley, R. Rose, J. Scherrer, and V. Zavorotny, “The CyGNSS nanosatellite constellation hurricane mission”, in Proceedings of the 2012 IEEE International Geoscience and Remote Sensing Symposium, pp. 214-216, Munich, Germany, July 2012.

[49] S. Gleason, et al., GNSS Applications and Methods, Artech House: Norwood, MA, USA, 2009.

[50] S. D’Addio, C. Buck, and Martín-Neira, “PARIS altimetry precision prediction with GALILEO-signals-in-space”, in Proceedings of the 2008 IEEE International Geoscience and Remote Sensing Symposium, vol. 3, pp. III-63–III-66, Boston, USA, July 2008.

[51] O. Nogués, A. Sumpsi, A. Camps, and A. Rius, “A 3 GPS-channels Doppler-delay receiver for remote sensing applications”, in Proceedings of the 2003 IEEE International Geoscience and Remote Sensing Symposium, pp. 4483-4485, Toulouse, France, July 2003.

[52] S. Esterhuizen, and D. Akos, “The design, construction, and testing of a modular GPS bistatic radar software receiver for small platforms,” in Proceedings of the Workshop on Reflectometry using GNSS (GNSS-R 2006), ESA/ESTEC, The Netherlands, June 2006.

[53] S. Dunne and F. Soulat, “A GNSS-R coastal instrument to monitor tide and sea state”, GNSS Reflection Workshop, Guildford, U.K.: Surrey University, June 2005.

[54] S. Gleason, S. Hodgart, Y. Sun, C. Gommenginger, S. Mackin, M. Adjrard, and M. Unwin, “Detection and processing of bistatically reflected GPS signals from low Earth orbit for the purpose of ocean remote sensing”, IEEE Transactions on Geoscience and Remote Sensing, vol. 43, no. 6, pp. 1229-1241, 2005.

-
- [55] J.L. Garrison, S.J. Katzberg, and M.I. Hill, "Effect of sea roughness on bistatically scattered range coded signals from the global positioning system", *Geophysical Research Letters*, vol. 25, no. 13, pp. 2257-2260, 1998.
- [56] J.L. Garrison, A. Komjathy, V.U. Zavorotny, and S.J. Katzberg, "Wind speed measurement using forward scattered GPS signals", *IEEE Transactions on Geoscience and Remote Sensing*, vol. 40, no. 1, pp. 50-65, 2002.
- [57] O. Nogués-Correig, E. Cardellach, J. Sanz, and A. Rius, "A GPS-reflections receiver that computes Doppler/delay maps in real time", *IEEE Transactions on Geoscience and Remote Sensing*, vol. 45, no. 1, pp. 156-174, 2007.
- [58] C. Kelley, J. Cheng, and J. Barnes, "Open source software for learning about GPS," in *Proceedings of the Institute of Navigation GPS Conference*, pp. 2800-2810, Long Beach, USA, September 2005.
- [59] E. Valencia, A. Camps, J.F. Marchán-Hernández, X. Bosch-Lluís, N. Rodríguez-Álvarez, and I. Ramos-Pérez, "Advanced architectures for real-time delay-Doppler map GNSS-reflectometers: the GPS reflectometer instrument for PAU (griPAU)", *Advances in Space Research*, vol. 46, no. 2, pp. 196-207, 2010.
- [60] O. Nogués-Correig, S. Ribó, J.C. Arco, E. Cardellach, A. Rius, E. Valencia, J. M. Tarongí, A. Camps, H. van der Marel, and M. Martín-Neira, "The proof of concept for 3-cm altimetry using the PARIS interferometric technique", in *Proceedings of the 2010 IEEE International Geoscience and Remote Sensing Symposium*, pp. 3620-3623, Hawaii, USA, July 2010.
- [61] A. Camps, J.F. Marchán-Hernández, E. Valencia, I. Ramos-Pérez, X. Bosch-Lluís, N. Rodríguez-Alvarez, H. Park, A. Alcayde, A. Mollfulleda, J. Galindo, P. Martínez, S. Chavero, M. Angulo, and A. Rius, "PAU instrument aboard INTA MicroSat-1: a GNSS-R demonstration mission for sea state correction in L-band radiometry", in *Proceedings of the 2011 IEEE International Geoscience and Remote Sensing Symposium*, pp. 4126-4129, Vancouver, Canada, July 2011.
- [62] A. Alonso-Arroyo, A. Camps, D. Pascual, H. Park, A. Alcayde, S. Chavero, P. Martinez, L. Crespo, and M. Angulo, "PAU instrument aboard INTA MicroSAT-1: initial results of the FM model from an airborne experiment", in *Proceedings of the*

Workshop on Reflectometry using GNSS and Other Signals of Opportunity (GNSS+R 2012), Purdue University, IN, USA, October 2012.

[63] R. de Vos van Steenwijk, M. Unwin, and P. Jales, "Introducing the SGR-ReSI: a next generation spaceborne GNSS receiver for navigation and remote-sensing", in Proceedings of the 5th ESA Workshop on Satellite Navigation Technologies and European Workshop on GNSS Signals and Signal Processing, ESA/ESTEC, The Netherlands, December 2010.

[64] A. Rius, O. Nogués-Correig, S. Ribó, E. Cardellach, S. Oliveras, E. Valencia, H. Park, J. M. Tarongí, A. Camps, H. van der Marel, R. van Bree, B. Altena, M. Martín-Neira, "Altimetry with GNSS-R interferometry: first proof of concept experiment", GPS Solutions, vol. 16, no. 2, pp. 231-241, 2012.

[65] A. Rius, F. Fabra, S. Ribó, S. Oliveras, J.C. Arco, E. Cardellach, A. Camps, O. Nogués-Correig, J. Kainulainen, C. Mancel, and M. Martín-Neira, "PARIS interferometric technique: first aircraft experiment", in Proceedings of the 2011 ESA Workshop on Advanced RF Sensors and Remote Sensing Instruments, ESA-ESTEC, Noordwijk, The Netherlands, November 2011.

[66] A. Rius, F. Fabra, S. Ribó, J.C. Arco, S. Oliveras, E. Cardellach, A. Camps, O. Nogués-Correig, J. Kainulainen, E. Rohue, and M. Martín-Neira, "PARIS interferometric technique proof of concept: sea surface altimetry measurements", in Proceedings of the 2012 IEEE International Geoscience and Remote Sensing Symposium, pp. 7067-7070, Munich, Germany, July 2012.

[67] S. D'addio and M. Martín-Neira, "Comparison of processing techniques for remote sensing of Earth-exploiting reflected radio-navigation signals", Electronics Letters, vol. 49, no. 4, pp. 203-294, 2013.

[68] F. Martín, S. D'Addio, A. Camps, M. Martín-Neira, H. Park, and D. Pascual-Biosca, "Comparison of GNSS-R processing techniques for spaceborne ocean altimetry", in Proceedings of the 2013 IEEE International Geoscience and Remote Sensing Symposium, pp. 2939-2942, Melbourne, Australia, July 2013.

[69] E. Cardellach, A. Rius, M. Martín-Neira, F. Fabra, O. Nogués-Correig, S. Ribó, J. Kainulainen, A. Camps, and S. D'Addio, "Consolidating the precision of

interferometric GNSS-R ocean altimetry using airborne experimental data”, IEEE Transactions on Geoscience and Remote Sensing, vol. 52, no. 8, pp. 4992-5004, 2014.

[70] J.L. Garrison, and S.J. Katzberg, “Detection of ocean reflected GPS signals: theory and experiment”, Engineering new New Century, in Proceedings of the IEEE Southeastcon, pp. 290-294, April 1997.

[71] A. Camps, “PAUSAT: a concept demonstrator of enabling technologies for Earth observation nanosatellite constellations using Global Navigation Satellite Signals Reflectometry (GNSS-R)”, ERC Advanced Grant proposal, call ERC-2009-AdG_20090325, 2009.

[72] H. Carreno-Luengo, A. Camps, I. Ramos-Pérez, and A. Rius, “P(Y) & C/A Reflectometer (PYCARO): high resolution sea measurements”, Workshop on Reflectometry using GNSS and Other Signals of Opportunity (GNSS+R 2012), Purdue University, IN, USA, October, 2012. Available online: <http://www.gnssr2012.org/topics/technical-program> (accessed on 12 08 2015).

[73] K.K. Abadi, R.J. Helkey, and R.G. Lorenz, “Global positioning system receiver digital processing technique”, United States Patent US 5134407 A, 1992.

[74] T.K. Woo, “Optimum semi-codeless carrier phase tracking of L2”, in Proceedings of the 12th International Technical Meeting of the Satellite Division of the Institute of Navigation, Nashville, Tennessee, USA, September 1999.

[75] Antcom[®] Antenna Products, 2011. Available online <http://www.antcom.com/documents/catalogs/L1L2GPSAntennas.pdf> (accessed on 17 08 2015); pp. 75, 118.

[76] VEGA[®] Products, 2013. Available online: http://www.vega.com/es/Medici%C3%B3n_de_nivel_Radar_VEGAPULS62.htm (accessed on visited 01 06 2015).

[77] M. Martín-Neira, “History of GNSS Reflectometry”, Gfg2 Second Summer School, GFZ, Potsdam, 1-3 July 2013. Available online: http://www.gfg2.eu/sites/gfg2.eu/files/martinneira_reflectometry.pdf (accessed on 20 10 2015).

-
- [78] C.P. Gommenginger, and M.A. Srokosz, “Sea state bias - 20 years on”, in Proceedings of the ESA Workshop 15 Years of Progress on Radar Altimetry, Venice, Italy, March 2006.
- [79] A. Rius, E. Cardellach, and M. Martín-Neira, “Altimetric analysis of the sea surface GPS-reflected signals”, IEEE Transactions on Geoscience and Remote Sensing, vol. 48, no. 4, pp. 2119-2127, 2010.
- [80] A. Ghavidel, Contributions to the Determination of Electromagnetic Bias in GNSS-R Altimetry, Ph.D. Dissertation, Universitat Politècnica de Catalunya, Barcelona, Spain, 2015.
- [81] G.A. Hajj, C. Zuffada, “Theoretical description of a bistatic system for ocean altimetry using the GPS signal”, Radio Science, vol. 38, no. 5, pp. 10-1–10-19, 2003.
- [82] D. Pascual, A. Camps, F. Martín-Aleman, H. Park, A. Alonso-Arroyo, and R. Onrubia, “Precision bounds in GNSS-R ocean altimetry, IEEE Journal of Selected Topics in Applied Earth Observation and Remote Sensing, vol. 7, no.5 pp. 1416-1423, 2014.
- [83] H. Carreno-Luengo, A. Camps, I. Ramos-Pérez, and A. Rius, “Experimental evaluation of GNSS-Reflectometry altimetric precision using the P(Y) and C/A signals”, IEEE Journal of Selected Topics in Applied Earth Observation and Remote Sensing , vol. 7, no. 5, pp. 1493-1500, 2014.
- [84] Canal d’Investigació I Experimentació Marítima. Available online: <http://ciemlab.upc.edu/instalaciones/icts-ciem> (accessed on 05 11 2015).
- [85] J.S. Löfgren, R. Haas, and J.M. Johansson, “High-rate local sea level monitoring with a GNSS-based tide gauge”, in Proceedings of the 2010 IEEE International Geoscience and Remote Sensing Symposium, pp. 3616-3619, Honolulu, HI, USA, July 2010.
- [86] K.M. Larson, J.S. Löfgren, and R. Haas, “Coastal sea level measurements using a single geodetic GPS receiver”, Advances in Space Research, vol. 51, no.8, pp. 1301-1310, 2013.

-
- [87] M.B. Rivas, M. Martín-Neira, “Coherent GPS reflections from the sea surface”, IEEE Geoscience Remote Sensing Letters, vol. 3, no.1, pp. 28-31, 2006.
- [88] K.M. Larson, R.D. Ray, F.G. Nievinski, J.T. Freymueller, “The accidental tide gauge: a GPS reflection case study from Kachemak bay Alaska”, IEEE Geoscience Remote Sensing Letters, vol. 10, no. 5, pp. 1200-1204, 2013.
- [89] J.S. Löfgren, R. Haas, H.G. Scherneck, and M.S. Bos, “Three months of local sea level derived from reflected GNSS signals”, Radio Science, vol. 46, no.6, RS0C05, 2011.
- [90] A.M. Semmling, J. Wickert, S. Schön, R. Stosius, M. Markgraf, T. Gerber, M. Ge, G. Beyerle, “A zeppelin experiment to study airborne altimetry using specular global navigation satellite system reflections”, Radio Science, vol. 48, no. 4, pp. 427-440, 2013.
- [91] Rohde & Schwarz SMU 200 A vector signal generator. Available online: www.rohde-schwarz.com/en/product/smu200a-productstartpage_63493-7555.html (accessed on 24 08 2015).
- [92] Bao-Yen Tsui, J. Fundamentals of Global Positioning System Receivers: A Software Approach, John Wiley & Sons: New York, NY, USA, 2000; pp.75.
- [93] K.M. Larson, and F.G. Nievinski, “GPS snow sensing: results from the EarthScope Plate Boundary Observatory”, GPS Solutions., vol. 17, no. 1, pp. 41-52, 2013.
- [94] N. Reul, and B. Chapron, “A simple algorithm for sea surface salinity retrieval from L-Band radiometric measurements at nadir”, in Proceedings of the 2003 IEEE International Geoscience and Remote Sensing Symposium, pp. 2783-2785, Toulouse, France, July 2003.
- [95] E. Cardellach, Sea Surface Determination Using GNSS Reflected Signals, Ph.D. Dissertation, Universitat Politècnica de Catalunya, Barcelona, Spain, 2001. Available online: http://www.ice.csic.es/view_theses.php?TID=2 (accessed on 16 08 2015).

-
- [96] T. Elfouhaily, D.R. Thompson, L. Linstrom, "Delay-Doppler analysis of bistatically reflected signals from the ocean surface: theory and application", IEEE Transactions on Geoscience and Remote Sensing, vol. 40, no. 3, pp. 560-573, 2002.
- [97] P. Beckmann, and A. Spizzichino. The Scattering of Electromagnetic Waves from Rough Surfaces, Artech House: Norwood, MA, USA, 1963; pp.125, 126, 150, 246.
- [98] V.C. Chen, F. Li, S.S. Ho, and H. Wechsler, "Micro-Doppler effect in radar: phenomenom, model and simulation study", IEEE Transactions on Aerospace and Electronics Systems, vol. 42, no.1, pp. 2-21, 2006.
- [99] T. Beltramonte, M. di Bisceglie, C. Galdi, and S.L. Ullo, "Space-time statistics for the number of specular points in sea surface GNSS reflectometry", in Proceedings of the 2014 IEEE International Geoscience and Remote Sensing Symposium, pp. 3818-3821, Quebec, Canada, July 2014.
- [100] A. Seyama, and A. Kimura, "The measured properties of irregular wave breaking and wave height change after breaking on the slope", in Proceedings of the 21st International Conference on Coastal Engineering, pp. 419-432, Malaga, Spain, June 1988,
- [101] K.S., Chen, A.K. Fung, and D.E., Weissman, "A backscattering model for ocean surface", IEEE Transactions on Antennas and Propagation, vol. 30, no. 4, pp. 811-817, 1992.
- [102] E. Valencia, Ocean Monitoring Using L-band Microwave Radiometry and GNSS-R, Ph. D. Dissertation, Universitat Politècnica de Catalunya, Barcelona, Spain, 2012. Available online: <http://www.tdx.cat/bitstream/handle/10803/96989/TEVD1de1.pdf?sequence=1> (accessed on 10 02 2015).
- [103] E. Valencia, A. Camps, J.F. Marchán-Hernandez, N. Rodríguez-Alvarez, I. Ramos-Pérez, and X. Bosch-Lluís, "Experimental determination of the sea correlation time using GNSS-R coherent data", IEEE Geoscience Remote Sensing Letters, vol. 7, no. 4, pp. 675-679, 2010.

-
- [104] J. Liang, and Q. Liang, "Outdoor propagation channel modeling in foliage environment", IEEE Transactions on Vehicular Technology, vol. 59, no. 5, pp. 2243-2252, 2010.
- [105] V. Rosmorduc, J. Benveniste, E. Bronner, S. Dinardo, O. Lauret, C. Maheu, M. Milagro, and N. Picot, Radar Altimetry Tutorial, Toulouse, France: ESA, CNES, 2011. Available online: <http://www.altimetry.info/> (accessed on 30 03 2015).
- [106] F. Martín, Interferometric GNSS-R Processing: Modeling and Analysis of Advanced Processing Concepts for Altimetry, Ph.D. Dissertation, Universitat Politècnica de Catalunya, Barcelona, Spain, 2015.
- [107] S. Gleason, C. Gommenginger, and D. Cromwell, "Fading statistics and sensing accuracy of ocean scattered GNSS and altimetry signals", Advances in Space Research, vol. 46, no. 2, pp. 208-220, 2010.
- [108] A. Rius, "PIRA: Pre-flight tests and flight plan", Technical Note from the PARIS-Phase A ESA project PIT-POC-CCN-2-TN0x, 2011.
- [109] C. Zuffada, T. Elfouhaily, and S. Lowe, "Sensitivity analysis of wind vector measurements from ocean reflected GPS signals", Remote Sensing of the Environment, vol. 88, no.3, pp. 341-350, 2003.
- [110] F. Martín, S. D'Addio, A. Camps, and M. Martín-Neira, "Modeling and analysis of GNSS-R waveforms sample-to-sample correlation", IEEE Journal of Selected Topics Applied Earth Observation and Remote Sensing, vol. 7, no. 5, pp. 1545-1559, 2014.
- [111] D.W. Allan, "Statistics of atomic frequency standards", in Proceedings of IEEE, vol. 54, no. 2, pp. 221-230, 1966.
- [112] NAVSTAR GPS Space User Segment Interfaces, IS-GPS-200F, 2011.
- [113] A. Rius, "PIT-POC Flight-2: First data analysis. PIT-POC-CCN-2-TN04", Technical Note from the PARIS-Phase A ESA project, 30 12 2011.
- [114] OSTM/Jason-2 Products Handbook, 2009. Available online: <http://www.osd.noaa.gov/ostm/> (accessed on 30 03 2012).

-
- [115] F. Fabra, GNSS-R as a Source of Opportunity for Remote Sensing of the Cryosphere, Ph.D. Dissertation, Universitat Politècnica de Catalunya, Barcelona, Spain, 2014. Available online: www.tdx.cat/bitstream/10803/117605/1/TFFC1de3.pdf (accessed on 10 08 2015).
- [116] N. Rodríguez-Alvarez, Contributions to Earth Observation Using GNSS-R Opportunity Signals, Ph.D. Dissertation, Universitat Politècnica de Catalunya, Barcelona, Spain, 2011. Available online: <http://www.tdx.cat/handle/10803/53636> (accessed on 04 09 2015).
- [117] D. Masters, V. Zavorotny, S. Katzberg, and W. Emery, “GPS signal scattering from land for moisture content determination”, in Proceedings of the 2000 IEEE International Geoscience and Remote Sensing Symposium, pp. 3090-3092, Honolulu, USA, July 2000.
- [118] K.M. Larson, E.E. Small, E.D. Gutmann, A.L. Bilich, J.J. Braun, and V.U. Zavorotny, “Use of GPS receivers as a soil moisture network for water cycle studies”, Geophysical Research Letters, vol. 35, no. 24, L2440, 2008.
- [119] N. Rodríguez-Alvarez, X. Bosch-Lluís, A. Camps, M. Vall-llossera, E. Valencia, J.F. Marchán-Hernandez, and I. Ramos-Pérez, “Soil moisture retrieval using GNSS-R techniques: experimental results over a bare soil field”, IEEE Transactions on Geoscience and Remote Sensing, vol. 47, no. 11, pp. 3616-3624, 2009.
- [120] N. Rodríguez-Alvarez, A. Monerris, X. Bosch-Lluís, A. Camps, M. Vall-llossera, J.F. Marchán-Hernandez, I. Ramos-Pérez, E. Valencia, J. Martínez-Hernandez, N. Sánchez-Martín, G. Baroncini-Turricchia, and C. Pérez-Gutiérrez, “Soil moisture and vegetation height retrieval using GNSS-R techniques”, in Proceedings of the 2000 IEEE International Geoscience and Remote Sensing Symposium, pp. III-869-III-872, Cape Town, South Africa, July 2009.
- [121] E.E. Small, K.M. Larson, and J.J. Braun, “Sensing vegetation growth with reflected GPS signals”, Geophysical Research Letters, vol. 37, no. 12, L12401, 2010.
- [122] A. Egido, M. Caparrini, G. Ruffini, S. Paloscia, E. Santi, L. Guerriero, N. Pierdicca, and N. Floury “Global navigation satellite systems reflectometry as a

remote sensing tool for agriculture”, MDPI Remote Sensing, vol. 4, no. 8, pp. 2356-2372, 2012.

[123] N. Pierdicca, L. Guerriero, M. Caparrini, A. Egido, S. Paloscia, E. Santi, and Floury, “GNSS reflectometry as a tool to retrieve soil moisture and vegetation biomass: experimental and theoretical activities”, in Proceedings of the International Conference on Localization and GNSS (ICL-GNSS), pp. 1-5, Torino, Italy, June 2013.

[124] N. Pierdicca, L. Guerriero, R. Giusto, M. Brogioni, and A. Egido, “SAVERS: a simulator of GNSS reflections from bare and vegetated soils”, IEEE Transactions on Geoscience and Remote Sensing, vol. 52, no. 10, pp. 6542-6554, 2014.

[125] A.K. Fung and H.J. Eom, “Coherent scattering of a spherical wave from an irregular surface”, IEEE Transactions on Geoscience and Remote Sensing, vol. AP-31, no. 1, pp. 68-72, 1983.

[126] N. Pierdicca, L. Guerriero, M. Brogioni, A. Egido, “On the coherent and non coherent components of bare and vegetated terrain bistatic scattering: modelling the GNSS-R signal over land”, in Proceedings of the 2012 IEEE International Geoscience and Remote Sensing Symposium, pp. 3407-3410, Munich, Germany, July 2012.

[127] M. Unwin, P. Jales, P. Blunt, S. Duncan, “Preparation for the first flight of SSTL’s next generation space GNSS receivers”, in Proceedings of the Satellite Navigation Technologies and European Workshop on GNSS Signals and Signal Processing, (NAVITEC), 6th ESA Workshop, pp. 1-6, ESA-ESTEC, Noordwijk, The Netherlands, December 2012.

[128] J. Wickert, G. Beyerle, E. Cardellach, C. Förste, T. Gruber, A. Helm, M.P. Hess, P. Hoeg, N. Jakowski, M. Kern, O. Montenbruck, A. Rius, M. Rothacher, C.K. Shum, and C. Zuffada, “GEROS-ISS - GNSS Reflectometry, Radio Occultation and Scatterometry on-board the International Space Station”, URSI Commission F Microwave Signatures 2013 Specialist Symposium on Microwave Remote Sensing of the Earth, Oceans, and Atmosphere, Espoo (Helsinki), Finland, October 2013.

[129] H. Carreno-Luengo, A. Camps, I. Ramos-Pérez, G. Forte, R. Onrubia, and R. Díez, “³Cat-2: A P(Y) and C/A experimental nanosatellite mission”, in Proceedings

of the 2013 IEEE International Geoscience and Remote Sensing Symposium, pp. 843-846, Melbourne, Australia, July 2013.

[130] A. Kinnaird, BEXUS User Manual, ID: BX_REF_BX_user manual v6-10_05Feb14, 2014. Available online: http://www.rexusbexus.net/index.php?option=com_content&view=article&id=51&Itemid=63, (accessed on 05 05 2015).

[131] J.J.V. Zyl, "The effect of topography on radar scattering from vegetated areas" IEEE Transactions on Geoscience and Remote Sensing, vol. 31, no.1, 153-160, 1993.

[132] P. Ferrazzoli, L. Guerriero, N. Pierdicca, and R. Rahmoune, "Forest biomass monitoring with GNSS-R: theoretical simulations", Advances in Space Research, vol. 47, pp. 1823-1832, 2011.

[133] A. Egido, S. Paloscia, E. Motte, L. Guerriero, N. Pierdicca, M. Caparrini, E. Santi, G. Fontanelli and N. Floury, "Airborne GNSS-R soil moisture and above ground biomass observations", IEEE Journal of Selected Topics in Applied Earth Observations and Remote Sensing, vol. 7, n.5, pp. 1522-1532, 2014.

[134] H. Park, A. Camps, E. Valencia, N. Rodríguez-Alvarez, X. Bosch-LLuís, I. Ramos-Pérez, and H. Carreno-Luengo, "Retracking considerations in spaceborne GNSS-R altimetry", GPS solutions, vol. 16, no. 4, pp. 507-518, 2012.

[135] A.T. Caicoya, F. Kugler, I. Hajnsek, and K. Papathanassiou, "Boreal forest biomass classification with TANDEM-X", in Proceedings of the 2012 IEEE International Geoscience and Remote Sensing Symposium, pp. 3439-3442, Munich, Germany, July 2012.

[136] Global map of forest height produced from NASA's ICESAT/GLAS, MODIS and TRMM sensors. Available online: <http://www.nasa.gov/topics/earth/features/earth20120217map.html> (accessed on 05 08 2015).

[137] R.D. De Roo, and F.T. Ulaby, "Bistatic specular scattering from rough dielectric surfaces", IEEE Transactions on Antennas and Propagation, vol. 42, no. 2, pp. 220-231, 1994.

-
- [138] J. Dampf, T. Pany, N. Falk, B. Riedl, and J.O. Winkel, "Galileo altimetry using AltBOC and RTK techniques", *Inside GNSS*, pp. 54-63, 2013. Available online: <http://www.insidegnss.com/auto/janfeb13-WP.pdf> (accessed on 12 04 2015).
- [139] T. Hobiger, R. Haas, and J.S. Löfgren, "GLONASS-R: GNSS reflectometry with a frequency division multiple access-based satellite navigation system", *Radio Science*, vol. 49, no, 4, pp. 271-282, 2014.
- [140] M. Arcioni, P. Bensi, M.W.J. Davidson, M. Drinkwater, F. Fois, C.C. Lin, R. Meynart, K. Scipal, and P. Silvestrin, "ESA's Biomass mission candidate system and payload overview", in *Proceedings of the 2012 IEEE International Geoscience and Remote Sensing Symposium*, pp. 5530-5533, Munich, Germany, July 2012.
- [141] M. Unwin, P. Jales, A.S. Curiel, M. Brenchley, M. Sweeting, C. Gommenginger, and J. Roselló, "Sea state determination with GNSS Reflectometry on TechDemoSat-1", in *Proceedings of the 2014 ESA Small Satellites, Systems & Services Symposium*, Mallorca, Spain, May 2014.
- [142] R. Rose, W. Wells, D. Rose, C. Ruf, A. Ridley, and K. Nave, "Nanosat technology and managed risk: an update of the CyGNSS microsatellite constellation mission development", in *Proceedings of the 28th AIAA/USU Conference on Small Satellites*, SSC14-VI-4, pp. 1-12, Logan, Utah, August 2014.
- [143] H. Carreno-Luengo, A. Camps, R. Jové, A. Alonso, R. Olivé, A. Amèzaga, D. Vidal, J. F. Munoz, "The ³Cat-2 Project: GNSS-R In-Orbit Demonstrator for Earth Observation", in *Proceedings of the 2014 ESA Small Satellites, Systems & Service Symposium*, Mallorca, Spain, May 2014.
- [144] M. I. Skolnik, *Radar Handbook*, McGraw Hill. 2nd ed. 1990.
- [145] D. Pascual, H. Park, A. Camps, A. Alonso-Arroyo and R. Onrubia, "Simulation and analysis of GNSS-R composite waveforms using GPS and Galileo Signals", *IEEE Journal of Selected Topics in Applied Earth Observations and Remote Sensing*, vol. 7, no. 5, pp. 1461-1468, 2014.
- [146] S.U. Qaisar and A.G. Dempster, "Cross-correlation performance comparison of L1 & L2 C GPS codes for weak signal acquisition", in *Proceedings of the International Symposium on GPS/GNSS*, Yokohama, Japan, November 2008.

-
- [147] GLONASS Interface Control Document, 2008. Available online: <http://www.spacecorp.ru/upload/iblock/1c4/cgs-aaixmyt%205.1%20ENG%20v%202014.02.18w.pdf> (accessed on 09 03 2015).
- [148] F. Boon, J.M. Sleewaegen, A. Simsky, and W. De Wilde, “GPS+GLONASS RTK: making the choice between civilian and military L2 GLONASS”, in Proceedings of the 21st International Technical Meeting of the Satellite Division of The Institute of Navigation, pp. 2860-2867, Savannah, GA, USA, September 2008.
- [149] K. Borre, “The E1 Galileo signal”, Aalborg University, Denmark, 2009. Available online: http://waas.stanford.edu/papers/Borre/galileo_sig.pdf (accessed on 09 03 2015).
- [150] V.U. Zavorotny, and A.G. Voronovich, “Bistatic GPS signal reflections at various polarizations from rough land surface with moisture content”, in Proceedings of the 2000 IEEE International Geoscience and Remote Sensing Symposium, pp. 2852-2854, Honolulu, Hawaii, USA, July 2000.
- [151] E. Cardellach, S. Ribó, and A. Rius, “Technical Note on POLarimetric Phase Interferometry (POPI)”, 2006. Available online: <http://arxiv.org/pdf/physics/0606099.pdf> (accessed on 01 03 2015).
- [152] D. Selva and D. Krejci, “A survey and assessment of the capabilities of cubesats for Earth observation”, *Acta Astronautica*, vol. 74, pp. 50-68, 2012.
- [153] S. Lee, A. Hutputasin, A. Toorian, W. Lan and R. Munakata, *Cubesat Design Specification*, California Polytechnic State University, 2009.
- [154] R. Hevner, W. Holemans, J. Puig-Suari, and B. Twiggs, “An advanced standard for cubesats”, in Proceedings of the 25th annual AIAA/USU Conference on Small Satellites, Logan, UT, USA, August 2011.
- [155] Planet labs Spire Web Site. Available online: <https://www.planet.com/solutions/#satellites> (accessed on 10 09 2015).
- [156] C. Wagner, and J. Klokocnik, “The value of oceans reflections of GPS signals to enhance satellite altimetry: data distribution and error analysis”, *Journal of Geodesy*, vol.77, no. 3, pp. 128-138, 2003.

-
- [157] M. Unwin, “TechDemoSat-1 and the GNSS Reflectometry experiment”, TechDemoSat-1 User Consultation Meeting, National Oceanography Centre, Southampton, United Kingdom, May 2015. Available online <http://www.merrbys.co.uk:8080/CatalogueData/Documents/TDS-1%20SGRReSI%20Experiment.pdf> (accessed on 05 06 2015).
- [158] M. Unwin, J. Pales, P. Blunt, S. Duncan, M. Brummitt, and C. Ruf, “The SGR-ReSI and its application for GNSS Reflectometry on the NASA EV-2 CyGNSS mission”, in Proceedings of the 2013 IEEE Aerospace Conference, Big Sky, MT, USA, March 2013.
- [159] J. Wickert, “Space based GNSS atmosphere sounding: radio occultation”, GfG² Summer School, GFZ Potsdam, July 2013. Available online http://www.gfg2.eu/sites/gfg2.eu/files/wickert_radio_occultation.pdf (accessed on 20 05 2015).
- [160] V.U. Zavorotny, S. Gleason, E. Cardellach and A. Camps, Tutorial on Remote Sensing Using GNSS Bistatic Radar of Opportunity, IEEE Geoscience and Remote Sensing Magazine, vol.2, n.5, December 2014.
- [161] H. Carreno-Luengo, A. Amèzaga, A. Bolet, D. Vidal, J. Jané, J.F. Munoz, R. Olivé, A. Camps, J. Carola, N. Catarino, M. Hagenfeldt, P. Palomo and S. Cornara, “³Cat-2: a 6U cubesat-based multi-constellation, dual-polarization, and dual-frequency GNSS-R and GNSS-RO experimental mission”, in Proceedings of the 2015 IEEE International Geoscience and Remote Sensing Symposium, pp. 5115-5118, Milan, Italy, July 2015.
- [162] Antenna Lab Web Site, Universitat Politècnica de Catalunya. Available online: <http://www.tsc.upc.edu/antennalab/> (accessed on 10 09 2015).
- [163] Gumstix Web Site. Available online: <https://www.gumstix.com/embedded-design/gumstix-in-space/> (accessed on 01 08 2015).
- [164] DAPCOM Data Services Web Site. Available online <http://www.dapcom.es/fapec.html> (accessed on 08 09 2015).
- [165] ISIS Magnetorquer board. Available online: http://www.cubesatshop.com/index.php?page=shop.product_details&flypage=flypa

ge.tpl&product_id=102&category_id=7&option=com_virtuemart&Itemid=69
(accessed on 15 09 2015).

[166] R. Wisniewski, Satellite Attitude Control Using Only Electromagnetic Actuation, Ph.D. Dissertation, Department of Control Engineering Aalborg University, Aalborg, Denmark, 1996. Available online: <http://citeseerx.ist.psu.edu/viewdoc/download?doi=10.1.1.467.832&rep=rep1&type=pdf> (accessed on 06 08 2015)

[167] J. Tuthill, Design and Simulation of a Nanosatellite Attitude Determination System, M.St. Thesis, Naval Postgraduate School, Monterrey, California, USA, 2009.

[168] E.J. Lefferts, F.L. Markley, and M.D. Shuster, "Kalman filtering for spacecraft attitude estimation", in Proceedings of the AIAA 20th Aerospace Sciences Meeting, Orlando, Florida, USA, 1982.

[169] J.W. Murrell, "Precision attitude determination for multimission spacecraft", in Proceedings of the AIAA Guidance, Navigation, and Control Conference, Palo Alto, CA, USA, 1978.

[170] GomSpace P31u Nanopower module. Available online: <http://gomspace.com/index.php?p=products-p31u> (accessed on 20 09 2015).

[171] B.R. Bowmann, W.K. Tobiskab, F.A. Marcos, and C. Valladares, "The JB2006 empirical thermospheric density model", Journal of Atmospheric and Solar-Terrestrial Physics, vol. 70, no. 5, pp. 774-793, 2008.

[172] ECSS-E-ST-10-04C. "Space environment, European Coordination for Space Standardization", ESA Publications Division, ESA-ESTEC, Issue 2.0, 15 Nov. 2008.

[173] J.R. Suggs, H.C. Euler, and S.W. Smith, "Future solar activity estimates for use in prediction of space environmental effects on spacecrafts orbital lifetime and performance", NASA, Marshall Space Flight Center, Huntsville, Alabama, 2013.

[174] Eigen-GL04 Combined Gravity Field Model GPZ Potsdam. Available online: <http://www.gfz-postdam.de/pb1/op/grace/results> (accessed on 10 08 2015).

-
- [175] Space debris mitigation. Available online: http://www.esa.int/Our_Activities/Space_Engineering_Technology/Clean_Space/Space_debris_mitigation (accessed on 17 09 2015).
- [176] W.J.Larson, and J.R.Wertz, Space Mission Analysis and Design, Space Technology Library. ISBN: 0-7923-5901-1, 2005.
- [177] J. Castellví and A. Camps, “MEPS SUM 1.01 MOS End-to-End Performance Simulator Software User Manual”, Universitat Politècnica de Catalunya and Institut Cartographic i Geologic de Catalunya, 2014.
- [178] D. Dinh, “Thermal modelling of nanosat”, M. St. Thesis, San José State University, San Jose, CA, USA, 2012. Available online: http://scholarworks.sjsu.edu/cgi/viewcontent.cgi?article=7740&context=etd_theses (accessed on 25 09 2015).
- [179] M.K. Frederiksen, S.V. Vedstesen, and T. Graversen, Attitude Control in AAU Cubesat, M.St. Thesis, Aalborg University, Denmark, 2002.
- [180] K.S. Nayar, K. Ikeuchi, and T. Kanade, “Surface reflection: physical and geometrical perspectives”, IEEE Transactions on Geoscience and Remote Sensing, vol. 13, no. 7, pp. 611-634, 1991.
- [181] H. Carreno-Luengo, A. Amèzaga, D. Vidal, R. Olivé, J.F. Munoz, and A. Camps, “First Polarimetric GNSS-R Measurements from a Stratospheric Flight and Coherent Reflectivity Simulations over Boreal Forests”, MDPI Remote Sensing, vol. 7, no. 10, pp. 13120-13138, 2015.